TSUNAMI AND STORM WAVE IMPACTS ON COASTAL BRIDGES

A DISSERTATION SUBMITTED TO THE GRADUATE DIVISION OF THE UNIVERSITY OF HAWAIʻI AT MĀNOA IN PARTIAL FULFILLMENT OF THE REQUIREMENTS FOR THE DEGREE OF

DOCTOR OF PHILOSOPHY

IN

OCEAN AND RESOURCES ENGINEERING

DECEMBER 2014

By

Betsy Rose Seiffert

Dissertation Committee :

R. Cengiz Ertekin, Chairperson

Kwok Fai Cheung

Eva-Marie Nosal

H. Ronald Riggs

Ian N. Robertson

.

Acknowledgements

I would like to express my sincerest gratitude to my advisor, Professor R. Cengiz Ertekin for his dedication, guidance and support through my studies. I would like to thank Professors H. Ronald Riggs and Ian N. Robertson for their valuable feedback during regular meetings. I would like to thank Professors Kwok Fai Cheung and Eva-Marie Nosal for their comments and discussion on this work. I would like to thank Professor Ian N. Robertson as well as Mitch Pinkerton and Kim Hartzog for their help with experiments. I would like to thank Natalie Nagai and Janis Kusatsu for help with administrative paperwork. Finally I would like to thank my family, who have always supported me in everything I set out to do.

This work is partially based on funding from the State of Hawaii's Department of Transportation (HDOT) and the Federal Highway Administration (FHWA), grant numbers DOT-08-004, TA 2009-1R. Any findings and opinions contained in this work are those of the author and do not necessarily reflect the opinions of the funding agencies.

Abstract

Wave loads on coastal bridges due to tsunami and storm waves are studied through a set of laboratory experiments and numerical calculations. Effects of wave nonlinearity and entrapped air on wave loading under conditions where the bridge may be partially or fully inundated are of particular interest. In addition, effects of compressibility and scaling are investigated through numerical calculations. With the destruction of bridges during recent events such as the 2011 Tohoku tsunami and hurricanes Katrina in 2005 and Ivan in 2004, this highlights the importance of this research in understanding the mechanisms of failure during such events to prevent future coastal bridge failures. Destruction of these bridges is not only financially costly, but can prevent emergency services from reaching coastal communities, thus potentially contributing to loss of life. Along with the bridges, this research is applicable to other coastal and offshore structures, such as piers, submerged breakwaters and offshore platforms, in which wave loading or entrapped air is of concern.

To investigate this problem, an extensive set of experiments is conducted on a flat plate, bridge model with girders, and a bridge model with varying percentages of trapped air that serves as a valuable benchmark for understanding wave loads on coastal structures, and bridges in particular. The wave cases tested include an extensive set of water depths, wave amplitudes and wave periods (for periodic waves) to cover a wide range of solitary and shallow-water to intermediate-water depth cnoidal waves. A range of model elevations was also tested to cover a range where the entire model is fully submerged below the water surface, to where the model is fully elevated above the water surface, and in the case of the model with girders, the girders are fully elevated as well. Experiments were conducted in a two-dimensional wave flume located in the University of Hawaii at Manoa's Hydraulics Lab in the Civil and Environmental Engineering Department. The models used were representative of a 1:35 scale model of a two-lane coastal bridge, typical in an island community. To study

the effects of entrapped air, a series of experiments is conducted where side panels were added to each side of the model to trap air between the girders. Then different percentages of air-relief openings are added to the panels to capture a range of cases where no air can escape between the girders, to where all the air can escape and the wave can freely interact with the bottom of the bridge deck.

Data from these experiments show the largest vertical uplift forces and forces in the direction of wave propagation on a flat plate and a bridge model occur when the structure is near the still-water level (SWL). For the cases where air is trapped, the addition of air relief openings significantly reduces uplift forces. Many current empirical relations estimating wave loads on coastal bridges only take hydrostatic effects into account. When compared with empirical estimations, data from these experiments show both hydrostatic and hydrodynamic forces must be taken into consideration. Comparison is also made with numerical calculations solving incompressible Euler's equations by use of the CFD software OpenFOAM, discussed in Hayatdavoodi (2013), Seiffert, Hayatdavoodi & Ertekin (2014), and Hayatdavoodi, Seiffert & Ertekin (2014*b*) with excellent agreement.

Effects of compressibility and scaling are tested numerically by solving compressible and incompressible Euler's equations. Numerical calculations show that the effects of compressibility on the long duration forces are small. Calculations also show that when Froude scaling is applied to forces on the model scale, the forces agree well with force calculations at the prototype scale. These results have important design implications for bridge engineers.

Contents

List of Figures

List of Tables

Nomenclature

$\%ARO$	Percentage of air relief opening area of air gap area
$\bar{U}$	Depth-averaged particle velocity
ϵ	Ratio of air relief opening to the area of the ceiling slab
η	Surface elevation
λ	Wavelength
$\mathbf{U}$	Velocity field
∇	Gradient vector
ν	Kinematic viscosity
ψ	Compressibility
ρ	Fluid density
θ	Phase angle
ξ	Wavemaker paddle board displacement
a	Wave amplitude
A_1	Projected area of the model onto the vertical plane
A_3	Projected area of the model onto the horizontal plane

A_c Area of air cavity between girders

A_r Area of air relief hole

B Width of the flat plate or bridge model in the direction parallel to wave propagation

c Wave celerity

C_1 Empirical coefficient

C_3 Empirical coefficient

C_o Courant number

C_r Reduction coefficient

C_ϵ Reduction coefficient due to air relief openings

Cn Jacobian elliptic function

$E(m)$ Second complete elliptic integral

F_x Horizontal force

F_z Vertical force

g Acceleration due to gravity

H Wave height

h Water depth

h_G Girder height

k Wave number

$K(m)$ First complete elliptic integral

L_G Girder spacing (CL to CL)

L_P Length of the flat plate or bridge model in the direction normal to wave propagation

m Jacobian elliptic parameter

N Number of girders

P Complex constant given by the LWA

P Complex constant

p Pressure

Q Complex constant given by the LWA

r_D Air relief hole diameter

T Wave period

t Time

t_f Wavemaker paddle stroke duration

t_G Girder height

t_P Thickness of the flat plate or bridge deck

z Distance between the SWL and the top of the submerged flat plate or bridge deck

z^* Distance between the SWL and the bottom of the elevated flat plate or bridge deck

z_B Distance between the SWL and the center of the submerged barge

z_G Distance between the SWL and the bottom of the bridge girders for an elevated bridge deck

Chapter 1

Introduction

1.1 Background

In post-disaster surveys taken after hurricane Katrina, such as by Robertson et al. (2007) and Chen et al. (2009), it was found that the major agent of failure of bridges, such as the US90 Bridge over Biloxi Bay, Mississippi, seen in Fig. 1.1, was a combination of sea level rise and increased wave action caused by storm surge. This led to increased hydrostatic and hydrodynamic forces on the inundated portions of the US90 bridge that ultimately led to its failure. Coastal bridges like those on the islands of the State of Hawaii are both close to the shoreline and at elevations near the water surface, making them particularly vulnerable to both storm surge and tsunami. Storm surge is the temporary rise in sea level during a major storm or hurricane. This increases the likelihood of a larger number of waves and waves with greater amplitude impinging on coastal structures which are normally located above the wave crest. During a tsunami event, large volumes of water may propagate onshore at high speeds. Coastal bridges are typically not designed for these increased loads and can be severely damaged or destroyed as witnessed most recently during Hurricanes Ivan and Katrina, and the 2004 Indian Ocean and 2011 Tohoku tsunamis.

Estimations of hydrodynamic forces on coastal bridges by analytical methods alone are not practical as the effects of trapped air, wave breaking, turbulence and green-water effects cannot be predicted analytically, in general, and thus, sometimes we must rely on empirical data. The blunt body of bridge structures, the presence of girders and proximity of coastal bridges to the water surface mean that these effects must be taken into consideration when predicting forces.

There is lack of experimental data covering cnoidal waves propagating over a bridge deck, and most existing experiments focus mainly on shorter-period periodic waves and do not include fully submerged cases. Also, there is limited experimental data covering periodic wave forces on a submerged horizontal plate or bridge. Cnoidal waves are of interest as they are highly nonlinear, shallow-water waves with very long periods, typical of waves that occur during a storm. There is limited experimental data covering solitary waves propagating over a horizontal plate or a bridge deck with girders, and those that exist do not focus on the submerged case. Solitary waves are of interest as they are a simple wave form, easy to reproduce numerically or in the laboratory, and are widely used as a simplified approximation of a tsunami, or the theoretically infinite limit of a cnoidal wave. To the author's knowledge, no experiments have been conducted that systematically measure effects of percentages of air relief openings on force on a coastal bridge deck.

Current methods for predicting wave loads on coastal bridges include Douglass et al. (2006), McPherson (2008) and AASHTO (2008). These methods are acceptable as a preliminary guideline but may not be suitable for partially or fully submerged bridges and have not been verified for cases involving solitary or cnoidal waves. Additionally, they rely on hydrostatic forces or coefficients estimated from experimental data for shorter-period waves under a small range of conditions. A more robust approach to determine wave loads on coastal bridges involving both the numerical and experimental approaches is necessary.

Figure 1.1: The US 90 Biloxi Bay Bridge was damaged during the 2005 Hurricane Katrina. The bridge spans were lifted off piles except at the higher elevations near a navigation channel, which received much less damage. Photo: J. O'Connor (for MCEER).

1.2 Literature Review

1.2.1 Laboratory Experiments

Much of the existing experimental work on submerged horizontal flat plates is concerned with wave reflection, diffraction and transmission as the wave passes over the plate, in the interest of the plate serving as a submerged breakwater or wave energy converter, such as described by Graw (1993), Carter et al. (2006), Liu et al. (2009) and Brossard et al. (2009), for example. Others, such as the experiments conducted by Brater et al. (1958), El Ghamry (1963), Wang (1970), Shih & Anastasiou (1992), Isaacson & Bhat (1996), Takaki (2001), Tirindelli et al. (2002), Cuomo et al. (2007), Marin (2009) and Rey & Touboul (2011), are mostly focused on periodic waves in deep or intermediate water regions. These studies are mainly motivated by the application of a flat plate, or an elevated slab of exposed piers, jetties, docks or bridges.

Existing experiments covering solitary wave forces on a horizontal plate are very limited. French (1979) conducted a series of experiments measuring wave peak-pressure on an elevated plate under solitary-wave flow, but the model geometry did not allow for overtopping and did not consider any submerged cases. Kulin (1958) conducted experiments on a solitary wave propagating over a submerged plate, testing a range of plate widths, water depths and wave amplitudes. However, the results were presented in the form of drag and inertia coefficients intended to be used in Morison's equation as an approach to calculating forces. More recently, Lo & Liu (2014) conducted experiments measuring vertical force on a submerged horizontal plate under a solitary-wave flow, as well as measuring the velocity field by use of particle image velocimetry (PIV). In those experiments, one water depth, two submergence depths and six wave amplitudes ranging from $a/h = 0.05 - 0.2$ were tested. Lo & Liu (2014) found that in the more nonlinear cases, where wave amplitude was large and the plate was at the

shallower submergence depth, linear shallow-water theory was unable to accurately predict the surface elevation and vertical force.

Existing laboratory experiments of wave loads on scaled bridge models focus mainly on periodic waves in deep or intermediate water regions, such as those conducted by Denson (1978), McPherson (2008), Bradner (2008), Marin (2009), and Cuomo et al. (2009). Denson (1978) conducted experiments on a 1:24 scale model of the Bay St. Louis Bridge which had been severely damaged during Hurricane Camille in 1969. Tests included a range of shallow and intermediate water depths, wave heights and both submerged and elevated bridge elevations. Unfortunately, only one wave period was tested and the wave heights were inconsistent so the experiments are not necessarily useful as they are not repeatable. With the exception of Cuomo et al. (2009), air relief openings were not included in the bridge models.

McPherson (2008) conducted experiments on a 1:20 scale model of a bridge section with girders and side rail under periodic intermediate water-depth waves and solitary wave loads. The bridge model was kept at a constant height while water depth was varied to simulate both elevated and submerged conditions. In that work, the guardrail was placed only at the leading edge of the model and was partially permeable and thus created three-dimensional effects. A horizontal flat plate was also tested for periodic intermediate water-depth waves. Bradner (2008) conducted experiments on a 1:5 reinforced concrete scale model of the I-10 Bridge over Escambia Bay, Florida, which failed during Hurricane Ivan in 2004. Waves tested were those estimated to have occurred at the U.S. 90 Bridge over Biloxi Bay during Hurricane Katrina in 2005 as presented by Chen et al. (2009). Only elevated bridge conditions were tested. One test was conducted where the top of the bridge deck was even with the SWL. Marin (2009) tested a horizontal flat plate and Sheppard & Marin (2009) tested a model based on a 1:8 scale of the spans that failed on the I-10 Escambia Bay Bridge during

Hurricane Ivan. Several configurations were tested including a horizontal slab, a slab with girders, a slab with girders and overhangs, and a slab with girders, overhangs and rails. Intermediate water-depth waves were tested for both elevated and submerged conditions. Rey & Touboul (2011) conducted experiments to measure forces on a submerged flat plate under intermediate and deep water wave conditions.

Lau et al. (2011) conducted laboratory experiments to measure solitary wave forces on an inland coastal bridge model. In that work, however, the model is located closer to the shore such that the initial solitary wave would transform into a bore before interacting with the structure.

Wave parameters considered in the above mentioned experiments as well as waves run in our experiments are plotted after Le Mehaute (1969) for regions of wave theories valid to give a visual representation of what has been done and how our proposed experiments will contribute to filling in the gaps in existing data (Figs. 1.2 and 1.3). The approximate line for breaking limit is given by $H/d = 0.78$ for shallow and intermediate water and $H/L = 0.14$. It is stressed that the different wave theories do not have exact boundaries, and the lines for shallow, intermediate and deep water and linear theory are meant only as a guideline for selecting the appropriate wave theory.

Cuomo et al. (2009) carried out large scale, three-dimensional experiments to study storm wave loading on a coastal bridge model. Air-relief slots added to the bridge deck surface were found to reduce the uplift forces. However, with larger wave amplitudes, the slots were found to not be of adequate size to effectively reduce uplift loads. Hoshikuma et al. (2013) observed the effect of buoyancy due to entrapped air in their experiments on a 1:20 scale bridge model impacted by a tsunami bore.

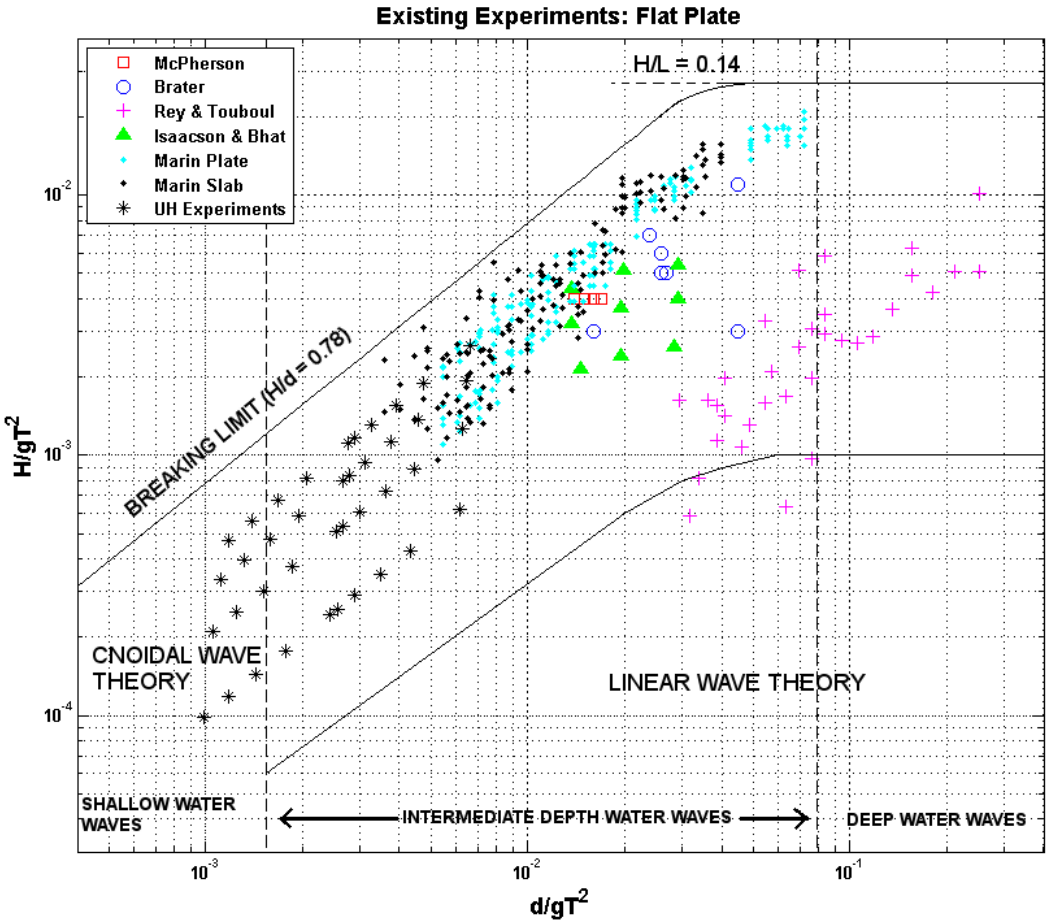

Figure 1.2: Waves ran during UH experiments to determine cnoidal wave loads on a horizontal flat plate are plotted along with those from existing experiments on the Le Mehaute (1969) graph for regions of wave theories valid.

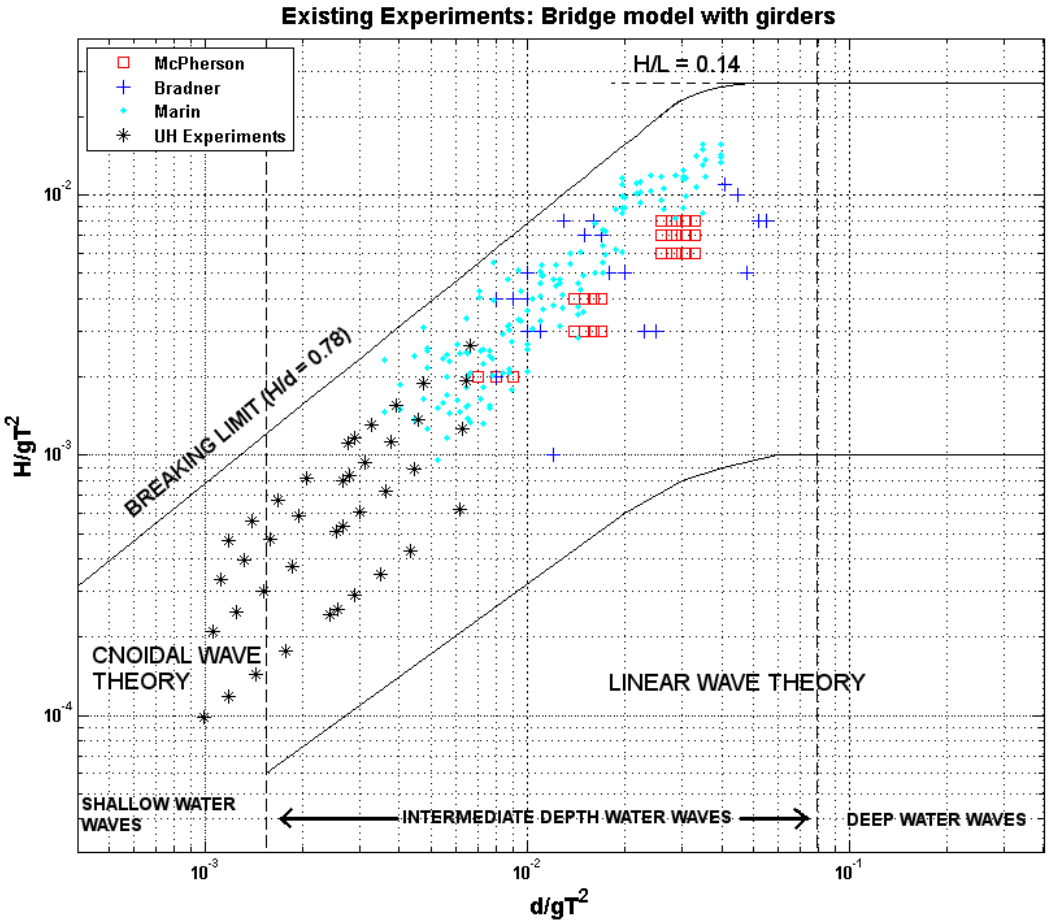

Figure 1.3: Waves ran during UH experiments to determine cnoidal wave loads on a bridge model with girders are plotted along with those from existing experiments on the Le Mehaute (1969) graph for regions of wave theories valid.

1.2.2 Calculations

OpenFOAM has demonstrated success in modeling waves, wave breaking, and run up as concluded by Higuera et al. (2013), flow separation (Lysenko et al. (2013)) and wave slamming forces (Chella et al. (2012)). Andersson (2011) calculated wave induced forces on a semi-submerged horizontal cylinder using the incompressible, two-phase OpenFOAM solver, *interfoam*. Calculations were compared with experimental data with good agreement. Bricker et al. (2012) used the OpenFOAM solver *interfoam* to model the Utatsu highway bridge which was damaged in the 2011 Tohoku tsunami. Although there is no direct experimental data to compare with in this case, OpenFOAM was able to predict the most likely damage mechanisms of the bridge during the tsunami.

Suponitsky et al. (2014) carried out simulations using the *compressibleInterFoam* solver in OpenFOAM to calculate compression of a gas bubble by an imploding molten lead shell. Trask (2010) also had success with simulation of spray formation using the *compressibleInterFoam* solver in OpenFOAM.

A numerical model that solves the nonlinear and unsteady Level 1 Green-Naghdi equations to estimate horizontal and vertical forces on a submerged horizontal plate was developed by Hayatdavoodi & Ertekin (2012) with further details found in Hayatdavoodi (2013). The GN equations are solved numerically by use of the finite-difference method employing a modified Euler method for time discretization, providing a second-order numerical approximation. Results for both vertical and horizontal forces are compared with the available experimental data with good agreement. Hayatdavoodi, Seiffert & Ertekin (2014*a*) performed calculations using the GN numerical model to determine wave loading on a submerged plate under cnoidal waves with good agreement with the experimental data presented in Hayatdavoodi, Seiffert & Ertekin (2014*a*) and in section 5.4.1 of this dissertation.

Bozorgnia (2012) calculated forces on highway bridge superstructures due to hurricane

waves by solving the compressible Euler's equations using the commercial CFD software STAR-CCM+. Calculations are validated by comparing with the experiments of French (1979) and then compared with Bradner (2008) with good agreement. The validated model is then applied to a 1:5 scale model and prototype scale of the Escambia Bay Bridge damaged during Hurricane Ivan. Bozorgnia (2012) concluded that the accuracy of the numerical model used was highly dependent on the mesh size and time step Δt. It was concluded that the failure of bridges, such as the Escambia Bay Bridge, was less likely due to short-duration impact forces and more likely due to the longer duration uplift forces. Calculations were compared with and without air vents on the deck surface, and it was concluded that venting significantly damps out wave energy and reduces uplift forces such that damage to the bridge could have been prevented. Bozorgnia (2012) also found that forces calculated at the model scale, then scaled to prototype scale using Froude scaling agreed well with the forces calculated at the prototype scale, even when the effect of air entrapment is considered.

Huang & Xiao (2009) investigated wave loads on the Escambia Bay Bridge during Hurricane Ivan by use of a numerical model that solved the incompressible Reynolds-averaged Navier-Stokes equations using a $\kappa - \epsilon$ turbulence closure and employing the volume of fluid method to capture the free surface. Results were validated with experimental data and then applied to three different scenarios for the deck elevation of the Escambia Bay Bridge to predict the failure mechanisms during the storm. Jin & Meng (2011) used two different numerical models to predict wave loads on coastal bridges during storm wave loading. The first solves the Navier-Stokes equations and employs the volume of fluid method to capture the free surface and was used to predict effects of green water on the structure at different bridge elevations. The second model solves for complex velocity potential from Laplace's equation and boundary conditions using the finite-difference method and was used to predict loads on fully submerged structures. Comparison was made between the numerical model and

large-scale experimental data with good agreement.

1.3 Objectives

The overall objective of this study is to provide a useful benchmark for understanding wave loads on coastal bridges during a storm or tsunami. By performing experiments with an extensive range of parameters, we seek to gain insight into the effects of wave amplitude, wave length, and submergence depth or elevation, on vertical and horizontal forces. Nonlinear shallow-water waves, typical during a storm or tsunami, are of particular interest. To have confidence in the accuracy of the presented laboratory data, a comparison is made between experimental measurements and numerical calculations. A comparison is also made with existing empirical relations to investigate the applicability of such relations to storm or tsunami conditions. In the interest of investigating ways of reducing forces on bridges during a storm or tsunami event, effects of entrapped air and air relief openings are also studied experimentally. To determine whether compressibility should be considered when calculating forces numerically, a set of calculations is done solving both incompressible and compressible Euler's equations. Furthermore, it is of interest to calculate numerically the forces at both the model and prototype scale. This allows us to have confidence that our experimental measurements can be scaled to the prototype scale using Froude scaling.

In Chapter 2, the design for a set of experiments to measure loading due to solitary and cnoidal waves on a horizontal flat plate, bridge model with girders, and bridge model with varying percentages of air relief openings is outlined in detail. In Chapter 3, a numerical method is described for calculating wave loads on the bridge model with girders using compressible Euler's equations. In Chapter 4, existing empirical methods are described that will be compared with laboratory measurements. Chapter 5 presents laboratory measurements

for solitary and cnoidal wave interaction with a horizontal flat plate and a bridge model with girders. Comparisons with numerical calculations and empirical relations are given. Chapter 6 presents laboratory measurements for solitary and cnoidal wave interaction with a bridge model that includes different percentages of air relief openings on the model. Forces calculated numerically on the bridge model with girders using incompressible and compressible Euler's equations at the model and prototype scale are also given in Chapter 6. Chapter 7 provides a summary and concluding remarks.

Chapter 2

Experiments

2.1 Facilities and Instrumentation

Experiments are conducted in a two-dimensional wave flume located in the University of Hawaii at Manoa's Hydraulics Laboratory in the Civil and Environmental Engineering Department. The wave flume measures 9.14 m length, 15.24 cm width and 15.5 cm height and waves are generated by a piston-type wavemaker. Parabolic-shaped foam wave absorbers manufactured by H.R. Wallingford are placed at each end of the wave flume, one as an absorbing beach and one to absorb reflections behind the wavemaker. Three capacitance-type wave gauges measure surface elevation with a spatial resolution of 0.1 mm and sampling rate of 71 Hz (manufactured by JFE Advantech Co., Ltd). Horizontal forces are measured using three 44.5 N load cells and vertical forces are measured using one 44.5 N load cell (manufactured by Omegadyne, Inc.). Horizontal force is obtained by adding measurements from the three horizontal load cells at each time step, whereas the vertical force is obtained directly from the vertical load cell measurements. The load cells have a resolution of 0.022 N. Force data are sampled at 100Hz or 1000Hz. Force sampling rate is discussed further in section 2.5. Air and water temperature were measured at $20°C$.

2.2 Wave Generation

2.2.1 Theory

Paddle motion of the piston-type wavemaker is controlled by the software LabVIEW and is dictated by an input time-velocity displacement series. The time-velocity displacement series is generated following a method outlined by Goring (1979) and discussed in Goring & Raichlen (1980) to solve for paddle displacement and initial stroke position using the solution for surface elevation (η) for shallow-water waves. This theory assumes that the horizontal velocity is constant over the water depth and equates the wave board velocity to the depth-averaged particle velocity:

$$\frac{d\xi(t)}{dt} = \bar{U}(\xi, t) = \frac{c\eta(\xi, t)}{h + \eta(\xi, t)}, \tag{2.1}$$

where ξ is the paddle board displacement, $\bar{U}$ is depth-averaged particle velocity, c is wave celerity, h is water depth, η is the surface elevation for the desired wave, and t is time. Goring (1979) assumes $\eta(\xi, t)$ has the following form:

$$\eta(\xi, t) = Hf(\theta), \tag{2.2}$$

where f is some function of the phase angle $\theta = k(ct - \xi)$, H is wave height and k is the wave number. From this, the implicit relationship,

$$\xi(t) = \frac{H}{kh} \int_0^\theta f(\omega) d\omega, \tag{2.3}$$

is derived. $\xi(t)$ can be obtained by using the Newton-Raphson method. First, the equation for phase angle can be re-arranged to obtain

$$\xi(t) = ct - \theta/k, \tag{2.4}$$

and then a function F can be defined as,

$$F = \theta - kct + \frac{H}{h} \int_0^\theta f(\omega) d\omega = 0. \tag{2.5}$$

F is evaluated iteratively using the Newton-Raphson method to solve for θ, which can then be used to solve for $\xi(t)$ using Eq. 2.4. A more detailed description outlining these derivations can be found in Goring (1979) and Hughes (1993).

In the present experiments, the solution of the Level I Green-Naghdi (GN) equations for the surface elevation of a solitary and cnoidal wave given by Ertekin & Wehausen (1986), Ertekin & Becker (1998) and Sun (1991), is used. For a solitary wave, the surface elevation is given by

$$\eta(x,t) = asech^2\left(\sqrt{\frac{3a}{4h^2(h+a)}}(x-ct)\right), \tag{2.6}$$

where a is the wave amplitude and x is horizontal coordinate in the direction of wave propagation. Wave celerity for a solitary wave is $c = \sqrt{g(h+a)}$, following the solution proposed by Russell (1844) and confirmed independently by Boussinesq (1871) and Rayleigh (1876); it is also the solution of the Level I GN equations, see e.g., Eq. (5.12) of Ertekin (1984). From Eq. (2.2),

$$f(\theta) = sech^2(\theta), \tag{2.7}$$

where $\theta = \kappa(ct - \xi)$ and

$$\kappa = \sqrt{\frac{3a}{4h^2(h+a)}}. \tag{2.8}$$

Solving for $\xi(t)$, we have

$$\xi(t) = \frac{a}{\kappa h} tanh(\theta). \tag{2.9}$$

Paddle position $\xi(t)$ is solved by using the Newton-Raphson method by defining the function F as,

$$F = \theta - \kappa ct + \frac{a}{h} tanh(\theta) = 0. \tag{2.10}$$

For each time step t,

$$\theta^{i+1} = \theta^i - \frac{\theta^i - \kappa ct + \frac{a}{h} tanh(\theta^i)}{1 + \frac{a}{h} sech^2(\theta^i)} \tag{2.11}$$

is evaluated iteratively for θ, and then paddle position $\xi(t)$ is given by

$$\xi(t) = ct - \frac{\theta}{\kappa} \tag{2.12}$$

at each time step. The initial stroke position $\xi(0)$ and stroke duration t_f are

$$\xi(0) = -\frac{H}{\kappa h}, \tag{2.13}$$

and

$$t_f \approx \frac{1}{\kappa c}\left(3.80 + \frac{H}{h}\right). \tag{2.14}$$

Paddle displacement calculated from the solution of the KdV equation for the surface elevation of a solitary wave follows closely that of the solution using the GN equations with the only difference being the parameter κ. For the KdV equations, $\kappa = \sqrt{\frac{3H}{fh^3}}$. Details of the calculation of these parameters can be found in Goring (1979) and Hughes (1993). It is noted that Eq. (2.6) is the same solution given by Rayleigh (1876), however the particle velocities given by the GN equations are different.

The dimensional form for the solution of the GN equations for surface elevation of a cnoidal wave is given as,

$$\eta = \eta_2 + HCn^2\left\{\theta, m\right\}, \tag{2.15}$$

where

$$\begin{aligned}
\theta &= 2K\left(\frac{x}{\lambda} - \frac{t}{T}\right), \\
c^2 &= gh\left(1 + \frac{\eta_1}{h}\right)\left(1 + \frac{\eta_2}{h}\right)\left(1 + \frac{\eta_3}{h}\right), \\
\eta_1 &= -\frac{HE}{mK}, \\
\eta_2 &= \frac{H}{m}\left(1 - m - \frac{E}{K}\right), \\
\eta_3 &= \frac{H}{m}\left(1 - \frac{E}{K}\right),
\end{aligned} \tag{2.16}$$

and the dispersion relation is given by

$$H\lambda^2 = \frac{16}{3}\left(\frac{c^2h^2}{g}\right)mK^2, \tag{2.17}$$

where H is the wave height, m is the Jacobian elliptic parameter, Cn is the Jacobian elliptic function, θ is the argument, $K(m)$ is the first complete elliptic integral, $E(m)$ is the second complete elliptic integral, c is the wave phase speed, x is displacement in the direction of wave propagation, λ is the wavelength, t is time, T is wave period, h is water depth, and g is gravitational acceleration. The dispersion relation is used to solve for the implicit parameter m using the Newton-Raphson method. Here Newton-Raphson method can be applied directly since the input parameter is the wave length λ. Cho (2003) gives a way to solve for m if the initial input parameter is the wave period T.

Referring to Eq.(2.2), and in the case of a cnoidal wave

$$f(\theta) = \frac{\eta_2}{H} + Cn^2\left\{\theta, m\right\}, \tag{2.18}$$

where $\theta = 2K\left(\frac{t}{T} - \frac{\xi}{\lambda}\right)$,

$$\xi(t) = ct - \frac{\lambda\theta}{2K}, \tag{2.19}$$

and

$$\frac{d\xi(t)}{d\theta} = \frac{\lambda H}{2KH} f(\theta), \tag{2.20}$$

leading to,

$$\xi(t) = \frac{\lambda H}{2Kh}\int_0^\theta \frac{\eta_2}{H} + Cn^2\left\{\omega, m\right\} d\omega. \tag{2.21}$$

Integrating Eq. (2.21) gives,

$$\xi(t) = \frac{\lambda}{2Kh}\left\{\eta_2\theta + \frac{H}{m}\left[E(\theta, m) - m'\theta\right]\right\}, \tag{2.22}$$

where $m' = 1 - m$. The function F is written as

$$F = \frac{\lambda\theta}{2K} - ct + \frac{\lambda}{2Kh}\left\{\eta_2\theta + \frac{H}{m}\left[E(\theta, m) - m'\theta\right]\right\} = 0, \tag{2.23}$$

and is then solved for θ at each time t using the Newton-Raphson method. Having found θ at each time t, the paddle displacement is given by Eq. (2.19).

Goring (1979) suggests the starting position of the wave board should correspond to when the paddle velocity and wave amplitude are zero:

$$\frac{d\xi}{dt} = \bar{U} = 0 \tag{2.24}$$

and

$$\eta_2 + HCn^2 \{\theta_0, m\} = 0, \tag{2.25}$$

giving,

$$\theta_0 = Cn^{-1} \left(\frac{\eta_2}{H}\right)^{1/2}. \tag{2.26}$$

Substituting θ_0 in Eq. (2.21), we obtain

$$\xi_{max} = -\xi_{min} = \frac{\lambda}{2Kh} \left\{ \eta_2 \theta_0 + \frac{H}{m} \left[E(\theta_0, m) - m' \theta_0 \right] \right\}, \tag{2.27}$$

and

$$\frac{t_0}{T} = \frac{\eta_{max}}{\lambda} + \frac{\theta_0}{2K}. \tag{2.28}$$

To start the paddle motion at the time where plate velocity and wave amplitude are zero, the initial time is calculated as $T - t_0$.

To match the water particle velocity of a solitary wave, the wave board moves with an initial acceleration and then deceleration, shown in Fig. 2.1 (a). For the wave board to match the depth-averaged particle velocity of a cnoidal wave, when the wave and the paddle are moving in the same direction, the paddle must move faster to match the water particle velocity. When the wave and paddle are moving in the opposite directions, the paddle must move slower to match the water particle velocity. This causes the saw-tooth pattern in cnoidal wave paddle displacement, shown in Fig. 2.2 (a). Figure 2.1 (a) - (c) shows the wave-board displacement, surface elevation and depth-integrated velocity for solitary waves generated using both the GN and KdV equations. The wave-board displacement calculated using the GN equations shows a larger displacement and a longer duration than

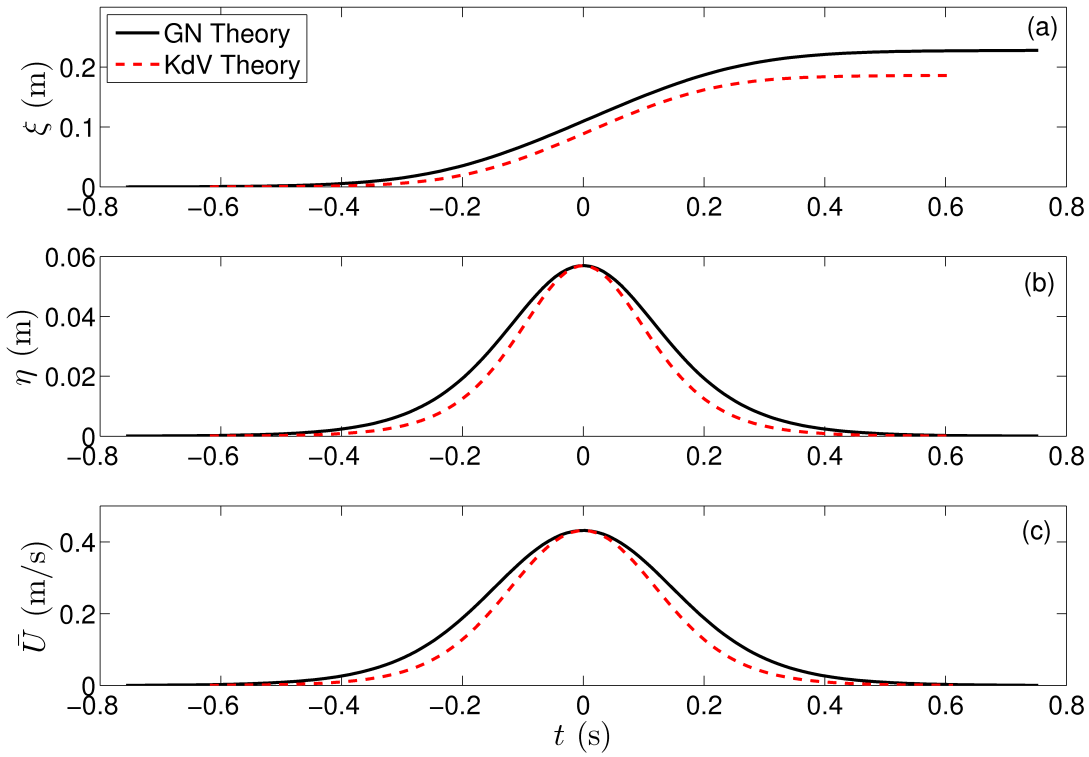

Figure 2.1: (a) Wave board displacement (b) surface elevation and (c) depth-integrated horizontal velocity for solitary waves generated using the GN and KdV equations for water depth $h = 0.114$ m and nondimensional wave amplitude of $a/h = 0.5$.

the displacement calculated using the KdV equations. This is due to the GN solitary wave having a fatter shape (Fig. 2.1 (b)) requiring a larger volume of water to be displaced. The shape of the wave and thus paddle displacement for the KdV generated cnoidal waves versus the GN generated cnoidal waves shown in Fig. 2.2 (a) - (c) are nearly identical. The largest difference is in the calculated wave period using the two theories. The wave period calculated using the GN equations for water depth $h = 0.071$ m, wave length $\lambda = 2.1$ m and nondimensional wave height of $H/h = 0.35$ is $T_{GN} = 2.3232$ s and for the KdV equations, $T_{KdV} = 2.2862$ s.

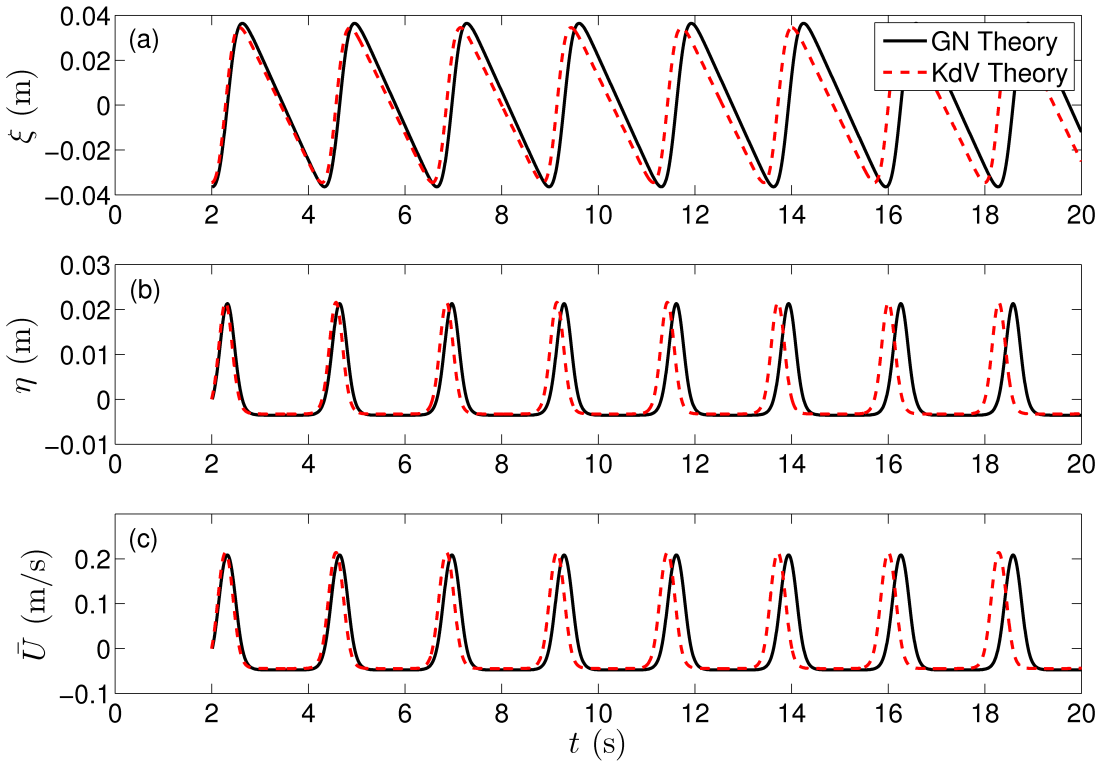

Figure 2.2: (a) Wave board displacement (b) surface elevation and (c) depth-integrated horizontal velocity for cnoidal waves generated using the GN and KdV equations for water depth $h = 0.071$ m, wave length $\lambda = 2.1$ m and nondimensional wave height of $H/h = 0.35$.

2.2.2 Measurements

Waves are measured in the wave flume in the absence of any obstruction at a location of 2.62 m from the wavemaker and 5.22 m from the end of the flume. Measured solitary waves generated using the GN and KdV equations are presented in Figs. 2.3 (a) - (e) for water depth $h = 0.114$ m and nondimensional wave amplitudes of $a/h = 0.1 - 0.5$. This figure shows that the GN equations are able to generate a wave with a more accurate amplitude but the KdV equations appear to generate a more accurate tail for larger wave amplitudes. The larger volume of water displaced generating a solitary wave using the GN equations may cause less attenuation of the wave, therefore generating a more accurate amplitude. This same displacement however causes the tail of the wave to remain slightly above the initial mean water level for larger waves, as in Fig. 2.3 (d). There are some instances where the tail of the wave becomes important in measurements, such as experiments involving wave dispersion or reflection, as discussed by, for example, Chen (2013). Goring & Raichlen (1980) saw the same wave-amplitude attenuation in larger wave amplitude experiments and concluded that it was due to frictional effects in the wave flume. That the GN equations are able to generate solitary waves with little attenuation indicates frictional effects are not the cause, but rather the KdV theory is not able to produce solitary waves with amplitudes as accurate as the GN equations are. Similar findings are also observed by Guizien & Barthelemy (2002) and Malek-Mohammadi & Testik (2010). A table including input wave amplitudes and measured GN and KDV generated solitary waves and their respective measurement errors can be found in Table 2.1.

Cnoidal wave measurements for waves generated using the GN and KdV equations for the water depth of $h = 0.071$ m, wave length $\lambda = 1$ m, and nondimensional wave height $H/h = 0.35$ are found in Fig. 2.4, and for the wave length $\lambda = 2.1$ m, and wave height $H/h = 0.2$ in Fig. 2.5, and for the wave length of $\lambda = 2.1$ m, and wave height $H/h = 0.35$ in

Table 2.1: Input solitary wave amplitude using the GN and KdV equations are compared with measured wave amplitude.

	GN		KdV	
a/h_{input}	a/h_{meas}	% Error	a/h_{meas}	% Error
0.1	0.093	**7.0**	0.090	**10.0**
0.2	0.192	**4.0**	0.182	**8.9**
0.3	0.301	**0.3**	0.281	**6.3**
0.4	0.408	**2.0**	0.366	**8.5**
0.5	0.525	**5.0**	0.454	**9.2**

Fig. 2.6. Both the GN and KdV generated waves show some attenuation in wave height, but the main difference is the accuracy of the period in the generated waves. Both wave theories are able to produce an accurate period for the shorter-period wave (Fig. 2.4) but the GN generated waves are much more accurate for the longer-period waves (Figs. 2.5 and 2.6). Table 2.2 gives the input wave length, λ_{input}, and the input nondimensional wave height, H/h_{input}, and the corresponding calculated wave period, T_{calc}, measured wave period, T_{meas}, measured wave height, H/h_{meas}, and the percentage of errors for both the GN generated cnoidal waves and the KdV generated cnoidal waves.

2.3 Model Specimen

The models used are constructed of clear acrylic and are representative of a 1:35 scale of a typical two-lane coastal bridge commonly found in an island community in Hawaii. The horizontal flat plate has dimensions of length $L_P = 14.9$ cm, width $B = 30.5$ cm, and thickness $t_P = 1.27$ cm, where length is defined as the direction normal to wave propagation (seen in Fig. 2.7). This model could represent, for example, a coastal bridge of width

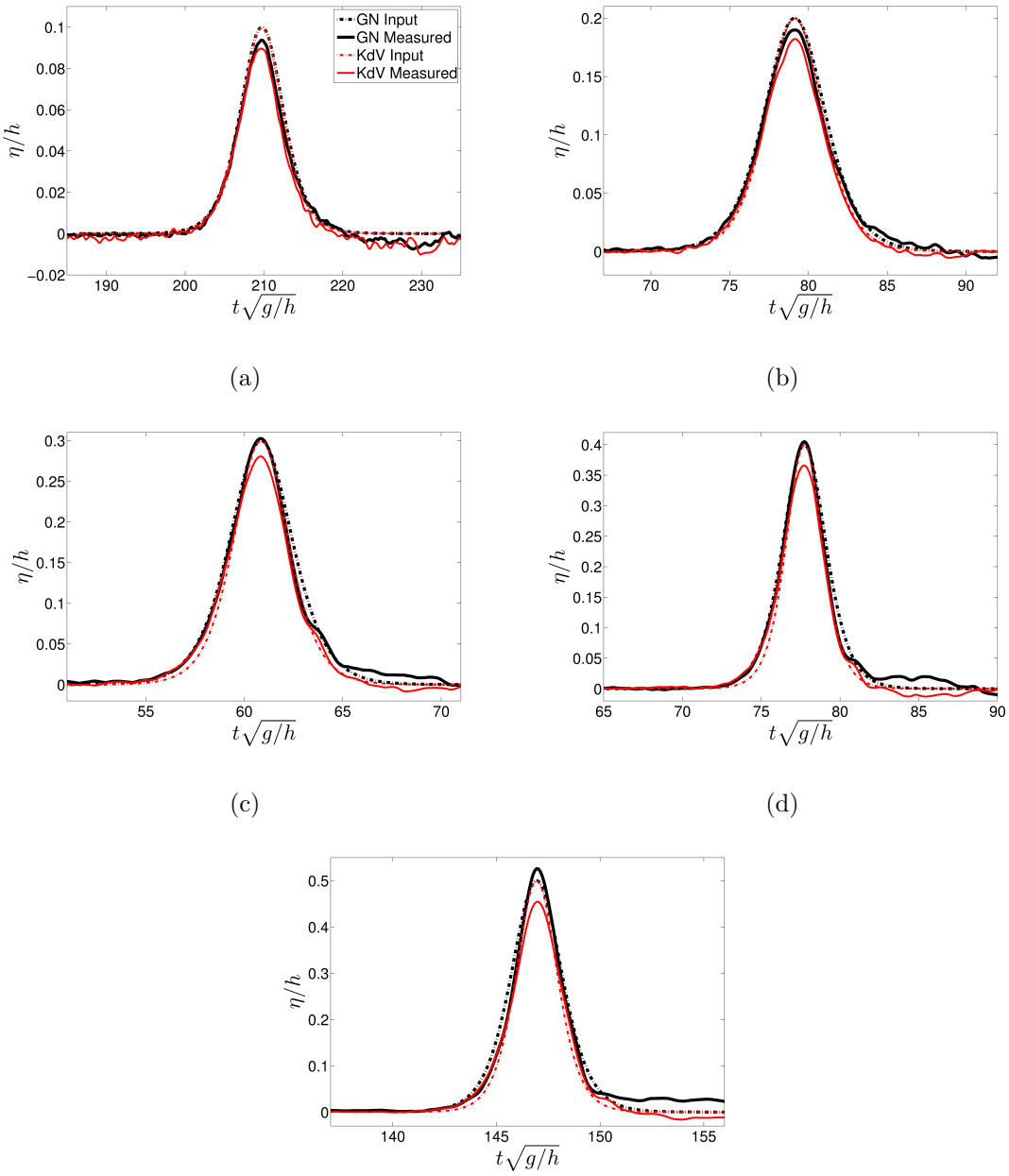

Figure 2.3: Measured solitary wave elevation is compared with input surface elevation generated using both the GN and KdV equations for water depth $h = 0.114$ m and nondimensional wave amplitudes of $a/h = 0.1 - 0.5$ in figures (a) - (e).

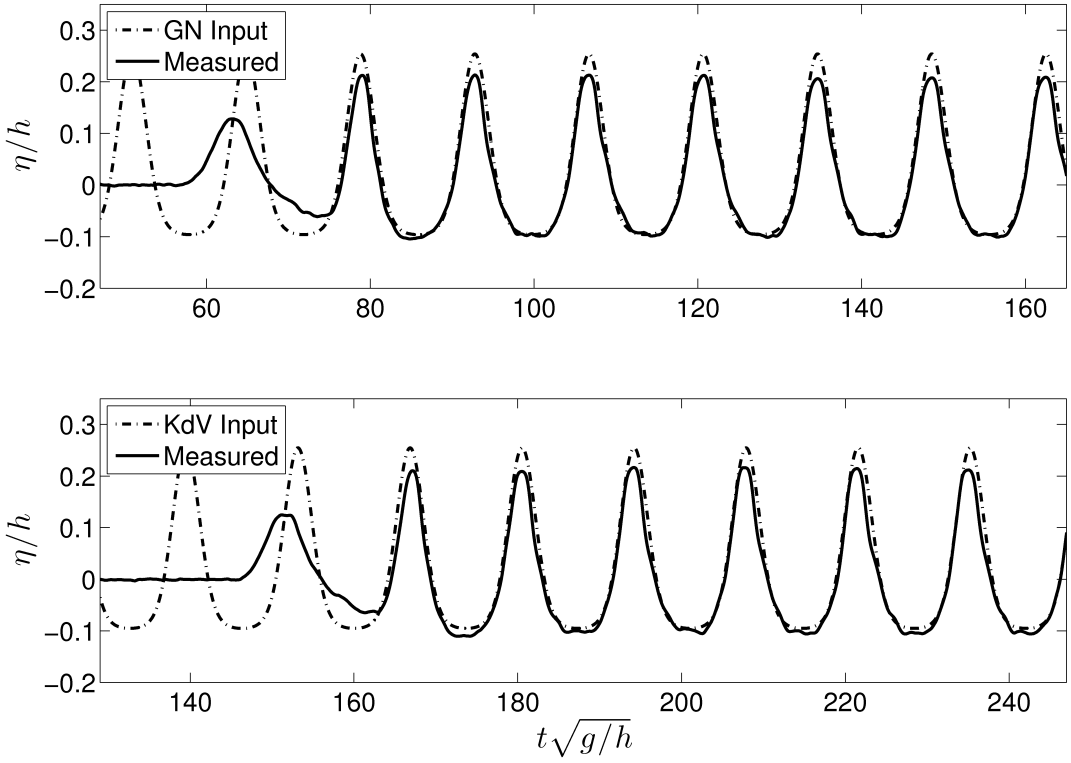

Figure 2.4: Measured cnoidal wave elevation is compared with input surface elevation generated using both GN and KdV equations for water depth $h = 0.071$ m, wave length $\lambda = 1$ m and nondimensional wave height of $H/h = 0.35$.

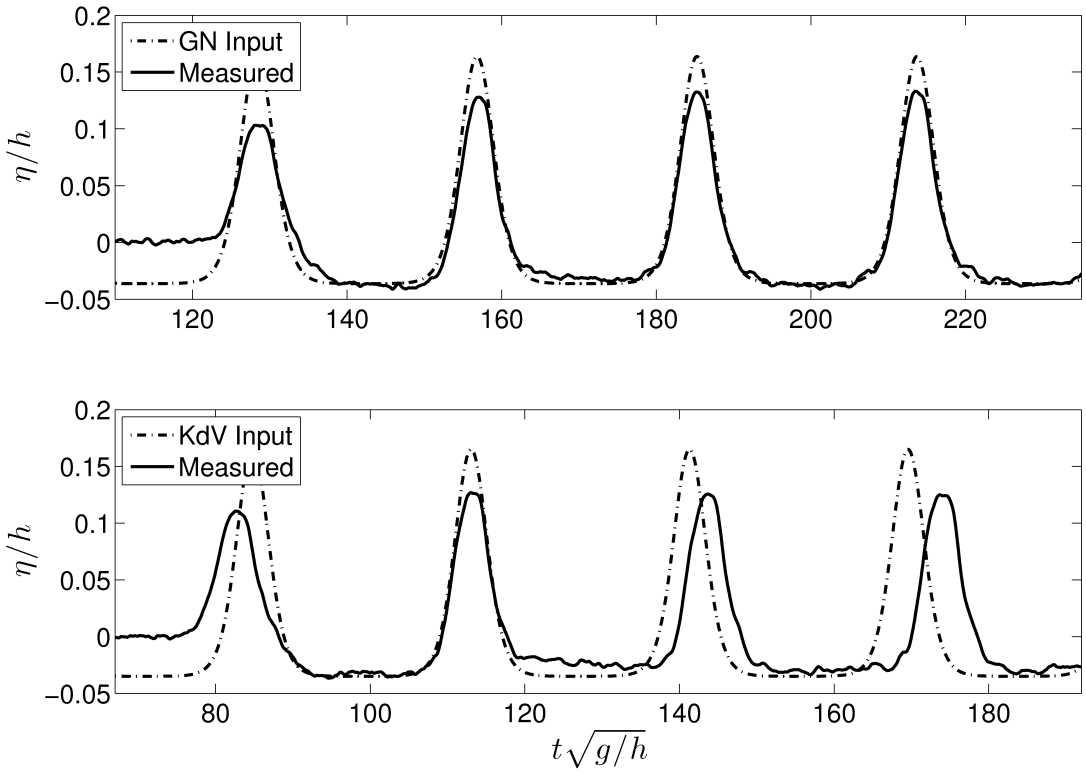

Figure 2.5: Measured cnoidal wave elevation is compared with input surface elevation generated using both GN and KdV equations for water depth $h = 0.071$ m, wave length $\lambda = 2.1$ m and nondimensional wave height of $H/h = 0.2$.

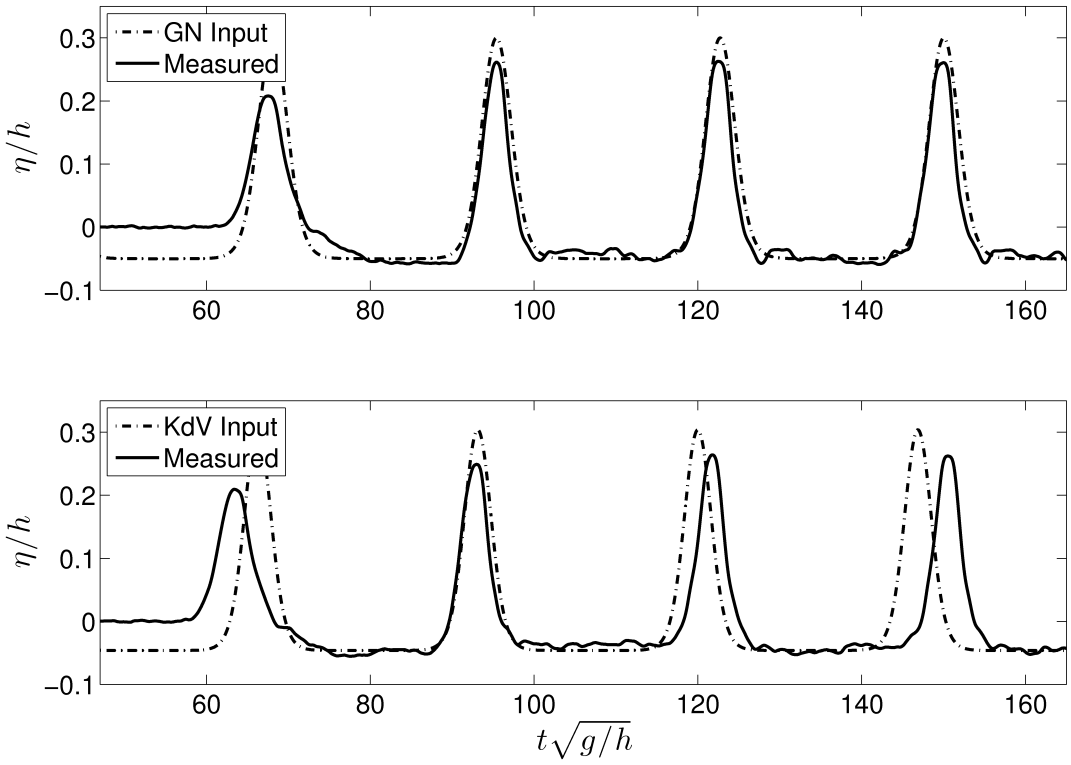

Figure 2.6: Measured cnoidal wave elevation is compared with input surface elevation generated using both GN and KdV equations for water depth $h = 0.071$ m, wave length $\lambda = 2.1$ m and nondimensional wave height of $H/h = 0.35$.

Table 2.2: Wave period is calculated using target wave length and wave height according to the GN and KdV equations. Calculated wave period and input wave height are compared with measured wave period and wave height for waves generated using either the GN or KdV equations. Water depth tested is $h = 0.071$ m.

		GN					KdV				
λ_{input}	H/h_{input}	T_{calc}	T_{meas}	% Error	H/h_{meas}	% Error	T_{calc}	T_{meas}	% Error	H/h_{meas}	% Error
1 m	0.35	1.187	1.186	**0.08**	0.312	**10.9**	1.164	1.156	**0.7**	0.320	**8.5**
2.1 m	0.2	2.420	2.410	**0.4**	0.168	**16.0**	2.404	2.585	**7.5**	0.157	**21.5**
2.1 m	0.35	2.323	2.310	**0.6**	0.318	**9.1**	2.286	2.450	**7.2**	0.305	**12.9**

10.675 m at a scale of 1:35. Dimensions of the bridge model with girders and corresponding prototype bridge are given in Table 2.3, and can also be seen in Figs. 2.8 and 2.9. Girder spacing (L_G) is measured from the center of one girder to the center of the next girder, and there are a total of six girders.

There is a 1.5 mm gap between the model and the flume side wall on each side of the model allowing air to escape between the girders. To trap air between the girders, 0.159 cm is shaved off each side of the model and a clear acrylic panel with thickness 0.159 cm, height 5.08 cm, and length 30.48 cm, is adhered to each side, maintaining the same model length, width and height. The air cavity area between each pair of girders is referred to as A_c and is a function of the model elevation z^* where z^* is measured from the SWL to the bottom of the bridge model deck, seen in Fig. 2.10. One, three or five 2.9 mm diameter holes are drilled into the panels between each pair of girders on each side of the model to provide different percentages of air relief, seen in Figs. 2.10-2.11. The area of one of these holes is referred to as A_r. The percentage of air relief opening area of air gap area is referred to as $\%ARO$ and is calculated by

$$\%ARO = \frac{iA_r}{A_c} \times 100, \tag{2.29}$$

where $i = 1, 3, 5$ for one, three or five drilled holes, respectively, and A_c includes the area iA_r. The case with panels attached to each side of the model but with no air relief openings is referred to as 0.0% ARO, and the case with no attached panels where air can escape freely is referred to as 100.0% ARO. Note that this definition is the same as in Seiffert, Ertekin & Robertson (2014*a*) and different from the definition used by Seiffert, Ertekin & Robertson (2014*b*).

The model is attached to an aerodynamically shaped aluminum strut which is then attached to a rigid support structure by three horizontal load cells and one vertical load cell as seen in Figs 2.9 and 2.12 (the model shown in Fig. 2.9 is the bridge model with girders

Table 2.3: Properties of the model test specimen and corresponding prototype bridge. *Constrained by flume width.

Parameter	**Model(1:35)**		**Prototype(1:1)**	
Span length (L_P)*	14.923 cm	5-7/8 in	5.215 m	17.135 ft
Width (B)	30.480 cm	12 in	10.668 m	35.000 ft
Girder height (t_G)	3.810 cm	1-1/2 in	1.33 m	4.375 ft
Girder spacing (CL to CL) (L_G)	5.080 cm	2 in	1.785 m	5.833 ft
Girder width	1.588 cm	5/8 in	0.560 m	1.823 ft
Deck thickness (t_P)	1.270 cm	1/2 in	0.455 m	1.458 ft
Air relief hole diameter (r_D)	2.9 mm	0.114 in	0.102 m	4 in

and the model shown in Fig. 2.12 is the horizontal flat plate). Three horizontal load cells are located on the trailing edge of the strut, two at a distance of 43.18 cm above the model and one at a distance of 68.6 cm above the model, and one vertical load cell is located above the center of the strut, at a distance of 77.0 cm above the model. The support structure is constructed such that the model elevation can be adjusted.

2.4 Setup and Test Procedure

2.4.1 Solitary Wave

The model is positioned in the wave flume at a distance of 2.62 m from the wavemaker and 5.22 m from the end of the flume (Fig. 2.13). Wave gauges are positioned at a distance of two plate widths upwave of the leading edge of the model (WG1) and two plate widths (WG2) and six plate widths (WG3) downwave of the trailing edge of the model (Fig. 2.13). These wave gauges were used to measure surface elevation in the presence of the model to

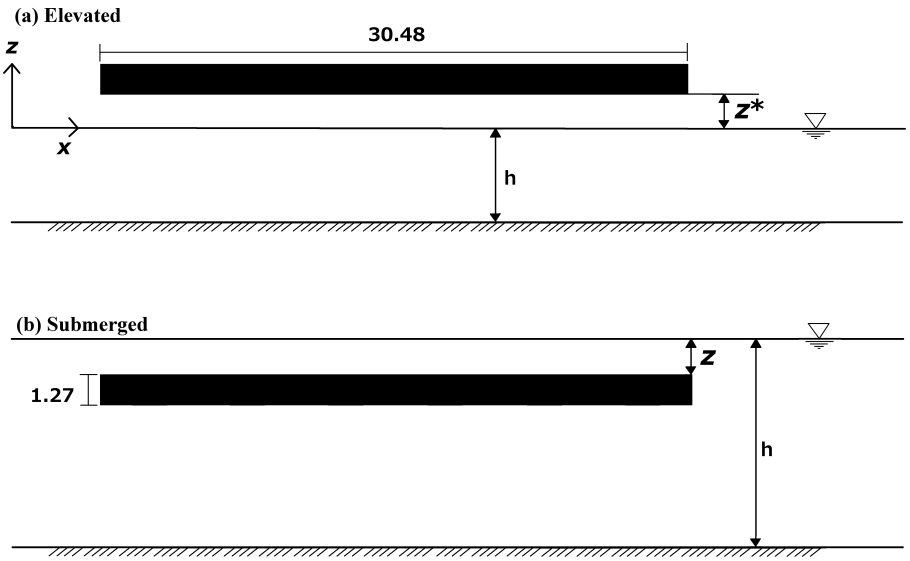

Figure 2.7: Forces are measured on the bridge model for both (a) elevated and (b) submerged conditions. The dimensions are given in centimeters. Not to scale.

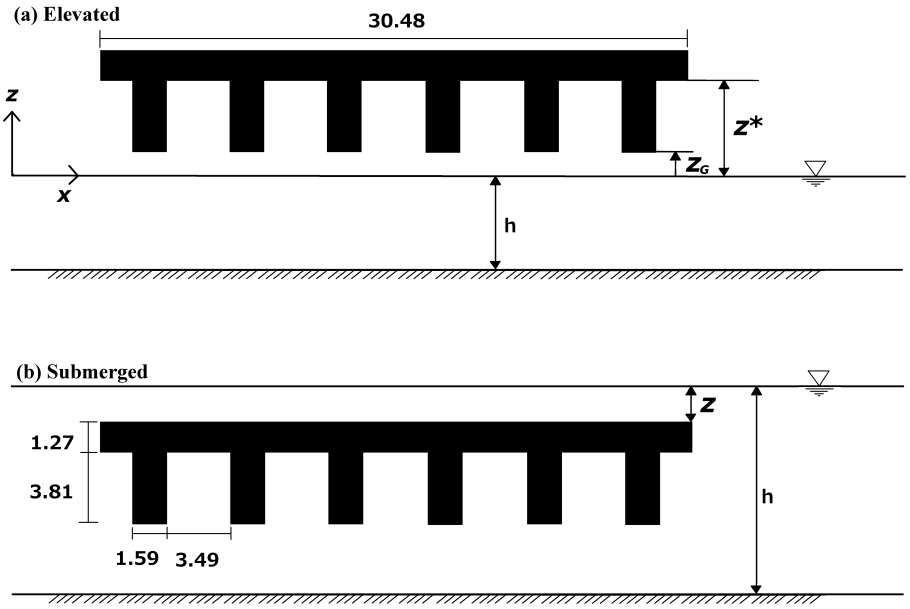

Figure 2.8: Forces are measured on the bridge model for both (a) elevated and (b) submerged conditions. The dimensions are given in centimeters. Not to scale.

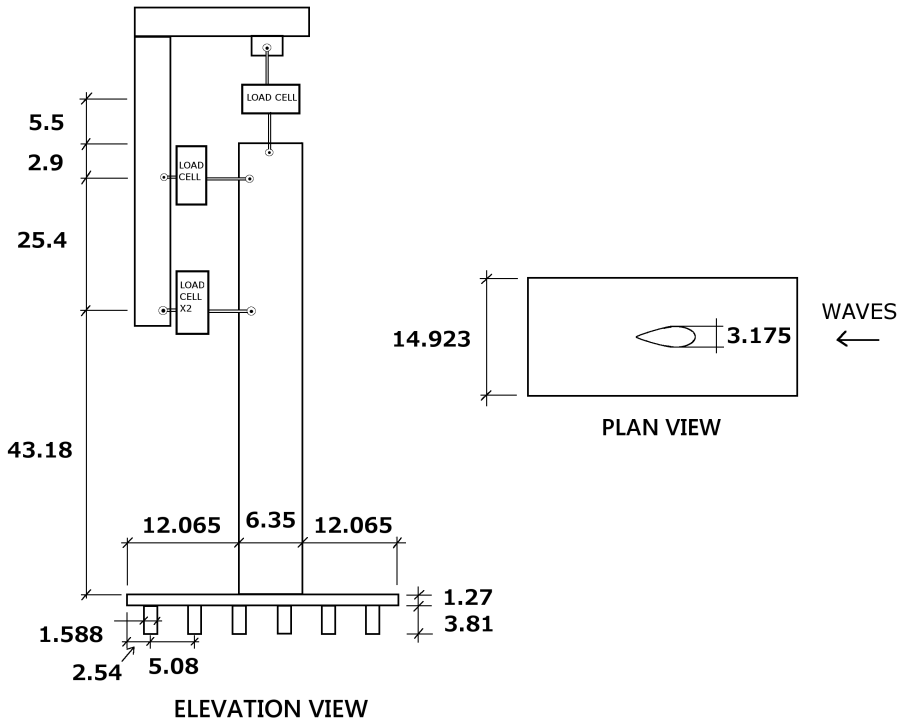

Figure 2.9: Elevation (side) view and plan (top) view of the bridge model and support structure are shown, where waves propagate from right to left. The model is attached to an aerodynamically shaped aluminum strut which is affixed to the support structure by two lower horizontal load cells (one is seen here and the second is behind it) one upper horizontal load cell in the center, and one vertical load cell seen at the top. Dimensions are in centimeters. Not to scale.

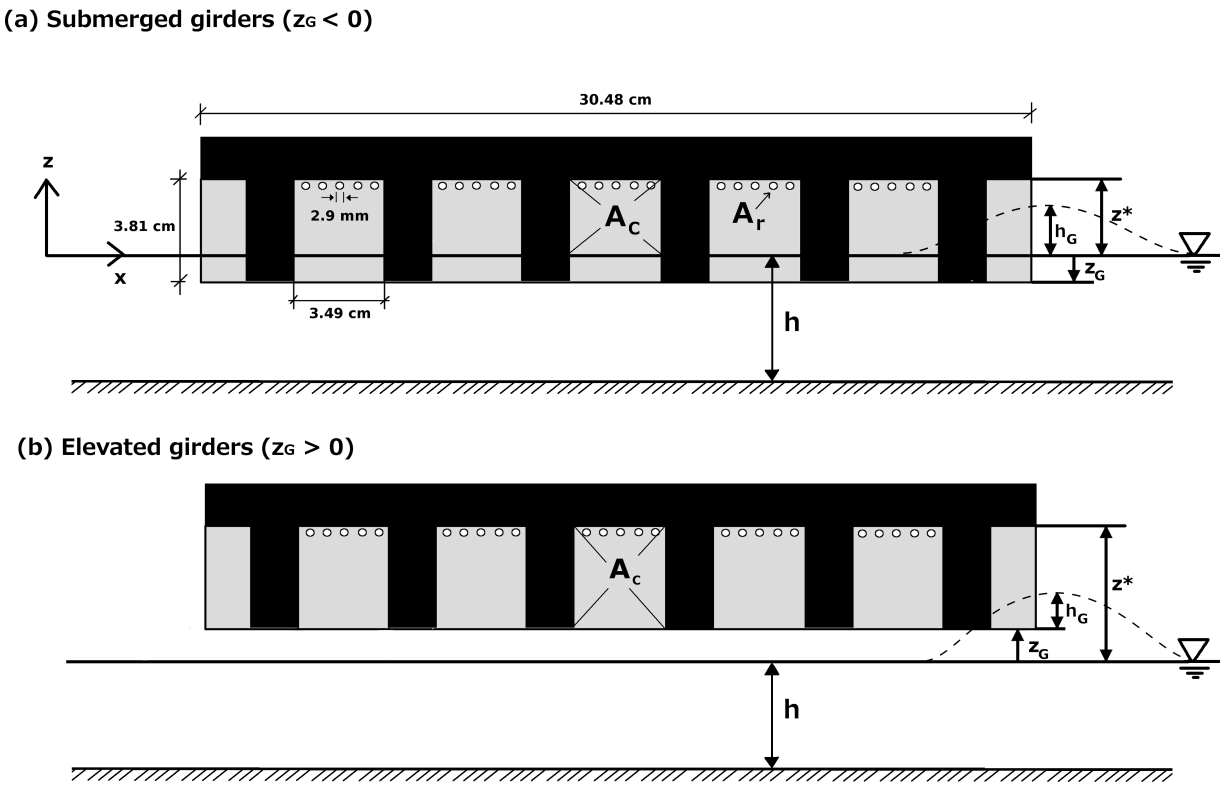

Figure 2.10: Model elevations tested are such that (a) the girders are submerged ($z_G < 0$) or (b) girders are elevated ($z_G > 0$) above the SWL, where z_G is the vertical coordinate from the SWL to the bottom of the girders. Air cavity area (A_c) is the area between each pair of girders and is a function of z^*, the distance between the SWL and the bottom of the bridge deck. h_G is the water surface elevation in the air cavity area in the absence of entrapped air. Not to scale.

(a) (b) (c)

Figure 2.11: (a) One, (b) three, or (c) five 2.9 mm diameter holes are drilled between each pair of girders, on each side of the model, to provide three additional percentages of air relief opening (ARO).

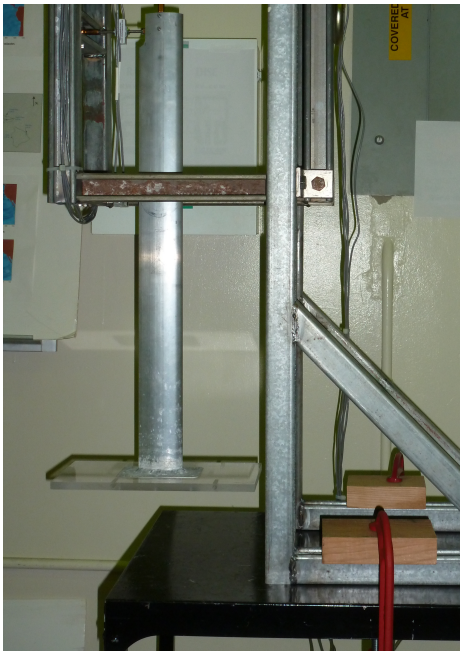

Figure 2.12: The model and strut are affixed to a rigid support structure that allows the model elevation to be adjusted according to the desired elevation or submergence depth.

compare the data with calculations.

A total of 133 cases were tested on a horizontal flat plate, and 118 cases were tested on a bridge model with girders. The wave parameters include water depths of $h = 0.143, 0.114, 0.086$ and 0.071 m, and nondimensional wave amplitudes of $a/h = 0.1, 0.2, 0.3, 0.4$ and 0.5. Note that for the water depth of 0.143 m, $a/h = 0.5$ was not tested due to the limitations of the wavemaker. Water depths were chosen to cover a range of realistic prototype water depths, specifically 2.5 m, 3 m, 4 m and 5 m. Wave amplitudes were chosen to cover very small, to very large non-breaking waves.

Each wave parameter was tested for a range of nondimensional submergence depths z/h, where z is measured from the SWL to top of the plate or bridge deck, and elevations z^*/h, where z^* is measured from the SWL to the bottom of the plate or bridge deck, seen in Figs. 2.7 and 2.8. The coordinate z_G measures the distance from the SWL to the bottom of the girders and is positive if the bottom of the girders are elevated above the SWL and is negative if any portion of the girders is submerged. For the horizontal flat plate, nondimensional elevations include $z^*/h = 0.03, 0.06$ and 0.1 and submergence depths include $z/h = 0.0, 0.2, 0.4$ and 0.6. For the bridge model, nondimensional elevations include $z^*/h = 0.06, 0.1$ and 0.3 and submergence depths include $z/h = 0.0, 0.2, 0.3$ and 0.4. Submergence depths and elevations were chosen to cover a range where the model is fully submerged below the SWL to where the bottom of the girders are fully elevated above the SWL in the case of the bridge model, and in the case of the plate, to the maximum elevation where all the waves would reach the bottom of the plate except the very smallest ($a/h = 0.1$). Tables 2.4 and 2.5 show which models were tested at a given water depth and submergence depth or elevation. Solitary wave experiments on a horizontal flat plate are indicated with the letters "SP" and bridge model with girders with the letters "SB".

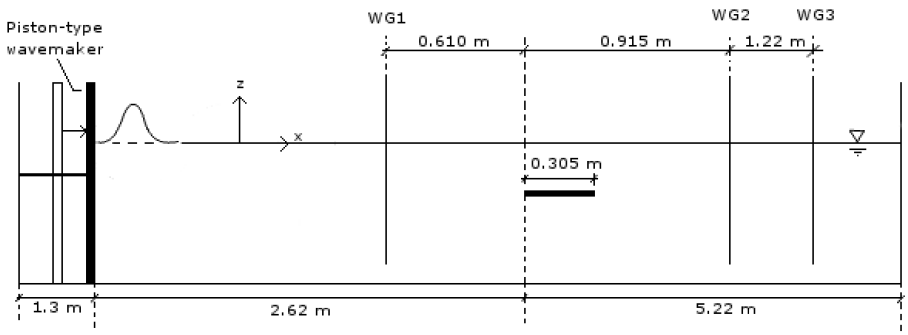

Figure 2.13: Wave gauges are positioned two plate widths upwave of the leading edge of the plate, and two plate widths and six plate widths downwave of the trailing edge. Not to scale.

Table 2.4: This table indicates which models were tested for a given water depth and submergence depth. The first letter indicates solitary "S" or cnoidal wave "C". The second letter indicates the model, and "P" indicates horizontal plate, "B" indicates bridge model with girders, and "T" indicates trapped air model.

	$h = 0.071$ m	$h = 0.083$ m	$h = 0.114$ m	$h = 0.143$ m
$z/h = 0.0$	SP, SB, CP, CB	SP, SB	SP, SB, CP, CB	SP, SB
$z/h = 0.2$	SP, SB, CP, CB	SP, SB	SP, SB, CP, CB	SP, SB
$z/h = 0.3$		SB	SB, CB	SB
$z/h = 0.4$	SP, CP	SP	SP, SB, CP, CB	SP, SB
$z/h = 0.6$	SP, CP	SP	SP, CP	SP

Table 2.5: This table indicates which models were tested for a given water depth and elevation. The first letter indicates solitary "S" or cnoidal wave "C". The second letter indicates the model, and "P" indicates horizontal plate, "B" indicates bridge model with girders, and "T" indicates trapped air model.

	$h = 0.071$ m	$h = 0.083$ m	$h = 0.114$ m	$h = 0.143$ m
$z^*/h = 0.03$	SP	SP	SP	SP
$z^*/h = 0.06$	SP, SB, CP, CB, CT	SP, SG, ST	SP, SB, CP, CB, ST, CT	SP, SB, ST
$z^*/h = 0.1$	SP, SB, CP, CB, ST, CT	SP, SB, ST	SP, SB, CP, CB, ST, CT	SP, SB, ST
$z^*/h = 0.3$	SB, CB, ST, CT	SB, ST	SB, ST, CT	SB, ST
$z^*/h = 0.35$	CB, ST, CT		CB, CT	
$z^*/h = 0.55$	CB, ST, CT			

2.4.2 Cnoidal Wave

For experiments measuring cnoidal wave forces on a horizontal flat plate and bridge model with girders, the model was positioned at a distance of 2.62 m from the wavemaker and 5.22 m from the end of the flume. Wave gauges are positioned at one (WG1) and two (WG2) plate widths upwave of the leading edge of the model and two plate widths (WG3) downwave of the trailing edge of the model, shown in Fig. 2.14.

The experimental testing procedure includes five wave lengths, four wave heights and two water depths to cover a range of nonlinear shallow-water waves to shallower intermediate-water waves suitable to characterization by cnoidal wave theory as suggested by, for example Figure 4.17 in Sarpkaya & Isaacson (1981) and Le Mehaute (1969). A table of water depths, input wave heights, wave lengths and wave periods and corresponding prototype conditions are given in Table 2.6. For experiments using the flat plate, each wave parameter was tested for submergence depths of $z/h = 0.0, 0.2, 0.4$ and 0.6, and elevations of $z^*/h = 0.06$, and 0.1. For the bridge model at the water depth of $h = 0.071$ m, the model was positioned at the submergence depths of $z/h = 0.0$, and 0.2 and elevations of $z^*/h = 0.06, 0.1, 0.3, 0.35$, and 0.55, and for water depth $h = 0.114$ m, the model was positioned at submergence depths of $z/h = 0.0, 0.2, 0.3$, and 0.4 and elevations of $z^*/h = 0.06, 0.1$, and 0.35. In Tables 2.4 and 2.5, tested water depths and submergence depths or elevations for cnoidal waves on a flat plate and bridge model with girders are indicated with the letters "CP" and "CB", respectively.

2.4.3 Entrapped Air

For experiments measuring the effects of entrapped air on a bridge model with girders, the model was positioned at a distance of 2.62 m from the wavemaker and 5.22 m from the end of the flume. Wave gauges are positioned at one (WG1) and two (WG2) plate widths upwave of the leading edge of the model and two plate widths (WG3) downwave of the

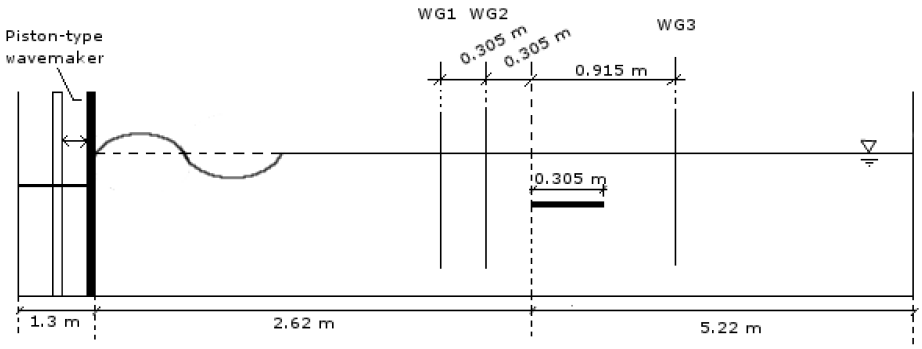

Figure 2.14: Wave gauges are positioned two plate widths (WG1) and one plate width (WG2) upwave of the leading edge of the plate and two plate widths downwave of the trailing edge of the plate (WG3). Not to scale.

Table 2.6: A range of wave heights and wavelengths are tested according to a realistic range of prototype conditions that may occur during a storm. All units are in meters unless otherwise specified.

Test Parameter		**Model(1:35)**	**Prototype(1:1)**
Water depth (h)		0.071, 0.114	2.5, 4
Wave height (H)	$h = 0.071$	0.007, 0.014, 0.021, 0.028	0.25, 0.5, 0.75, 1
	$h = 0.114$	0.011, 0.023, 0.034, 0.046	0.4, 0.8, 1.2, 1.6
Wavelength (λ)		1.4, 1.7, 1.9, 2.1, 2.3	49.0, 59.5, 66.5, 73.5, 80.5
Wave period (T)	$h = 0.071$	1.58 s - 2.71 s	9.347 s - 16.033 s
	$h = 0.114$	1.32 s - 2.18 s	7.809 s - 12.897 s

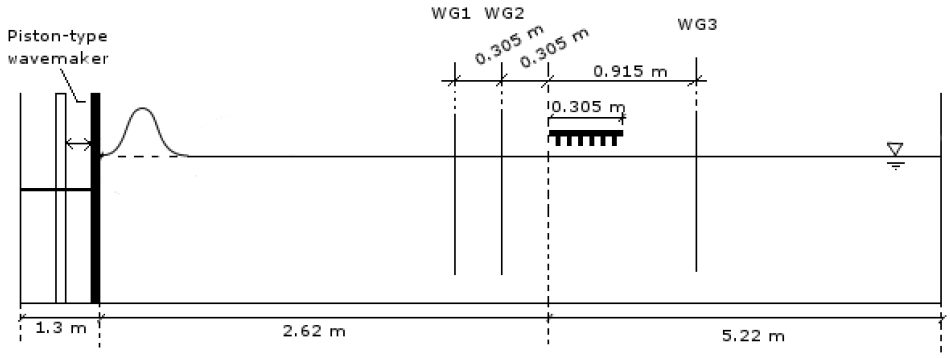

Figure 2.15: The bridge model is positioned where the leading edge is 5.22 m, from the end of the tank and 2.62 m from the wavemaker. Three wave gauges are positioned at one and two span widths upwave of the leading edge and two span widths downwave of the trailing edge of the model. Not to scale.

trailing edge of the model, as shown in Fig. 2.15.

Solitary-wave cases included water depths of $h = 0.071, 0.086, 0.114$, and 0.143 m, corresponding to prototype depths of $h = 2.5, 3, 4$, and 5 m, and nondimensional wave amplitudes of $a/h = 0.1, 0.2, 0.3, 0.4$, and 0.5. Non-dimensional elevations tested include $z^*/h = 0.06, 0.1, 0.3, 0.35$, and 0.55 and cover a range where the bottom of the bridge deck is just above the SWL to where the bottom of the girders are fully elevated above the SWL. Cnoidal wave cases included $z^*/h = 0.1, 0.3, 0.35$, and 0.55 for water depths $h = 0.071$ m and $h = 0.114$ m. Note however, only the 0.0% ARO and 100.0% ARO cases were tested for the water depth of $h = 0.114$ m. In Table 2.5, tested water depths and elevations for solitary wave cases with the entrapped air model are indicated with the letters "ST" and cnoidal wave cases are indicated with the letters "CT".

2.5 Measurements

2.5.1 Waves

In these experiments, solitary and cnoidal waves are generated using the GN theory as they were shown in section 2.2.2 to have the most accurate wave amplitude and period. Waves are measured at the location of the leading edge of the model without the model present to measure incoming wave height and period, and determine accuracy and repeatability of each generated solitary and cnoidal wave. These measurements are used when plotting force data.

Measurements for solitary wave amplitude at the four water depths is given in Table 2.7. For cnoidal waves, the input wavelength (λ_{input}) and wave height (H/h_{input}) are used to calculate the target wave period (T_{calc}) using the GN theory. Wave period and wave height are measured at the location of the model (T_{meas} and H/h_{meas}) and then wavelength is calculated from these measured values using the GN theory (λ_{calc}). A list of these results is found in Tables 2.8 and 2.9, for water depths $h = 0.071$ m and $h = 0.114$ m, respectively. The percent difference between measurements is well within $\pm 5\%$ for both solitary and cnoidal waves. Solitary waves had an average of $\pm 1.75\%$ difference. For cnoidal waves, the average repeatability error for wave period is 0.32% and 0.46% and for wave height is 1.02% and 0.64% for water depths $h = 0.071$ m and $h = 0.114$ m, respectively.

Although most of the waves were generated cleanly, a second harmonic was observed in the trough of the wave generated at water depth $h = 0.071$ m, wave length $\lambda = 1.4$ m and nondimensional wave height $H/h = 0.4$, shown in Fig. 2.16 (b). It is interesting to note that the second harmonic is not visible in measurements taken at the other two wave gauges, located at 2.01 m (WG1) and 3.535 m (WG3) from the wavemaker, shown in Fig. 2.16 (a) and (c). In Fig. 2.16, waves are generated using the GN equations, but the same harmonic

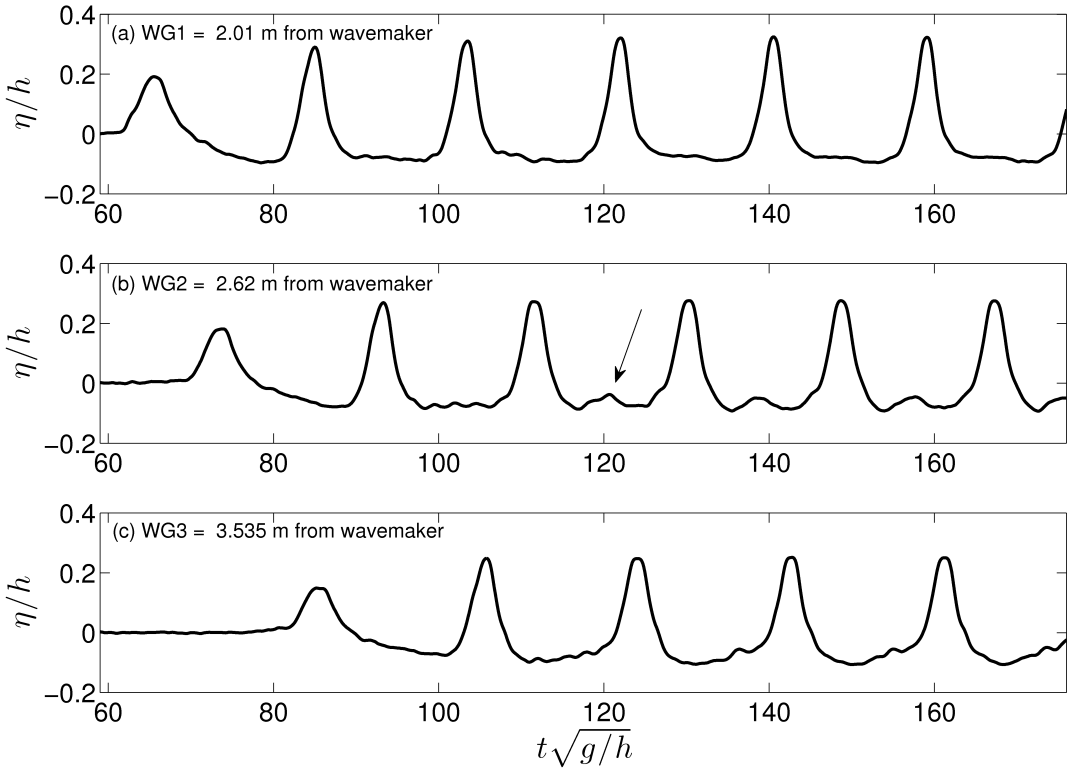

Figure 2.16: A higher harmonic is visible at (b)WG2 located at a distance of 2.62 m from the wavemaker but not visible at (a) WG1 or (c)WG3 located at 2.01 m and 3.535 m from the wavemaker, respectively.

Table 2.7: Solitary-wave amplitude is measured at the location of the model and compared with the input wave amplitude at the wavemaker, for non-dimensional wave amplitudes of $0.1 - 0.5$.

a/h Input	a/h Measured			
	$h = 0.143m$	$h = 0.114m$	$h = 0.086m$	$h = 0.071m$
0.1	0.095	0.093	0.087	0.088
0.2	0.195	0.192	0.177	0.180
0.3	0.302	0.301	0.287	0.282
0.4	0.407	0.408	0.396	0.386
0.5	–	0.525	0.505	0.500

is seen when generating waves using the KdV equations. Additionally, waves generated using the KdV equations for the same water depth and wave length in a three-dimensional wave basin show the same harmonic, albeit the generated wave had a larger wave height ($H/h \approx 0.6$) (personal communication with Yeh (2013)). However, when the same wave was generated numerically the second harmonic does not appear (personal communication with Hayatdavoodi (2014)).

Madsen (1971) witnessed a second free harmonic when trying to generate second-order stokes waves in the laboratory using the sinusoidal motion dictated by the first-order solution for wavemaker motion. This led to the second-order solution for wavemaker paddle motion. This theory, however is suitable for waves such that $\frac{H\lambda^2}{h^3} < \frac{8\pi^2}{3}$, whereas the waves generated in these experiments are much more non-linear ($\frac{H\lambda^2}{h^3} = 350 >> \frac{8\pi^2}{3}$, for example). Goring (1979) witnessed a second harmonic when he used a trajectory programmed for $h = 20$ cm, $H/h = 0.2$, $T = 2.90$ s but changed T to 4.28 s. He used this example to support the claim that each cnoidal wave has a unique trajectory. In these experiments, each cnoidal wave is

Table 2.8: Target wave period is calculated from input wavelength and wave height for water depth $h = 0.071$ m. Wave period and wave height are measured at the location of the model and final wavelength is calculated using these measured values.

$\lambda_{\mathbf{input}}$ (m)	$\mathbf{T_{calc}}$ (s)	$(\mathbf{H/h})_{\mathbf{input}}$	$\mathbf{T_{meas}}$ (s)	$\lambda_{\mathbf{calc}}$ (m)	$(\lambda/\mathbf{B})_{\mathbf{calc}}$	$(\mathbf{H/h})_{\mathbf{meas}}$
1.4	1.684	0.1	1.684	1.386	4.546	0.065
	1.650	0.2	1.648	1.381	4.530	0.155
	1.614	0.3	1.614	1.381	4.531	0.255
	1.580	0.4	1.579	1.383	4.537	0.364
1.7	2.026	0.1	2.038	1.695	5.562	0.073
	1.978	0.2	1.985	1.682	5.519	0.155
	1.929	0.3	1.933	1.680	5.511	0.258
	1.883	0.4	1.885	1.685	5.527	0.371
1.9	2.254	0.1	2.260	1.887	6.192	0.073
	2.196	0.2	2.200	1.888	6.160	0.160
	2.139	0.3	2.145	1.882	6.174	0.260
	2.086	0.4	2.085	1.874	6.149	0.360
2.1	2.482	0.1	2.478	2.073	6.800	0.068
	2.414	0.2	2.418	2.070	6.792	0.156
	2.349	0.3	2.348	2.072	6.797	0.264
	2.288	0.4	2.293	2.075	6.807	0.358
2.3	2.710	0.1	2.705	2.266	7.434	0.063
	2.633	0.2	2.625	2.250	7.380	0.146
	2.558	0.3	2.563	2.270	7.444	0.257
	2.490	0.4	2.480	2.258	7.407	0.359

Table 2.9: Target wave period is calculated from input wavelength and wave height for water depth $h = 0.114$ m. Wave period and wave height are measured at the location of the model and final wavelength is calculated using these measured values.

$\lambda_{\mathbf{input}}$ (m)	$\mathbf{T_{calc}}$ (s)	$(\mathbf{H/h})_{\mathbf{input}}$	$\mathbf{T_{meas}}$ (s)	$\lambda_{\mathbf{calc}}$ (m)	$(\lambda/\mathbf{B})_{\mathbf{calc}}$	$(\mathbf{H/h})_{\mathbf{meas}}$
1.4	1.374	0.1	1.380	1.403	4.603	0.074
	1.361	0.2	1.361	1.395	4.577	0.173
	1.344	0.3	1.340	1.399	4.588	0.275
	1.325	0.4	1.327	1.393	4.571	0.393
1.7	1.643	0.1	1.653	1.705	5.592	0.077
	1.620	0.2	1.623	1.695	5.560	0.177
	1.593	0.3	1.598	1.697	5.557	0.279
	1.566	0.4	1.575	1.710	5.561	0.401
1.9	1.823	0.1	1.833	1.904	6.246	0.082
	1.793	0.2	1.803	1.902	6.240	0.181
	1.760	0.3	1.775	1.910	6.265	0.282
	1.726	0.4	1.735	1.906	6.252	0.391
2.1	2.004	0.1	1.998	2.083	6.832	0.072
	1.966	0.2	1.965	2.083	6.835	0.171
	1.926	0.3	1.928	2.087	6.847	0.272
	1.887	0.4	1.890	2.101	6.891	0.396
2.3	2.184	0.1	2.175	2.276	7.467	0.070
	2.139	0.2	2.125	2.265	7.430	0.168
	2.092	0.3	2.090	2.281	7.482	0.273
	2.047	0.4	2.038	2.280	7.480	0.388

programmed according to its unique water depth, wave length and wave height so this is not the cause of the second harmonic in our case. Cho (2003) discusses the importance of the accuracy of the parameter m in generating accurate cnoidal waves. Indeed, when using a less accurate parameter m, higher harmonics were observed in numerical simulations (personal communication with Hayatdavoodi (2014)). However, in the waves generated experimentally, the parameter m is solved to the order of 10^{-20}, so is generated with sufficient accuracy.

This leaves a few possibilities for the cause of the higher harmonic. For such highly non-linear waves, even if the paddle motion inputs are highly accurate, the wavemaker may be unable to move as accurately. In addition, unlike a numerical flume, the experimental flume is not perfectly two-dimensional so the harmonic may be due to the small scale of the flume and leakage around the wave board when moving. Another possible solution to this would be to solve for paddle motion using a higher level of equations, such as the Green-Naghdi Level II equations or a higher order of Boussinesq equations.

Another possible cause for the higher harmonic is the error associated with assuming that the wave has the same celerity as it develops as a fully developed wave. It has been noted in Synolakis (1990) that Eq. (2.3) is not strictly correct because during wave generation, the wave is evolving continuously and cannot be assumed it is of permanent form during this process. However, agreement between the laboratory data and the theory is good, and Synolakis suggests this is likely due to the relatively short length of the wave generation region. Malek-Mohammadi & Testik (2010) expanded on this by developing a new method for generating solitary waves that takes the evolution of the wave during paddle motion into consideration. Applying this method to the generation of cnoidal waves may eliminate the higher harmonic. In the present experiments, however, it is concluded that the higher harmonic does not affect the peak forces.

2.5.2 Force

Force data are sampled at 100 Hz during the experiments using the plate model at both elevated and submerged conditions, and the bridge model for submerged cases only. Force data are sampled at 1000 Hz for the bridge model for the elevated cases, including all entrapped air experiments. The 100 Hz sampling rate was deemed sufficient for the flat plate and submerged cases as the maximum and minimum force events occur within a 1-2 s window, as can be seen in the time series shown in Figs. 2.17 and 2.18. This assures that there are approximately 100-200 samples per force event, which sufficiently captures the peak forces in these cases. The higher sampling rate for elevated cases of the bridge model was used to capture any short-duration forces that may occur on the model due to the presence of air.

In the elevated cases, high-frequency oscillations were observed that correspond to the natural frequency of the model, which was measured at approximately 25 Hz in the horizontal direction and 50 Hz in the vertical direction. A smoothing function was applied to the force data using the MATLAB function "csaps", and the smoothing parameter of $p = 0.99999$ was chosen for both the horizontal and vertical forces, and for both the submerged and elevated cases. This parameter was chosen as it sufficiently filtered the structural noise and other vibrations along the sidewalls due to the movement of the wavemaker, while capturing long-duration force peaks. As a consequence, the smoothing parameter reduced the impulse force measurements seen in the elevated cases. However, priority in this set of data is given to accurately measure the long-duration forces on the structure. To capture impulse forces without any effect of structural vibrations, the experiments can be repeated in the future at a larger scale and with a heavier model.

Figures 2.17 and 2.18 show raw force data measured on the bridge model with girders, sampled at 100 Hz and applied smoothing parameters $p = 0.999999$ and $p = 0.99999$ for

vertical forces (a) and $p = 0.99999$ and $p = 0.9999$ for horizontal forces (b) for the submerged cases $h = 0.114$ m, $z/h = 0.2$, and $a/h = 0.3$ and $h = 0.071$ m, $z/h = 0.2$, $\lambda = 1.4$ m, and $H/h = 0.4$, respectively. Figures 2.19 and 2.20 show raw force data measured on the bridge model with girders, sampled at 1000 Hz, and applied smoothing parameters $p = 0.999999$ and $p = 0.99999$ for vertical forces (a) and $p = 0.99999$ and $p = 0.9999$ for horizontal forces (b), for the elevated cases $h = 0.114m$, $z^*/h = 0.1$, and $a/h = 0.3$ and $h = 0.071m$, $z^*/h = 0.06$, $\lambda = 1.4$ m, and $H/h = 0.4$, respectively. These figures show that the smoothing parameter $p = 0.99999$ effectively captures the long-duration uplift, downward, positive and negative forces while smoothing out forces due to structural vibrations for solitary and cnoidal wave experiments on the bridge model with girders. In experiments measuring forces on the flat plate model, a smoothing parameter of $p = 0.9999$ was chosen for horizontal forces and a smoothing parameter of $p = 0.99999$ was chosen for vertical forces in the submerged cases and vertical downward forces in the elevated cases. A higher smoothing parameter for vertical uplift forces in the elevated position was required to accurately capture an initial short impulse force seen in these cases, so the parameter $p = 0.999999$ was chosen.

To ensure accuracy and repeatability of experimental data, each solitary wave case, where water depth, wave amplitude and model submergence depth or elevation above the SWL remain constant, was repeated five times in the experiments, leaving 5 solitary wave measurements. Wave force measurements are taken during cnoidal wave experiments such that the initial wave has already propagated past the model but has not yet been reflected back to the model, leaving 2-3 waves for analysis. Each case (one water depth, one wave length, one wave height and one submergence depth or elevation) is repeated 3 times giving 6-9 measurements for each case. The maxima and minima of the peak force results are removed from each of the vertical uplift and downward and horizontal positive and negative forces, and the remaining measurements of each one are averaged to obtain the data presented here.

To insure repeatability, data with a standard deviation greater than ±5.5% from the mean are removed from the presented results.

The same wave conditions and submergence depths and elevations were tested on the strut alone to determine contribution of the strut to horizontal forces. Average measured horizontal forces on the strut in the direction of wave propagation (positive) and opposite the direction of wave propagation (negative) are subtracted from the measured forces on the model and the strut taken during experiments to get the final horizontal positive and negative forces. Measurements of wave elevation taken from wave gauges positioned upwave and downwave of the model location during the experiments when only the strut was present indicate that the strut does not have any appreciable effect on the wave as it propagates over the plate.

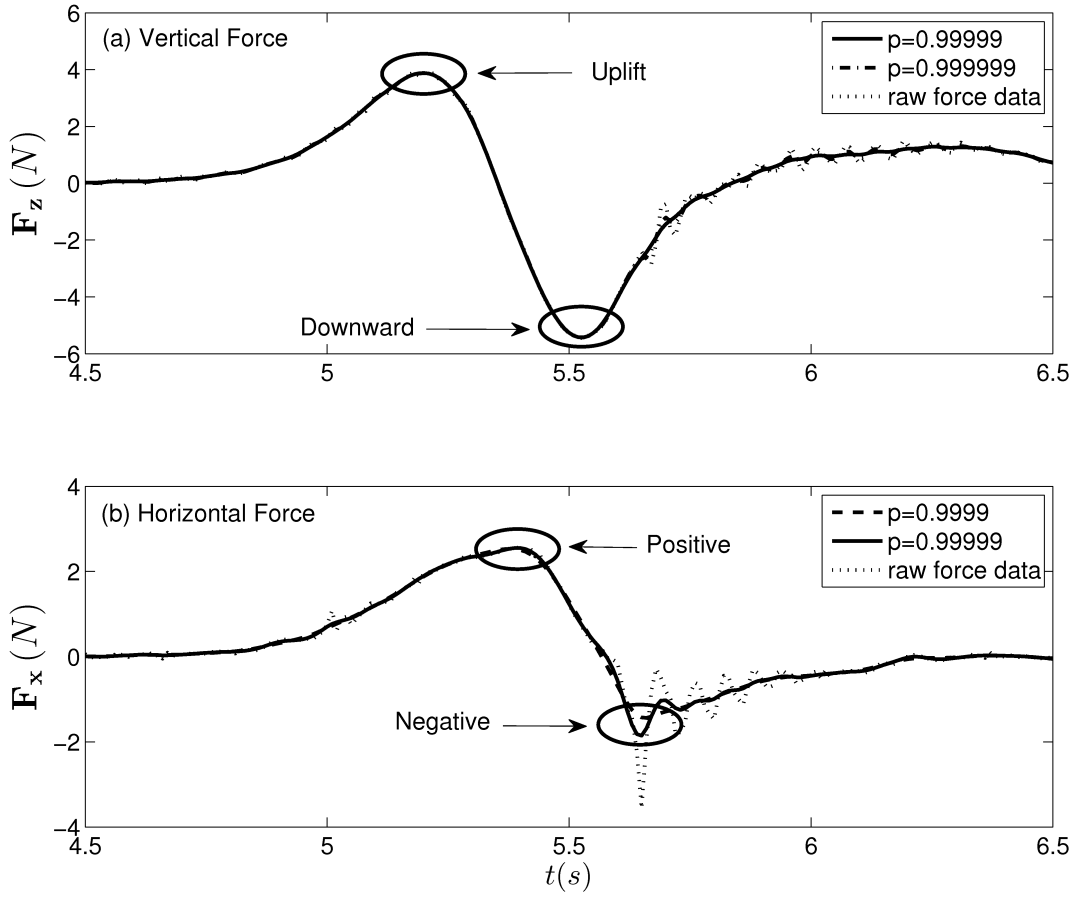

Figure 2.17: Time histories for solitary wave force measurements on the bridge model with girders, taken at 100 Hz for (a) vertical forces with smoothing parameters $p = 0.999999$ and $p = 0.99999$ and (b) horizontal forces with smoothing parameters $p = 0.99999$ and $p = 0.9999$ for the submerged case $h = 0.114m$, $z/h = 0.2$, and $a/h = 0.3$.

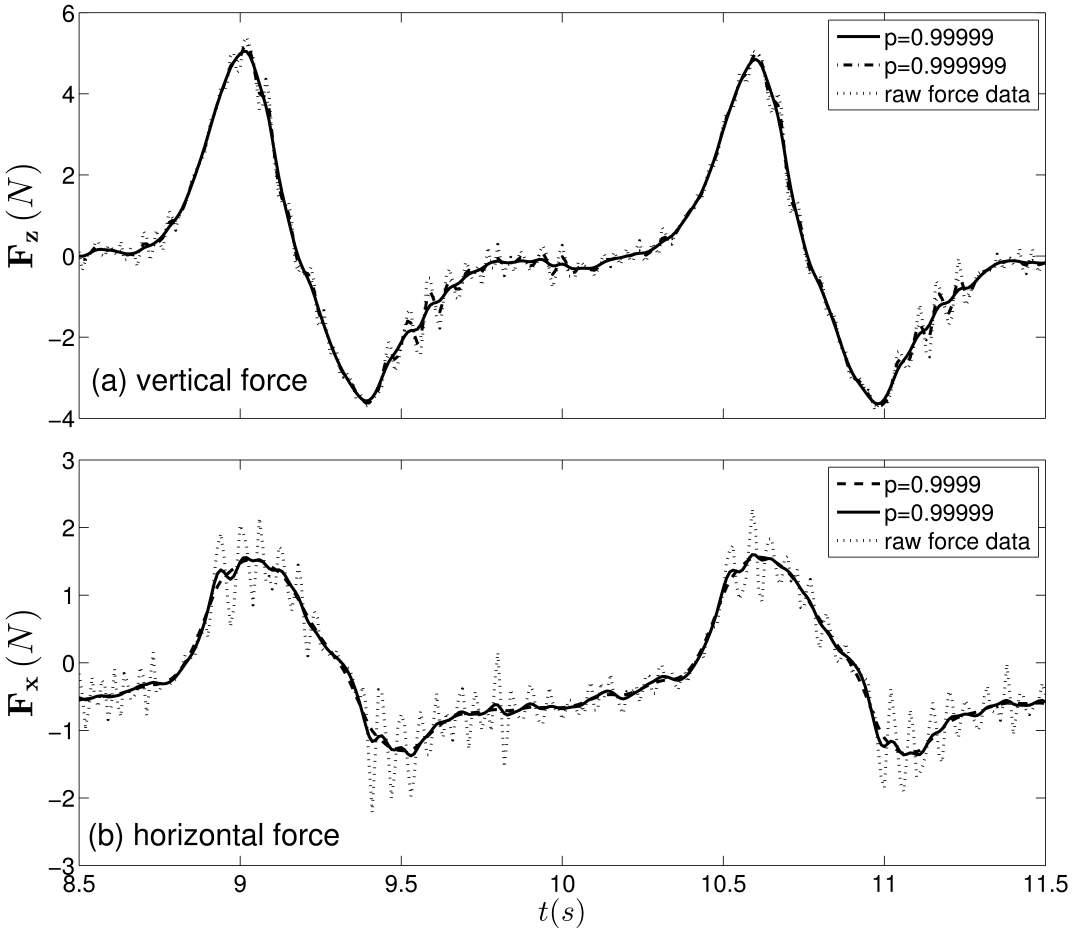

Figure 2.18: Time histories for cnoidal wave force measurements on the bridge model with girders, taken at 100 Hz for (a) vertical forces with smoothing parameters $p = 0.999999$ and $p = 0.99999$ and (b) horizontal forces with smoothing parameters $p = 0.99999$ and $p = 0.9999$ for the submerged case $h = 0.071m$, $z/h = 0.2$, $\lambda = 1.4$ m, and $H/h = 0.364$.

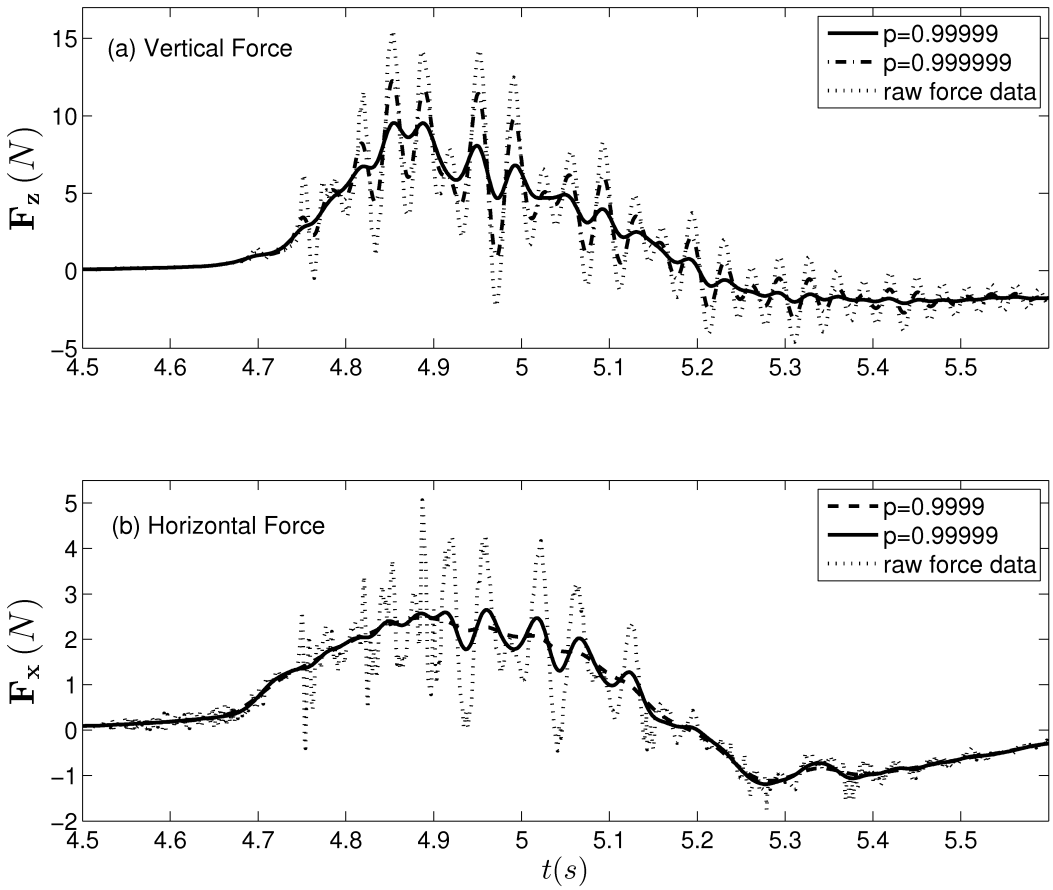

Figure 2.19: Time histories for solitary wave force measurements on the bridge model with girders, taken at 1000 Hz for (a) vertical forces with smoothing parameters $p = 0.999999$ and $p = 0.99999$ and (b) horizontal forces with smoothing parameters $p = 0.99999$ and $p = 0.9999$ for the elevated case $h = 0.114m$, $z^*/h = 0.1$, and $a/h = 0.3$.

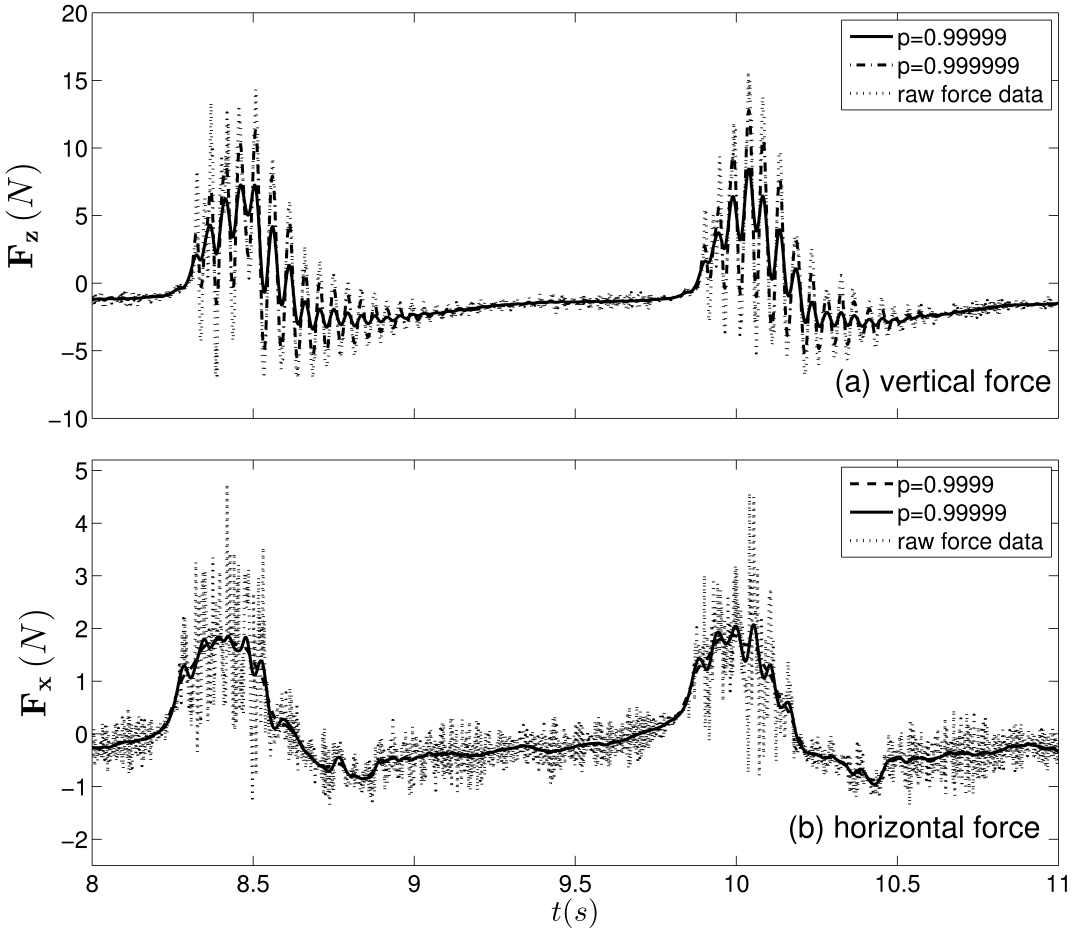

Figure 2.20: Time histories for cnoidal wave force measurements on the bridge model with girders, taken at 1000 Hz for (a) vertical forces with smoothing parameters $p = 0.999999$ and $p = 0.99999$ and (b) horizontal forces with smoothing parameters $p = 0.99999$ and $p = 0.9999$ for the elevated case $h = 0.071m$, $z^*/h = 0.06$, $\lambda = 1.4$ m, and $H/h = 0.364$.

Chapter 3

Euler's Equations

3.1 Governing Equations and Boundary Conditions

Effects of viscosity in fluid-structure interaction problems are confined to a thin boundary layer around the body and to the wake region downstream of the body. The maximum Reynolds number calculated at the model scale classifies the flow as "transitional", see e.g., frictional drag data over a flat plate given in Newman (1978). However, we expect viscous forces on the body to be negligible, except in the case of wave breaking, and therefore the fluid is assumed inviscid in the present calculations. Air is assumed compressible, thereby reducing the governing equations to the compressible Euler's Equations,

$$\frac{\partial \rho}{\partial t} + \nabla \cdot (\rho \mathbf{U}) = 0, \tag{3.1}$$

$$\frac{\partial (\rho \mathbf{U})}{\partial t} + \nabla \cdot (\rho \mathbf{U}\mathbf{U}) = -\nabla p + \rho g, \tag{3.2}$$

where ∇ is the gradient vector, ρ is density, t is time, $\mathbf{U} = (u, v, w)$ is the velocity field, p is pressure, and g is the acceleration due to gravity. The solver used, *compressibleInterFoam*, solves for the Navier-Stokes equations. To solve for Euler's Equations, fluid viscosity is set to $\nu \approx 0$. The viscosity of air is set to $\nu = 1.48 \times 10^{-5}\, m^2/s$.

Table 3.1: Boundary conditions are input for the fields of air or water phase (α), dynamic pressure (p_d), and velocity ($\mathbf{U}$).

Boundary	α	p_d	$\mathbf{U}$
inlet	waveAlpha	buoyantPressure	waveVelocity
outlet	zeroGradient	buoyantPressure	fixedValue (0,0,0)
bottom	zeroGradient	buoyantPressure	slip
atmosphere	inletOutlet	totalPressure	pressureInletOutletVelocity
body	zeroGradient	buoyantPressure	slip
frontBack	empty	empty	empty

To close the governing equations (Eqs. (3.1) and (3.2)), a barotropic equation of state is implemented in the solver for the fluid and air phase by,

$$\rho_i = \rho_0 + \psi_i p \tag{3.3}$$

where ψ_i is the compressibility factor of the phase, ρ_0 is a reference density and $i = 1, 2$ for the water phase and air phase, respectively. In these calculations, water is set to be incompressible by setting $\rho_0 = \rho_1$. Air is set to be compressible by setting $\rho_0 = 0$, thereby resulting in the ideal gas equation of state for isothermal flow. In these calculations, $\rho_1 = 1000\, kg/m^3$, $\rho_2 = 1\, kg/m^3$, and $\psi_2 = 1 \times 10^{-5}\, s^2/m^2$.

To run the simulations in OpenFOAM, boundary conditions and initial conditions are input for the fields of dynamic pressure p_d, velocity $\mathbf{U}$, and the air-water phase fraction α, where $\alpha = 1$ for the water phase and $\alpha = 0$ for the air phase. A summary of the boundary conditions used for each of these fields is found in Table 3.1 and definitions for the boundary conditions in OpenFOAM are given in Table 3.2.

Table 3.2: Definitions for boundary conditions for a given patch field ϕ (OpenFOAM (2014)).

Boundary condition	Definition for patch field ϕ
waveAlpha	Input wave surface elevation determined by waves2Foam
waveVelocity	Input wave velocity determined by waves2Foam
zeroGradient	Normal gradient of ϕ is zero
fixedGradient	Normal gradient of ϕ is specified
inletOutlet	Switches $\mathbf{U}$ and p between *fixedValue* and *zeroGradient*
fixedValue	Value of ϕ is specified
buoyantPressure	Sets fixedGradient pressure based on the atmospheric pressure gradient
slip	zeroGradient if ϕ is a scalar; if ϕ is a vector, normal component is fixedValue zero, tangential components are zeroGradient
totalPressure	Total pressure $p_0 = p + \frac{1}{2}\rho \left\|\mathbf{U}\right\|^2$ is fixed; when $\mathbf{U}$ changes, p is adjusted accordingly
pressureInletOutletVelocity	Combination of pressureInletVelocity and inletOutlet
pressureInletVelocity	When p is known at inlet, $\mathbf{U}$ is evaluated from the flux, normal to the patch
empty	Instructs OpenFOAM to solve in two dimensions

3.2 Numerical Method

Numerical calculations are performed using the open-source, computational fluid dynamics (CFD) software, OpenFOAM, short for Open Field Operation and Manipulation. OpenFOAM solves the governing equations, in this case Euler's equations, by use of the finite-volume method for spatial discretization and the Euler method for time discretization. The solver used, *compressibleInterFoam*, solves for two compressible, isothermal, immiscible fluids using a volume of fluid (VOF) phase-fraction based interface capturing approach. The velocity and pressure are coupled using the PIMPLE algorithm, which is a combination of the PISO (Pressure-Implicit Split-Operator) and SIMPLE (Semi-Implicit Methods Pressure-Linked Equation) algorithms.

Details on the design of OpenFOAM, including solvers, utilities and pre- and post-processing tools can be found in OpenFOAM (2014), Jasak et al. (2007), and Weller et al. (1998), for example.

3.3 Numerical Wave Tank

Solitary waves are generated using the wave generation and absorbtion toolbox *waves2Foam* developed by Jacobsen et al. (2012). The *waves2Foam* toolbox provides a framework for generating waves using a selection of wave theory, and implementing wave absorbtion zones to mitigate reflection inside the wave generation zone and at the outlet boundary. *waves2Foam* was originally written to be utilized with the incompressible solver *interFoam* by modifying the *interFoam* source code. The toolbox was successfully applied to the compressible version of this solver *compressibleInterFoam* by modifying the source code for *compressibleInterFoam* in the same manner. It is noted that while *interFoam* solves for the gauge pressure, *compressibleInterFoam* solves for the absolute pressure. Therefore, to run *waves2Foam* using the

compressible solver, the pressure must be initially set to atmospheric pressure ($P_{atm} = 1 \times 10^5$ Pa).

Waves are generated by a user-defined boundary condition based on the Green-Naghdi solution for solitary wave surface elevation given in Eq. (2.6), and the horizontal and vertical components of particle velocity given by,

$$u(x,t) = \sqrt{g(a+h)}\frac{a\,sech^2(\kappa\bar{x})}{h + a\,sech^2(\kappa\bar{x})}\,, \tag{3.4}$$

$$w(x,z,t) = \frac{z}{h + a\,sech^2(\kappa\bar{x})}(2a\,sech^2(\kappa\bar{x})tanh(\kappa\bar{x}))(\sqrt{g(a+h)} - u), \tag{3.5}$$

where κ is defined in Eq. (2.8). These solutions are given in Green & Naghdi (1974), Ertekin (1984), and Hayatdavoodi (2013), for example. It was found in Hayatdavoodi (2013) that a solitary wave generated numerically using the GN theory is not significantly different from a wave generated using the KdV theory. However, to make a direct comparison with calculations given in Hayatdavoodi (2013), the wave generated using the GN equations is used for these calculations. When the solitary wave generated using the GN equations was scaled to the prototype scale, there were issues with the wave generation that we were unable to resolve. Therefore, at the prototype scale, the original boundary condition for generation of a solitary wave based on the KdV solution that came with the *waves2Foam* package was used for both the model and prototype scale.

The same domain and mesh used in Hayatdavoodi (2013) are used in the present calculations as well. Figure 3.1 shows a zoomed in view of the bridge showing the mesh at the water surface and around the bridge. The case chosen from the incompressible calculations performed by Hayatdavoodi (2013) to be calculated using the compressible version of Euler's equations, is the case where adding compressibility should have the most effect on forces. This corresponds to the case where air cannot escape between the girders (0.0% ARO), with a water depth of $h = 0.143$ m and where the girders are fully elevated above the SWL, and

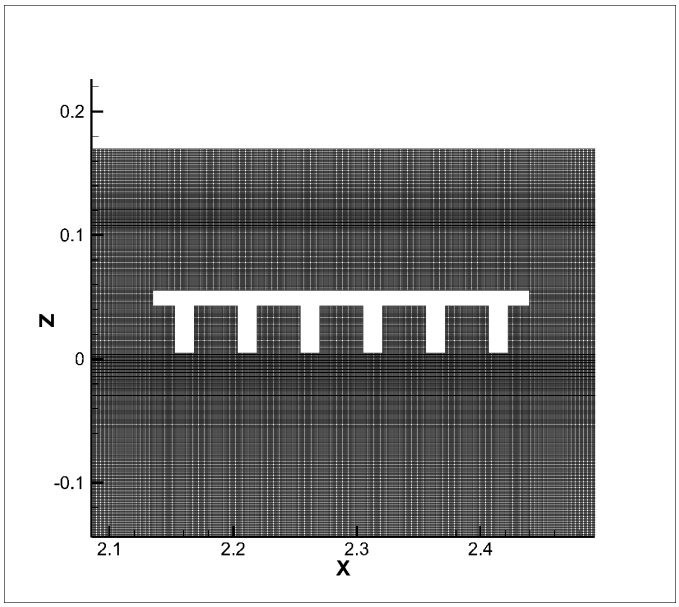

(a)

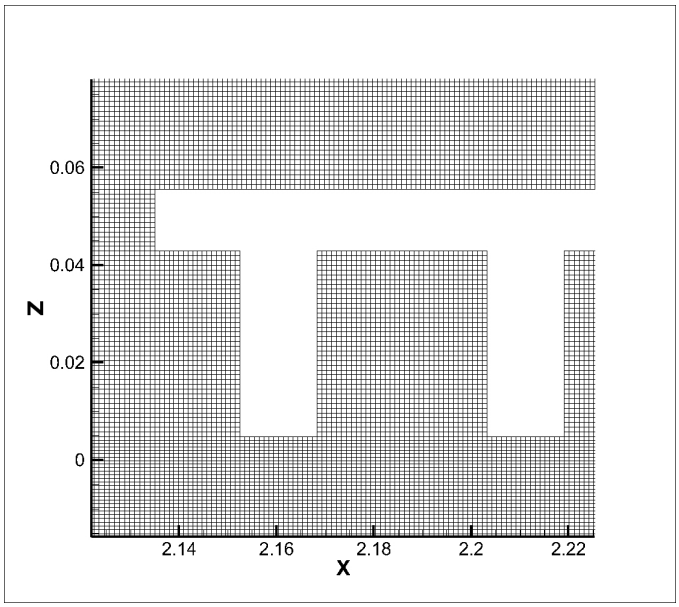

(b)

Figure 3.1: An unstructured mesh is used with a finer mesh at the water surface and around the bridge deck with girders. (a) shows a zoomed in view of the bridge and (b) zooms in further to show the mesh around the bridge. Water depth is $h = 0.143$ m and nondimensional bridge elevation is $z^*/h = 0.3$ for all computational cases.

at a bridge elevation of $z^*/h = 0.3$.

The two-dimensional domain has a length of 4.575 m and a height of 0.313 m and contains an unstructured mesh, where the mesh is finer along the body and the free surface. In this case, the mesh on the body is $\Delta x = 0.001$ m and $\Delta z = 0.001$ m and the total number of cells in the domain is 982935. The Δt is chosen such that the Courant number,

$$C_o = \frac{\Delta t\,|U|}{\Delta x} < 1 \tag{3.6}$$

is satisfied everywhere in the domain. The maximum velocity U_{max} occurs for the maximum wave amplitude tested in this case, $a/h = 0.4$, and can be calculated using Eqs. (2.1) and (2.6). In this case, $U_{max} = 0.40$ m/s and therefore $\Delta t = 0.001$ s is chosen. To allow the wave to propagate through the entire domain, the simulation is run for a total of 3.5 s. To capture surface elevation and maximum and minimum forces on the body, the fields α, velocity $\mathbf{U}$ and total pressure p are output every 0.02 s.

A prototype scale (1:1) version is also run for the case of the bridge model with girders. The model scale is 1:35, so at the prototype scale, the water depth is $h = 5.005$ m. The mesh is scaled by 35 in the z and x directions, making the domain length 160.125 m and height 10.955 m. The mesh is unstructured, the same as in the model scale, giving the same number of cells in the domain. The mesh on the body is $\Delta x = 0.0035$ m and $\Delta z = 0.0035$ m. For the prototype case, $U_{max} = 2.862$ m/s, so Δt is set to 0.005 s to satisfy the Courant number. The simulation is run for 20 s and the fields α, velocity $\mathbf{U}$ and total pressure p are output every 0.1 s.

3.4 Calculations

OpenFOAM outputs the phase field α, velocity $\mathbf{U}$, and total pressure p at each predetermined time step. Surface elevation is determined by utilizing the run-time utility *surfaceEl-*

Table 3.3: Execution times and PC used for calculating compressible Euler's equations at the model and prototype scale. PCI has an Intel Core i7-4770 processor (8M cache, 3.4 GHz) and PCII has an Intel Core i7-2600 processor (8M cache, 3.4 GHz.)

	Model Scale (GN)	Model Scale (KdV)	Prototype Scale (KdV)
$a/h = 0.1$	PCII: 36606 s	PCI: 32479 s	PCI: 32062 s
0.2	PCI: 45744 s	PCI: 49940 s	PCII: 51937 s
0.3	PCII: 71420 s	PCI: 72369 s	PCI: 72894 s
0.4	PCII: 16123 s	PCI: 101922 s	PCI: 99995 s

evation included in the *waves2Foam* package that measures the location of the water surface by integrating the phase field α along a vertical line. Two-dimensional horizontal force is calculated by integrating pressure along the leading edge of the model, including the upwave facing sides of the girders, and trailing edges of the model, including the downwave sides of the girders, and finding the difference at each time step. Vertical force is similarly calculated by integrating the pressure on the top of the model, and the bottom of the model, including the bottom of the girders, and finding the difference. Integrals are solved numerically using Simpson's first method. A more detailed description on calculating force by integrating pressure on the body can be found in Hayatdavoodi (2013). Two computers were used when running calculations: PCI has an Intel Core i7-4770 processor (8M cache, 3.4 GHz) and PCII has an Intel Core i7-2600 processor (8M cache, 3.4 GHz.) A table of execution times for each of the cases run is given in Table 3.3.

Chapter 4

Empirical Methods

The vertical uplift and positive horizontal forces due to cnoidal waves propagating over an elevated plate and bridge model measured during laboratory experiments are compared with the empirical relations of Douglass et al. (2006), who gave them as

$$F_z = C_3 \left(\rho g(\eta_{max} - z^*)A_3\right) , \tag{4.1}$$

$$F_x = C_1 \left(1 + C_r(N-1)\right) \left(\rho g(\eta_{max} - (z^* + \frac{t_p}{2}))A_1\right) , \tag{4.2}$$

where C_3 and C_1 are empirical coefficients, $C_r = 0.4$ is the reduction coefficient, N is the number of girders, and A_3 and A_1 are the projected areas of the model onto the horizontal and vertical planes, respectively. When solving Douglass' equations, we use the suggested conservative empirical coefficient of 2.0 for vertical and horizontal forces on the bridge model, but use the coefficient of 1.0 for the flat plate. The larger coefficient significantly overestimated forces on the flat plate, in some cases by more than 100%. As 1.0 is also a suggested coefficient by Douglass, this is deemed acceptable in these estimations. The equations developed by Douglass et al. (2006) follow closely those given by Wang (1970), Overbeek & Klabbers (2001) and McConnell et al. (2004) and assume that wave loads are linearly proportional to hydrostatic pressure due to an unbroken wave crest.

In their empirical relations, Douglass et al. (2006) makes the assumption that the wave crest is higher than the bridge deck, or $\eta_{max} > z^*$, where η_{max} is the distance from the SWL to the peak of the wave and is approximated for the long waves used in experiments here as $\eta_{max} = 0.7H$. Recall from chapter 2 that z^* is the distance between the SWL and the bottom of the plate or bridge deck. In addition, Douglass et al. (2006) does not take the presence of girders into consideration when estimating uplift forces. Therefore, comparisons to the present experiments can only be made for cases where $\eta_{max} > z^*$.

Experimental measurements for cnoidal waves on an elevated flat plate are also compared with the empirical relations of McPherson (2008), which expanded on the Douglass et al. (2006) relations by adding the weight of wave overtopping for vertical forces, and taking into account the difference in the hydrostatic forces of the leading and trailing edge of the plate for horizontal forces. The vertical force on the plate is given as the sum of hydrostatic force from the plate itself, hydrostatic force from the wave, and force due to air entrapment (assumed zero for flat plate). The equations are as follows:

$$F_{total} = F_{hydro} + F_{bridge} + F_{air}\,, \tag{4.3}$$

$$F_{hydro} = \gamma \delta_z A_3 - F_w\,, \tag{4.4}$$

$$F_{bridge} = \gamma Vol_{bridge}\,, \tag{4.5}$$

$$F_w = 0.5\gamma \delta_z A_3 \tag{4.6}$$

where γ is the specific weight of water, and $\delta_z = \eta_{max} - (z^* + tp)$ is the distance between the wave crest and the top of the plate. Note that $F_w = 0$ if there is no wave overtopping and δ_z may be negative if the crest is below the top of the plate. The relations for horizontal forces are given by Eqs. (6-8) - (6-12) in McPherson (2008). The McPherson relations were not compared with experimental measurements for cnoidal wave loads on the bridge deck with girders because as they are written, they do not account for circumstances where the bridge

girders may be partially submerged.

The empirical relations proposed by AASHTO (2008) were also considered for comparison in this study. However, these equations and are not directly applicable to this study as they are not suitable for the nonlinear, shallow-water waves presented here. In addition, the results of the AASHTO (2008) equations rely heavily on a term called the "trapped air factor" (TAF) which is difficult to estimate in these experiments due to the small scale.

Vertical and horizontal forces measured during laboratory experiments are also compared with the Long Wave Approximation (LWA), studied by Siew & Hurley (1977) and presented in the form of wave loads on a submerged plate by Patarapanich (1984). The LWA assumes the wave length and plate width are large compared with the water depth. The equations are as follows,

$$\bar{F_x} = -ie^{-ikl}(2)Pe^{-i\sigma t}\,, \tag{4.7}$$

$$\bar{F_z} = -ie^{-ikl}Q\left(\frac{sin(k'l) - k'l\,cos(k'l)}{k'l\,cos(k'l)}\right)e^{-i\sigma t} \tag{4.8}$$

where k and k' are the wave numbers upwave and above the plate, $l = B/2$, σ is the angular wave frequency, and P and Q are the complex constants given by,

$$P = ikl\,e^{ikl}/(ikl+1)\,, \tag{4.9}$$

$$Q = e^{ikl}. \tag{4.10}$$

$\bar{F_x}$ and $\bar{F_z}$ are normalized as,

$$\bar{F_x} = \frac{F_x}{\rho g a t_P}\,, \tag{4.11}$$

$$\bar{F_z} = \frac{F_z}{\rho g a B}\,, \tag{4.12}$$

$$\tag{4.13}$$

where a is wave amplitude, t_P is plate thickness and B is plate width.

A theoretical model to approximate the impulse force on a vertical wall due to compression of an air layer during wave impact was developed by Bagnold (1939). The model was extended by Mitsuyasu (1966) to include air leakage, and is known as the "Bagnold-Mitsuyasu" model. Takahashi et al. (1985) adapted the Bagnold-Mitsuyasu model to investigate uplift forces due to compression of air enclosed in a wave-dissipating caisson. Cuomo et al. (2009) further adapted the model to evaluate uplift forces on a bridge where air is trapped between girders. The model is based on the equation of motion for a water mass hitting a ceiling slab:

$$\rho k_t \frac{d^2x}{dt^2} = p_a - p_0, \tag{4.14}$$

where p_a and x are coupled using the following equation of state,

$$p_a = p_0[(D - q(t))/x]^\gamma. \tag{4.15}$$

ρ is the density of water, k_t is the thickness of the water mass contributing to wave momentum, x is the varying thickness of the trapped air layer, D is the initial thickness of the trapped air layer, p_0 is atmospheric pressure, p_a is the absolute pressure of air inside the chamber, and $\gamma = 1.4$ is the polytropic index for air. $q(t)$ is the amount of air leakage given by,

$$q(t) = \epsilon C_a C_v \int_0^t \sqrt{2(p_a - p_0)/\rho_a}\, d\tau, \tag{4.16}$$

where ϵ is the ratio of the area of air relief opening to the area of the ceiling slab, ρ_a is the density of air, and C_a and C_v are the contraction and velocity coefficients, and when multiplied together are $C_a C_v = 0.66$. Equations (4.14) - (4.16) are solved numerically using the initial conditions $x_0 = D$ and $dx/dt = w_0$, where w_0 is the maximum vertical velocity of the wave. Following Cuomo et al. (2009), in the case of wave impact on a bridge, D is taken as the height of the girders and k is the water depth. The pressure differential $p_a - p_0$ is solved for several values of ϵ, and then a reduction coefficient C_ϵ is calculated due to the

presence of openings as,

$$C_\epsilon = \frac{(p_a - p_0)_{\epsilon=0} - (p_a - p_0)_{\epsilon=n}}{(p_a - p_0)_{\epsilon=0}}, \tag{4.17}$$

where $\epsilon = 0$ indicates no air relief openings and $\epsilon = n$ refers to the selected value for ϵ.

It is of interest to compare the reduction coefficient suggested by Cuomo et al. (2009), with the experimental measurements of cnoidal wave loading with different percentages of air relief openings presented in Sec. 6.2. Equations (4.14) - (4.16) are solved numerically using girder height $D = 1.33$ m and water depth $h = 2.485$ m, corresponding to the prototype scale of the model experiments. Calculations were made at the prototype scale as Cuomo et al. (2009) observes that peak pressures do not scale according to Froude scale. Initial vertical velocity w_0, is solved for $H/h = 0.1 - 0.4$ and $\lambda = 49 - 80.5$ m using the solution for vertical particle velocity under a cnoidal wave given by the GN equations, which can be found in Sun (1991) and Hayatdavoodi (2013), for example. In dimensional form, it is given as,

$$w = c\frac{1 + z/h}{(1 + \eta/h)^2}\frac{4HK}{\lambda}CnDnSn \tag{4.18}$$

where c, K, and Cn are defined in Sec. 2.2.1, and Dn and Sn are the Jacobian elliptic functions. w_0 is solved for the maximum vertical velocity, which occurs at $z = 0$ and $\eta_{max} = 0.7H$, as described above. ϵ is calculated for experimental measurements as,

$$\epsilon = \frac{2iA_r}{L_G L_P} \tag{4.19}$$

where $i = 1, 3, 5$ corresponds to one, three or five drilled holes, L_P is the model length, and L_G is the distance between the girders (CL to CL), as described in Section 2.3. For experimental measurements, the reduction coefficient is calculated using measurements for vertical uplift force as,

$$C_\epsilon = \frac{F_{z,\epsilon=0} - F_{z,\epsilon=n}}{F_{z,\epsilon=0}}. \tag{4.20}$$

Chapter 5

Wave Forces on a Flat Plate and Bridge Model with Girders

Vertical ($\mathbf{F_z}$) and horizontal ($\mathbf{F_x}$) force magnitudes on the horizontal flat plate and bridge model are presented in normalized two-dimensional form as force per unit span length (L_P) or

$$\bar{\boldsymbol{F}}_{\boldsymbol{x}} = \frac{\boldsymbol{F}_{\boldsymbol{x}}}{L_P}\,, \quad \bar{\boldsymbol{F}}_{\boldsymbol{z}} = \frac{\boldsymbol{F}_{\boldsymbol{z}}}{L_P}\,. \tag{5.1}$$

Initial hydrostatic forces are removed from the model, or "zeroed" out, so the force measurements are solely due to the impinging wave. First, a series of experiments scaled to those of Brater et al. (1958) are presented. Then, solitary wave forces on a horizontal flat plate and bridge model with girders are presented, followed by cnoidal wave forces on a horizontal flat plate and bridge model with girders.

5.1 Brater Experiments

To have confidence in the accuracy of experimental force data, a preliminary set of experiments was conducted at a 4:5 scale as in those of Brater et al. (1958) who conducted

	Brater (1:1)	UH (4:5)
Barge Length* (L)	0.762 m	0.149 m
Width (B)	0.254 m	0.203 m
Thickness (t_P)	0.048 m	0.038 m
Water depth (h)	0.305 m	0.244 m
Wave Period (T)	1.1 s	0.984 s
	1.09 s	0.975 s
Wave height (H/h)	0.2	
Submergence depth (z_B/h)	0.17, 0.25, 0.33, 0.42, 0.5, 0.58, 0.67, 0.75, 0.83	

Table 5.1: Model dimensions and input parameters for the University of Hawaii Experiments, which are at a scale of 4:5 with those of Brater et al. (1958). *Constrained by flume width.

experiments to measure vertical and horizontal force on a horizontal submerged barge during periodic waves. The model dimensions and input parameters for the Brater experiments and the UH experiments are given in Table 5.1. The model dimensions and water depth for the UH experiments are scaled at 4:5 of the Brater parameters, except for barge length which is constrained by the flume width. Froude scaling is used to scale the wave period.

Figure 5.1 (a) and (b) shows vertical and horizontal force measurements per unit barge length (L) for the UH experiments and the Brater experiments for each of the nondimensional submergence depths z_B/h given in Table 5.1, where z_B is measured from the SWL to the center of the barge. The UH experimental force measurements are scaled using Froude scaling. Figure 5.1 (c) shows the percentage difference between the UH and Brater measurements for the vertical and horizontal forces.

Recall from Section 2.5.2, horizontal force measurements are presented with the strut force removed. Figure 5.1 (b) shows the original horizontal force measurements including

the forces on the strut to demonstrate the difference made by removing the strut forces. The force on the strut contributes significantly to the overall horizontal force on the structure, particularly for deeper submergence depths ($z_B/h = 0.42 - 0.83$), supporting the removal of the strut force to get accurate horizontal force data. For the shallower submergence depths ($z_B/h = 0.17 - 0.33$), the removal of the forces on the strut causes a larger percentage of difference between the Brater and the UH forces. This is likely due to the forces on the strut alone at these elevations being very small and subject to vibrations, likely causing measurements to be slightly larger than the actual force, leading to an overestimation of the actual force due to the contribution of the strut at this elevation. However, to remain consistent, strut forces are removed from all submerged horizontal force experimental measurements. There is generally good agreement between both horizontal and vertical forces for the UH and Brater experiments, and percentage difference can be attributed to the different scales of the experiments, particularly the dimensions of barge length which may introduce three-dimensional effects.

5.2 Solitary Wave Forces on a Horizontal Flat Plate

Vertical and horizontal forces on a fixed and rigid horizontal flat plate due to solitary wave flow are presented in this section. Time series of surface elevation and vertical and horizontal forces measured during laboratory experiments compared with those calculated using incompressible Euler's equations given in Hayatdavoodi (2013) and Seiffert, Hayatdavoodi & Ertekin (2014) are shown in Fig. 5.2 for water depth $h = 0.086$ m, $a/h = 0.287$ and $z/h = 0.2$, and in Figs. 5.3 and 5.4 for $h = 0.114$ m, $a/h = 0.301$, $z/h = 0.0$, and $z^*/h = 0.1$, respectively. Calculations agree well with laboratory measurements for surface elevation with the calculations able to effectively capture wave reflection, dispersion and

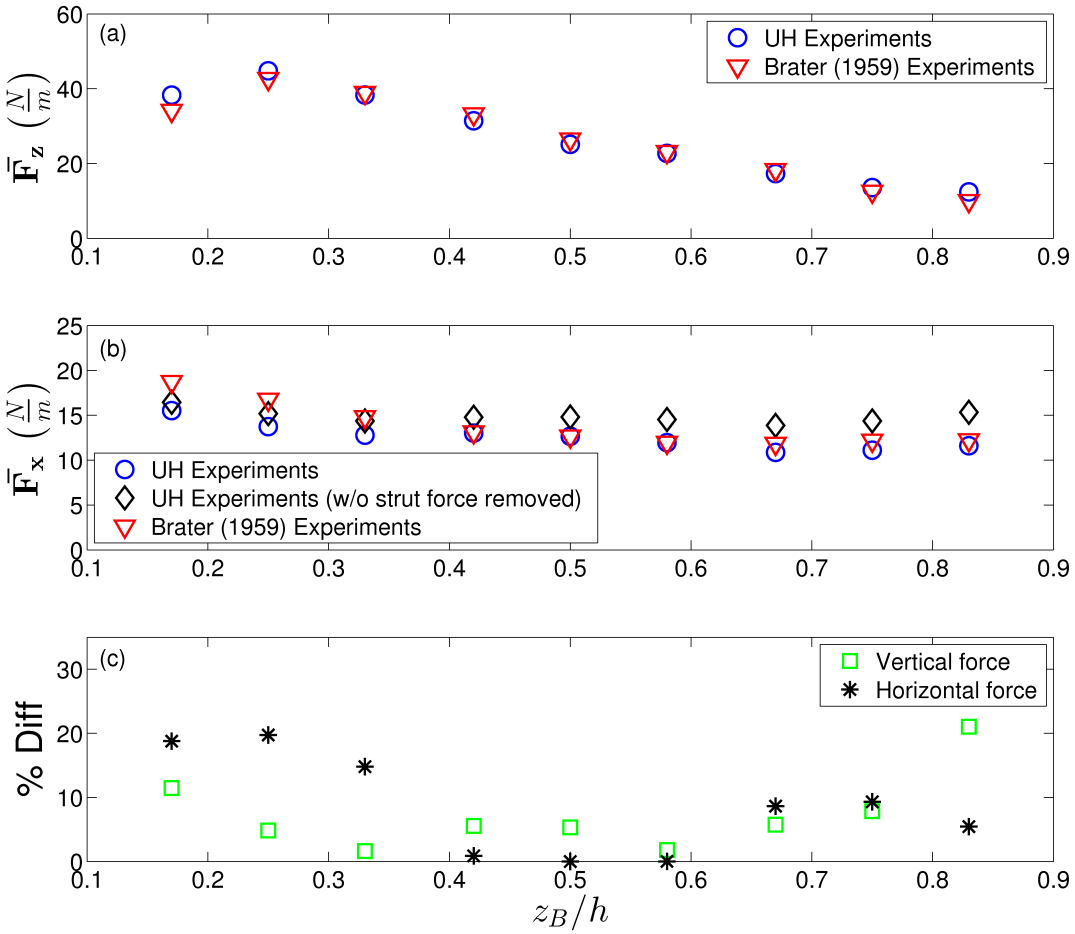

Figure 5.1: (a) Vertical and (b) horizontal force per unit barge length (L) for the UH and Brater experiments and (c) percent difference between Brater and UH vertical and horizontal forces at each nondimensional submergence depth z_B/h. (b) includes measurements for horizontal forces before the strut forces are removed.

transmission (Figs. 5.2 (a) - (c)). The wave measured during laboratory experiments down-wave of the plate is slightly smaller than the calculated wave (Figs. 5.2 (b) and (c)), likely due to wave attenuation as the wave propagates down the flume.

Both calculations and measurements show an initial vertical uplift force followed slightly later by a positive horizontal force as the wave initially interacts with the plate (Figs. 5.2 (d) and (e), and Figs. 5.3 (a) and (b)). As the wave travels over the plate, there is a downward force, followed slightly later by a negative horizontal force as the wave leaves the plate. The elevated case shown in Fig. 5.4 (a) shows a short duration uplift force due to water particle accelerations causing an abrupt pressure differential during the wave impact, followed by a long duration uplift force as effects of buoyancy are felt on the plate as the wave progresses further over the plate and breaks. There is a small downward force as green water is left by the broken wave slowly drains off the plate. Figure 5.4 (b) shows an initial positive horizontal force as the wave impacts the plate but little or no negative horizontal force as the wave has broken and lost most of its energy by the time it leaves the plate.

Figure 5.5 shows the velocity vectors and dynamic pressure calculated using incompressible Euler's equations at the water depth $h = 0.086$ m, $a/h = 0.287$, and $z/h = 0.2$. The four figures correspond to the times at which the largest vertical uplift, positive horizontal, vertical downward and negative horizontal forces are calculated, at time $t = 1.92, 2.02, 2.26$ and 2.4 s, respectively. At time $t = 1.92$ s, pressure underneath the plate is much larger than on top of the plate, causing the large vertical uplift force. As the wave advances, at $t = 2.02$ s, large horizontal particle accelerations create a large positive pressure differential between the leading and trailing edges of the plate causing the large positive horizontal force. The largest vertical downward force is caused by the large pressure difference between the top and bottom of the plate, as well as the weight of the water above the plate and under the wave crest at $t = 2.26$ s. As the wave leaves the plate at $t = 2.4$ s, pressure is larger

downwave of the plate than upwave, causing a negative horizontal force. The beginning of a reverse flow, as described by Carter et al. (2006) and Lo & Liu (2014) can also be seen downwave of the plate at $t = 2.4$ s. A uniform flow underneath the plate is observed at each of the four time steps. This same phenomena has been described by Graw (1993) and Carter (2005), who suggest the conversion of this uniform flow into energy by submerged turbines.

The experimental data for submerged cases for the vertical uplift force, vertical downward force, horizontal positive force and horizontal negative force for water depths of $h = 0.143$ m, 0.114 m, 0.086 m and 0.071 m are presented in Figs. 5.6, 5.7, 5.8 and 5.9, respectively. Figs. 5.6 - 5.9(a), show larger uplift forces when both the wave amplitude is larger and the submergence depth is shallower. The greatest uplift forces occur when the top of the plate is even with the still-water surface ($z/h = 0$), and were in some cases, up to four times larger than the deepest submergence depth. Vertical downward forces (Figs. 5.6 - 5.9(b)) are also larger with larger wave amplitude and shallower submergence depth, with the exception of $z/h = 0$, where forces are smaller around a/h =0.2-0.3. This is also where we begin to see wave breaking as it propagates over the plate, explaining the smaller force results.

In general, the horizontal forces were around a tenth of the magnitude of the vertical forces. For water depths of 0.143 m and 0.114 m (Figs. 5.6(c)and 5.7(c)), the positive horizontal forces are again larger with a larger wave amplitude and shallower submergence depth. However, for water depths of 0.086 m and 0.071 m (Figs. 5.8(c) and 5.9(c)), forces remain nearly constant with the submergence depth, with the exception of $h = 0.071$ m and $z/h = 0$. This behavior may be related to the fact that the width ratio of B/h and the thickness ratio of t_p/h change as the water depth changes even if the amplitude ratio of a/h remains constant. As B/h and t_P/h increase, the role of z/h on the horizontal force becomes less. The inconsistencies seen at $h = 0.071$ m and $z/h = 0$ (Fig. 5.9(c)) may partially be due to turbulent effects due to the plate being at the still-water surface. Negative horizontal

forces (Figs. 5.6 - 5.9(d)), while still showing larger values with larger wave amplitudes and shallower submergence depths, are very much affected by the nonlinear effects, strong dispersion and flow separation, as evident in the data that are not so much ordered unlike the data for the vertical uplift forces.

The following elevated, flat plate cases were tested in this work: $z^*/h = 0.03$, 0.06, 0.1, where z^* is measured from the SWL to the bottom of the plate. The elevated-case experimental data for the vertical uplift force, vertical downward force, and horizontal positive force for water depths of $h = 0.143$ m, 0.114 m, 0.086 m and 0.071 m are presented in Figs. 5.10 - 5.13. Horizontal negative forces on the plate are not included in these figures, but rather in Table 5.2, as most measurements for these forces contained a significant amount of noise, likely due to turbulence at the trailing edge of the plate where negative forces act, and were generally small in magnitude.

Figs. 5.10 - 5.13(a) show larger uplift forces when both the wave amplitude is larger and the plate elevation is smaller. Similarly, Figs. 5.10 - 5.13(c) show larger horizontal positive forces with larger wave amplitudes and smaller elevations. Figs. 5.10 - 5.13(b)) show that larger wave amplitudes have little affect on the vertical downward forces, as does the plate elevation. The data for the vertical downward force for $h = 0.071$ m, $z^*/h = 0.03$ (Fig. 5.13(b)) are absent due to the fact that percent error in measurements was quite large for each wave amplitude. This may be due to the effect of surface tension as the bottom of the plate was only 0.002 m from the SWL.

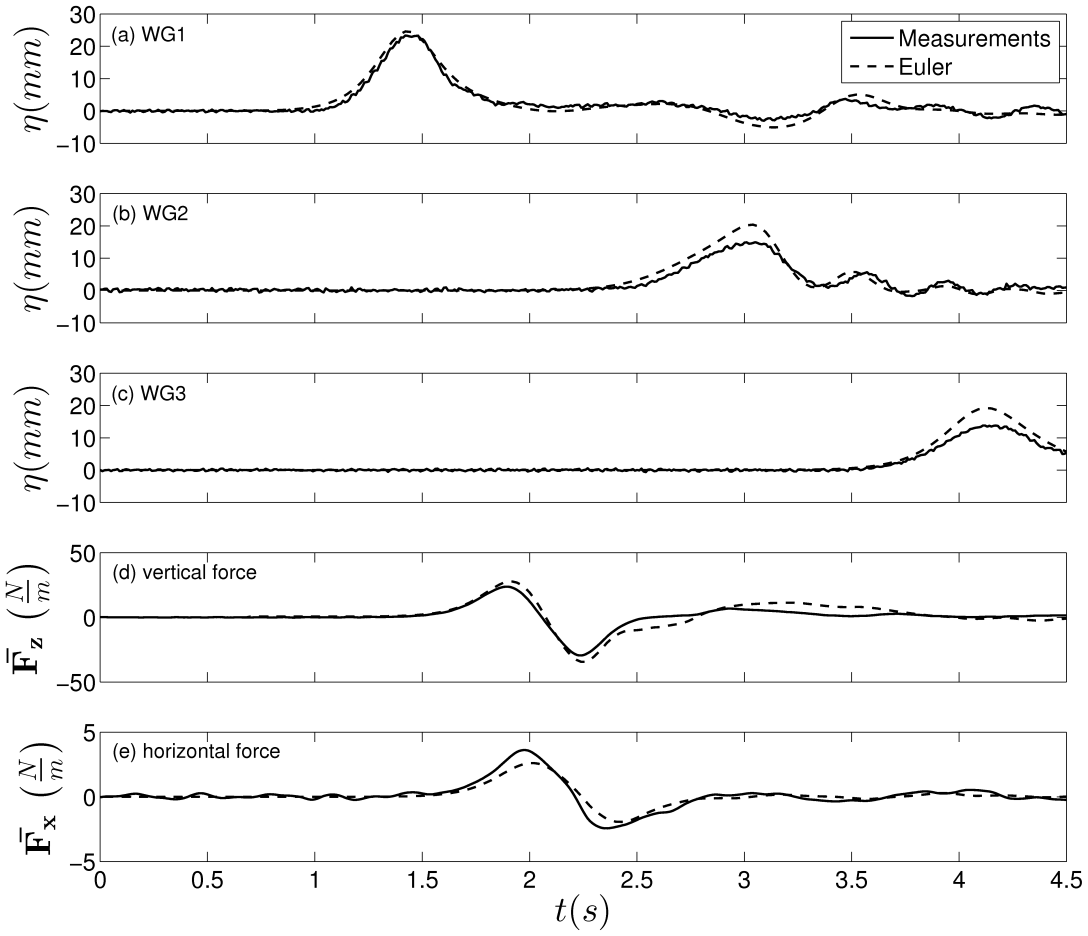

Figure 5.2: Surface elevation and vertical and horizontal forces measured during laboratory experiments for a solitary wave propagating over a submerged horizontal flat plate are compared with those calculated using Euler's equations from Hayatdavoodi (2013) and Seiffert, Hayatdavoodi & Ertekin (2014) for water depth $h = 0.086$ m, $a/h = 0.287$ and $z/h = 0.2$.

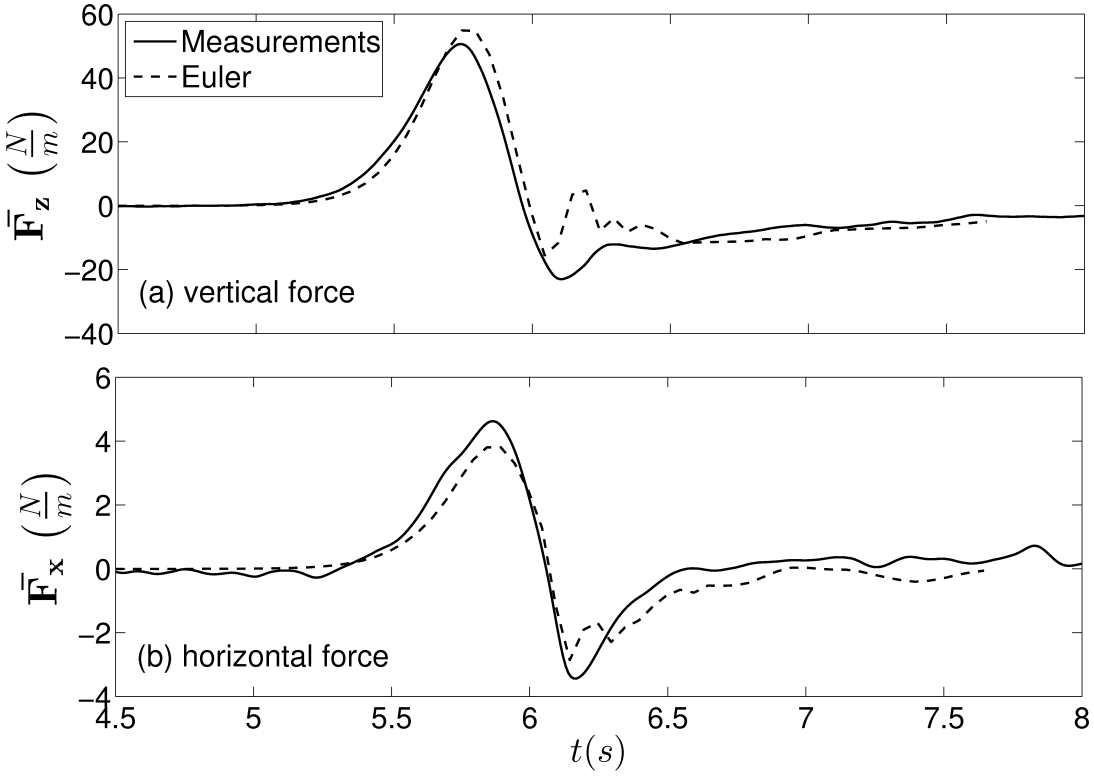

Figure 5.3: Vertical and horizontal forces measured during laboratory experiments for a solitary wave propagating over a flat plate at the water surface are compared with those calculated using Euler's equations from Hayatdavoodi (2013) and Seiffert, Hayatdavoodi & Ertekin (2014) for water depth $h = 0.114$ m, $a/h = 0.301$ and $z/h = 0.0$.

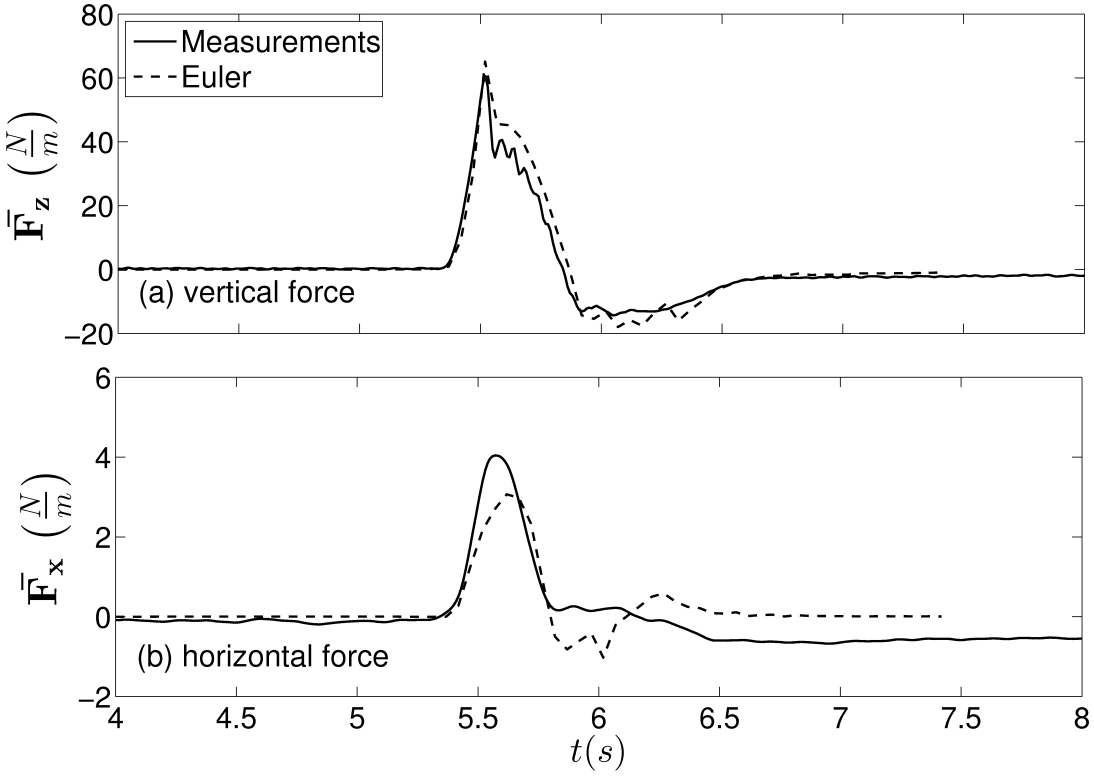

Figure 5.4: Vertical and horizontal forces measured during laboratory experiments for a solitary wave propagating over an elevated flat plate are compared with those calculated using Euler's equations from Hayatdavoodi (2013) and Seiffert, Hayatdavoodi & Ertekin (2014) for water depth $h = 0.114$ m, $a/h = 0.301$ and $z^*/h = 0.1$.

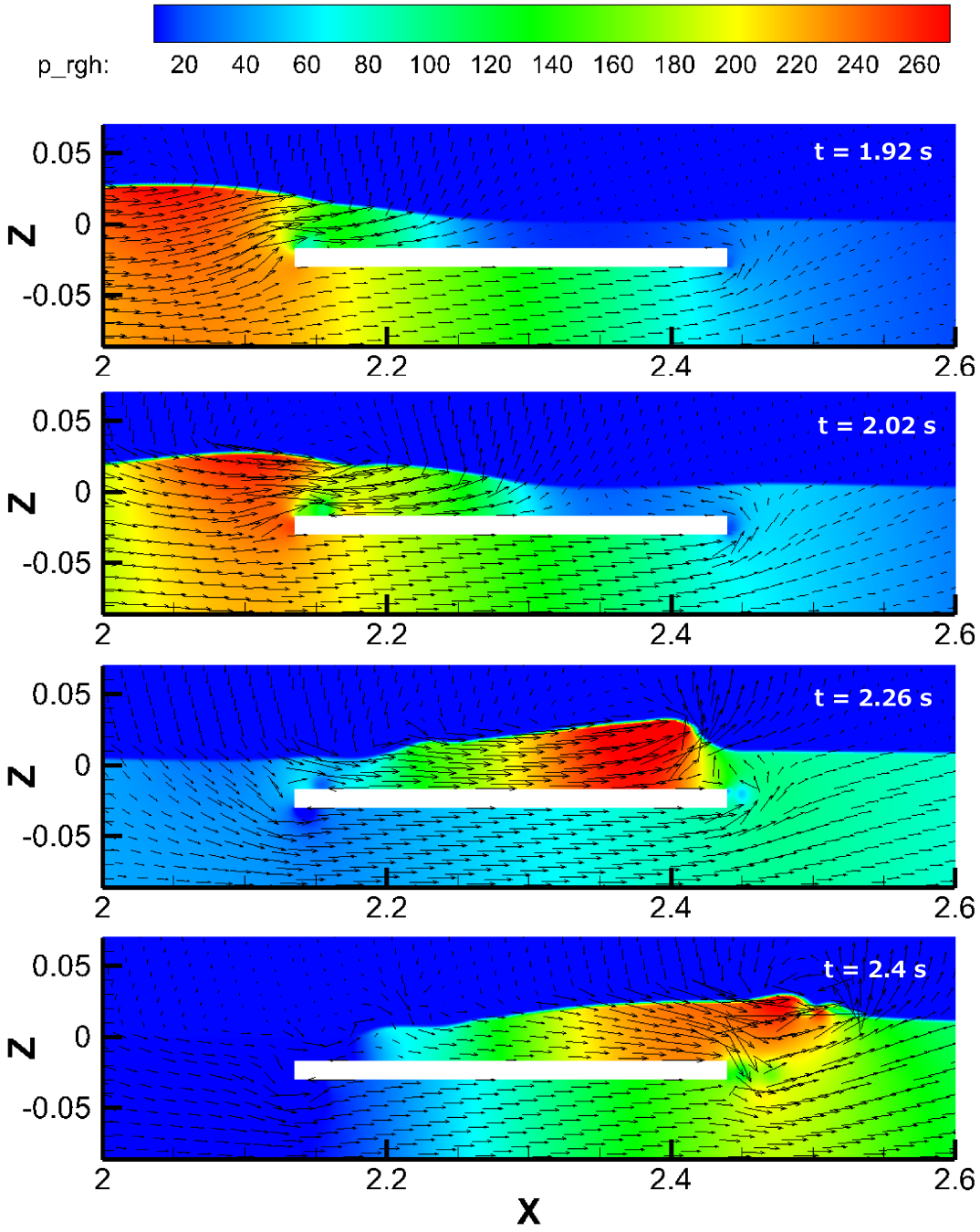

Figure 5.5: Velocity vectors are plotted along with dynamic pressure (p_d) calculated using incompressible Euler's equations, at the time at which vertical uplift, positive horizontal, vertical downward and negative horizontal forces are the largest, at times $t = 1.92, 2.02, 2.26$ and 2.4 s, respectively. Pressure is given in N/m^2. Water depth is $h = 0.086$ m, $a/h = 0.287$, and $z/h = 0.2$.

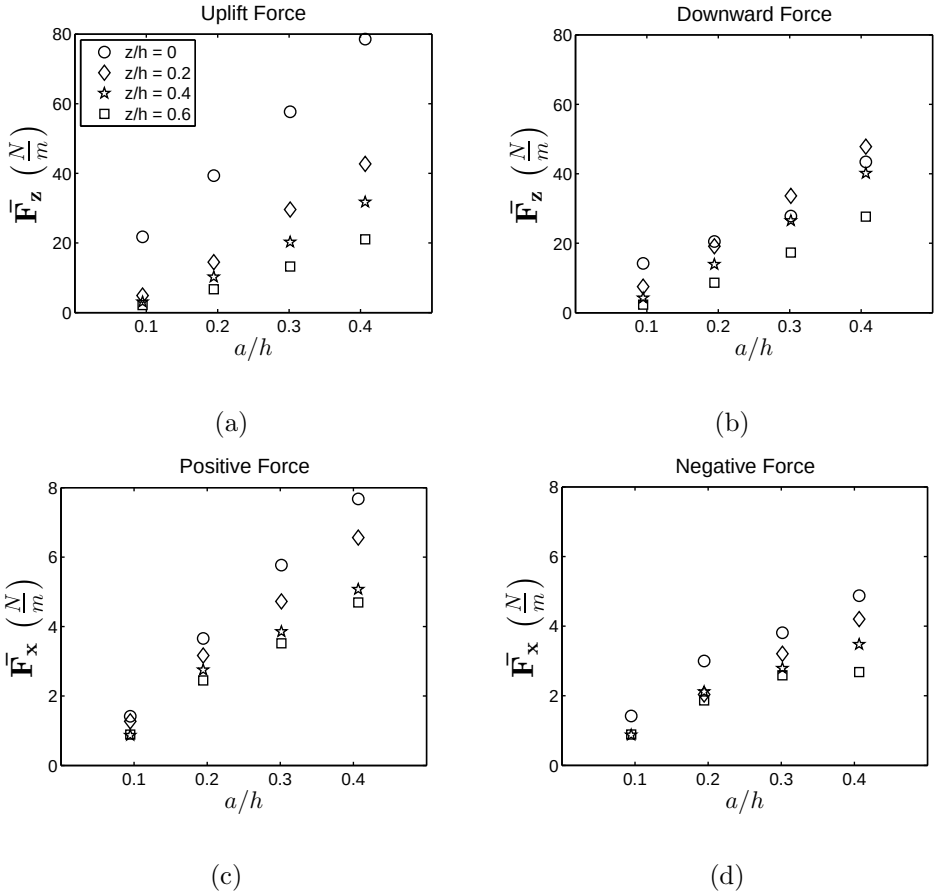

Figure 5.6: (a) Vertical uplift force, (b) vertical downward force, (c) horizontal positive force, and (d) horizontal negative force are measured on the plate at submergence depths of 0, 0.2, 0.4 and 0.6 times the water depth and wave amplitudes of 0.1 - 0.4 times the water depth of $h = 0.143\,m$.

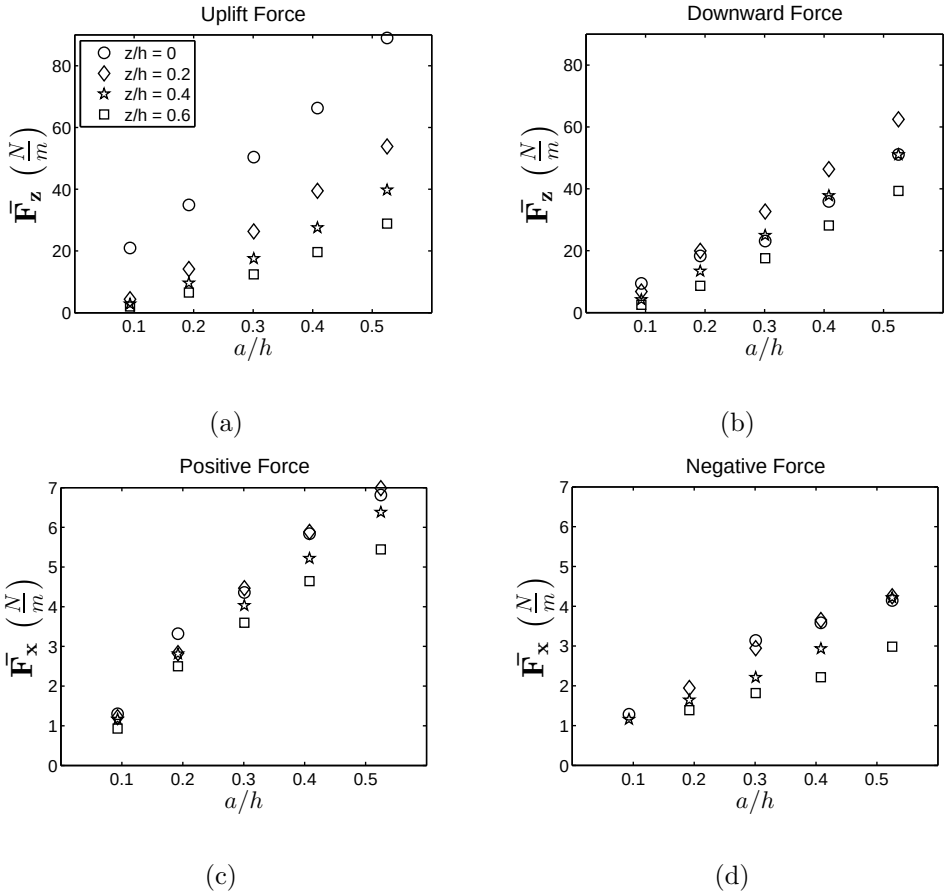

Figure 5.7: (a) Vertical uplift force, (b) vertical downward force, (c) horizontal positive force and (d) horizontal negative force are measured on the plate at submergence depths of 0, 0.2, 0.4 and 0.6 times the water depth and wave amplitudes of 0.1 - 0.5 times the water depth of $h = 0.114\,m$.

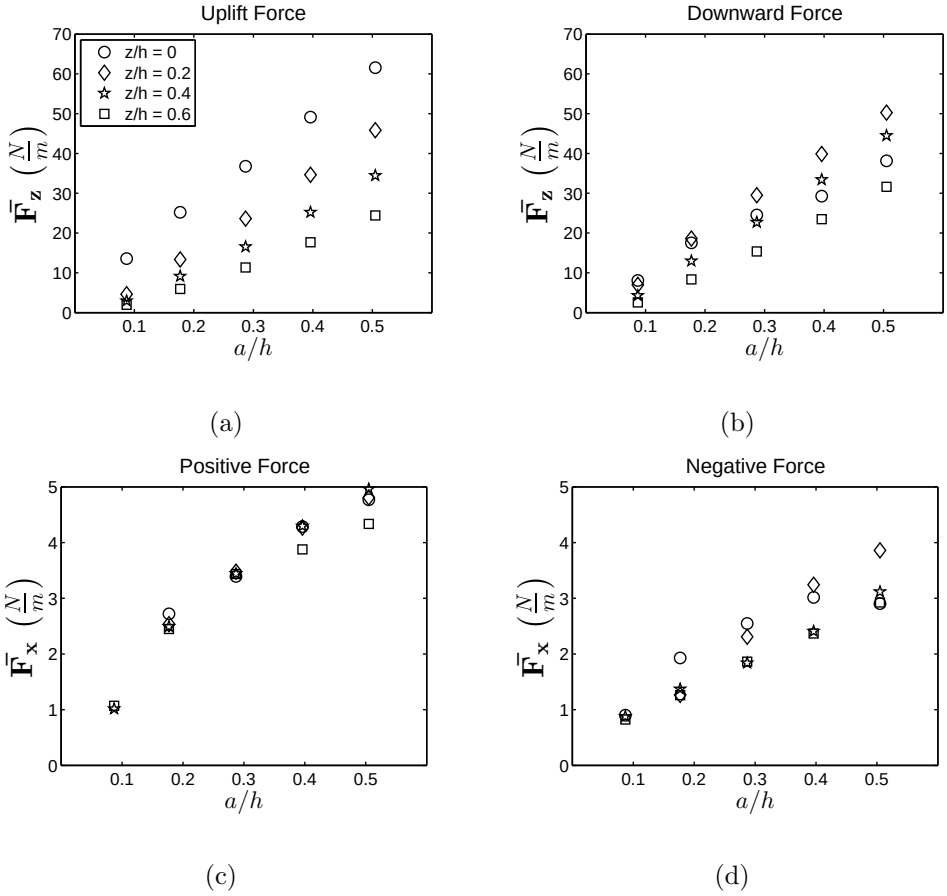

Figure 5.8: (a) Vertical uplift force, (b) vertical downward force, (c) horizontal positive force and (d) horizontal negative force are measured on the plate at submergence depths of 0, 0.2, 0.4 and 0.6 times the water depth and wave amplitudes of 0.1 - 0.5 times the water depth of $h = 0.086\,m$.

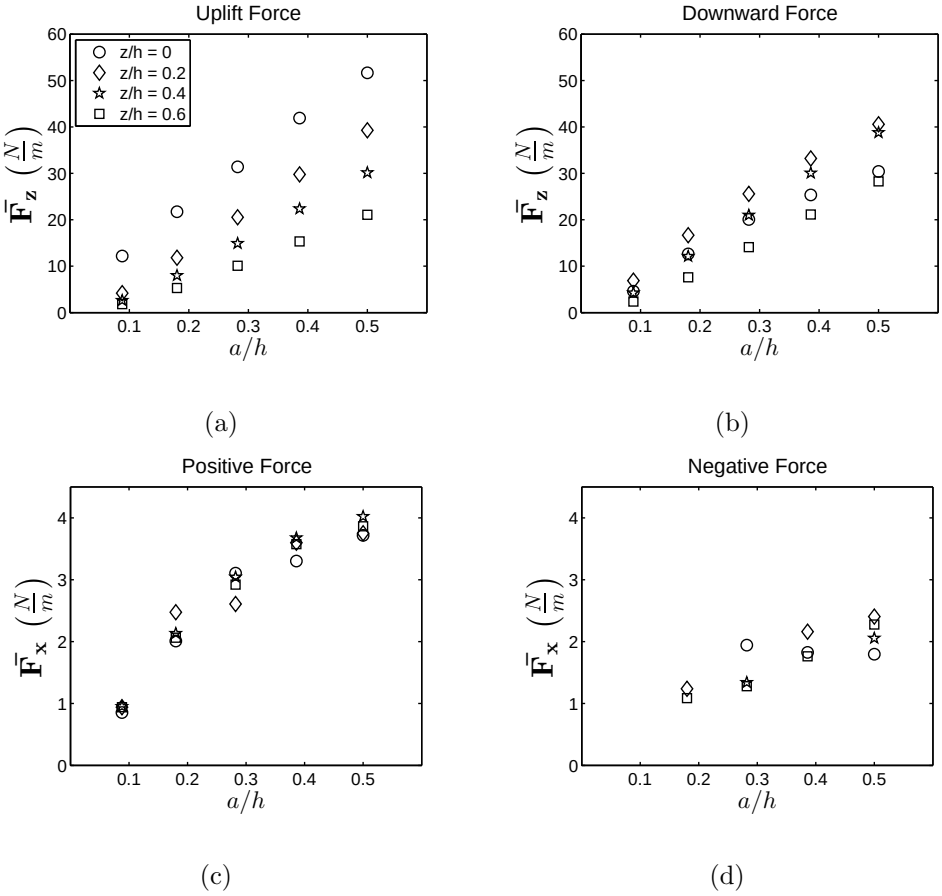

Figure 5.9: (a) Vertical uplift force, (b) vertical downward force, (c) horizontal positive force and (d) horizontal negative force are measured on the plate at submergence depths of 0, 0.2, 0.4 and 0.6 times the water depth and wave amplitudes of 0.1 - 0.5 times the water depth of $h = 0.071\,m$.

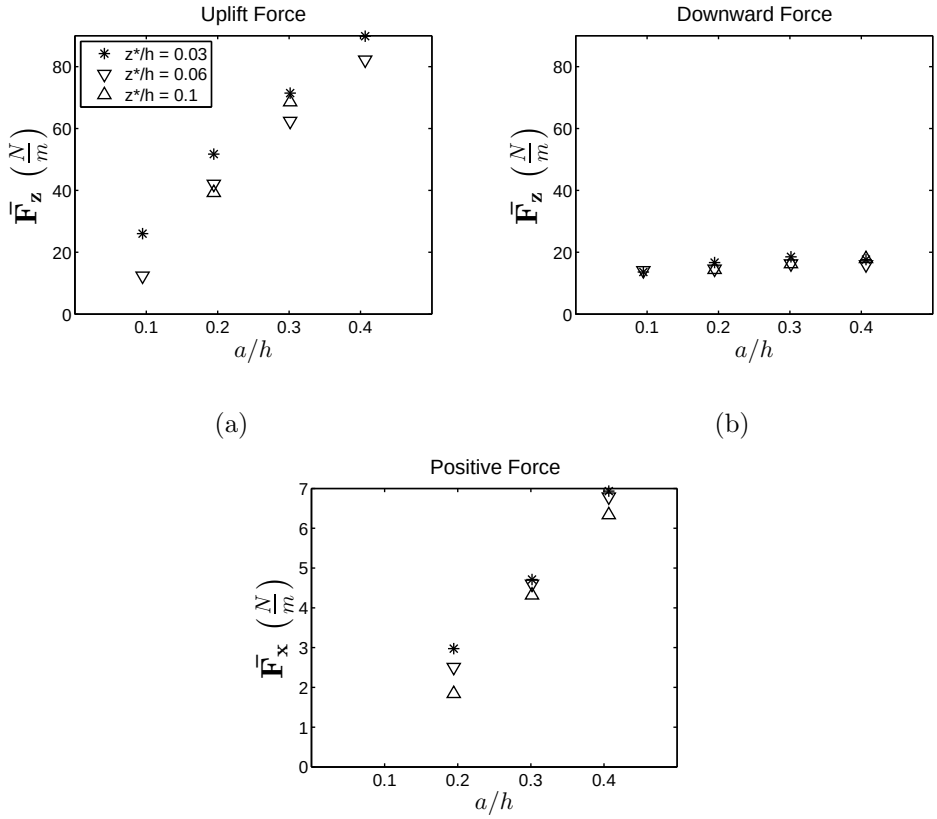

(a) (b)

(c)

Figure 5.10: (a) Vertical uplift force, (b) vertical downward force, and (c) horizontal positive force are measured on the plate at elevations above the SWL of z^*/h =0.03, 0.06, 0.1 times the water depth and wave amplitudes of 0.1 - 0.4 times the water depth of $h = 0.143\,m$.

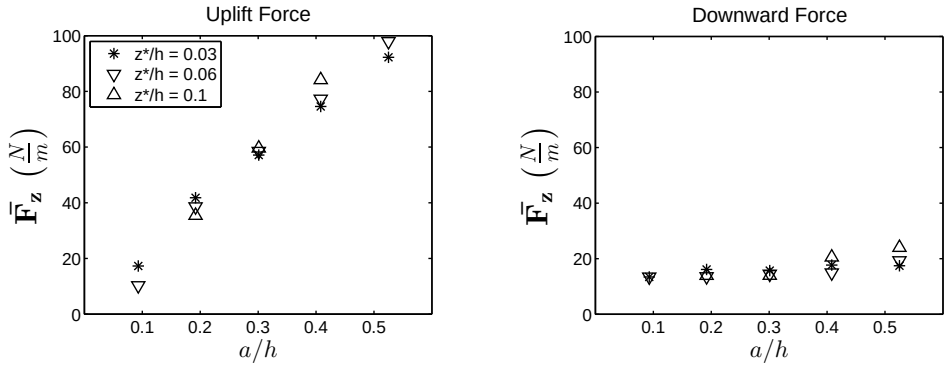

(a)

(b)

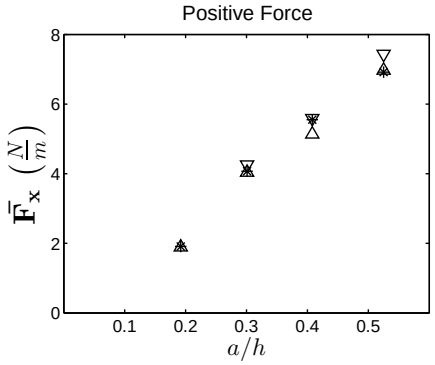

(c)

Figure 5.11: (a) Vertical uplift force, (b) vertical downward force, and (c) horizontal positive force measured on the plate at elevations above the SWL of z^*/h =0.03, 0.06, 0.1 times the water depth and wave amplitudes of 0.1 - 0.5 times the water depth of $h = 0.114\,m$.

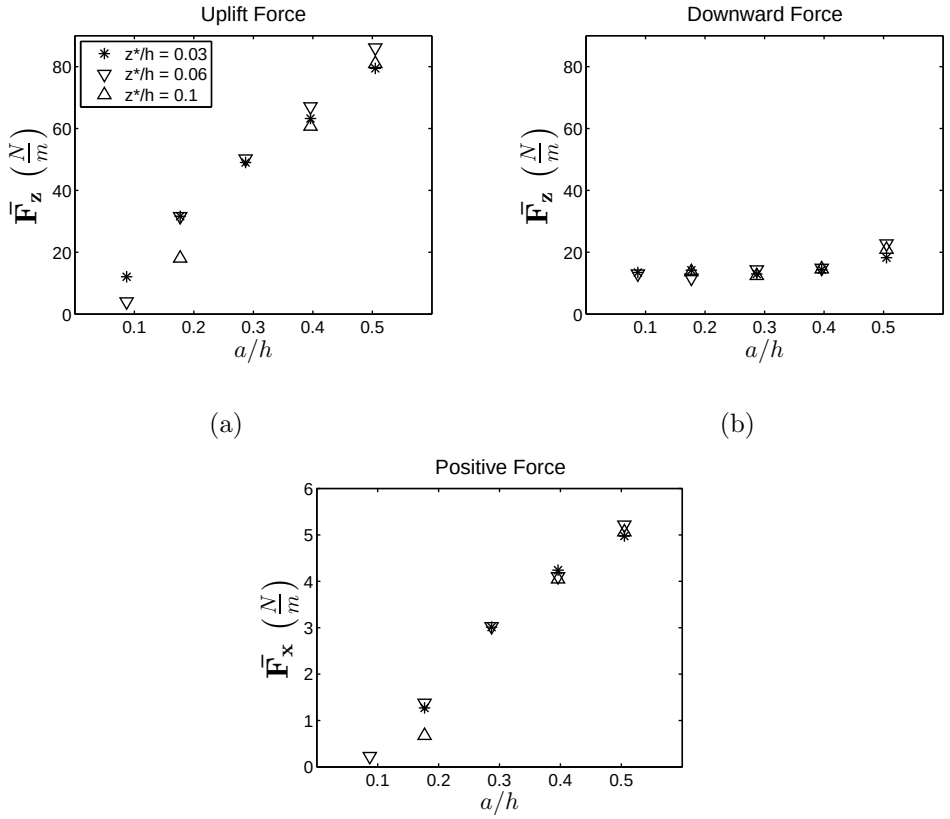

Figure 5.12: (a) Vertical uplift force, (b) vertical downward force, and (c) horizontal positive force measured on the plate at elevations above the SWL of z^*/h =0.03, 0.06, 0.1 times the water depth and wave amplitudes of 0.1 - 0.5 times the water depth of $h = 0.086\,m$.

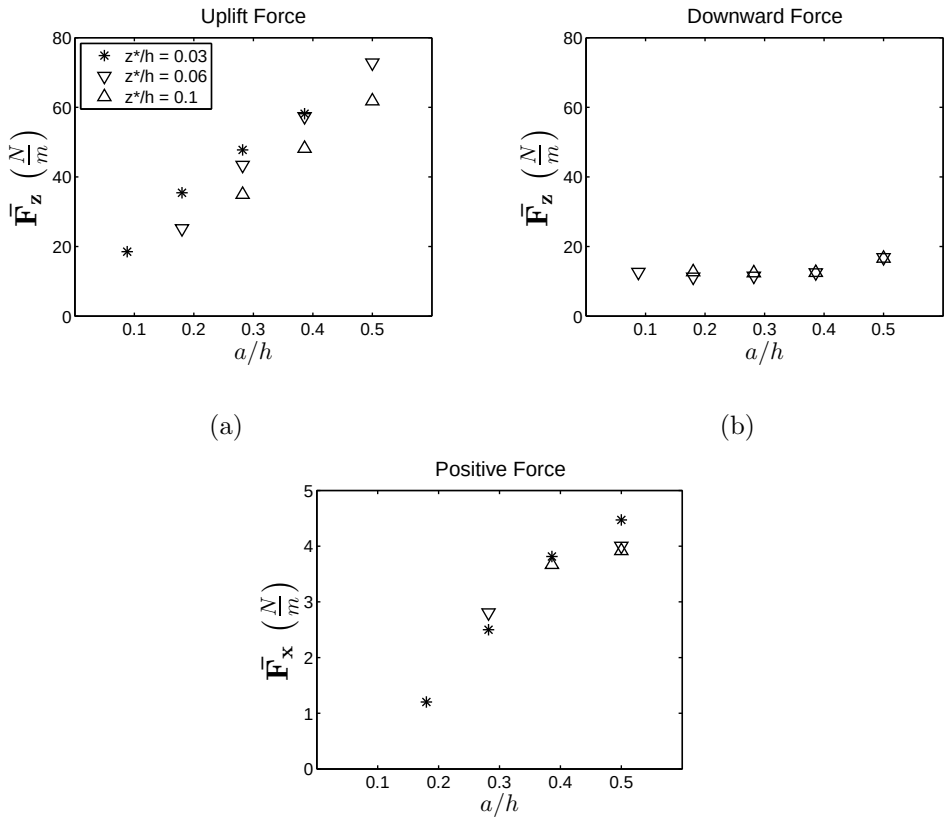

Figure 5.13: (a) Vertical uplift force, (b) vertical downward force, and (c) horizontal positive force measured on the plate at elevations above the SWL of z^*/h =0.03, 0.06, 0.1 times the water depth and wave amplitudes of 0.1 - 0.5 times the water depth of $h = 0.071\,m$.

Water Depth (m)	z^*/h	a/h	Force (N/m^2)
0.143	0.03	0.407	268.04
0.143	0.1	0.407	207.16
0.114	0.03	0.408	137.12
0.114	0.03	0.525	259.11
0.114	0.06	0.408	87.44
0.114	0.06	0.525	282.78
0.114	0.1	0.525	163.84
0.086	0.03	0.505	74.61
0.086	0.06	0.505	59.16

Table 5.2: Experimental data for the horizontal negative force per unit plate length and thickness.

5.3 Solitary Wave Forces on a Bridge Model with Girders

Vertical and horizontal forces due to a solitary wave propagating over a bridge model with girders are presented in this section. Time series for surface elevation and horizontal and vertical forces measured during laboratory experiments are compared with those calculated using the incompressible Euler's equations from Hayatdavoodi (2013) and Hayatdavoodi, Seiffert & Ertekin (2014*b*) for a submerged bridge model with water depth $h = 0.086$ m, $a/h = 0.287$ and $z/h = 0.2$ in Fig. 5.14. Time series for vertical and horizontal forces for the case where the model is located at the water surface, at water depth $h = 0.114$ m, $a/h = 0.301$, $z/h = 0.0$ are given in Fig. 5.15 and for the elevated case $z^*/h = 0.1$ in Fig. 5.16. Calculations for surface elevation given in Figs. 5.14 (a) - (c) show good agreement

with laboratory measurements with calculations able to predict reflection, dispersion and transmission as the wave propagates over the model. The calculated wave is slightly larger on the downwave side of the model (Figs. 5.14 (b) and (c)), likely due to wave attenuation as the wave travels down the flume during the laboratory experiments. Calculations and measurements for force (Figs. 5.14 (d) and (e) and Figs. 5.15 and 5.16) show an initial uplift force followed by a positive horizontal force as the wave initially interacts with the model. These forces are due both to hydrostatic force of the wave, as well as pressure differentials caused by water particle accelerations under the wave crest. As the wave travels over the model, a downward force due to the weight of the water is followed by a negative force as the wave leaves the model, due to both a hydrostatic force, as well as a pressure differential due to water particle accelerations, this time acting in the opposite direction.

Laboratory measurements for submerged cases for the vertical uplift force, vertical downward force, horizontal positive force and horizontal negative force for water depths of $h =$ 0.143 m, 0.114 m, 0.086 m and 0.071 m are presented in Figs. 5.17, 5.18, 5.19 and 5.20, respectively. Similar trends are found in the vertical uplift and downward forces for the bridge model with girders as with the horizontal flat plate as presented in Section 5.2. Vertical uplift forces are larger for a shallower submergence depth, and in some cases, forces on the model at $z/h = 0$ are up to four times larger than the model submerged at $z/h = 0.4$. Downward forces are larger for both larger wave amplitude and shallower submergence depth, (Figs. 5.17 - 5.20(a) and (b)) with the exception of $z/h = 0$. For water depths $h = 0.114$ m, 0.086 m and 0.071 m, downward forces at $z/h = 0$ are consistently smaller than forces at deeper submergence depths at each wave amplitude and are about the same magnitude as forces at $z/h = 0.3$ for $h = 0.143$ m. In the case of $z/h = 0$, for every amplitude and water depth, however, there is wave breaking on top of the model. At other submergence depths, the wave breaks either behind the model or does not break at all. This explains the smaller downward

force results seen for $z/h = 0$.

At each water depth, positive horizontal forces are less than half the amplitude of vertical forces (Figs. 5.17(c) - 5.20(c)). For water depth $h = 0.143$ m, forces remain nearly constant with a change in the submergence depth. For $h = 0.114$ m and amplitudes $a/h = 0.4$ and 0.5, and at all amplitudes for water depths $h = 0.086$ m and $h = 0.071$ m, forces are smaller as the model gets closer to the water surface. In Section 5.2, it was found that, for a submerged flat plate at water depths of $h = 0.143$ m and 0.114 m, positive horizontal forces were larger at shallower submergence depths, and for water depths $h = 0.086$ m and 0.071 m, the forces remained constant with shallower submergence depth. This suggests a correlation between the positive horizontal force results and model width to water depth ratio, B/h, and model thickness to water depth ratio (plate thickness, t_P/h, in the case of flat plate and deck thickness plus girder height to water depth ratio, $(t_P + t_G)/h$, in the case of the bridge model with girders). For smaller B/h and t_P/h or $(t_P + t_G)/h$ ratios (i.e., deeper water), forces are larger for shallower submergence depth. For larger B/h and t_P/h or $(t_P + t_G)/h$ ratios (i.e., shallow water), forces are smaller for shallower submergence depths.

For water depths of $h = 0.143$ m and 0.114 m, negative horizontal forces are larger for both the larger wave amplitude and shallower submergence depth cases (Figs. 5.17(d), 5.18(d)). However, for water depths of $h = 0.086$ m and 0.071 m, there is again an increase in force with larger wave amplitude, and submergence depth has less of an effect on the forces. As with positive horizontal force, these results may be related to the ratios of B/h and $(t_P + t_G)/h$, where larger ratios mean forces do not change for different submergence depths.

Results from experiments conducted on the elevated bridge model for water depths of $h = 0.143$ m, 0.114 m, 0.086 m and 0.071 m are presented in Figs. 5.21 - 5.24, respectively. These figures show larger vertical and horizontal forces for larger wave amplitudes. Figs.

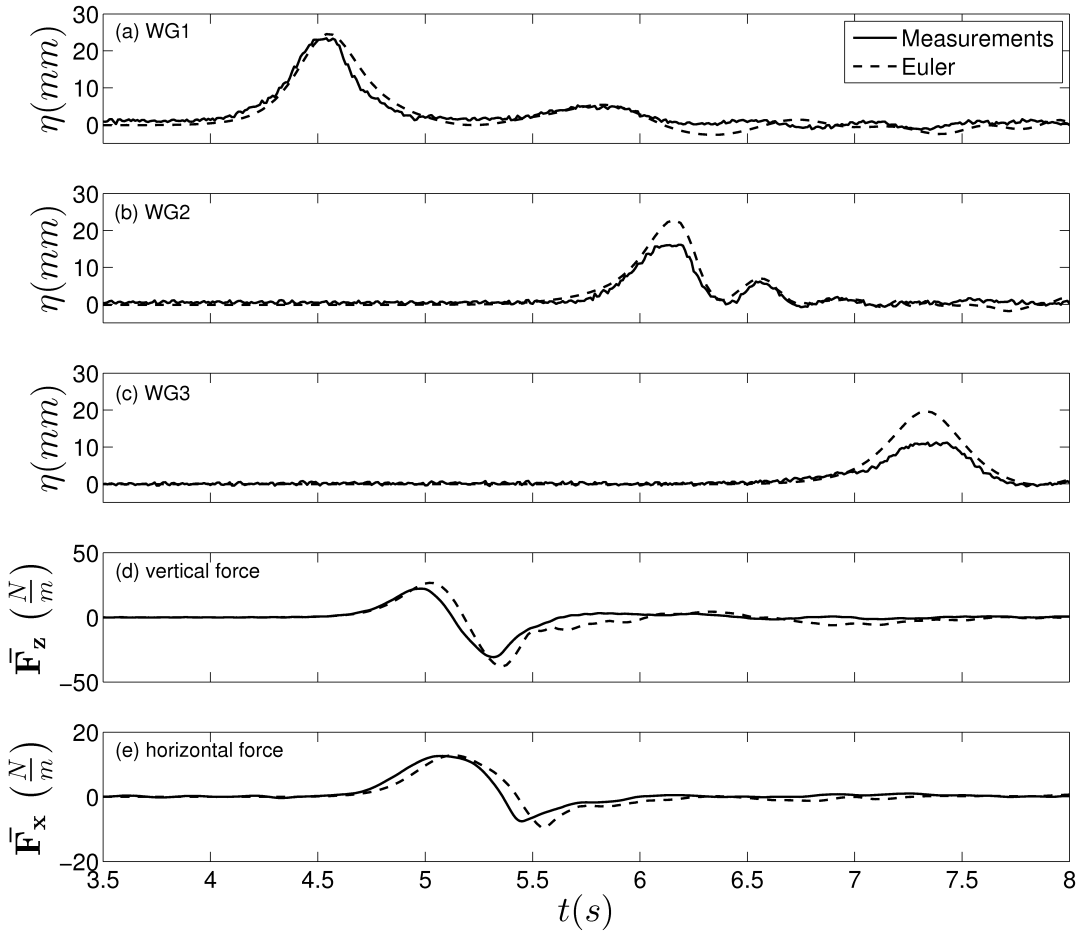

Figure 5.14: Surface elevation and vertical and horizontal forces measured during laboratory experiments for a solitary wave propagating over a submerged bridge deck are compared with those calculated using Euler's equations from Hayatdavoodi (2013) and Hayatdavoodi, Seiffert & Ertekin (2014*b*) for water depth $h = 0.086$ m, $a/h = 0.287$ and $z/h = 0.2$.

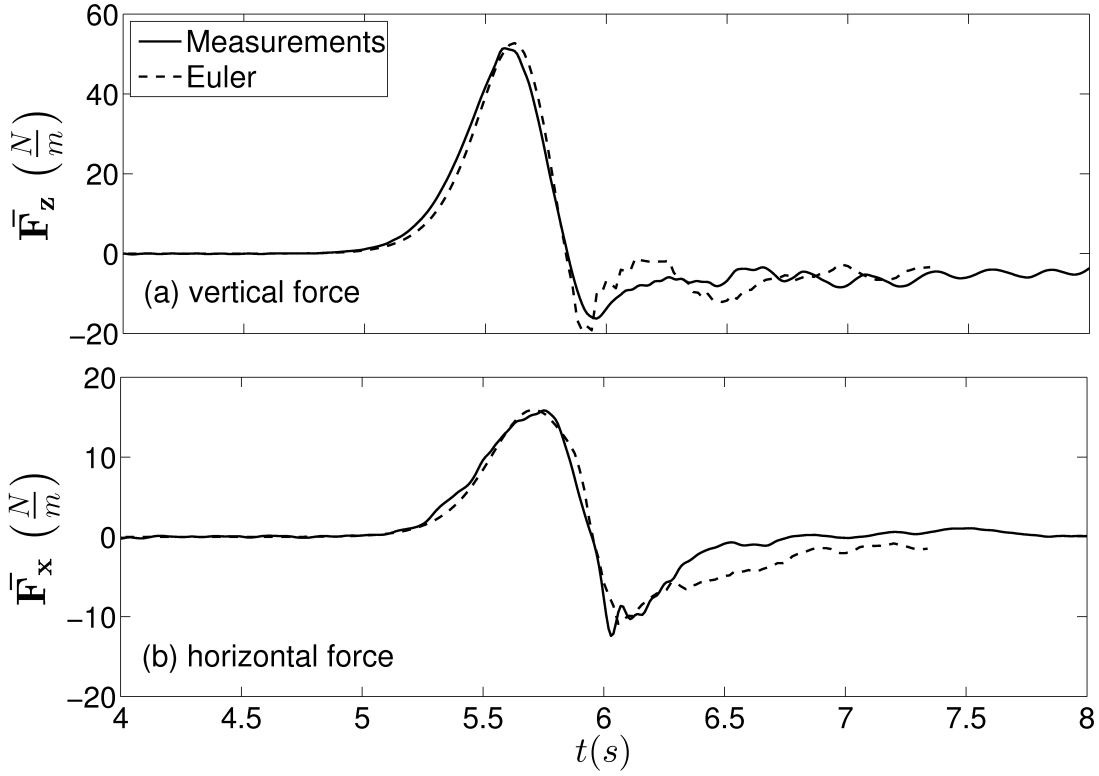

Figure 5.15: Vertical and horizontal forces on a bridge deck measured during laboratory experiments for a solitary wave propagating over a bridge deck on the water surface are compared with those calculated using Euler's equations from Hayatdavoodi (2013) and Hayatdavoodi, Seiffert & Ertekin (2014*b*) for water depth $h = 0.114$ m, $a/h = 0.301$ and $z/h = 0.0$.

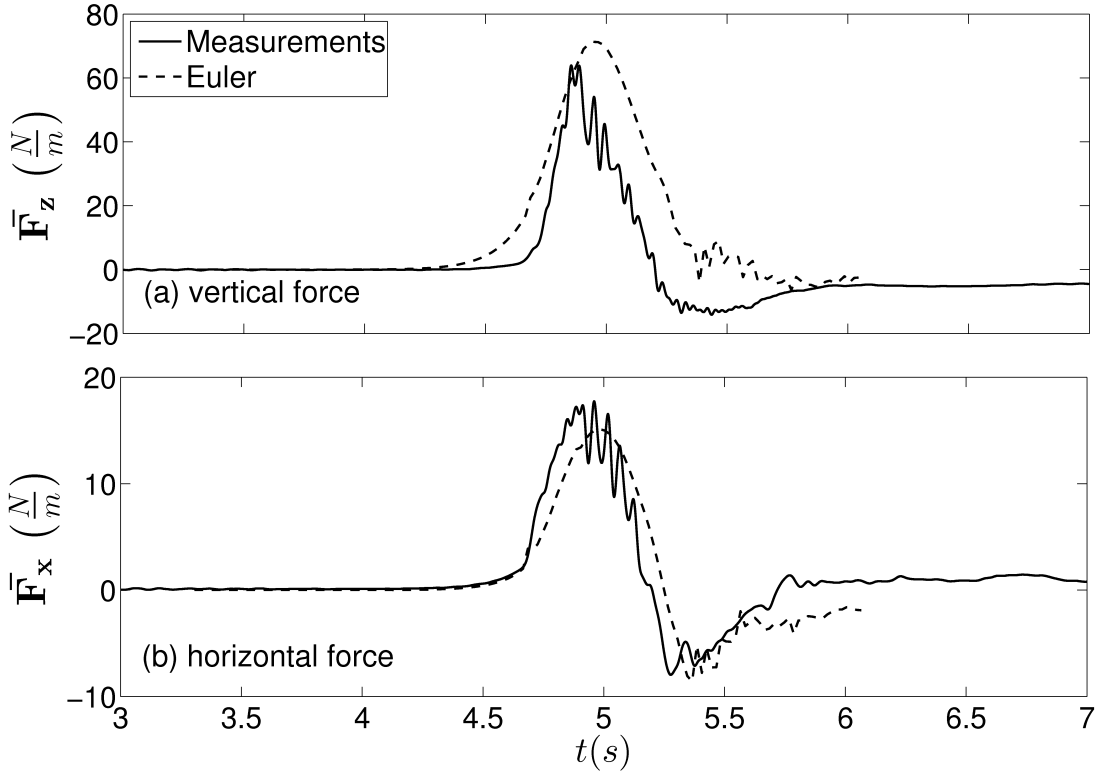

Figure 5.16: Vertical and horizontal forces on a bridge deck measured during laboratory experiments for a solitary wave propagating over an elevated bridge deck are compared with those calculated using Euler's equations from Hayatdavoodi (2013) and Hayatdavoodi, Seiffert & Ertekin (2014*b*) for water depth $h = 0.114$ m, $a/h = 0.301$ and $z^*/h = 0.1$.

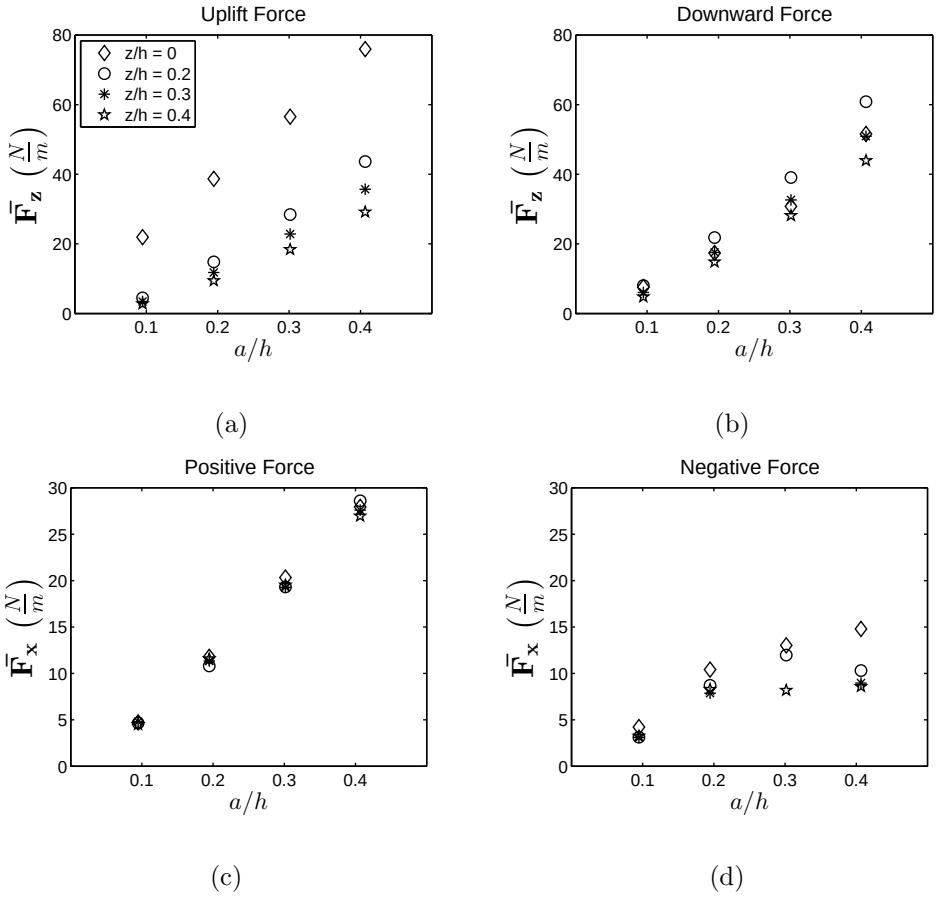

Figure 5.17: (a) Vertical uplift force, (b) vertical downward force, (c) horizontal positive force, and (d) horizontal negative force are measured on the model at submergence depths of 0, 0.2, 0.3 and 0.4 times the water depth and wave amplitudes of 0.1 - 0.4 times the water depth of $h = 0.143\,m$.

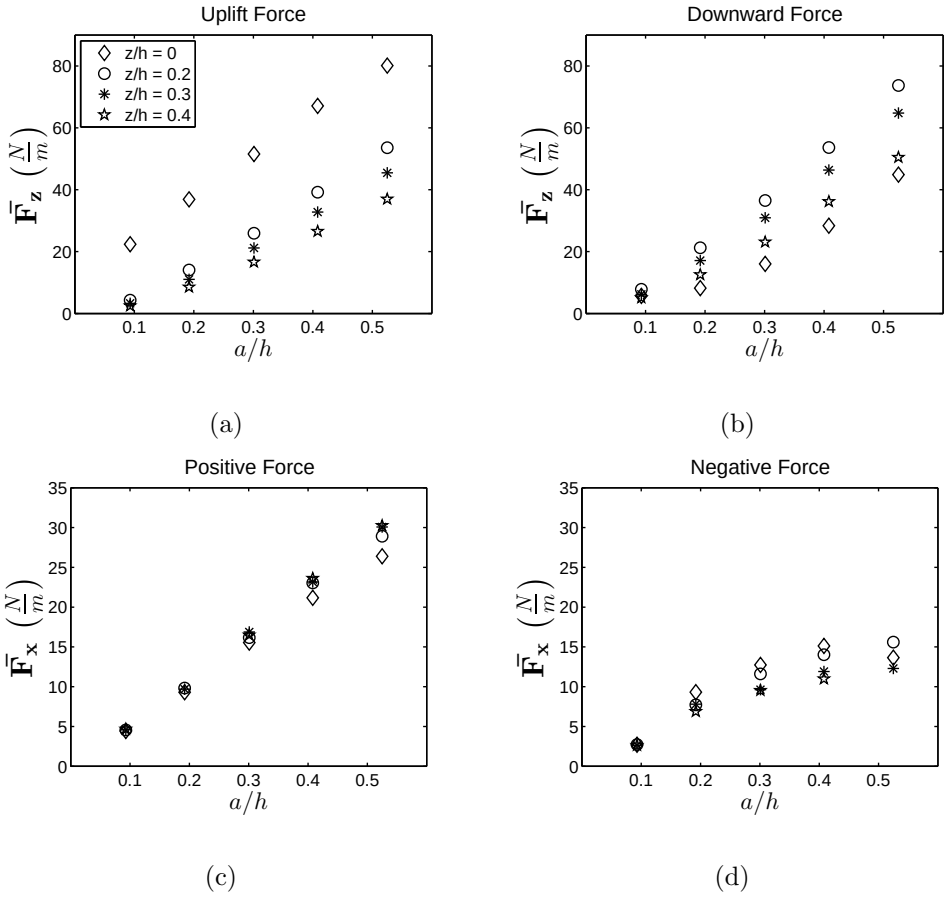

Figure 5.18: (a) Vertical uplift force, (b) vertical downward force, (c) horizontal positive force and (d) horizontal negative force are measured on the model at submergence depths of 0, 0.2, 0.3 and 0.4 times the water depth and wave amplitudes of 0.1 - 0.5 times the water depth of $h = 0.114\,m$.

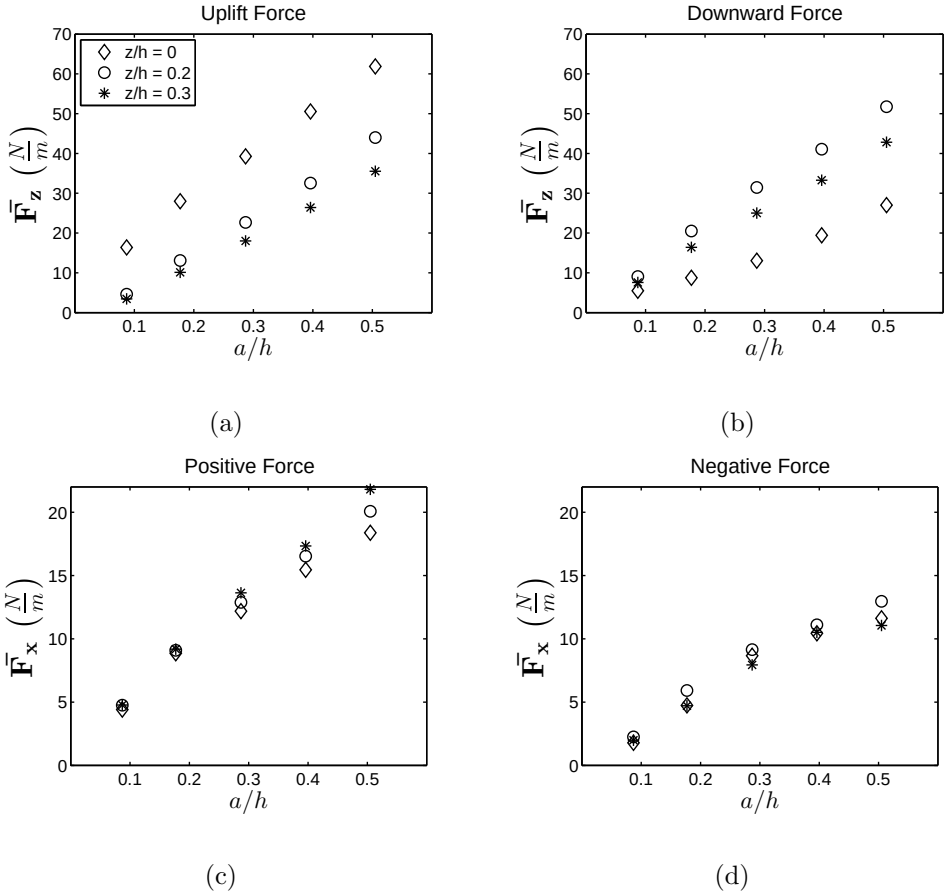

Figure 5.19: (a) Vertical uplift force, (b) vertical downward force, (c) horizontal positive force and (d) horizontal negative force are measured on the model at submergence depths of 0, 0.2 and 0.3 times the water depth and wave amplitudes of 0.1 - 0.5 times the water depth of $h = 0.086\,m$.

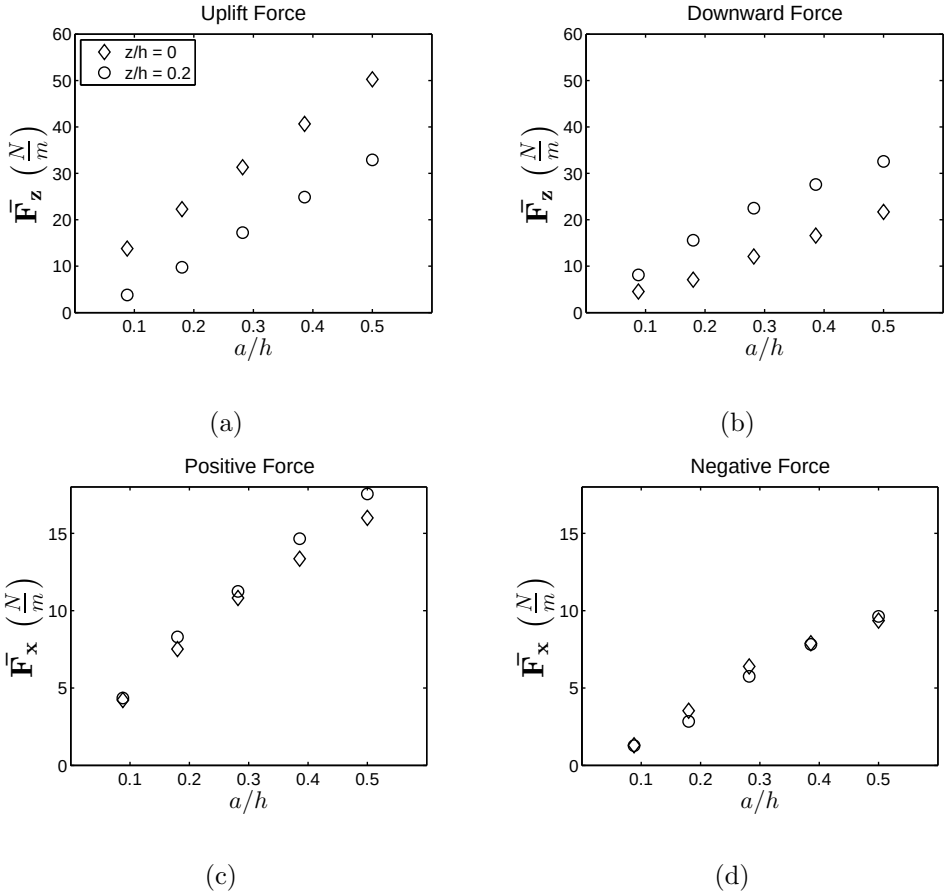

Figure 5.20: (a) Vertical uplift force, (b) vertical downward force, (c) horizontal positive force and (d) horizontal negative force are measured on the model at submergence depths of 0 and 0.2 times the water depth and wave amplitudes of 0.1 - 0.5 times the water depth of $h = 0.071\,m$.

5.21 - 5.24(a) show nearly the same vertical uplift forces for z^*/h =0.06 and 0.1 with slightly larger forces for $z^*/h = 0.1$ at water depths of $h = 0.143$ m and 0.114 m and slightly larger forces for $z^*/h = 0.06$ at water depths of h =0.086 m and 0.071 m. In each of the water depths, the force for z^*/h =0.3 is much smaller than they are for z^*/h =0.06 and 0.1. In these cases, the wave crest does not reach the deck ($a/h = 0.1, 0.2$) or just barely reaches the deck ($a/h = 0.3 - 0.5$) indicating interaction of the wave with the bridge deck contributes significantly to the uplift forces. Figs. 5.21 - 5.24(b) show smaller force results for vertical downward force for larger elevations. In fact, several of the points for the case of elevation z^*/h =0.3 are absent due to the fact that forces were too small for the load cells to detect.

Positive horizontal forces shown in Figs. 5.21(c) - 5.24(c) show slightly larger forces for z^*/h =0.1 compared with z^*/h =0.06 for each wave amplitude and water depth. For elevation z^*/h =0.3, forces are smaller than or nearly equal to the z^*/h =0.06 and 0.1 cases for wave amplitudes of a/h =0.1, 0.2, 0.3, and larger for wave amplitude a/h =0.5 (and a/h =0.4 for water depth h =0.143 m). As with the uplift forces, this indicates wave interaction with the bridge deck contributes significantly to positive horizontal forces. Although both horizontal and vertical forces increase with an increased wave amplitude, we cannot conclude that this is a linear relation. In fact, downward vertical forces and negative horizontal forces for both submerged and elevated cases show forces increase nonlinearly with increasing wave amplitude. Furthermore, changing the ratio of plate width to water depth, B/h, may show more nonlinear results, particularly in uplift and positive horizontal forces.

By performing many of the same experimental conditions for both the horizontal flat plate (Section 5.2) and the bridge model with girders (presented in this section), we are able to determine whether forces on a bridge deck with girders can be accurately estimated by using the data for a flat plate. When comparing results for submerged cases for uplift forces for the same water depth, wave amplitude and submergence depth for the plate and bridge

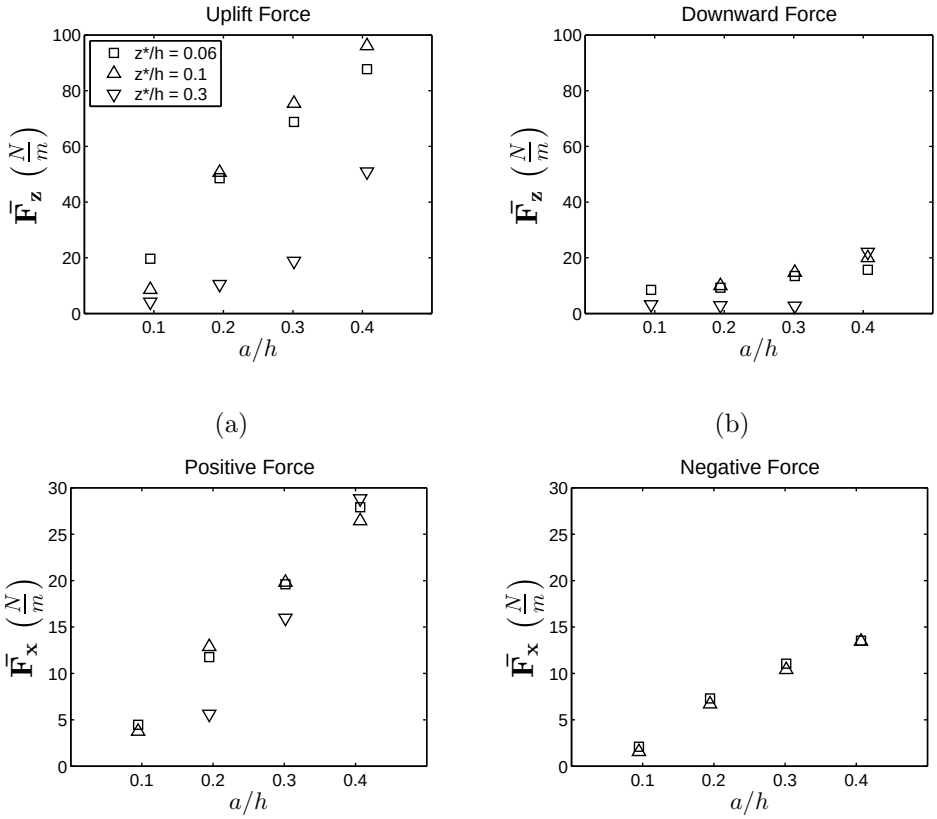

Figure 5.21: (a) Vertical uplift force, (b) vertical downward force, (c) horizontal positive force and (d) horizontal negative force are measured on the model at elevations above the SWL of z^*/h =0.06, 0.1, 0.3 times the water depth and wave amplitudes of 0.1 - 0.4 times the water depth of $h = 0.143\,m$.

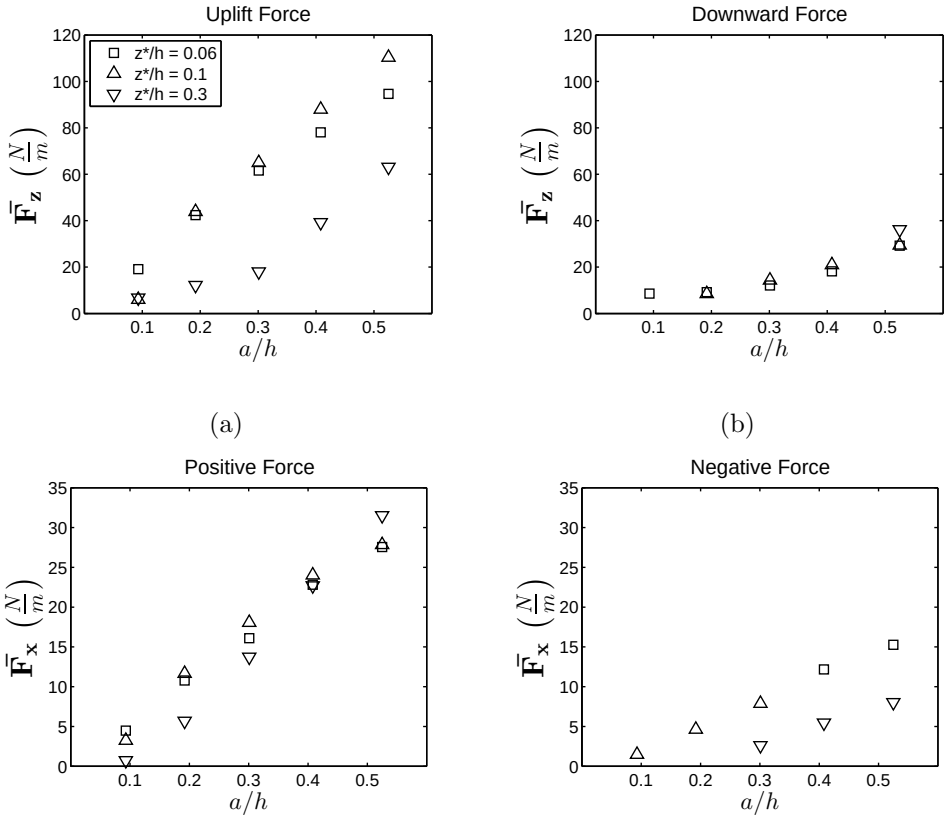

Figure 5.22: (a) Vertical uplift force, (b) vertical downward force, (c) horizontal positive force and (d) horizontal negative force are measured on the model at elevations above the SWL of z^*/h =0.06, 0.1, 0.3 times the water depth and wave amplitudes of 0.1 - 0.5 times the water depth of $h = 0.114\,m$.

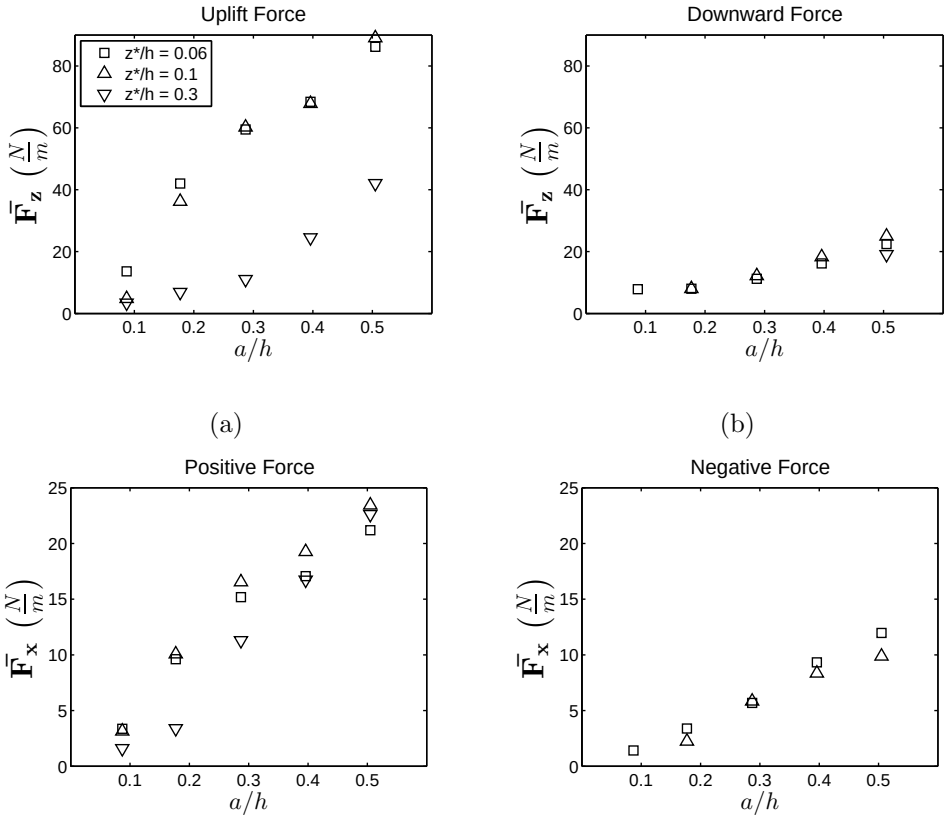

Figure 5.23: (a) Vertical uplift force, (b) vertical downward force, (c) horizontal positive force and (d) horizontal negative force are measured on the model at elevations above the SWL of z^*/h =0.06, 0.1, 0.3 times the water depth and wave amplitudes of 0.1 - 0.5 times the water depth of $h = 0.086\,m$.

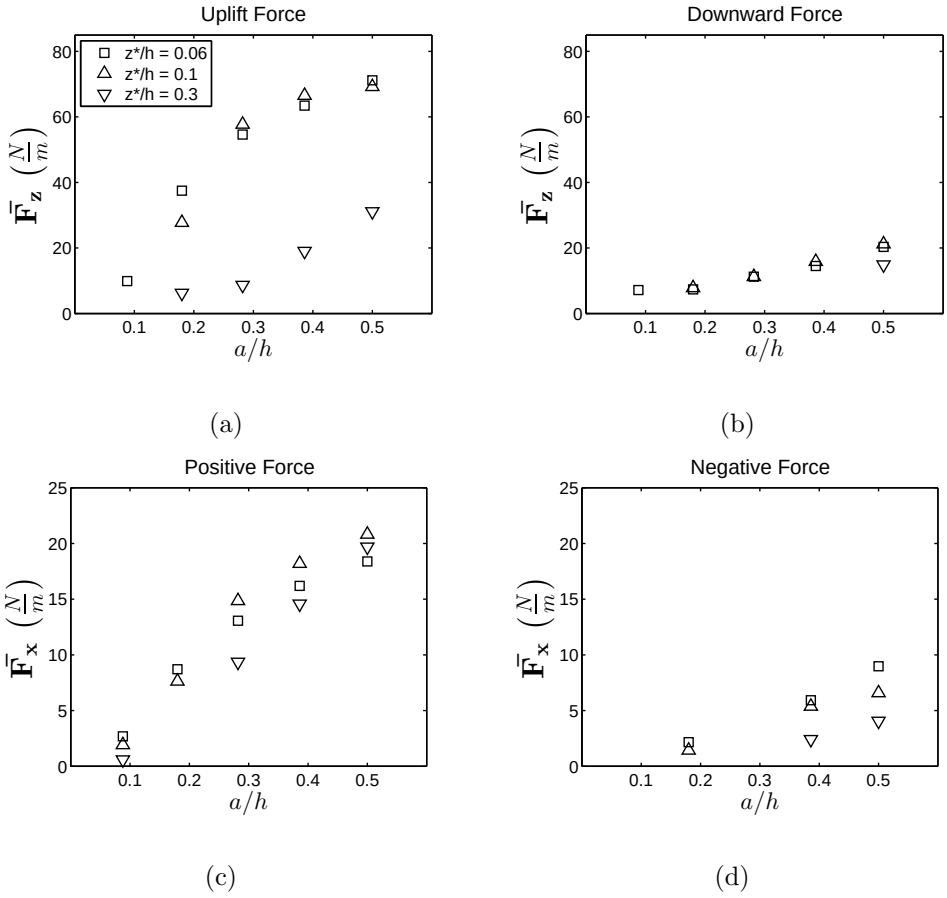

Figure 5.24: (a) Vertical uplift force, (b) vertical downward force (c) horizontal positive force and (d) horizontal negative force are measured on the model at elevations above the SWL of z^*/h =0.06, 0.1, 0.3 times the water depth and wave amplitudes of 0.1 - 0.5 times the water depth of $h = 0.071\,m$.

model with girders, we find that the forces are generally the same. For $z/h = 0.2$ and 0.4, vertical downward forces are slightly larger on the model with girders for water depths of $h = 0.143$ m and 0.114 m, and are slightly smaller for water depths of $h = 0.086$ m and 0.071 m, but are overall very close. The case of $z/h = 0$ is more difficult to compare as not all waves break on top of the plate as they do on the model with girders at this submergence depth. In the cases where the wave breaks on top of the plate, the forces are much closer in magnitude to those on the model with girders. Where the wave remains unbroken, forces on the plate are larger.

When comparing results from elevated cases for the flat plate model versus the model with girders, we find that for the same water depth, wave amplitude and elevation, uplift forces on the flat plate are slightly smaller than the model with girders. Downward forces on the plate for the same water depth and elevation are slightly larger for small a/h and slightly smaller for large a/h.

5.4 Cnoidal Wave Forces on a Horizontal Flat Plate

5.4.1 Submerged Cases

Experimental measurements for cnoidal wave loads on a submerged flat plate are presented in this section. Measurements are compared with calculations made by solving the GN equations and Euler's equations from Hayatdavoodi (2013) and Hayatdavoodi, Seiffert & Ertekin (2014*a*), as well as calculations made by solving the LWA relations, described in Chapter 4. Solitary wave forces are also included in plotting the forces as they represent a cnoidal wave of infinite length, and are indicated by $\lambda/h = \infty$.

Figures 5.25 and 5.27 show time series measurements for surface elevation and vertical and horizonal forces compared with calculations done by solving Euler's equations. Water

depth is $h = 0.071$ m, $\lambda = 1.9$ m and $H/h = 0.260$ in Fig. 5.25 and $H/h = 0.360$ in Fig. 5.27. The horizontal plate is at the deepest submergence depth of $z*/h = 0.6$ in Fig. 5.25 and shallowest submergence depth of $z*/h = 0.0$ in Fig. 5.27. There is good agreement between laboratory measurements and Euler's equations for surface elevation as well as vertical and horizontal forces. Both measurements and calculations show wave reflection as the wave interacts with the leading edge of the plate, and dispersion as the wave travels over the plate in Figs. 5.25 and 5.27 (a) - (c). When the plate is closer to the water surface, a large portion of wave energy is reflected back towards the wavemaker in Fig. 5.27 (a) and (b) and a significantly smaller portion of wave energy is transmitted downwave of the plate due to the wave breaking as it travels over the plate in Fig. 5.27 (c).

There is generally good agreement between laboratory measurements and calculations done using Euler's equations for vertical and horizontal forces, although Euler's equations somewhat under predict horizontal forces. This may be the result of turbulent effects and viscosity, or three-dimensional effects not included in Euler's calculations. The downward force in Fig. 5.25 (d) is larger than the uplift force where the opposite is true in Fig. 5.27. The deeper submergence depth in Fig. 5.25 means a larger volume of water travels over the plate, causing a large downward force. In Fig. 5.27, the plate is much shallower, and because of reflection and wave breaking, there is a much smaller volume of water to contribute to the downward force.

Figure 5.26 shows velocity vectors plotted along with dynamic pressure (p_d) calculated using Euler's equations for the water depth $h = 0.071$ m, $\lambda = 1.9$ m, $H/h = 0.260$, and $z/h = 0.6$. The four figures are calculations made at the time at which vertical uplift, positive horizontal, vertical downward and negative horizontal forces are the largest, at times $t = 8.5, 8.6, 8.8$ and 9 s, respectively. Both measurements and calculations show an initial vertical uplift force as the wave initially interacts with the plate, and a horizontal

positive force as the wave advances further toward the plate. The uplift force is explained by hydrostatic force due to the incoming wave as well as water particle accelerations causing a large pressure differential, shown at $t = 8.5$ s in Fig. 5.26. The horizontal force is due horizontal particle accelerations contributing to the difference in pressure between the upwave and downwave edges of the plate when the crest is at the leading edge of the plate, as seen at time $t = 8.6$ s in Fig. 5.26. As the wave travels over the plate, a downward force is measured on the plate, mainly due to the weight of the water under the wave crest ($t = 8.8$ s in Fig. 5.26). As the wave leaves the plate, a negative horizontal force is measured on the plate due to the horizontal particle accelerations causing a pressure differential between the downwave and upwave edges of the plate ($t = 9$ s in Fig. 5.26).

Figures 5.28 - 5.35 show experimental measurements for vertical and horizontal forces on a submerged plate versus nondimensional wave length, at nondimensional wave heights of $H/h \approx 0.1, 0.2, 0.3$, and 0.4, for water depths $h = 0.071$ m and $h = 0.114$, and nondimensional submergence depths of $z/h = 0.6, 0.4, 0.2$ and 0.0. For the deeper submergence depths of $z/h = 0.4$ and 0.6, where the wave travels over the plate unbroken, comparisons are made between the experimental measurements and the LWA relations (Fig. 5.29) or calculations made using the GN equations given in Hayatdavoodi (2013) (Figs. 5.32 and 5.33).

At the deeper submergence depths of $z/h = 0.6$ and 0.4, shown in Figs. 5.28, 5.29, 5.32 and 5.33 (a) and (b), the downward forces are larger than the uplift forces, mainly due to the weight of the wave crest as it passes over the plate. This effect decreases in shallower submergence depths and larger wave heights as wave breaking and reflection causes a smaller volume of water to travel over the surface, seen in Figs. 5.30, 5.31, 5.34 and 5.35 (a) and (b).

For the deeper submergence depths where the wave travels over the plate unbroken, the vertical forces have a weakly linear relationship with the wave height even though the waves

are nonlinear. The horizontal forces, although generally larger with a larger wave height, appear to also be a function of wave speed, wave length and submergence depth. There is little variation in the vertical forces with wavelength, but wavelength does seem to have an effect on horizontal forces.

The LWA relations do not accurately predict forces on the submerged horizontal plate, shown in Fig. 5.29, apart from when the wave height is very small ($H/h \approx 0.1$). This is likely due to the LWA being a linear theory, as well as the B/L in this experimental case being relatively small compared to the applicability of the theory. The GN theory agrees better than the LWA but tends to underpredict both vertical and horizontal forces. This may be due to three-dimensional or viscous effects or the thickness of the plate in experiments, t_P/h, compared with the GN calculations which assume a plate with zero thickness.

5.4.2 Elevated Cases

Experimental measurements for cnoidal wave loads on an elevated flat plate are presented in this section. Measurements are compared with calculations done by following the Douglass et al. (2006) and McPherson (2008) methods described in Chapter 4.

Time-series measurements for surface elevation and vertical and horizontal forces taken during the laboratory experiments are compared with those calculated using Euler's equations in Fig. 5.36 for water depth $h = 0.071$ m, $\lambda/h = 1.9$ m, $H/h = 0.360$ and at elevation $z^*/h = 0.1$. There is good agreement between laboratory measurements and calculations made using Euler's equations for surface elevation with both indicating significant reflection of wave energy as the wave interacts with the plate (Fig. 5.36 (a) and (b)) and reduction in transmitted energy downwave of the plate as the wave breaks as it travels over the plate (Fig. 5.36 (c)). The vertical force calculated by Euler's equations is larger than that measured during experiments. This may be partially explained by viscous effects as wave breaking and

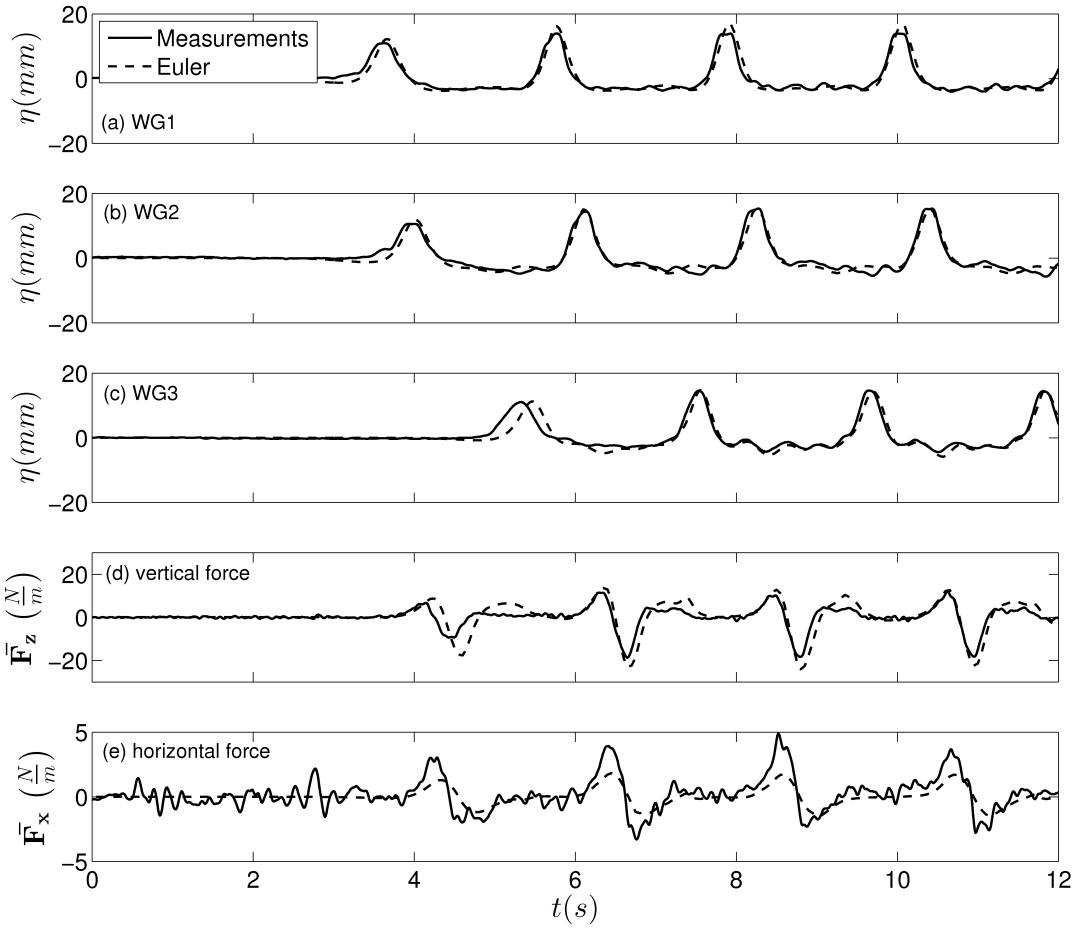

Figure 5.25: Time series for surface elevation and vertical and horizontal forces measured during laboratory experiments are compared with the results of Euler's equations for a cnoidal wave propagating over a submerged horizontal flat plate at $h = 0.071$ m, $z/h = 0.6$, $\lambda = 1.9$ m and $H/h = 0.260$.

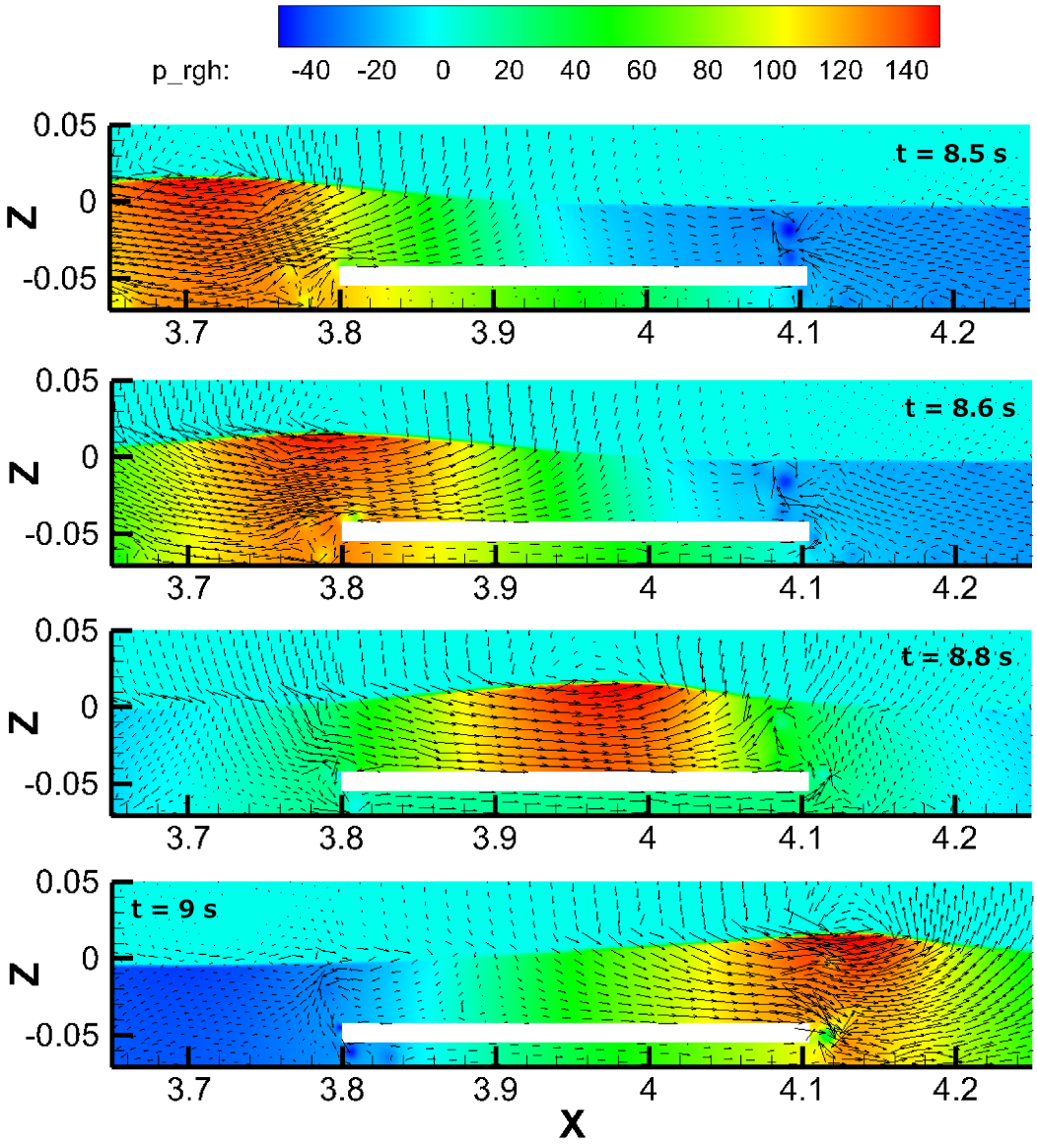

Figure 5.26: Velocity vectors are plotted along with dynamic pressure (p_d) calculated using incompressible Euler's equations, at the time at which vertical uplift, positive horizontal, vertical downward and negative horizontal forces are the largest, at times $t = 8.5, 8.6, 8.8$ and 9 s, respectively. Pressure is given in N/m^2. Water depth is $h = 0.071$ m, $\lambda = 1.9$ m $H/h = 0.260$, and $z/h = 0.6$.

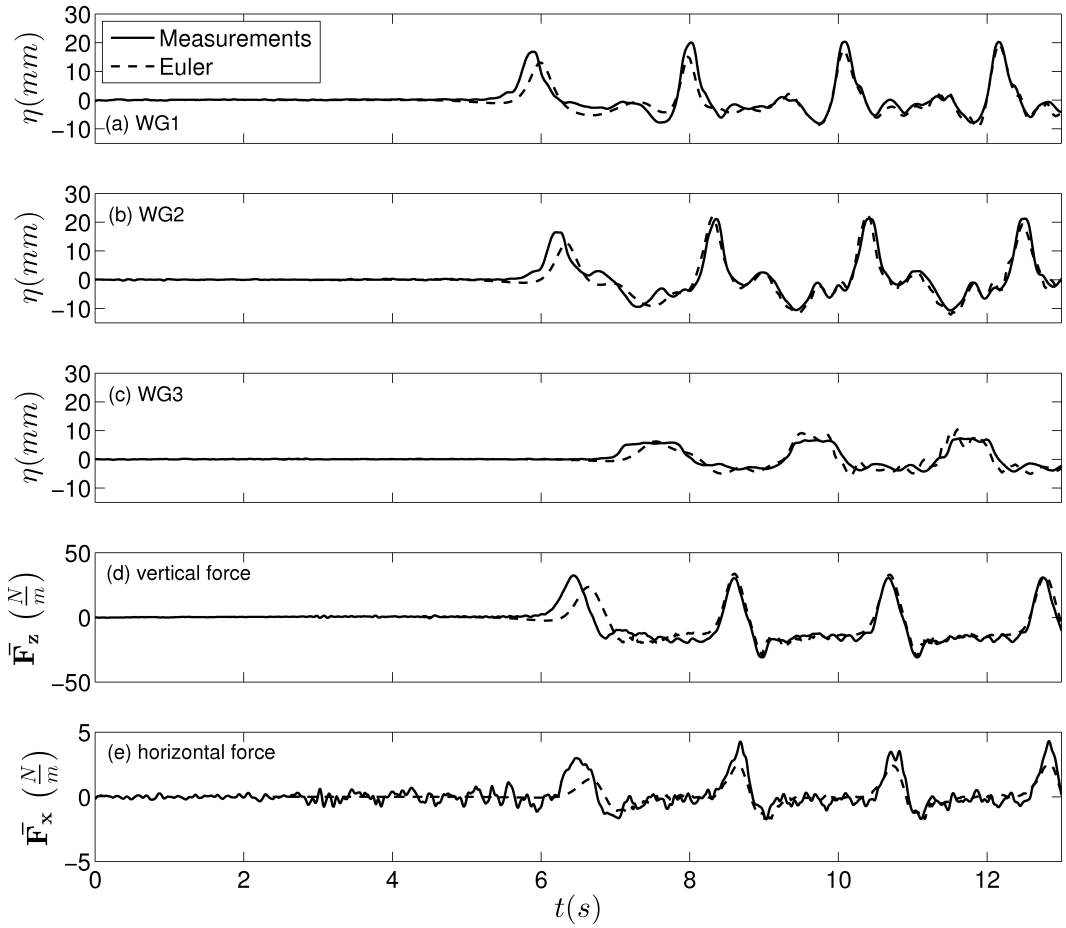

Figure 5.27: Time series for surface elevation and vertical and horizontal forces measured during laboratory experiments are compared with the results of Euler's equations for a cnoidal wave propagating over a horizontal flat plate at $h = 0.071$ m, $z/h = 0.0$, $\lambda = 1.9$ m and $H/h = 0.360$.

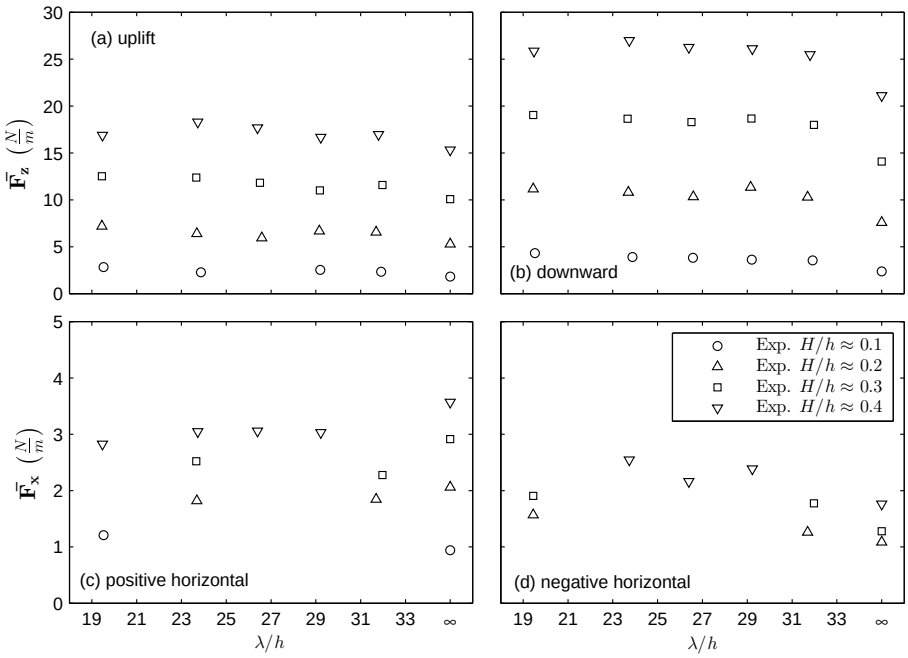

Figure 5.28: Laboratory measurements of (a) Vertical uplift, (b) vertical downward, (c) positive horizontal, and (d) negative horizontal forces on the horizontal flat plate are presented versus nondimensional wavelength for wave heights of $H/h \approx 0.1 - 0.4$ at a water depth of $h = 0.071$ m and nondimensional submergence depth of $z/h = 0.6$.

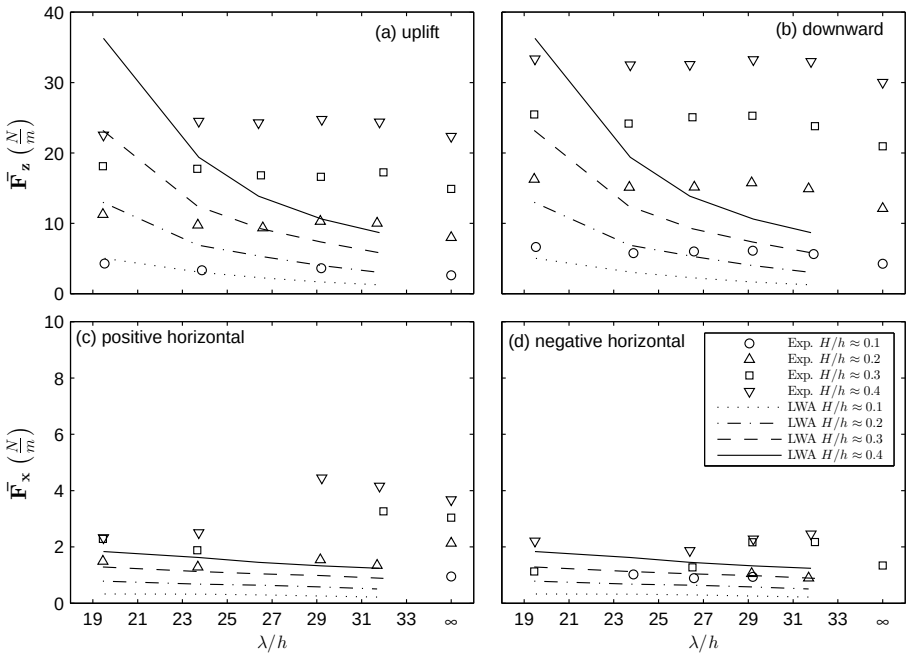

Figure 5.29: Laboratory measurements and LWA relations for (a) Vertical uplift, (b) vertical downward, (c) positive horizontal, and (d) negative horizontal forces on the horizontal flat plate are presented versus nondimensional wavelength for wave heights of $H/h \approx 0.1 - 0.4$ at a water depth of $h = 0.071$ m and nondimensional submergence depth of $z/h = 0.4$.

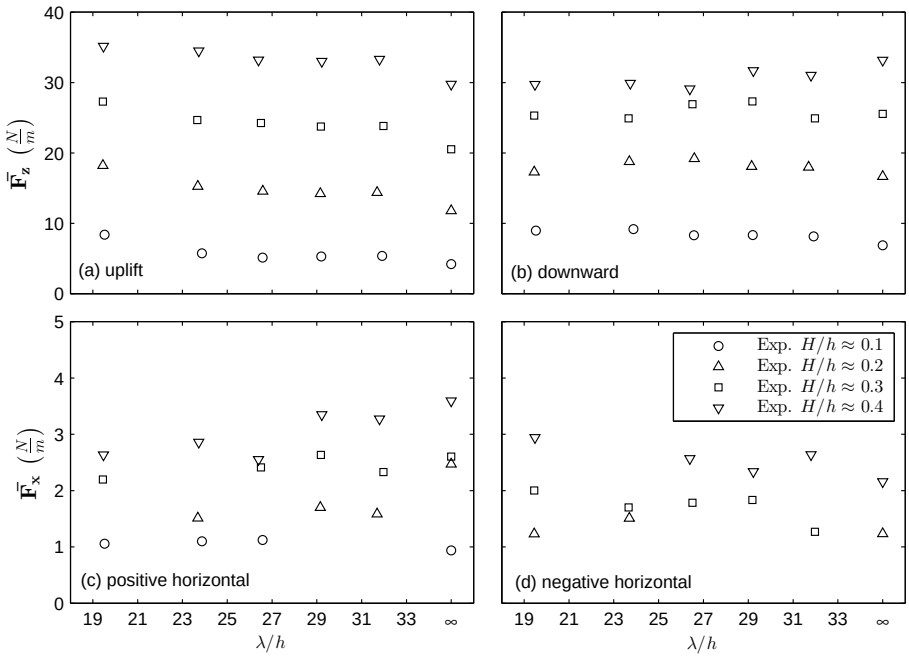

Figure 5.30: Laboratory measurements for (a) Vertical uplift, (b) vertical downward, (c) positive horizontal, and (d) negative horizontal forces on the horizontal flat plate are presented versus nondimensional wavelength for wave heights of $H/h \approx 0.1 - 0.4$ at a water depth of $h = 0.071$ m and nondimensional submergence depth of $z/h = 0.2$.

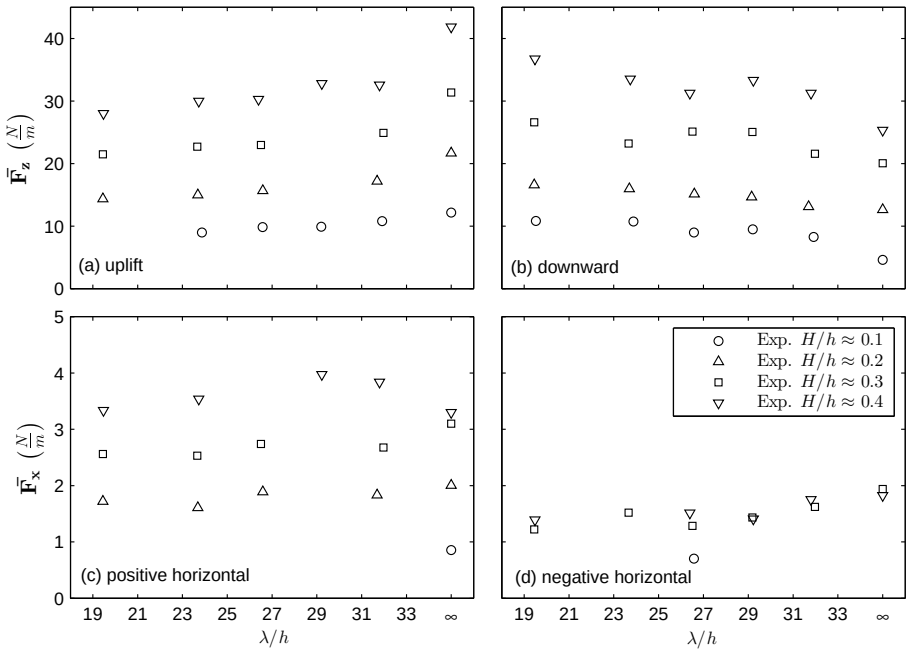

Figure 5.31: Laboratory measurements for (a) Vertical uplift, (b) vertical downward, (c) positive horizontal, and (d) negative horizontal forces on the horizontal flat plate are presented versus nondimensional wavelength for wave heights of $H/h \approx 0.1 - 0.4$ at a water depth of $h = 0.071$ m and nondimensional submergence depth of $z/h = 0.0$.

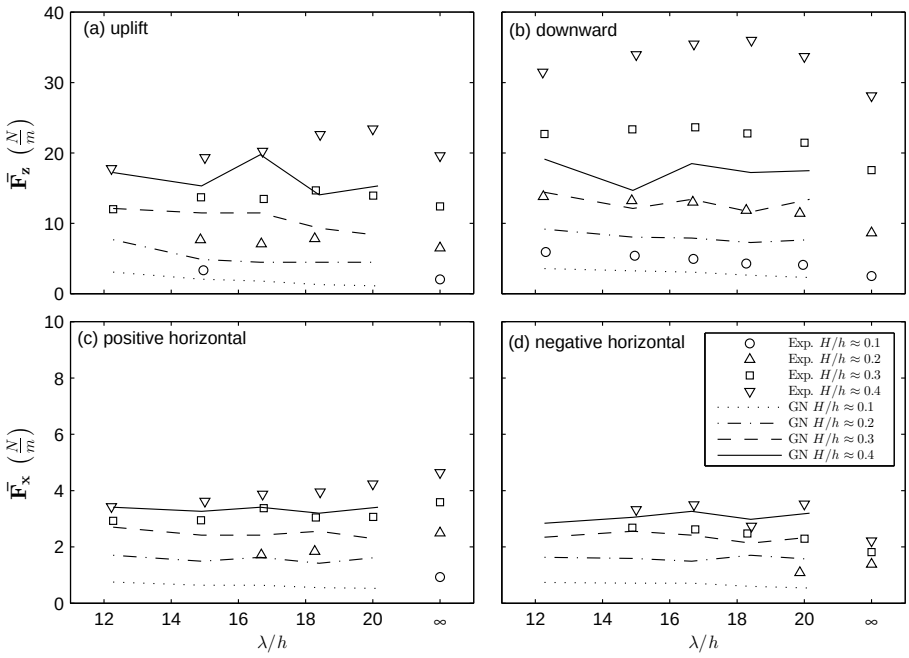

Figure 5.32: Laboratory measurements and GN calculations for (a) Vertical uplift, (b) vertical downward, (c) positive horizontal, and (d) negative horizontal forces on the horizontal flat plate are presented versus nondimensional wavelength for wave heights of $H/h \approx 0.1-0.4$ at a water depth of $h = 0.114$ m and nondimensional submergence depth of $z/h = 0.6$.

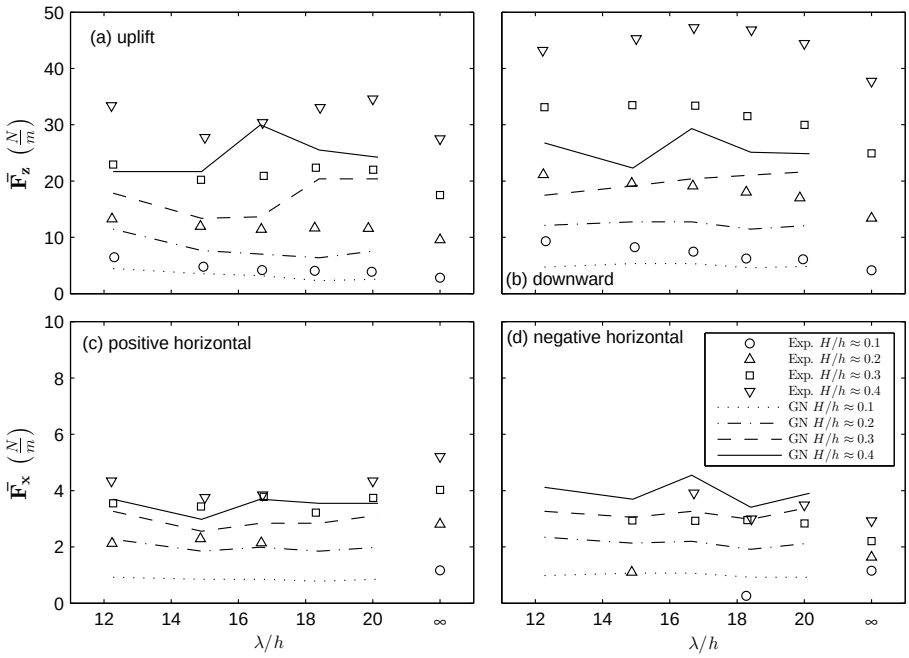

Figure 5.33: Laboratory measurements and GN calculations for (a) Vertical uplift, (b) vertical downward, (c) positive horizontal, and (d) negative horizontal forces on the horizontal flat plate are presented versus nondimensional wavelength for wave heights of $H/h \approx 0.1-0.4$ at a water depth of $h = 0.114$ m and nondimensional submergence depth of $z/h = 0.4$.

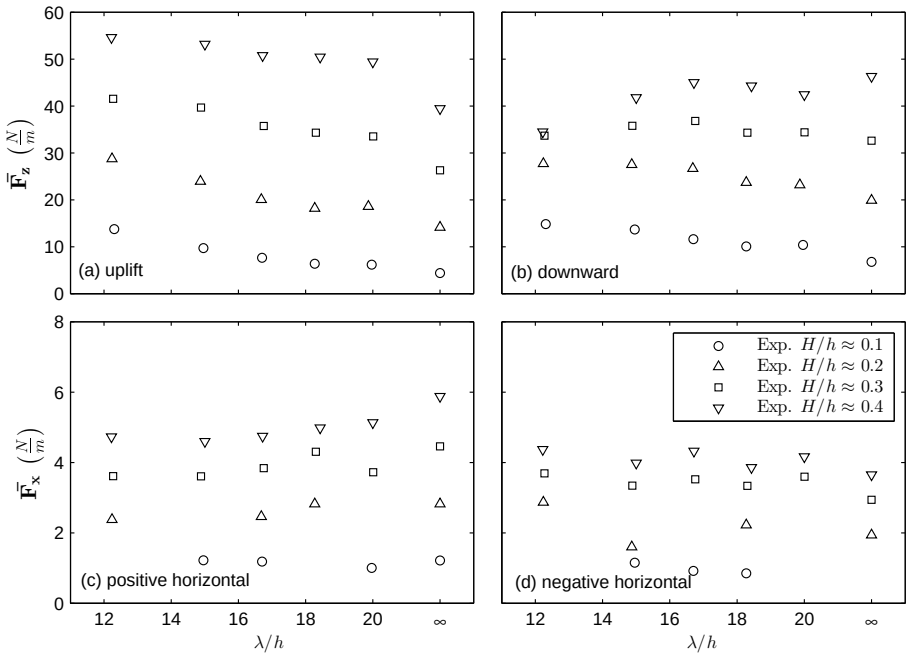

Figure 5.34: Laboratory measurements for (a) Vertical uplift, (b) vertical downward, (c) positive horizontal, and (d) negative horizontal forces on the horizontal flat plate are presented versus nondimensional wavelength for wave heights of $H/h \approx 0.1 - 0.4$ at a water depth of $h = 0.114$ m and nondimensional submergence depth of $z/h = 0.2$.

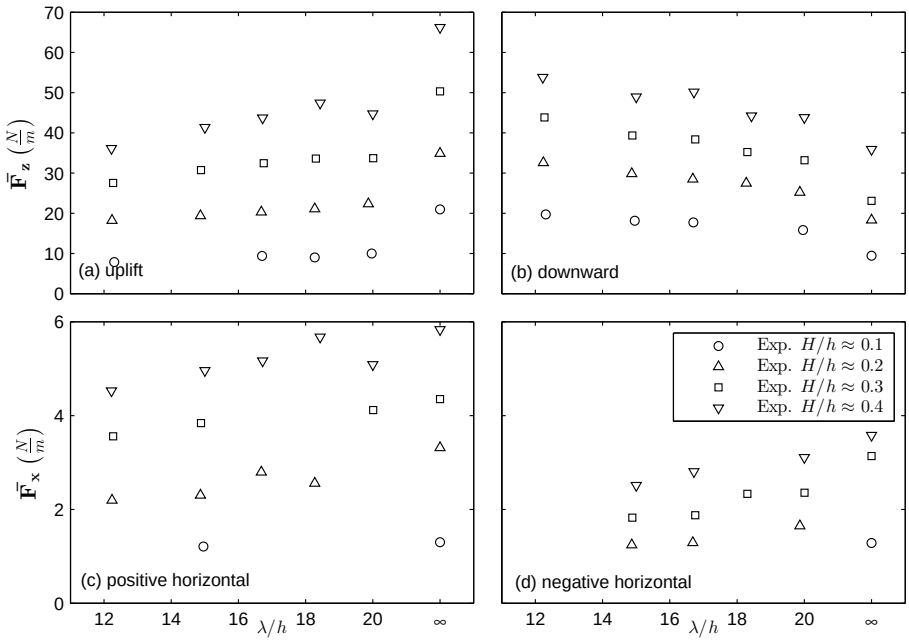

Figure 5.35: Laboratory measurements for (a) Vertical uplift, (b) vertical downward, (c) positive horizontal, and (d) negative horizontal forces on the horizontal flat plate are presented versus nondimensional wavelength for wave heights of $H/h \approx 0.1 - 0.4$ at a water depth of $h = 0.114$ m and nondimensional submergence depth of $z/h = 0.0$.

turbulence occurs as the wave travels over the plate, not included in Euler's equations. The horizontal forces calculated by Euler's equations are smaller than those measured during the experiments. However, significant variation in horizontal forces occurred in experiments such that the accuracy and repeatability of these measurements is not confirmed. As a result, horizontal force measurements are not included in figures including force measurements for the elevated plate.

Figures 5.37 - 5.40 present (a) vertical uplift and (b) downward forces versus nondimensional wave height measured during the experiments compared with estimations based on the Douglass et al. (2006) and McPherson (2008) methods for water depths $h = 0.071$ m and 0.114 m, and wavelengths $\lambda = 1.4 - 2.3$ m and $\lambda = \infty$ (solitary wave) for elevations $z^*/h = 0.06$ and 0.1. The Douglass et al. (2006) and McPherson (2008) relations are not a function of wavelength so they are represented as one line. Vertical uplift forces shown in Figs. 5.37 - 5.40 (a) show slightly larger forces for longer wavelengths. One possibility of this is the presence of green water on the plate. For shorter wavelengths, green water has less time to drain off the top of the plate before hit by another wave, leaving more weight for the uplift force to counteract. This is supported by the much larger forces due to solitary waves, where the top of the plate is initially dry before the wave impacts it.

The Douglass and McPherson empirical relations agree relatively well with experimental measurements, with better agreement for smaller wave heights and some overprediction for larger wave heights. The empirical relations however, underpredict solitary wave forces, thereby supporting the intended applicability of these relations to only periodic waves.

The largest forces overall for both the submerged and elevated cases occur when the plate is just above the SWL at $z*/h = 0.06$. This is also where the largest water particle velocities occur in the wave.

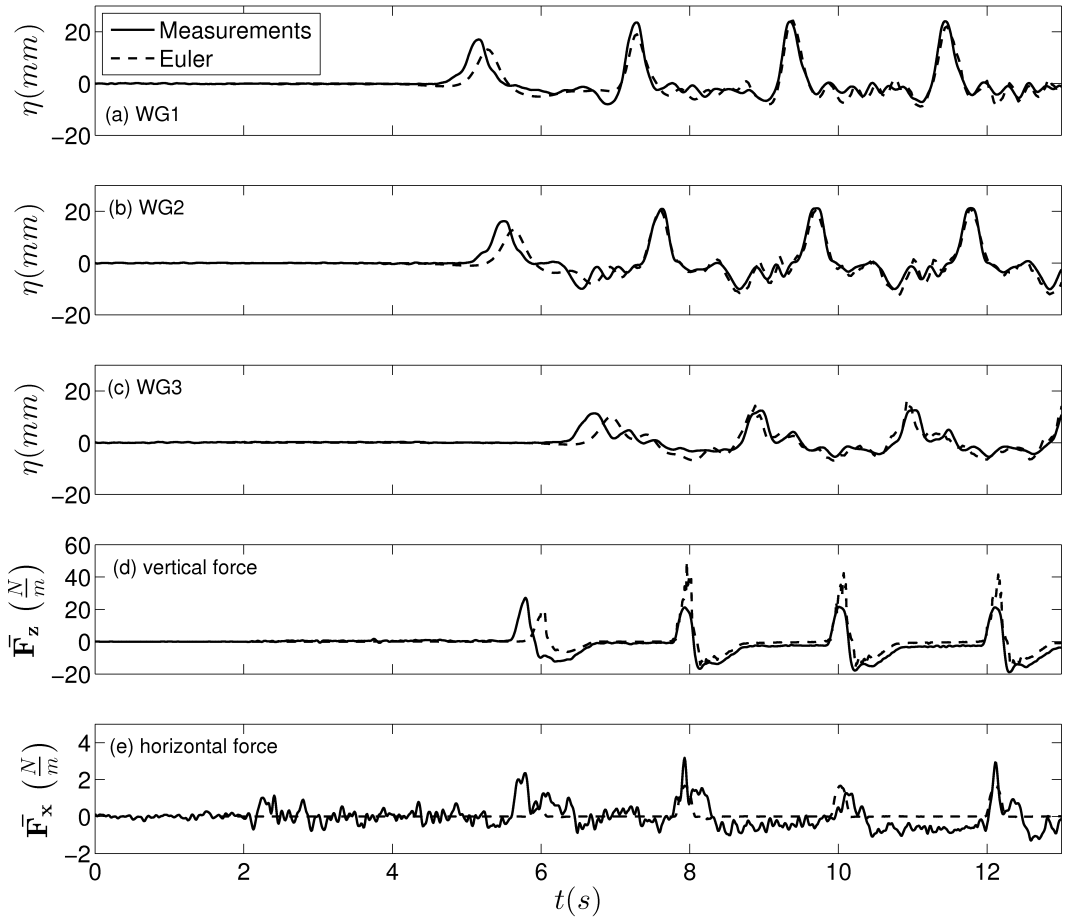

Figure 5.36: Time series for surface elevation and vertical and horizontal forces measured during laboratory experiments are compared with the results of Euler's equations for a cnoidal wave propagating over an elevated horizontal flat plate at $h = 0.071$ m, $z^*/h = 0.1$, $\lambda = 1.9$ m and $H/h = 0.360$.

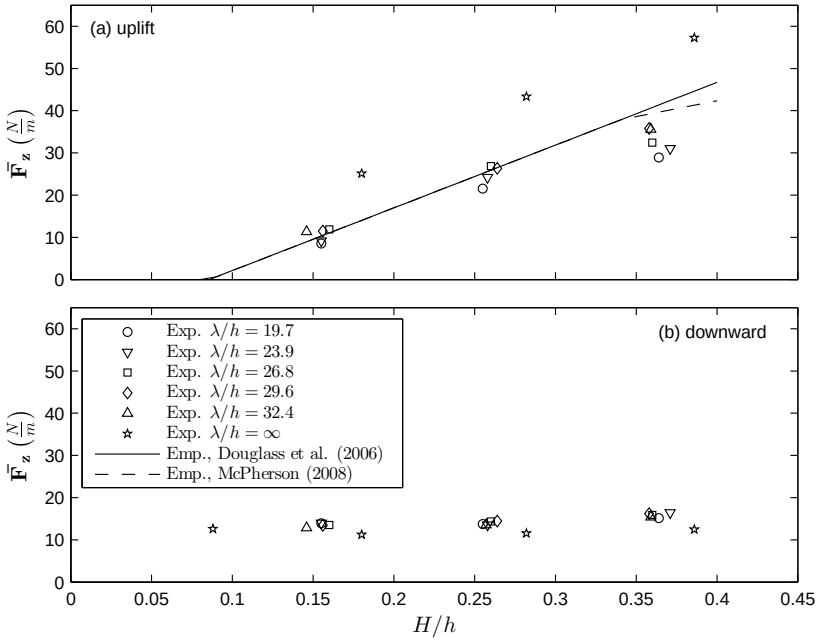

Figure 5.37: Laboratory measurements and Douglass et al. (2006) and McPherson (2008) relations for (a) Vertical uplift, and (b) vertical downward forces on the horizontal flat plate are presented versus nondimensional wave height at a water depth of $h = 0.071$ m and nondimensional elevation of $z^*/h = 0.06$.

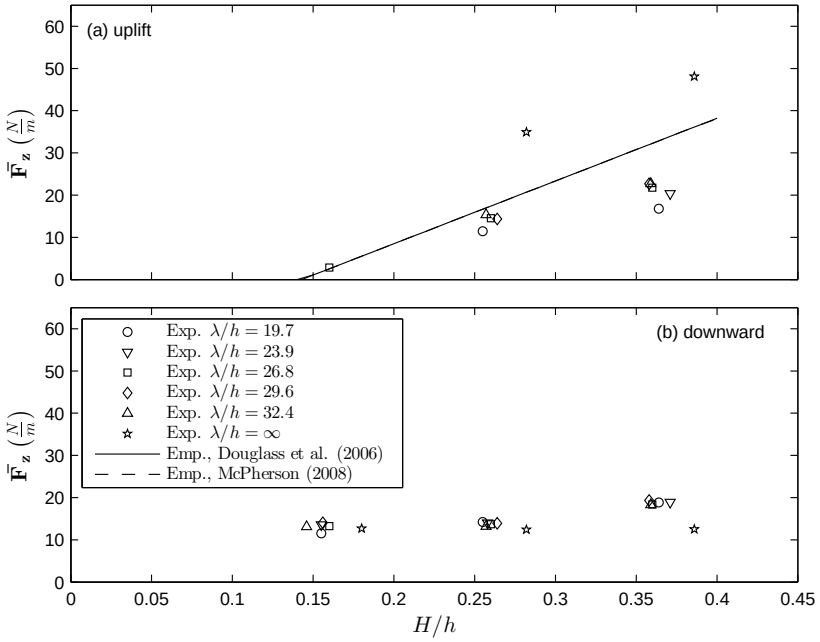

Figure 5.38: Laboratory measurements and Douglass et al. (2006) and McPherson (2008) relations for (a) Vertical uplift, and (b) vertical downward forces on the horizontal flat plate are presented versus nondimensional wave height at a water depth of $h = 0.071$ m and nondimensional elevation of $z^*/h = 0.01$.

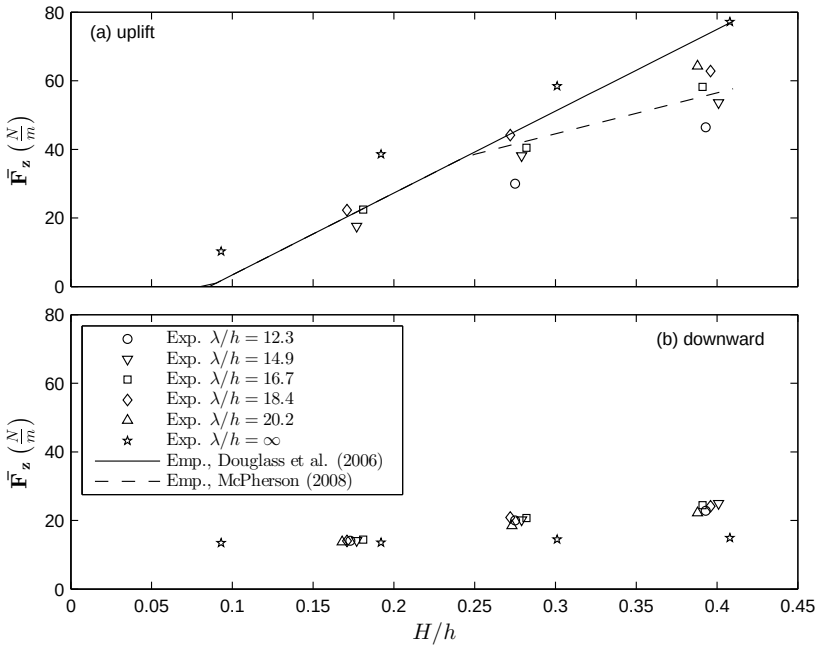

Figure 5.39: Laboratory measurements and Douglass et al. (2006) and McPherson (2008) relations for (a) Vertical uplift, and (b) vertical downward forces on the horizontal flat plate are presented versus nondimensional wave height at a water depth of $h = 0.114$ m and nondimensional elevation of $z^*/h = 0.06$.

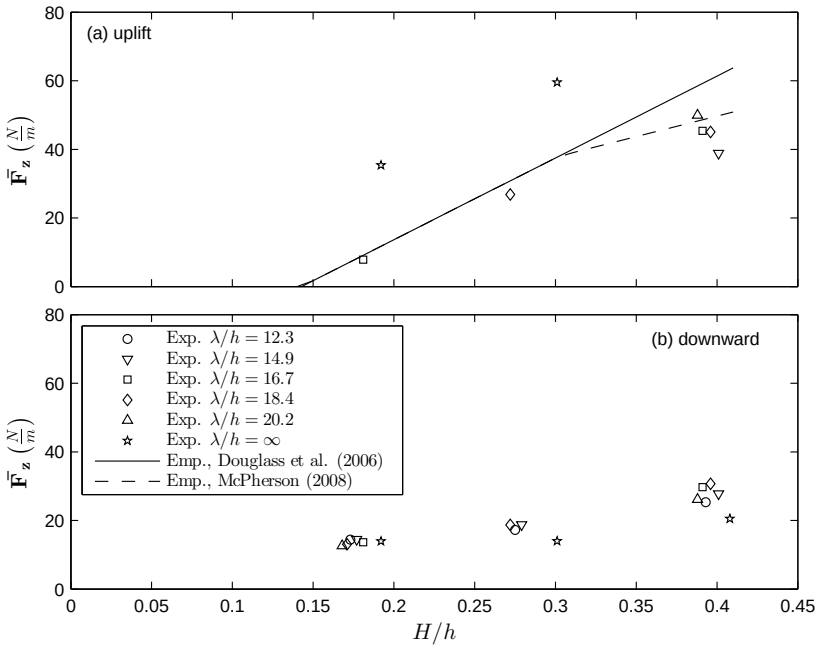

Figure 5.40: Laboratory measurements and Douglass et al. (2006) and McPherson (2008) relations for (a) Vertical uplift, and (b) vertical downward forces on the horizontal flat plate are presented versus nondimensional wave height at a water depth of $h = 0.114$ m and nondimensional elevation of $z^*/h = 0.1$.

5.5 Cnoidal Wave Forces on a Bridge Model with Girders

5.5.1 Submerged Cases

In this section, results for horizontal and vertical forces on a submerged bridge model are presented. Figures 5.41 - 5.44 compare time series measurements obtained in the laboratory with the results of Euler's equations for $h = 0.071m$, $z/h = 0.2$, $\lambda = 2.3m$ and $H/h \approx 0.1 - 0.4$, respectively. Figures 5.42 - 5.44 compare (a) vertical and (b) horizonal force measurements and calculations while Figure 5.41 compares measurements and calculations taken at the three wave gauges, (a) - (c), as well as for (d) vertical and (e) horizontal forces. Calculations based on Euler's equations for vertical uplift and downward forces are slightly larger than the laboratory measurements for the larger wave heights ($H/h \approx 0.3 - 0.4$), but overall agreement is good. Measurements and calculations for vertical forces show an initial uplift force as the wave crest initially reaches the model. This is followed by a downward force as the wave propagates over the model, and the weight of the wave crest are acting on the model. Downward forces are larger than upward forces for smaller wave heights ($H/h \approx 0.1 - 0.3$, Figs. 5.42 - 5.43(a)), and smaller than upward forces for $H \approx 0.4$ (Fig. 5.44(a)). This is likely due to the wave breaking as it travels over the model for the larger wave-height case.

Horizontal forces for calculations and experiments show good agreement, with laboratory measurements being slightly larger for $H/h = 0.063$ and 0.146 and slightly smaller for $H/h = 0.257$ and 0.359 for both positive and negative horizontal forces (Figs. 5.41 - 5.44(b)). Horizontal forces show an initial positive force as the wave crest reaches the model and there is a large pressure differential acting on the model, followed by a negative force as the wave

leaves the model due to a pressure difference in the opposite direction, as well as a reverse flow (as discussed by Carter et al. (2006)) acting on the model. There also appears to be a slight phase shift between the maximum horizontal force and maximum vertical force.

Surface elevation calculations are in excellent agreement with laboratory experiments, shown in Fig. 5.41(a) - (c), with Euler's calculations able to predict both the reflected and transmitted waves accurately. Smaller measurements for experiments versus calculations shown in Fig. 5.41(c) are likely due to attenuation of the wave as it travels down the wave flume.

Laboratory measurements for maximum vertical uplift, downward and horizontal positive and negative forces versus wave length (calculated from measured wave period) for water depth $h = 0.071m$ and submergence depths $z/h = 0.2$ and 0.0 are given in Figs. 5.45 and 5.46(a) - (d), respectively. Measurements for maximum vertical uplift, downward and horizontal positive and negative forces versus wave length for water depth $h = 0.114m$ and submergence depths $z/h = 0.4, 0.3, 0.2$ and 0.0 are given in Figures 5.47 - 5.50(a) - (d). Overall, larger vertical forces are measured for submergence depth $z/h = 0.2$ than $z/h = 0.0$ for water depth $h = 0.071m$ shown in Figs. 5.45 and 5.46(a) and (b). Both show that uplift forces are similar in magnitude to downward forces for wave heights $H/h \approx 0.1 - 0.3$ but downward forces are smaller than uplift forces for $H/h \approx 0.4$. Little change in forces is measured with a change in wave length in these cases.

For water depth $h = 0.114m$, and at the deeper submergence depths $z/h = 0.4$ and 0.3, shown in Figs. 5.47 and 5.48(a) and (b), larger downward forces than uplift forces for each of the wave heights are seen. For the shallower submergence depth $z/h = 0.2$, shown in Fig. 5.49(a) and (b), downward forces are larger than uplift forces only for the smaller wave heights $H/h \approx 0.1 - 0.3$. Just as the case for water depth $h = 0.071m$, this is likely due to the wave breaking over the model for the larger wave height. For the submergence depth

$z/h = 0.0$, the downward forces are larger again for each wave height. This is likely due to the decrease in uplift buoyancy caused by the trough of the wave as it exposes the model to air. The largest overall vertical forces for water depth $h = 0.114m$ are seen at submergence depth $z/h = 0.2$.

Horizontal forces show only small variations over change in submergence depth, likely due to the small ratio between model thickness $(t_P + t_G)$ versus water depth, where $(t_P + t_G)/h = 0.715$ for water depth $h = 0.071m$ and $(t_P + t_G)/h = 0.446$ for water depth $h = 0.114m$. Overall, horizontal forces are much smaller than vertical forces.

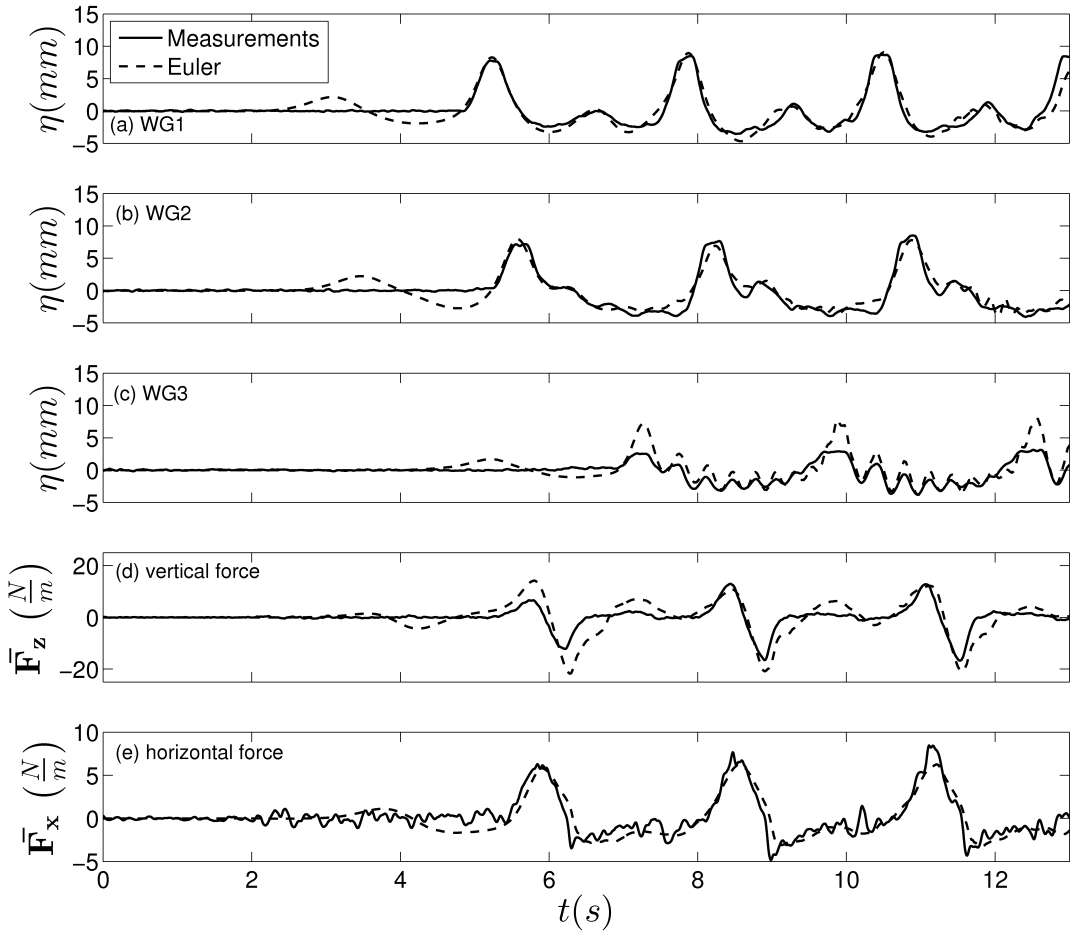

Figure 5.41: Time series for surface elevation and vertical and horizontal forces measured during laboratory experiments are compared with the results of Euler's equations for a cnoidal wave propagating over a submerged bridge model with girders at $h = 0.071m$, $z/h = 0.2$, $\lambda = 2.3m$ and $H/h = 0.146$.

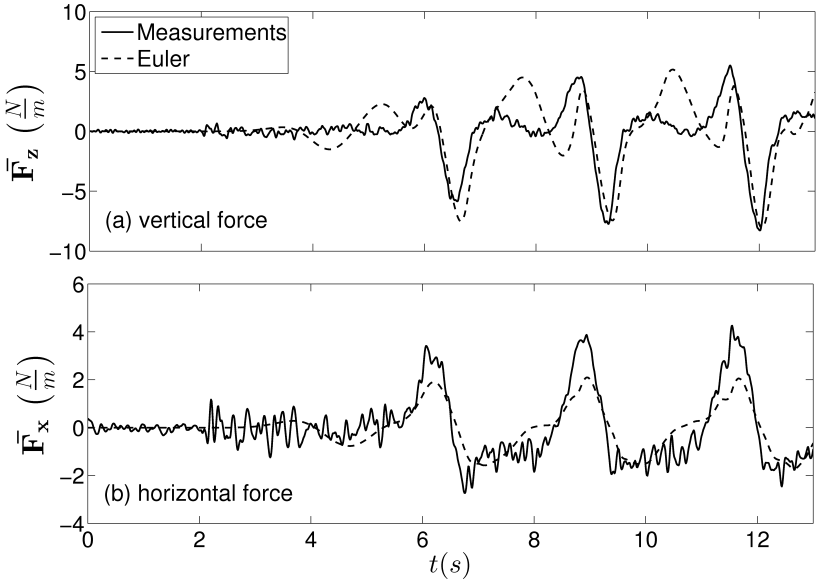

Figure 5.42: Time series for vertical and horizontal forces measured during laboratory experiments are compared with the results of Euler's equations for a cnoidal wave propagating over a submerged bridge model with girders at $h = 0.071m$, $z/h = 0.2$, $\lambda = 2.3m$ and $H/h = 0.063$.

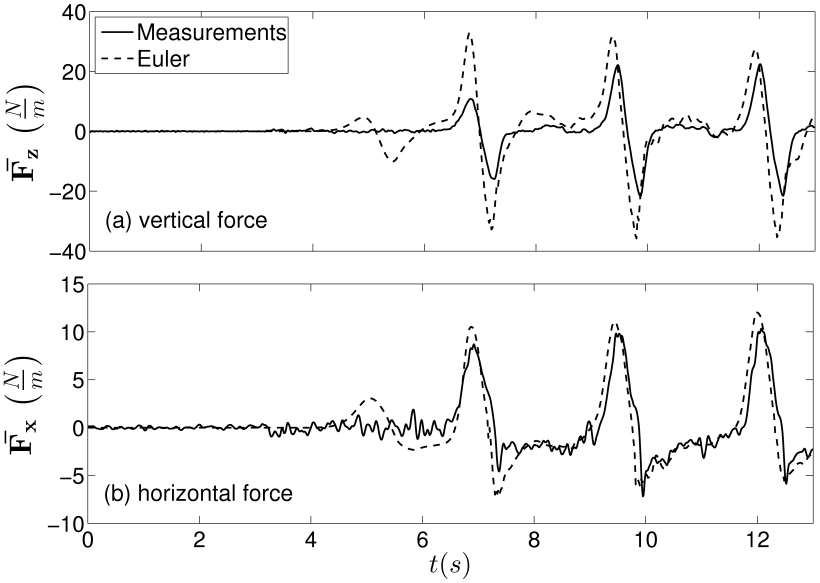

Figure 5.43: Time series for vertical and horizontal forces measured during laboratory experiments are compared with the results of Euler's equations for a cnoidal wave propagating over a submerged bridge model with girders at $h = 0.071m$, $z/h = 0.2$, $\lambda = 2.3m$ and $H/h = 0.257$.

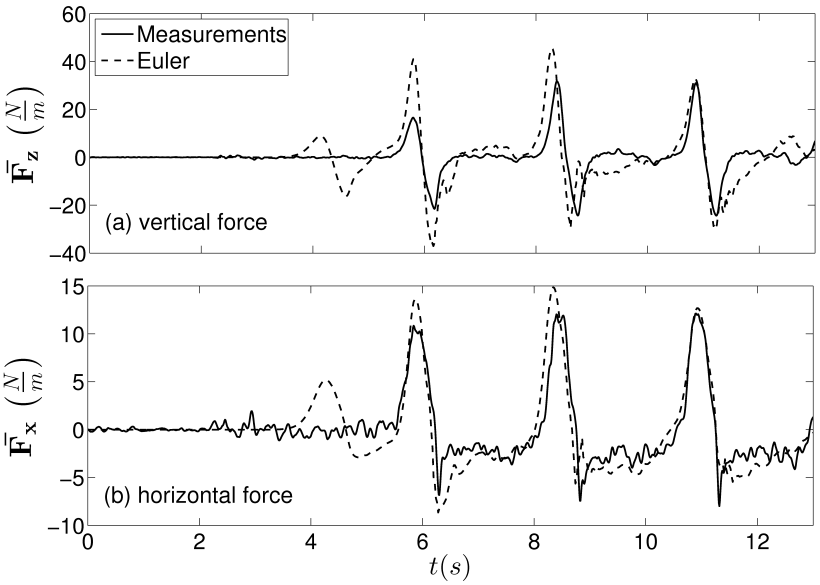

Figure 5.44: Time series for vertical and horizontal forces measured during laboratory experiments are compared with the results of Euler's equations for a cnoidal wave propagating over a submerged bridge model with girders at $h = 0.071m$, $z/h = 0.2$, $\lambda = 2.3m$ and $H/h = 0.359$.

5.5.2 Elevated Cases

In this section, results for horizontal and vertical forces on an elevated bridge model are presented. Time series, comparing calculations based on Euler's equations with laboratory experiments for $h = 0.071m$, $z^*/h = 0.06$ ($z_G/h = -0.477$), $\lambda = 1.9$, and $H/h \approx 0.4$, are presented in Fig. 5.51 for surface elevation at the three wave gauges, (a) - (c), and for (d) vertical and (e) horizontal forces. Calculations agree well with measurements for vertical force (Fig. 5.51(d)) with both showing an initial uplift force due to added buoyancy and wave impact force and a much smaller downward force due to the weight of the water overtopping the model as the wave breaks and water drains off. Good agreement is also

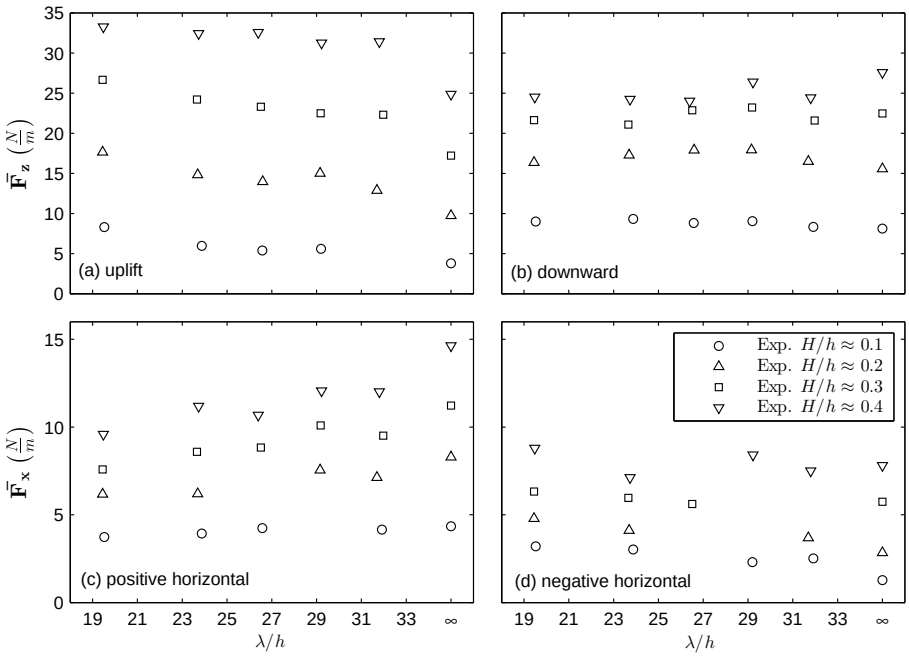

Figure 5.45: Laboratory measurements of (a) Vertical uplift, (b) vertical downward, (c) positive horizontal, and (d) negative horizontal forces on the bridge model with girders are presented versus nondimensional wavelength for wave heights of $H/h \approx 0.1 - 0.4$ at a water depth of $h = 0.071m$ and nondimensional submergence depth of $z/h = 0.2$.

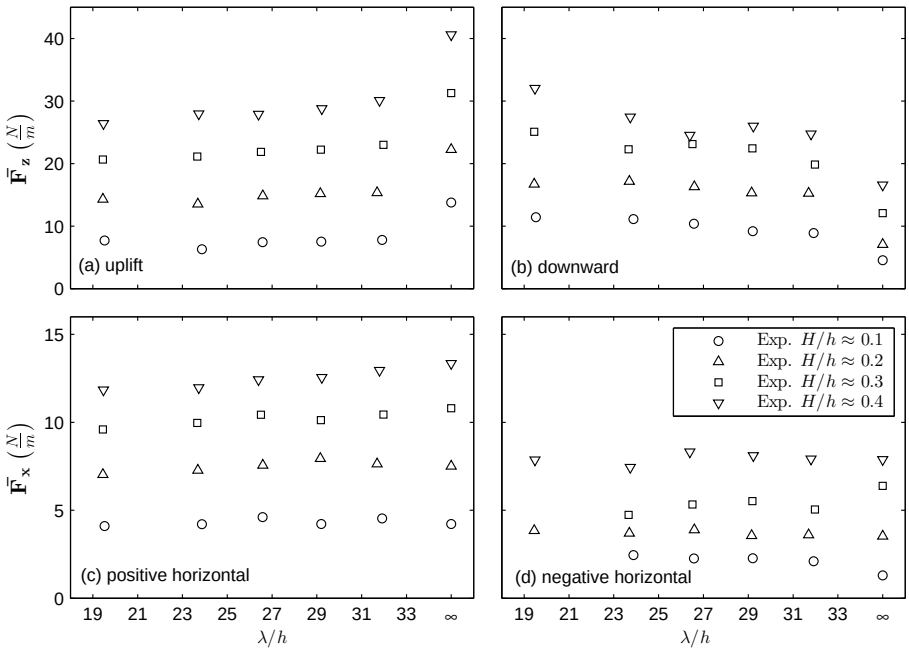

Figure 5.46: Laboratory measurements of (a) Vertical uplift, (b) vertical downward, (c) positive horizontal, and (d) negative horizontal forces on the bridge model with girders are presented versus nondimensional wavelength for wave heights of $H/h \approx 0.1 - 0.4$ at a water depth of $h = 0.071m$ and nondimensional submergence depth of $z/h = 0.0$.

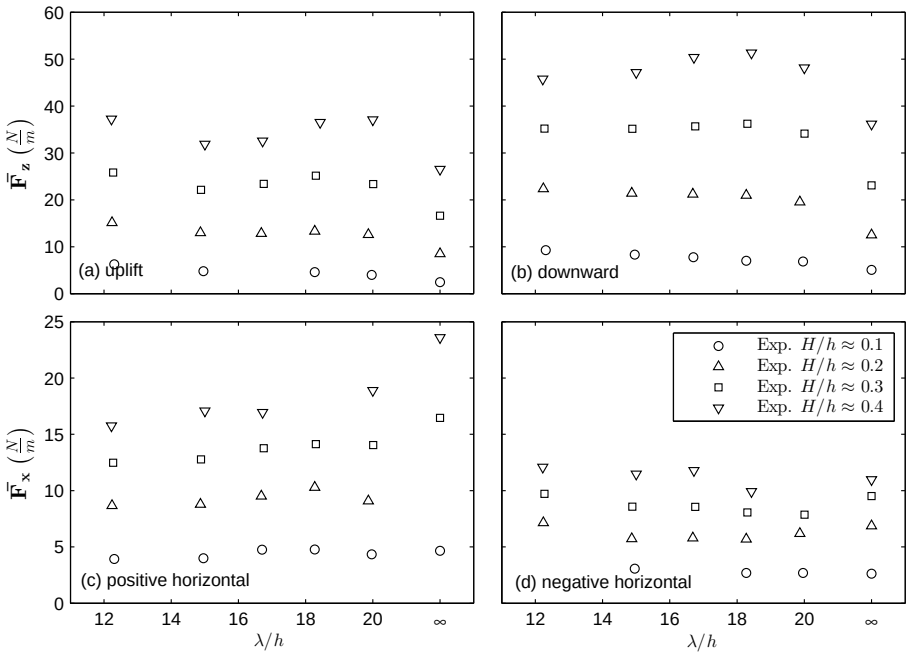

Figure 5.47: Laboratory measurements of (a) Vertical uplift, (b) vertical downward, (c) positive horizontal, and (d) negative horizontal forces on the bridge model with girders are presented versus nondimensional wavelength for wave heights of $H/h \approx 0.1 - 0.4$ at a water depth of $h = 0.114m$ and nondimensional submergence depth of $z/h = 0.4$.

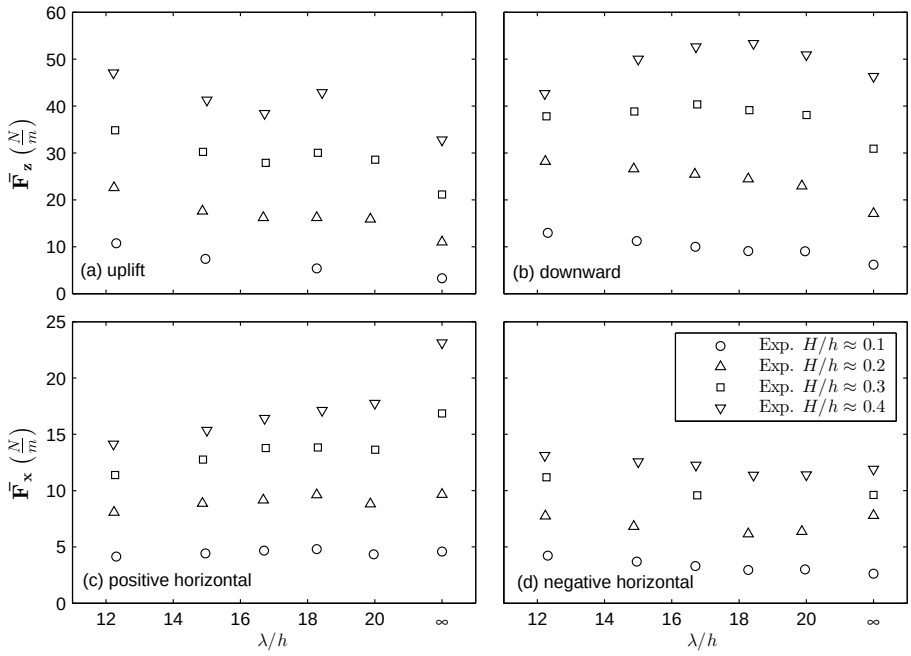

Figure 5.48: Laboratory measurements of (a) Vertical uplift, (b) vertical downward, (c) positive horizontal, and (d) negative horizontal forces on the bridge model with girders are presented versus nondimensional wavelength for wave heights of $H/h \approx 0.1 - 0.4$ at a water depth of $h = 0.114m$ and nondimensional submergence depth of $z/h = 0.3$.

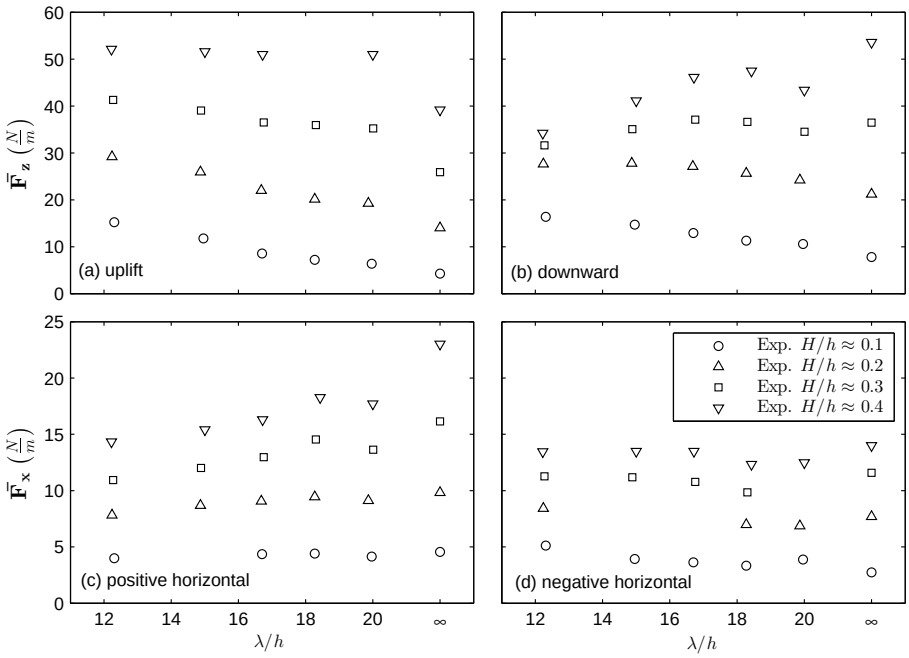

Figure 5.49: Laboratory measurements of (a) Vertical uplift, (b) vertical downward, (c) positive horizontal, and (d) negative horizontal forces on the bridge model with girders are presented versus nondimensional wavelength for wave heights of $H/h \approx 0.1 - 0.4$ at a water depth of $h = 0.114m$ and nondimensional submergence depth of $z/h = 0.2$.

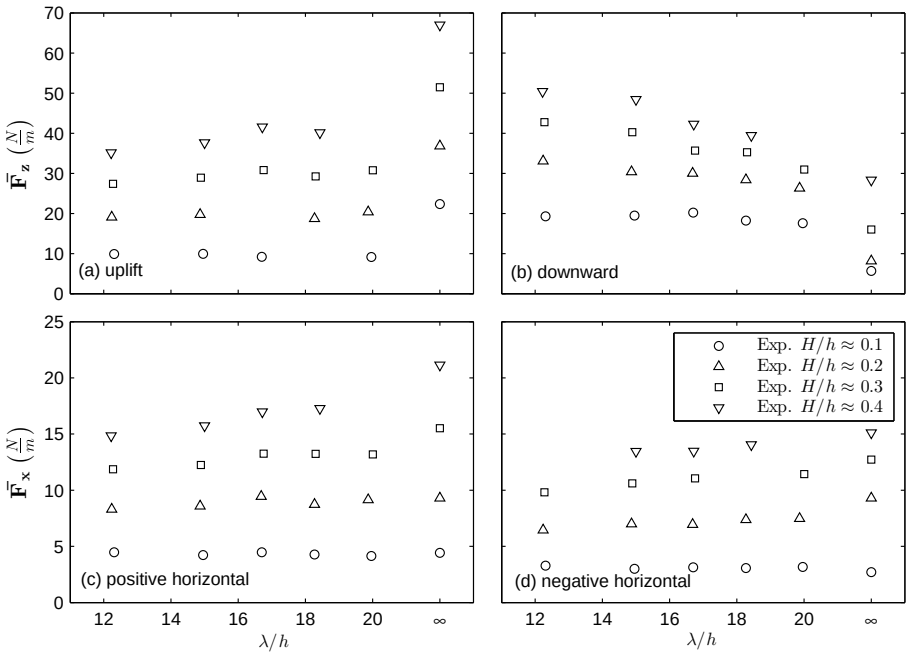

Figure 5.50: Laboratory measurements of (a) Vertical uplift, (b) vertical downward, (c) positive horizontal, and (d) negative horizontal forces on the bridge model with girders are presented versus nondimensional wavelength for wave heights of $H/h \approx 0.1 - 0.4$ at a water depth of $h = 0.114m$ and nondimensional submergence depth of $z/h = 0.0$.

seen with horizontal forces in Fig. 5.51(e) with both Euler's equations and measurements showing a large initial positive force as the wave impacts the model and a much smaller negative force as the wave passes over the model.

Time series calculations for surface elevation at the three wave gauges (Fig. 5.51(a) - (c)) are in excellent agreement with measurements, as the calculations accurately predict both the reflected and transmitted waves.

Figures 5.52 and 5.53 show laboratory measurements for vertical (a) uplift, (b) downward, horizontal (c) positive and (e) negative forces, and Figs. 5.54 - 5.56 show vertical (a) uplift, (b) downward, and (c) horizontal positive forces versus measured wave height for $\lambda = 1.4 - 2.3$, and those forces estimated by Douglass et al. (2006)'s empirical relations for $h = 0.071m$ and $z^*/h = 0.06$, 0.1, 0.3, 0.35 and 0.55, respectively. Figures 5.57 and 5.58 show laboratory measurements for vertical (a) uplift, (b) downward, horizontal (c) positive and (e) negative forces, and Fig. 5.59 shows (a) vertical uplift and (b) horizontal positive forces versus measured wave height for $\lambda = 1.4 - 2.3$ and those forces estimated by Douglass et al. (2006)'s empirical relations for $h = 0.114m$ and $z^*/h = 0.06$, 0.1, and 0.35, respectively. When estimating positive horizontal forces using Douglass et al. (2006)'s equations, estimations are done using both the coefficient of $C_r = 0.4$, suggested by Douglass, as well as $C_r = 0.2$, and the results are presented in Figs. 5.52, 5.53, 5.57, and 5.58. Horizontal negative forces are not shown in Figs. 5.54 - 5.56 and horizontal positive and negative forces are not shown in Fig. 5.59 as they were either too small and the load cells measured only noise or they were not repeatable. Note that the empirical relations are not a function of wave length so no wave length variation is included for these.

A large decrease in vertical uplift forces is measured between $z^*/h = 0.1$ and 0.3 for both $h = 0.071m$ and $h = 0.114m$ (Figs. 5.53, 5.54, 5.58 and 5.59(a)). This difference is attributed to the model experiencing both added buoyancy force and wave impact force underneath the

deck at $z^*/h = 0.1$ but mainly buoyancy forces at $z^*/h = 0.3$ where the wave does not reach the underside of the deck. The Douglass et al. (2006) relations tend to underpredict uplift forces for smaller wave heights and overpredict uplift forces for larger wave heights. When using the suggested coefficient of $C_r = 0.4$, the Douglass relations overpredict positive horizontal forces. The coefficient of $C_r = 0.2$ shows better agreement with the experimental data.

Downward forces shown in Figs. 5.52 - 5.59(c) are much smaller than uplift forces and are due mostly to the weight of the broken wave and green water on top of the bridge deck. Overall, the largest uplift and positive horizontal forces for both submerged and elevated conditions occur when the bottom of the model deck is elevated just above the SWL at $z^*/h = 0.06$ for both water depths.

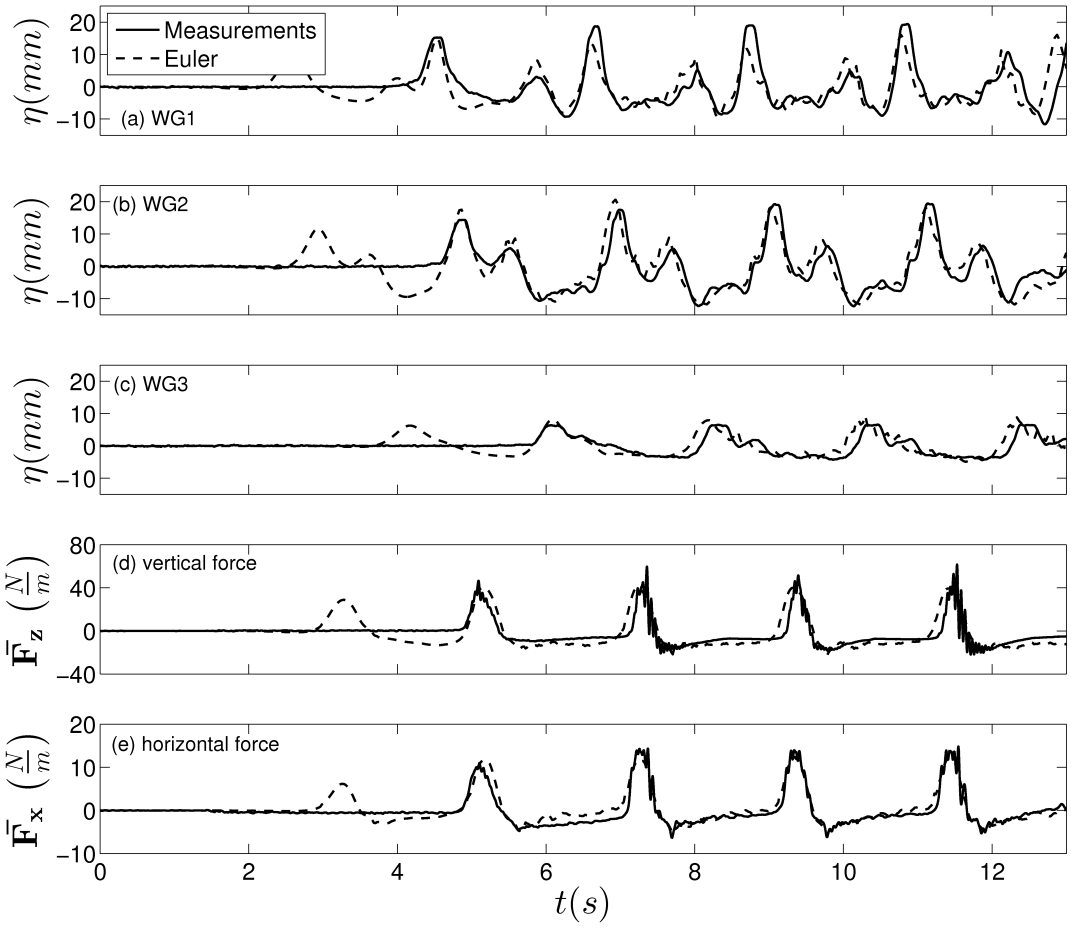

Figure 5.51: Time series for surface elevation and vertical and horizontal forces measured during laboratory experiments are compared with the results of Euler's equations for a cnoidal wave propagating over an elevated bridge model with girders at $h = 0.071m$, $z^*/h = 0.06$ ($z_G/h = -0.477$), $\lambda = 1.9$ and $H/h \approx 0.4$.

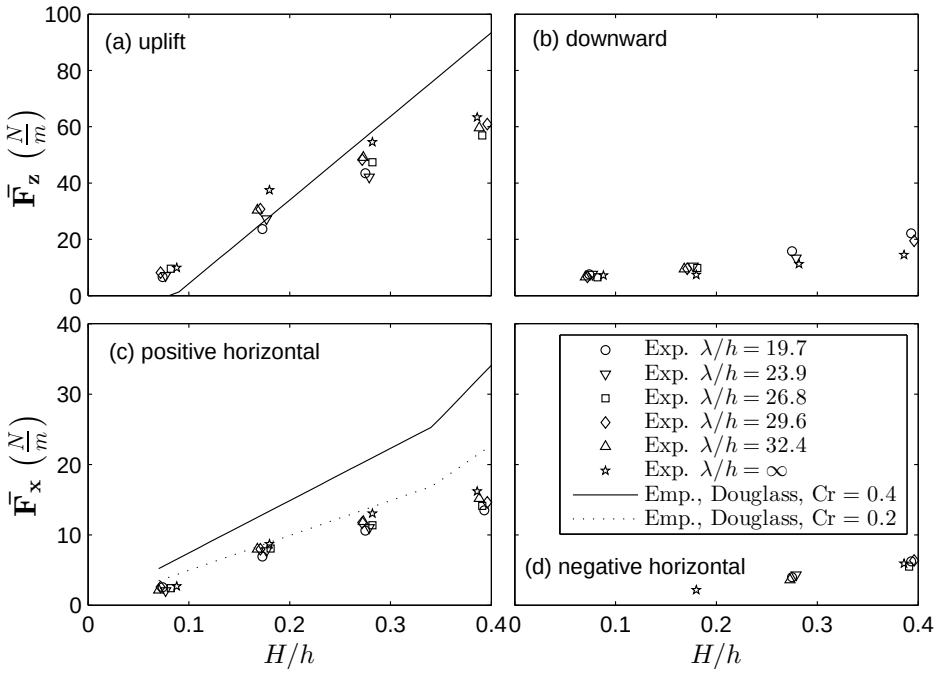

Figure 5.52: Laboratory measurements of (a) Vertical uplift, (b) vertical downward, (c) positive horizontal, and (d) negative horizontal forces on the bridge model with girders are presented versus nondimensional wavelength for wave heights of $H/h \approx 0.1 - 0.4$ at a water depth of $h = 0.071m$ and nondimensional elevation of $z^*/h = 0.06$, $z_G/h = -0.477$.

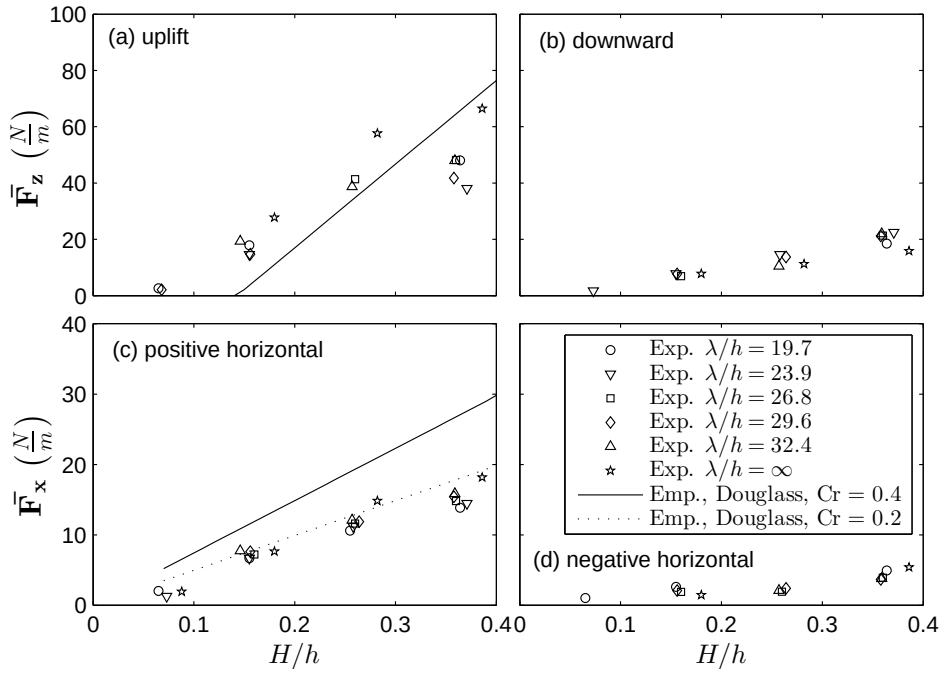

Figure 5.53: Laboratory measurements of (a) Vertical uplift, (b) vertical downward, (c) positive horizontal, and (d) negative horizontal forces on the bridge model with girders are presented versus nondimensional wavelength for wave heights of $H/h \approx 0.1 - 0.4$ at a water depth of $h = 0.071m$ and nondimensional elevation of $z^*/h = 0.1$, $z_G/h = -0.437$.

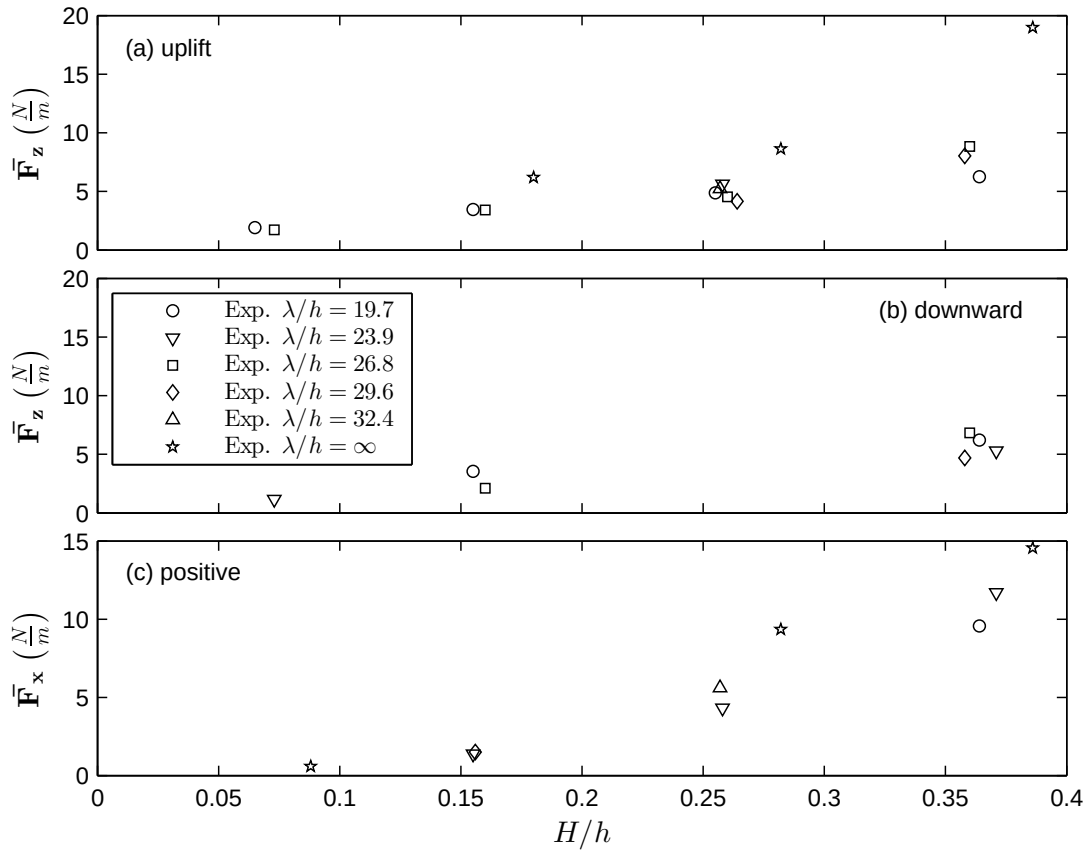

Figure 5.54: Laboratory measurements of (a) Vertical uplift, (b) vertical downward, and (c) positive horizontal forces on the bridge model with girders are presented versus nondimensional wavelength for wave heights of $H/h \approx 0.1 - 0.4$ at a water depth of $h = 0.071m$ and nondimensional elevation of $z^*/h = 0.3$, $z_G/h = -0.237$.

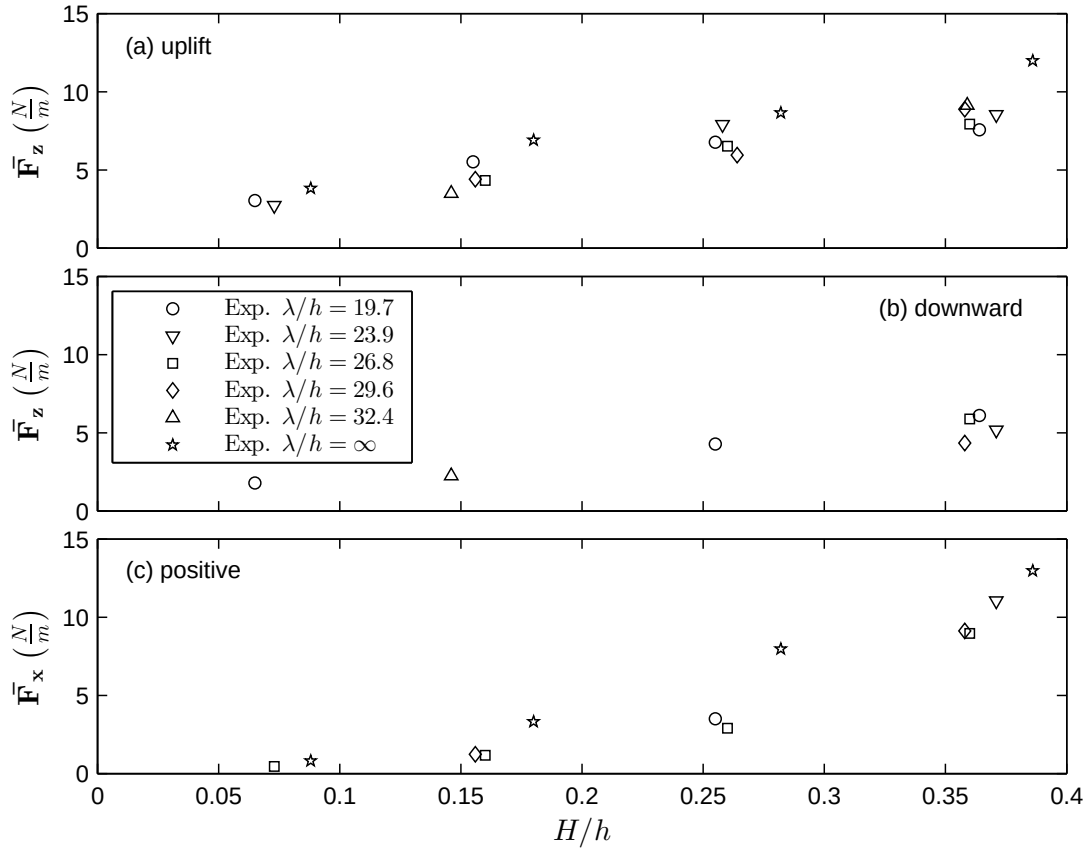

Figure 5.55: Laboratory measurements of (a) Vertical uplift, (b) vertical downward, and (c) positive horizontal forces on the bridge model with girders are presented versus nondimensional wavelength for wave heights of $H/h \approx 0.1 - 0.4$ at a water depth of $h = 0.071m$ and nondimensional elevation of $z^*/h = 0.35$, $z_G/h = -0.187$.

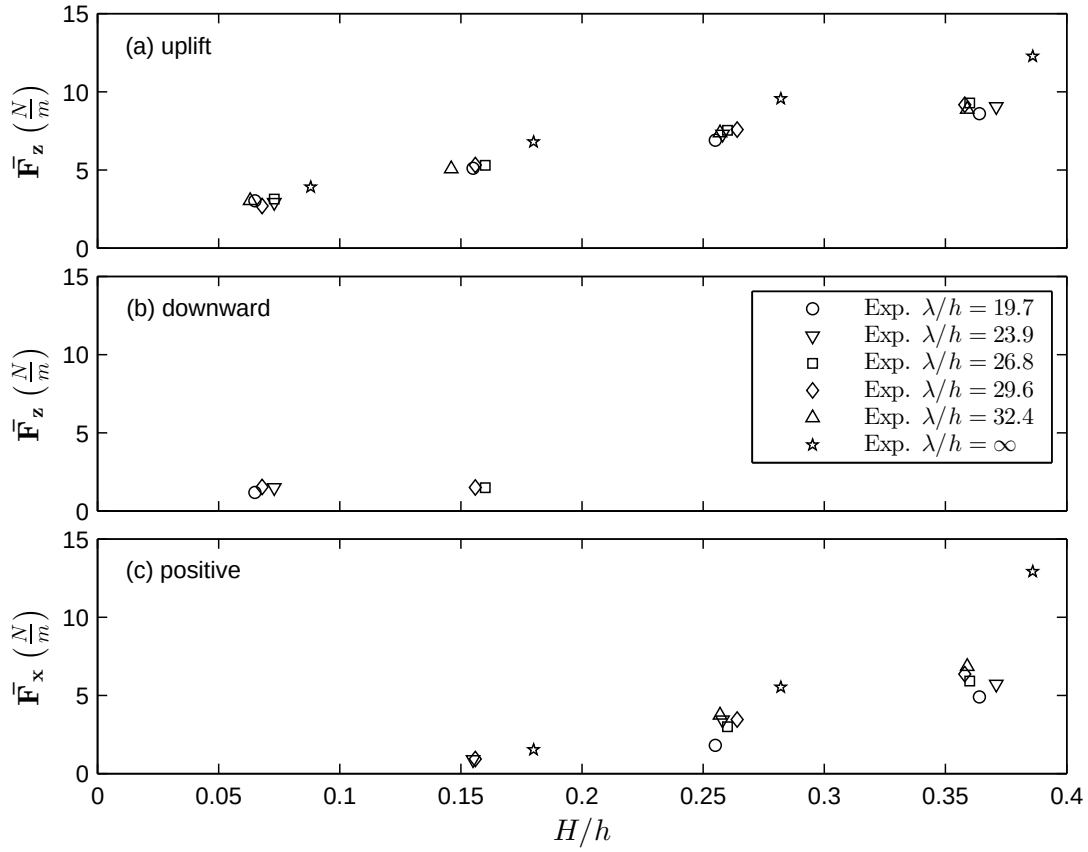

Figure 5.56: Laboratory measurements of (a) Vertical uplift, (b) vertical downward, and (c) positive horizontal forces on the bridge model with girders are presented versus nondimensional wavelength for wave heights of $H/h \approx 0.1 - 0.4$ at a water depth of $h = 0.071m$ and nondimensional elevation of $z^*/h = 0.55$, $z_G/h = 0.013$.

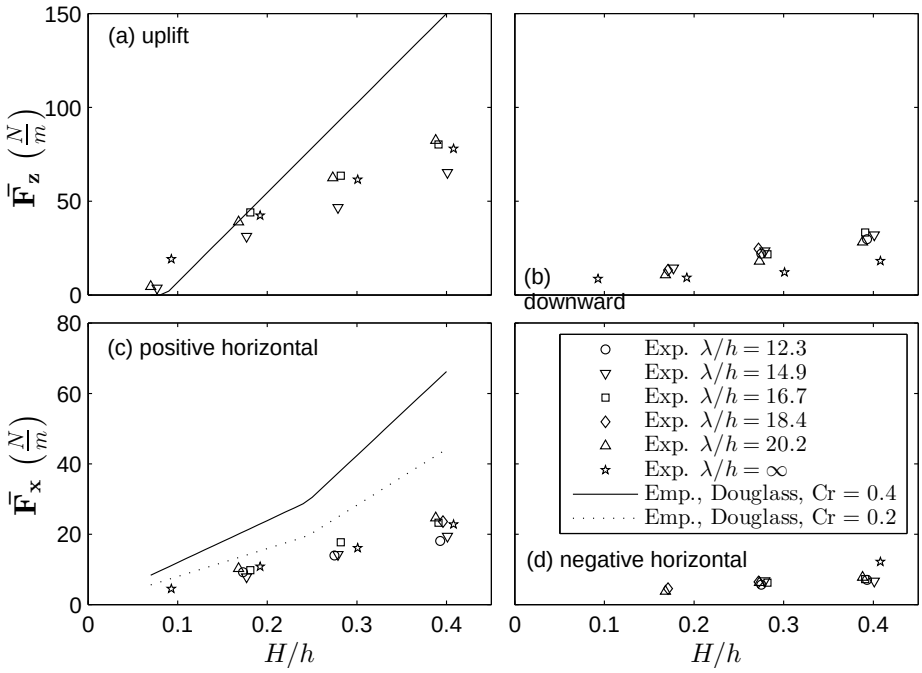

Figure 5.57: Laboratory measurements of (a) Vertical uplift, (b) vertical downward, (c) positive horizontal, and (d) negative horizontal forces on the bridge model with girders are presented versus nondimensional wavelength and are compared with the Douglass et al. (2006) relations for wave heights of $H/h \approx 0.1 - 0.4$ at a water depth of $h = 0.114m$ and nondimensional elevation of $z^*/h = 0.06$, $z_G/h = -0.274$.

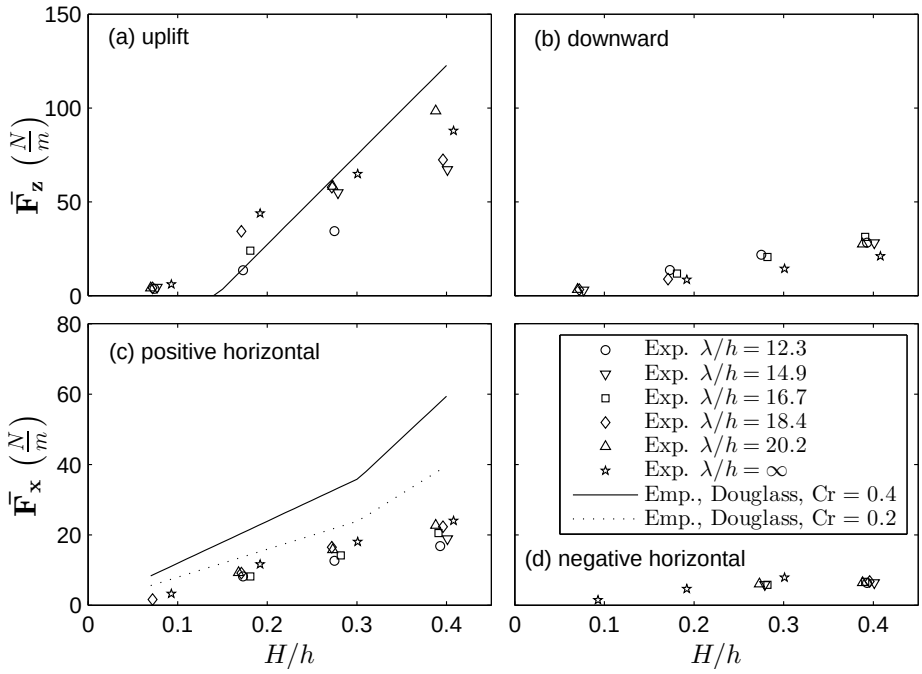

Figure 5.58: Laboratory measurements of (a) Vertical uplift, (b) vertical downward, (c) positive horizontal, and (d) negative horizontal forces on the bridge model with girders are presented versus nondimensional wavelength for wave heights of $H/h \approx 0.1 - 0.4$ at a water depth of $h = 0.114m$ and nondimensional elevation of $z^*/h = 0.1$, $z_G/h = -0.234$.

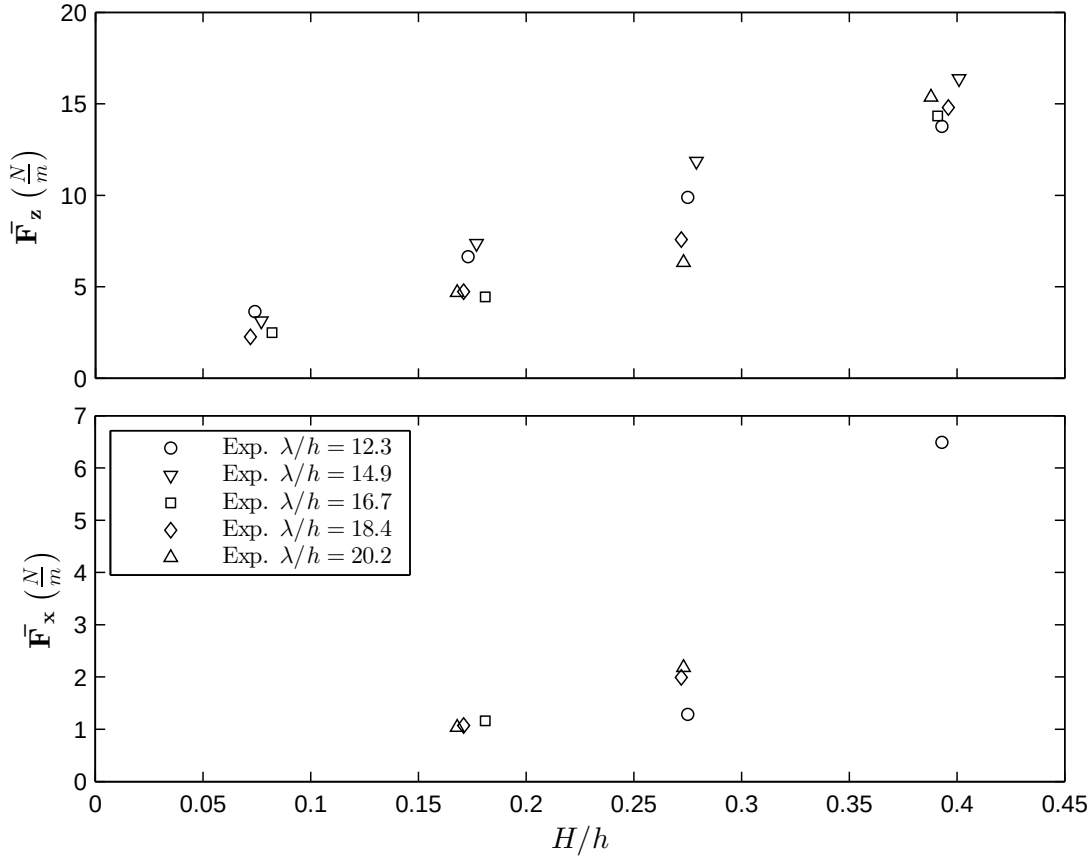

Figure 5.59: Laboratory measurements of (a) Vertical uplift and (b) positive horizontal on the bridge model with girders are presented versus nondimensional wavelength for wave heights of $H/h \approx 0.1 - 0.4$ at a water depth of $h = 0.114m$ and nondimensional elevation of $z^*/h = 0.35$, $z_G/h = 0.016$.

Chapter 6

Entrapped Air

6.1 Effects of Entrapped Air: Solitary Wave

In this section solitary wave forces on a bridge model with different percentages of entrapped air between the girders are presented. Normalized force measurements for vertical uplift force and horizontal positive force for the five ARO configurations described in Section 2.3 are plotted with respect to the measured dimensionless wave amplitude for each constant water depth $h = 0.071m$, $0.086m$, $0.114m$, and $0.143m$ in Figs. 6.1 - 6.8. There is a significant reduction in vertical uplift forces with each larger percentage of air relief opening when the bridge model elevation is such that the bottom of the girders are above the SWL or only slightly submerged, as seen in Figs. 6.1 (b) - (d), 6.2 (c), 6.3 (c), and 6.4 (c). The largest reduction is seen in the case of $h = 0.071m$, $z^*/h = 0.55$ and $a/h = 0.5$, where the 0.0% ARO measurement is more than four times the 100.0% ARO case. When the bridge model is closer to the water surface as in Figs. 6.1 (a), 6.2 (a) and (b), 6.3 (a) and (b), and 6.4 (a) and (b), the percentage of air relief opening has less of an effect, which is expected since less air can be trapped and the overall percentages of ARO are larger.

Percentage of ARO appears to have relatively less of an effect on the positive horizontal

forces, as seen in Figs. 6.5 – 6.8. In fact, forces are slightly smaller for a smaller percent ARO, likely due to the presence of air preventing the wave from interacting with any but the first upwave girder in the 0.0% ARO case, but a lessening of this effect as water can more freely enter the chambers with a larger percent ARO as seen in Fig. 6.9.

Time series measurements for vertical forces given in Fig. 6.10(a) show both larger forces and a longer sustained force for smaller percentage of ARO. Positive horizontal force measurements given in Fig. 6.10(b), show a slight delay of maximum force between percentages as the maximum force for the 0.0% ARO case happens as the wave impacts the first upwave girder, and the maximum force for the 100.0% case occurs slightly later, when the wave is impacting each of the six girders. Wave gauge measurements upwave of the model shown in Fig. 6.10 (c) and (d) show that smaller percentage of ARO results in a larger reflected wave due to conservation of energy, and wave gauge measurements downwave of the model shown in Fig. 6.10 (e) show that the presence of air also has the effect of slowing down the wave.

It is interesting to note, that when the bridge model is close to the water surface, it is not always the case that 100.0% ARO is the smallest uplift force. For the water depth of $h = 0.143m$, $z^*/h = 0.1$ and $a/h = 0.2$ for example, shown in Figs. 6.4 (b), it is the 4.0% ARO case that results in the smallest uplift force. In this case, uplift force for the 100.0% case is a shorter duration impact force as the wave is able to freely interact with the bottom of the bridge deck, as seen in the time series measurements for this case given in Fig. 6.11. The presence of air serves to slow down the wave, resulting in a smaller force, provided that all the air can eventually leave the chamber, which occurs in the 4.0% ARO case. This is confirmed by the series of snapshots taken at approximately the time of maximum force for this case, shown in Fig. 6.12. Vertical uplift and horizontal positive forces are plotted versus dimensionless wave speed $\bar{c} = \sqrt{1 + (a/h)}$ in Figs. 6.13 and 6.14.

The reduction in the uplift force can mostly be attributed to a reduction in hydrostatic

force as more water is allowed to enter the chambers between the girders, as seen for example in Fig. 6.9. The hydrostatic effect of entrapped air between the girders (F_{hyd}) can be calculated by

$$F_{hyd} = \rho g \nabla_{2D}, \tag{6.1}$$

where $\rho = 1000$ kg/m^3 is the density of fresh water, $g = 9.81$ m/s^2 is the acceleration due to gravity and ∇_{2D} is defined by

$$\nabla_{2D} = nS_G h_G, \tag{6.2}$$

where $S_G = 0.0349m$ is the distance between girders (shown in Fig. 2.10) and h_G is the water surface elevation in the chamber in the absence of entrapped air between the girders, measured from the bottom of the girders. Eqs. (6.1) and (6.2) are the same as used in Hayatdavoodi, Seiffert & Ertekin (2014*b*). In this case, $h_G = 0.035m$ for $h = 0.071m$, $a/h = 0.500$, $z^*/h = 0.55$ and $h_G = 0.038m$ for $h = 0.143m$, $a/h = 0.407$, $z^*/h = 0.3$. n is the number of chambers filled with air that would have otherwise been filled with water, and may be a fraction if only a portion of a chamber is filled with air at a given time.

Tables 6.1 and 6.2 list the maximum uplift force for each percentage of ARO, the force differential between the listed percentage and 100.0% ARO, the percent reduction in uplift force, the calculated value for n, the calculated hydrostatic force due to entrapped air (F_{hyd}) and the percentage of uplift force due to entrapped air for $h = 0.071m$, $a/h = 0.500$, $z^*/h = 0.55$ and $h = 0.143m$, $a/h = 0.407$, $z^*/h = 0.3$. n is calculated by using snapshots taken at the time of maximum uplift force, such as shown in Fig. 6.9. The uplift force differential is nearly the same as the force due to entrapped air in Table 6.1, indicating that the reduction in uplift force is almost entirely due to the reduction of hydrostatic force of the entrapped air when the bridge model is such that the girders are elevated above the SWL and the wave amplitude is less than the deck elevation. Table 6.2 shows that when girders are elevated but the wave amplitude is greater than the deck elevation, the hydrostatic force

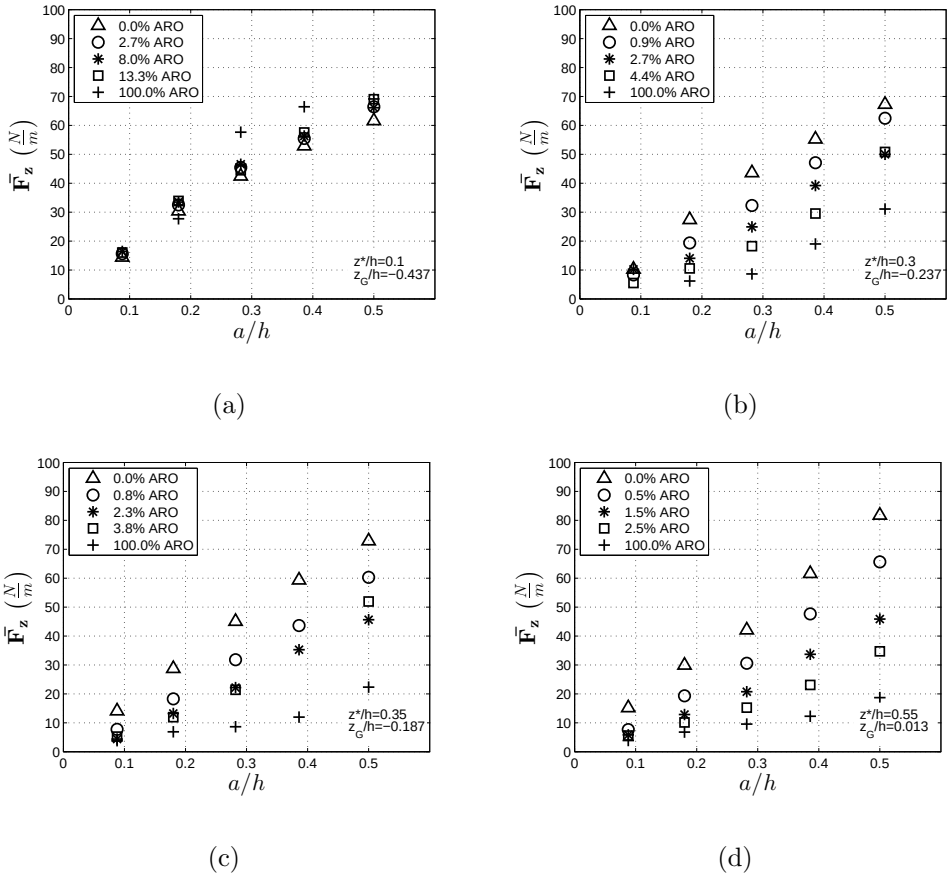

Figure 6.1: Vertical uplift forces are measured on the bridge model for percentages of air relief opening (ARO) from $0.0\% - 100.0\%$ and at wave amplitudes 0.1 - 0.5 times the water depth of $h = 0.071\,m$ for elevations (a) $z^*/h = 0.1$,$z_G/h = -0.437$ (b) $z^*/h = 0.3$, $z_G/h = -0.237$ (c) $z^*/h = 0.35$, $z_G/h = -0.187$ (d) $z^*/h = 0.55$, $z_G/h = 0.013$

due to the presence of air between the girders makes a smaller contribution to increases in overall uplift forces and a larger portion of uplift force is due to wave impact. The uplift force differentials in this case are smaller since the force in the 100% ARO case is still relatively large due to the wave impacting the bridge deck. In both of these cases, hydrostatic force and wave impact force must be taken into consideration.

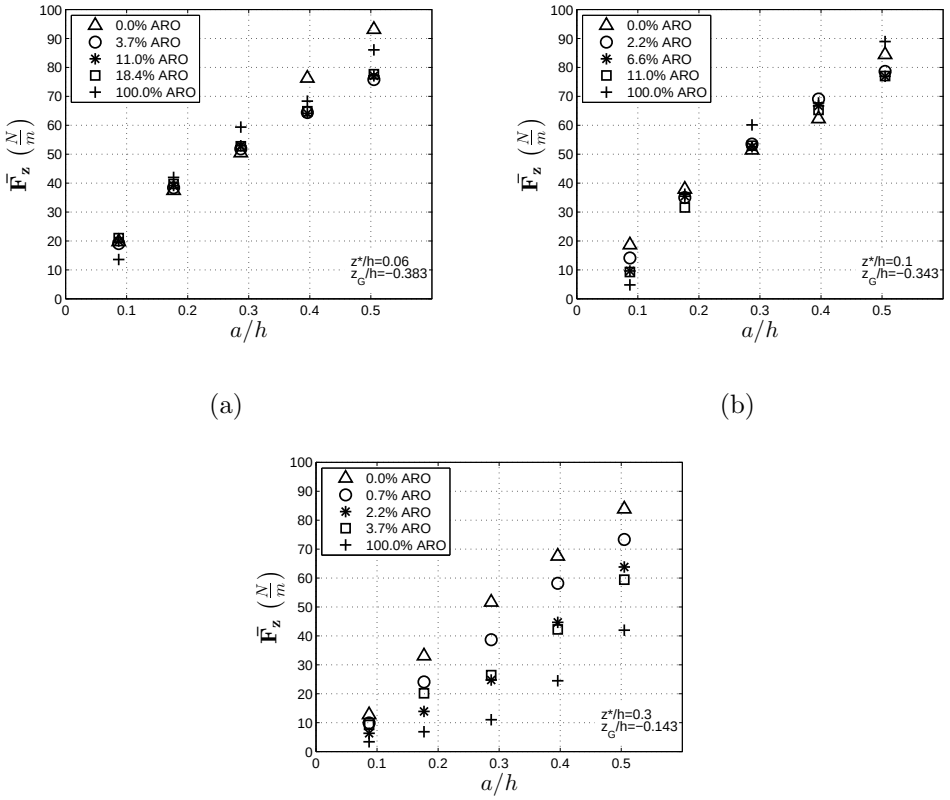

Figure 6.2: Vertical uplift forces are measured on the bridge model for percentages of air relief opening (ARO) from $0.0\% - 100.0\%$ and at wave amplitudes 0.1 - 0.5 times the water depth of $h = 0.086\,m$ for elevations (a) $z^*/h = 0.06$, $z_G/h = -0.383$ (b) $z^*/h = 0.1$, $z_G/h = -0.343$ (c) $z^*/h = 0.3$, $z_G/h = -0.143$

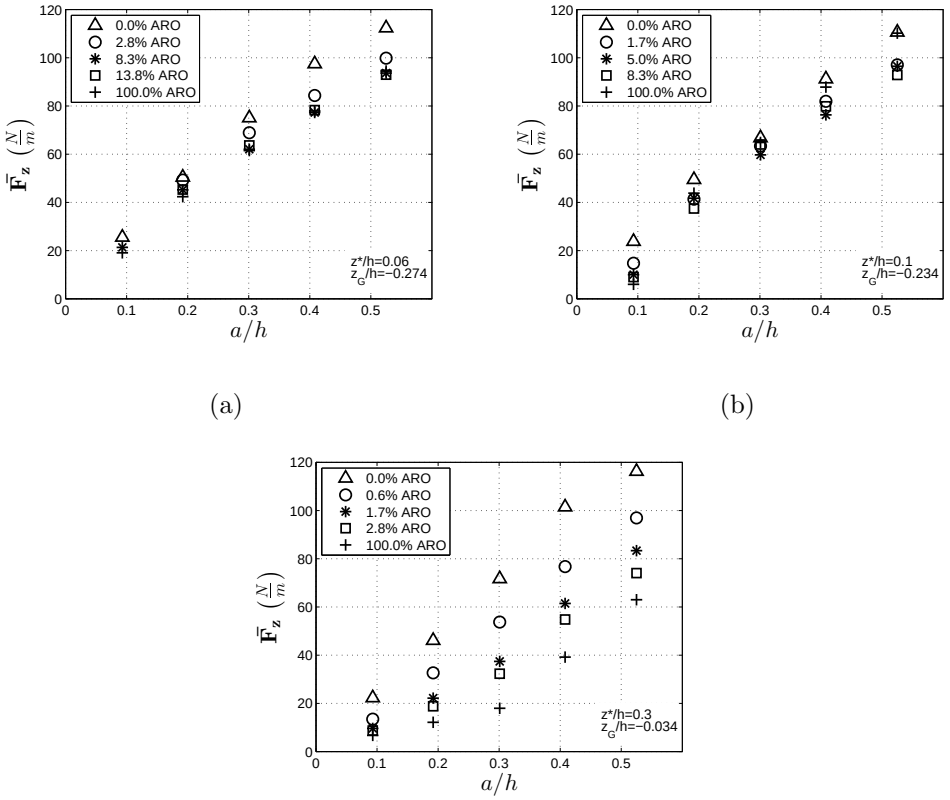

Figure 6.3: Vertical uplift forces are measured on the bridge model for percentages of air relief opening (ARO) from $0.0\% - 100.0\%$ and at wave amplitudes 0.1 - 0.5 times the water depth of $h = 0.114\,m$ for elevations (a) $z^*/h = 0.06$, $z_G/h = -0.274$ (b) $z^*/h = 0.1$, $z_G/h = -0.234$ (c) $z^*/h = 0.3$, $z_G/h = -0.034$

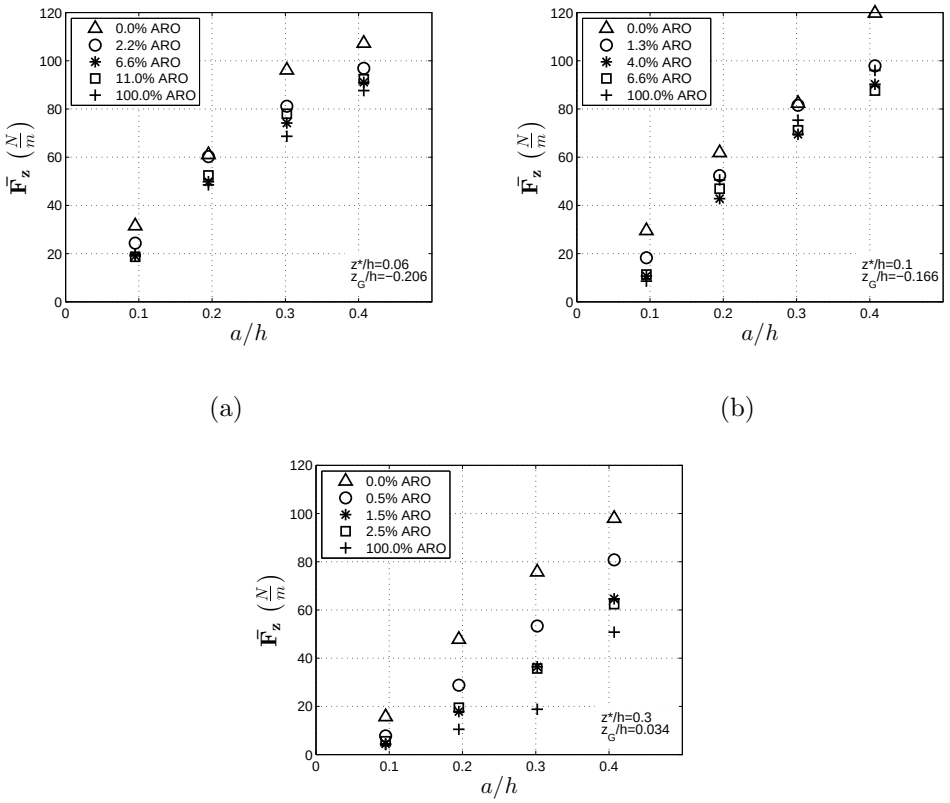

Figure 6.4: Vertical uplift forces are measured on the bridge model for percentages of air relief opening (ARO) from $0.0\% - 100.0\%$ and at wave amplitudes 0.1 - 0.5 times the water depth of $h = 0.143\,m$ for elevations (a) $z^*/h = 0.06$, $z_G/h = -0.206$ (b) $z^*/h = 0.1$, $z_G/h = -0.166$ (c) $z^*/h = 0.3$, $z_G/h = 0.034$

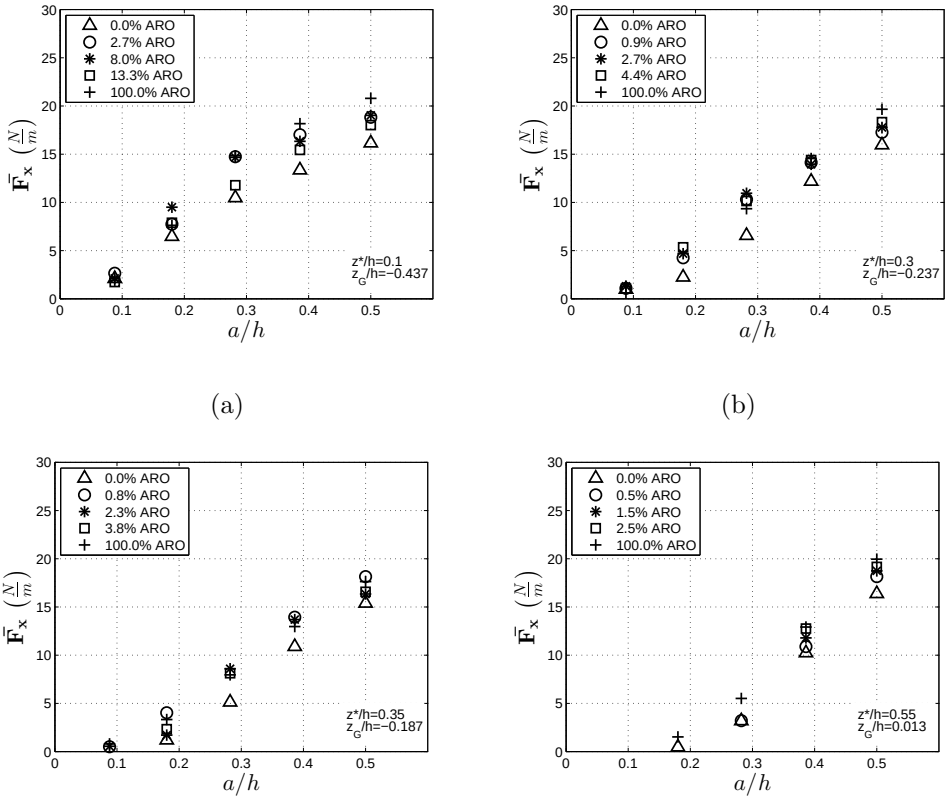

Figure 6.5: Horizontal positive forces are measured on the bridge model for percentages of air relief opening (ARO) from $0.0\% - 100.0\%$ and at wave amplitudes 0.1 - 0.5 times the water depth of $h = 0.071\,m$ for elevations (a) $z^*/h = 0.1$,$z_G/h = -0.437$ (b) $z^*/h = 0.3$, $z_G/h = -0.237$ (c) $z^*/h = 0.35$, $z_G/h = -0.187$ (d) $z^*/h = 0.55$, $z_G/h = 0.013$

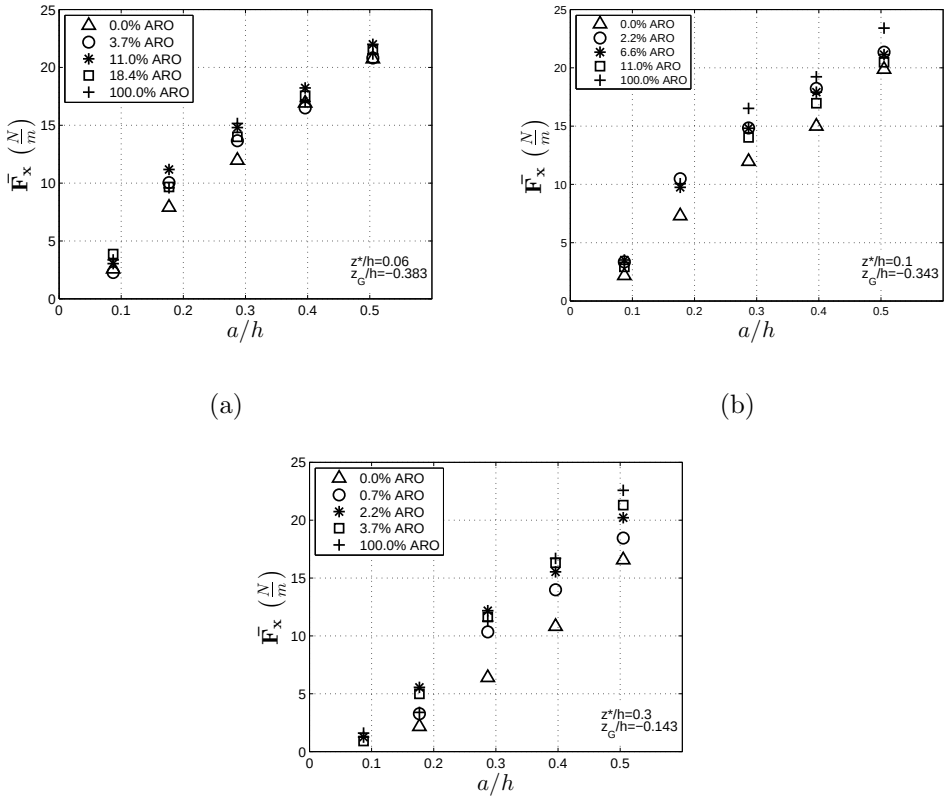

Figure 6.6: Horizontal positive forces are measured on the bridge model for percentages of air relief opening from (ARO) $0.0\% - 100.0\%$ and at wave amplitudes 0.1 - 0.5 times the water depth of $h = 0.086\,m$ for elevations (a) $z^*/h = 0.06$, $z_G/h = -0.383$ (b) $z^*/h = 0.1$, $z_G/h = -0.343$ (c) $z^*/h = 0.3$, $z_G/h = -0.143$

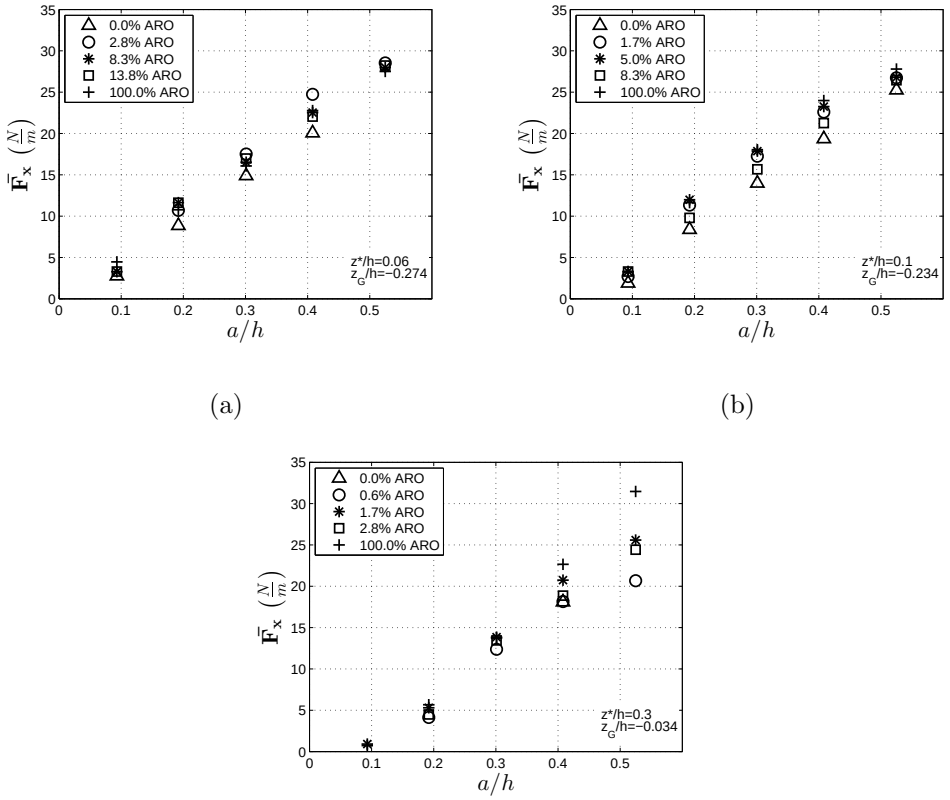

Figure 6.7: Horizontal positive forces are measured on the bridge model for percentages of air relief opening from (ARO) $0.0\% - 100.0\%$ and at wave amplitudes 0.1 - 0.5 times the water depth of $h = 0.114\,m$ for elevations (a) $z^*/h = 0.06$, $z_G/h = -0.274$ (b) $z^*/h = 0.1$, $z_G/h = -0.234$ (c) $z^*/h = 0.3$, $z_G/h = -0.034$

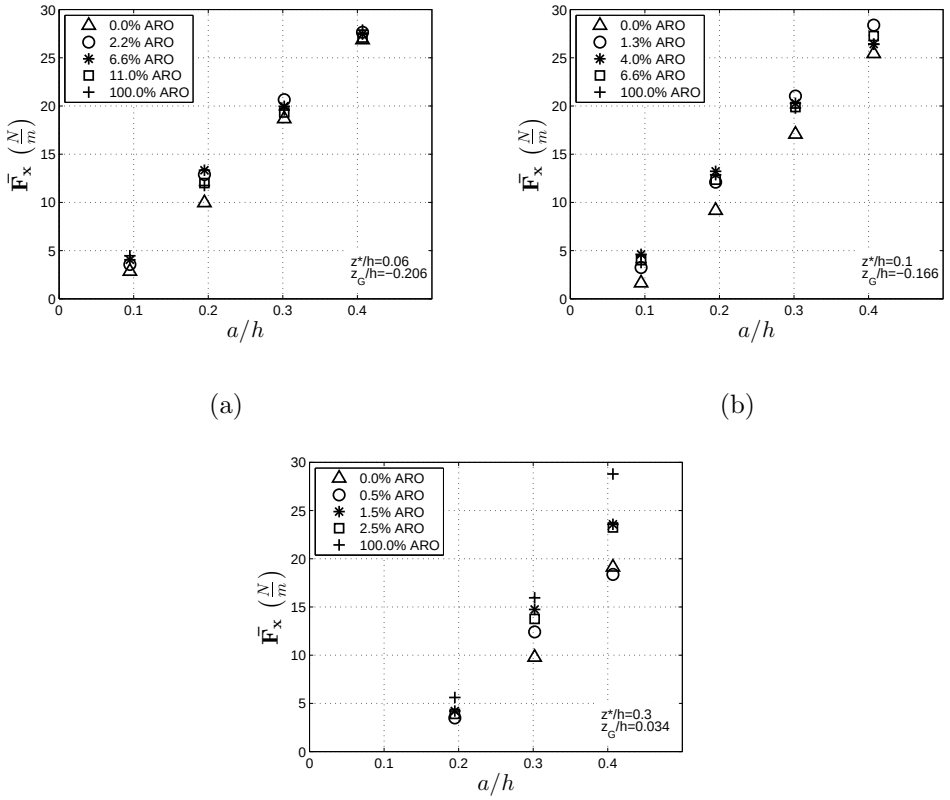

Figure 6.8: Horizontal positive forces are measured on the bridge model for percentages of air relief opening (ARO) from $0.0\% - 100.0\%$ and at wave amplitudes 0.1 - 0.5 times the water depth of $h = 0.143\,m$ for elevations (a) $z^*/h = 0.06$, $z_G/h = -0.206$ (b) $z^*/h = 0.1$, $z_G/h = -0.166$ (c) $z^*/h = 0.3$, $z_G/h = 0.034$

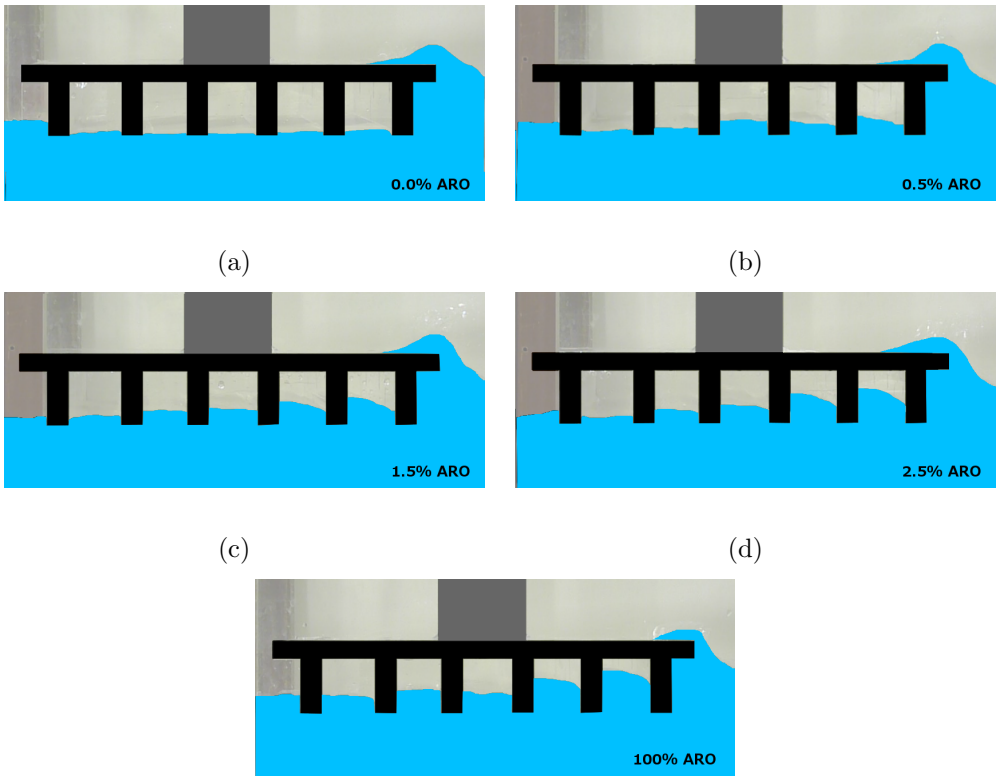

(a) (b) (c) (d) (e)

Figure 6.9: Snapshots are taken of the initial interaction of a solitary wave with the bridge model at (a) 0.0% ARO, (b) 0.5% ARO, (c) 1.5% ARO, (d) 2.5% ARO, and (e) 100.0% ARO for water depth $h = 0.071m$, $a/h = 0.5$ and $z^*/h = 0.55$.

Table 6.1: Maximum uplift force differential and contribution to uplift forces due to entrapped air for $0.0\%, 0.5\%, 1.5\%, 2.5\%$, and 100.0% ARO at water depth $h = 0.071$ m, $a/h = 0.5$, and $z^*/h = 0.55$.

ARO	0.0%	0.5%	1.5%	2.5%	100.0%
Max. F_z (N)	12.20	9.80	6.84	5.18	2.79
Uplift force differential (N)	9.41	7.01	4.05	2.39	-
Reduction in uplift force	77%	72%	59%	46%	-
n	5	3.7	2.2	1.3	-
F_{hyd} (N) due to entrapped air	8.92	6.61	3.92	2.32	-
$\%F_z$ due to entrapped air	73%	67%	57%	45%	-

Table 6.2: Maximum uplift force differential and contribution to uplift forces due to entrapped air for $0.0\%, 0.5\%, 1.5\%, 2.5\%$, and 100.0% ARO at water depth $h = 0.143$ m, $a/h = 0.407$, and $z^*/h = 0.3$.

ARO	0.0%	0.5%	1.5%	2.5%	100.0%
Max. F_z (N)	14.62	12.05	9.64	9.31	7.58
Uplift force differential (N)	7.04	4.47	2.06	1.73	-
Reduction in uplift force	48%	37%	21%	19%	-
n	5	3.3	2.5	1.8	-
F_{hyd} (N) due to entrapped air	9.69	6.40	4.85	3.49	-
$\%F_z$ due to entrapped air	66%	53%	50%	37%	-

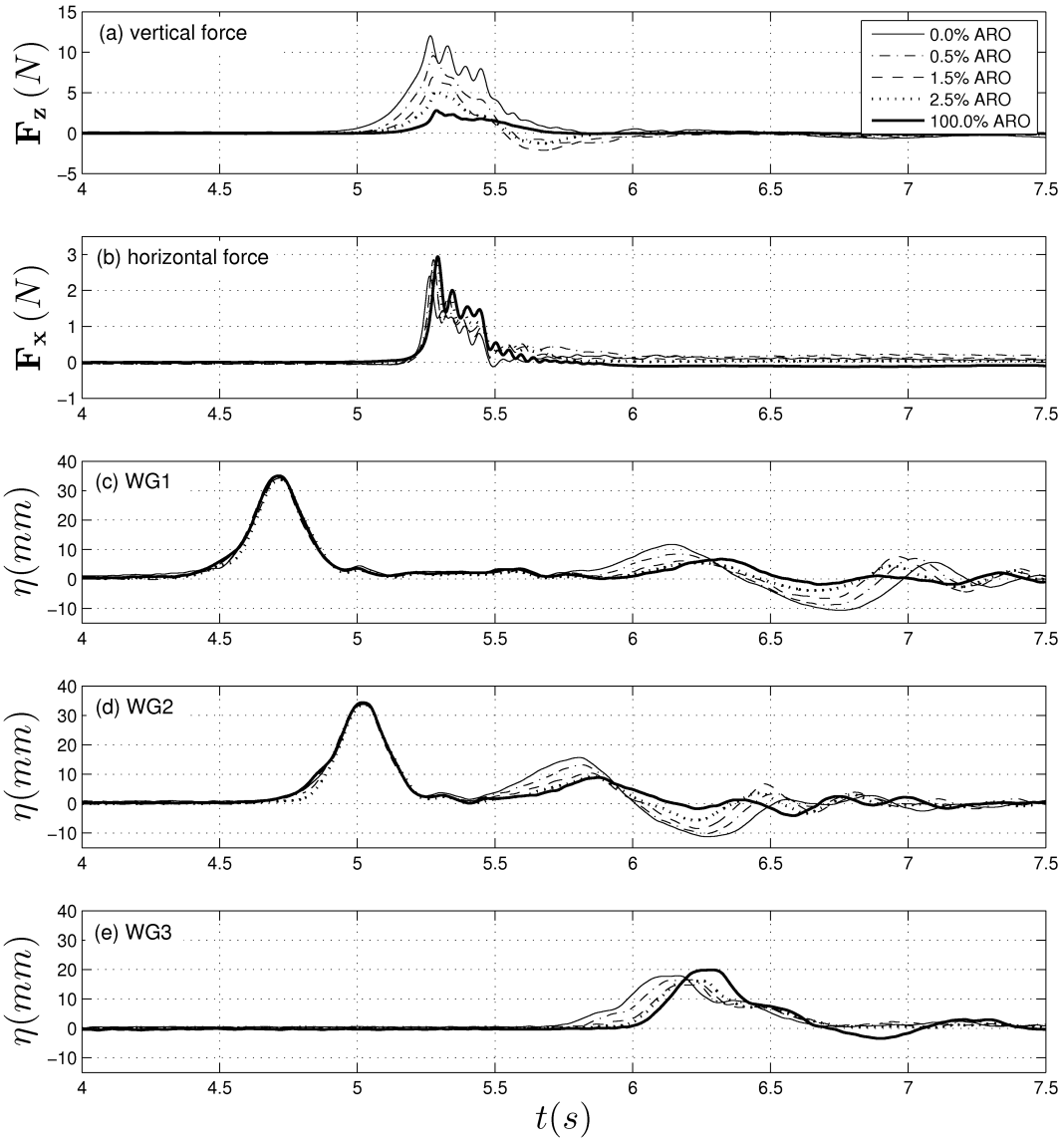

Figure 6.10: Time series measurements for (a) vertical ($\boldsymbol{F_z}$) and (b) horizontal ($\boldsymbol{F_x}$) force on the bridge model for percentages of air relief opening (ARO) from 0.0% – 100.0% for h =0.071 m, a/h =0.5 and z^*/h =0.55.

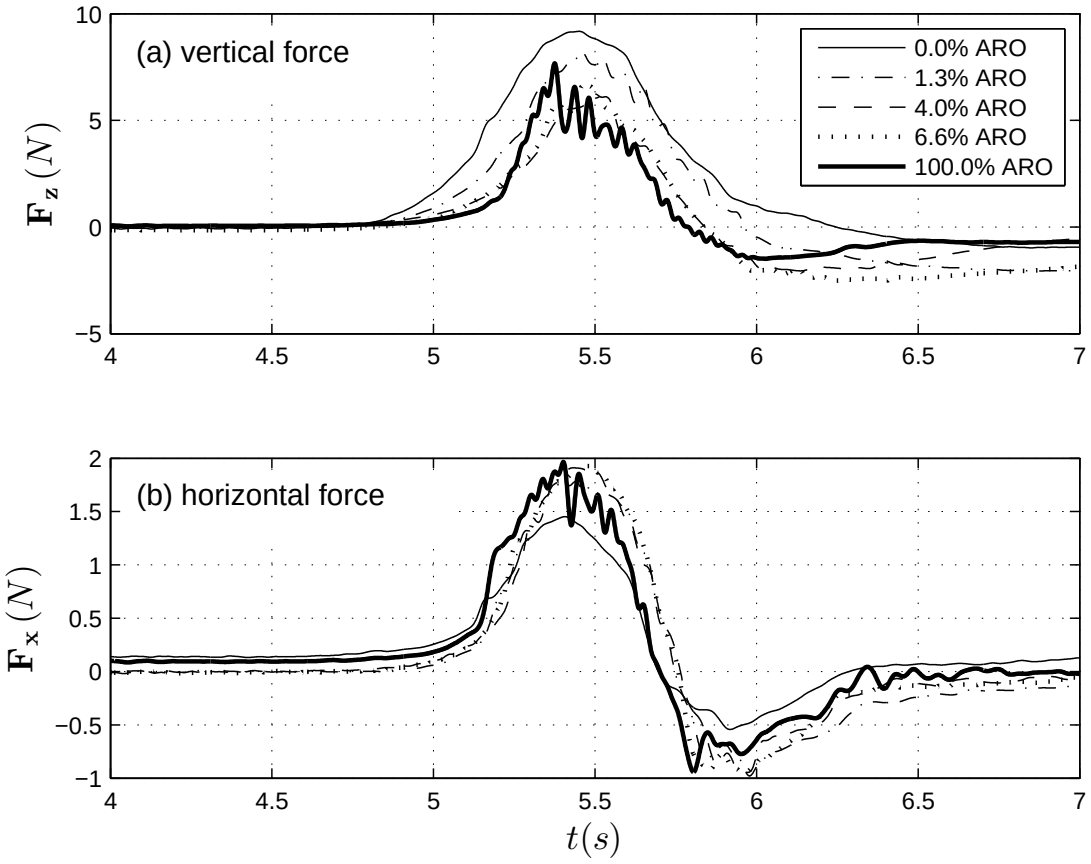

Figure 6.11: Time series measurements for (a) vertical ($\boldsymbol{F_z}$) and (b) horizontal ($\boldsymbol{F_x}$) force on the bridge model for percentages of air relief opening (ARO) from $0.0\% - 100.0\%$ for h =0.143 m, a/h =0.2 and z^*/h =0.1.

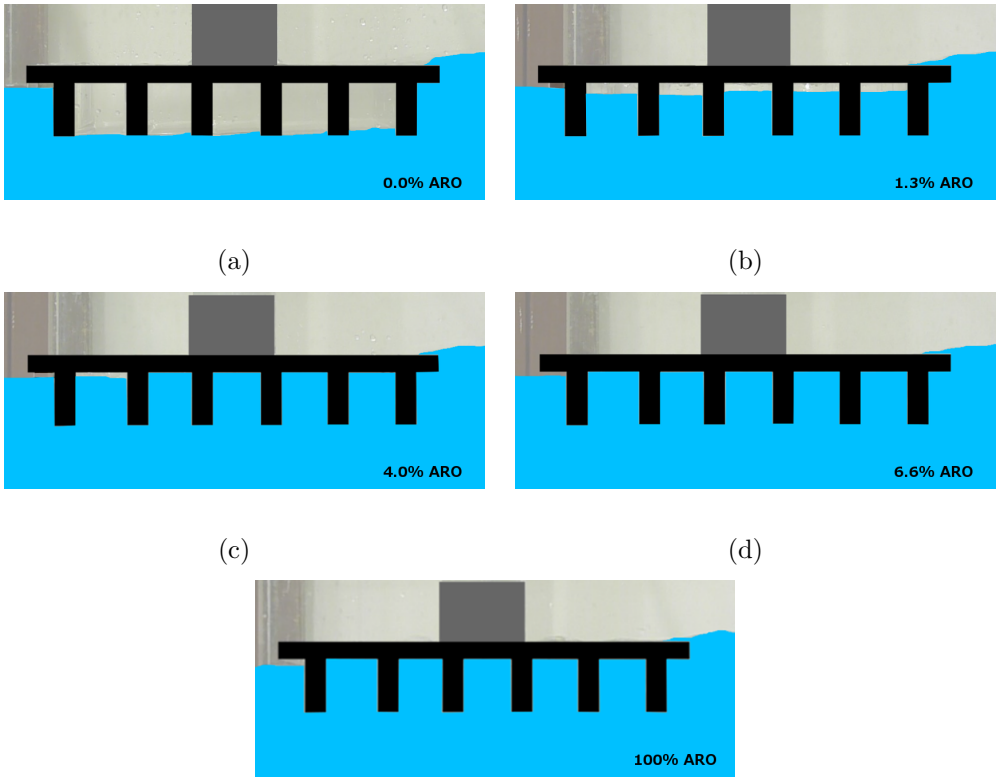

(a) (b) (c) (d) (e)

Figure 6.12: Snapshots are taken of the initial interaction of a solitary wave with the bridge model at (a) 0.0% ARO, (b) 1.3% ARO, (c) 4.0% ARO, (d) 6.6% ARO, and (e) 100.0% ARO for water depth $h = 0.143\,m$, $a/h = 0.2$ and $z^*/h = 0.1$.

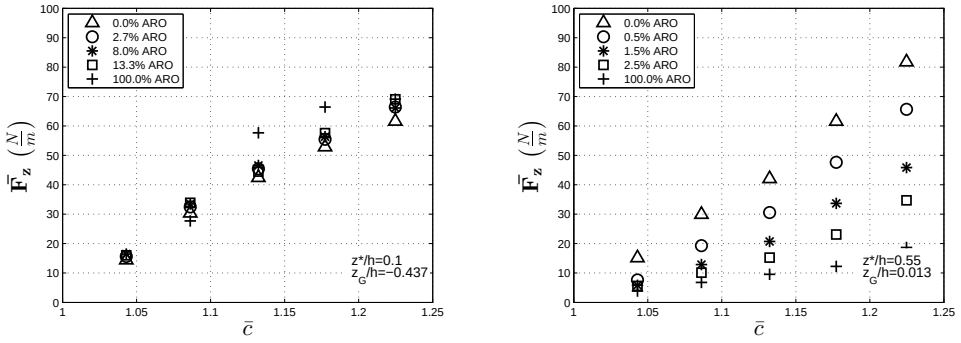

(a) (b)

Figure 6.13: Vertical uplift forces are presented versus dimensionless wave speed for percentages of air relief opening (ARO) from $0.0\% - 100.0\%$ and at wave amplitudes 0.1 - 0.5 times the water depth of $h = 0.071\,m$ for elevations (a) $z^*/h = 0.1$, $z_G/h = -0.437$ (b) $z^*/h = 0.55$, $z_G/h = 0.013$

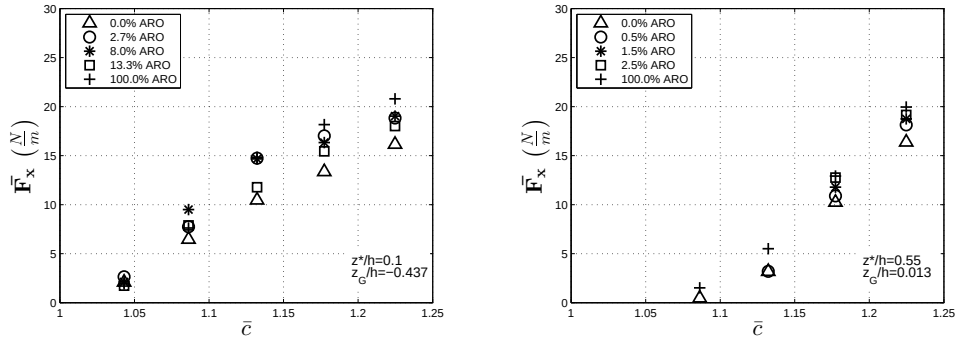

(a) (b)

Figure 6.14: Horizontal positive forces are presented versus dimensionless wave speed for percentages of air relief opening (ARO) from $0.0\% - 100.0\%$ and at wave amplitudes 0.1 - 0.5 times the water depth of $h = 0.071\,m$ for elevations (a) $z^*/h = 0.1$, $z_G/h = -0.437$ (b) $z^*/h = 0.55$, $z_G/h = 0.013$

6.2 Effects of Entrapped Air: Cnoidal Wave

In this section, cnoidal wave forces on a bridge model with girders and different percentages of entrapped air are presented. Vertical uplift forces for the five percentages of ARO discussed in Section 6.1 are presented in Figs. 6.15 - 6.19, and positive horizontal forces are presented in Figs. 6.20 - 6.24 for water depth $h = 0.071$ m, wave heights $H/h \approx 0.1 - 0.4$, model elevations $z*/h = 0.1, 0.3, 0.35$ and 0.55, and wave lengths $1.4 - 2.3$ m. There is significant reduction in uplift forces for each larger percentage of ARO, particularly for the cases where the bottom of the deck is elevated well above the SWL, as in Figs. 6.15 - 6.19 (b) - (d). The largest reduction is when the bottom of the girders are elevated above the SWL, in Figs. 6.15 - 6.19 (d), where uplift forces are as much as 6 times larger for the 0.0% ARO case than the 100.0% ARO case. There is less of an effect on uplift forces when the bridge model is closer to the water surface, as in Figs. 6.15 - 6.19 (a). This is not surprising as much less air is trapped and the overall percentages of ARO are larger. These findings are consistent with the findings from the solitary wave cases discussed in Section 6.1.

There is less of an effect of entrapped air on positive horizontal forces, seen in Figs. 6.20 - 6.24. There is significant variation in the results suggesting turbulence, wave breaking, wave interaction with girders and nonlinear effects are all contributing to these forces. Although there is some oscillation, wave length in the range tested does not appear to have any appreciable effect on the forces.

A reduction coefficient (C_ϵ) is calculated using experimental measurements for uplift forces at the water depth $h = 0.071$, $z^*/h = 0.55$, $H/h \approx 0.1 - 0.4$ and $\lambda = 1.4 - 2.3$ m, following the method outlined in Chapter 4. ϵ is calculated for $0.5, 1.5$ and 2.5% ARO cases as, $\epsilon = 0.0017, 0.0052$ and 0.0087, respectively. A comparison is made with calculations following the Bagnold-Mitsuyasu model, and is presented in Fig. 6.25. There is some agreement between measurements and the model, particularly with the smaller wave heights

and for $\epsilon = 0.0017$. For the larger values of ϵ, the reduction calculated using experimental measurements is much smaller than that predicted using the theoretical model. In addition, the experimental measurements show a larger reduction coefficient for $H/h \approx 0.4$ than $H/h \approx 0.2$, while the opposite is true for the Bagnold-Mitsuyasu model. Disagreement could be due to the small scale of experiments, or the nonlinearity of waves used in experiments.

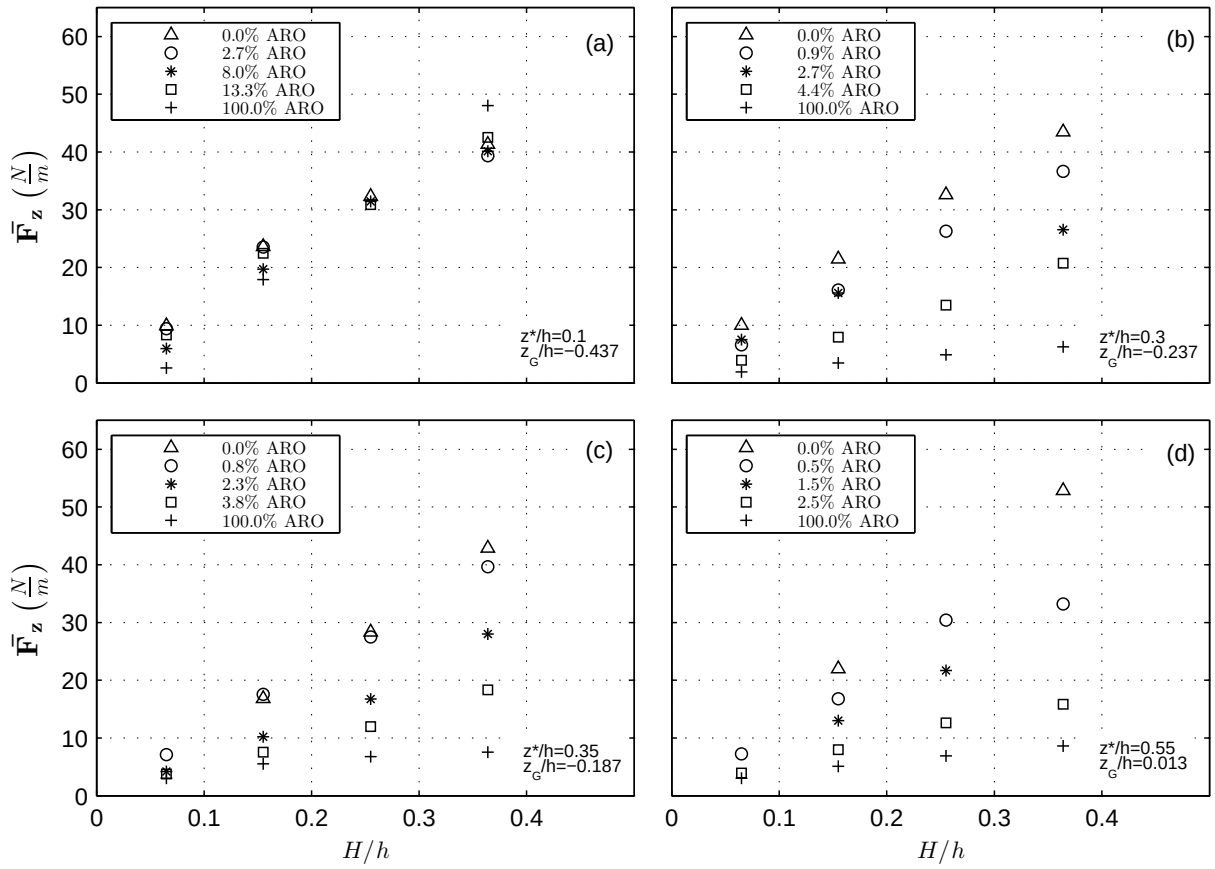

Figure 6.15: Vertical uplift forces are measured on the bridge model for percentages of air relief opening (ARO) from $0.0\% - 100.0\%$ and at wave heights approximately 0.1 - 0.4 times the water depth of $h = 0.071$ m with wavelength $\lambda = 1.4$ m for elevations (a) $z^*/h = 0.1$,$z_G/h = -0.437$ (b) $z^*/h = 0.3$, $z_G/h = -0.237$ (c) $z^*/h = 0.35$, $z_G/h = -0.187$ (d) $z^*/h = 0.55$, $z_G/h = 0.013$

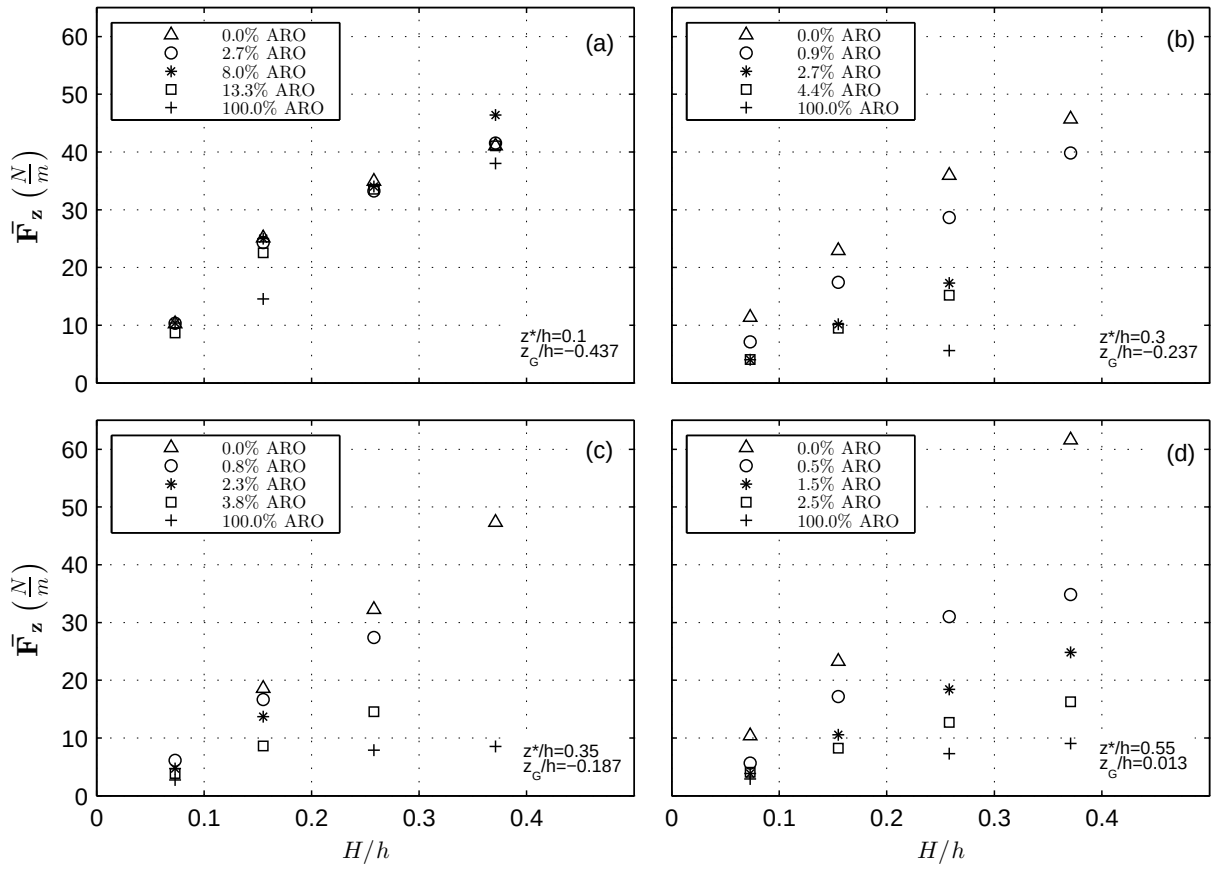

Figure 6.16: Vertical uplift forces are measured on the bridge model for percentages of air relief opening (ARO) from $0.0\% - 100.0\%$ and at wave heights approximately 0.1 - 0.4 times the water depth of $h = 0.071$ m with wavelength $\lambda = 1.7$ m for elevations (a) $z^*/h = 0.1$,$z_G/h = -0.437$ (b) $z^*/h = 0.3$, $z_G/h = -0.237$ (c) $z^*/h = 0.35$, $z_G/h = -0.187$ (d) $z^*/h = 0.55$, $z_G/h = 0.013$

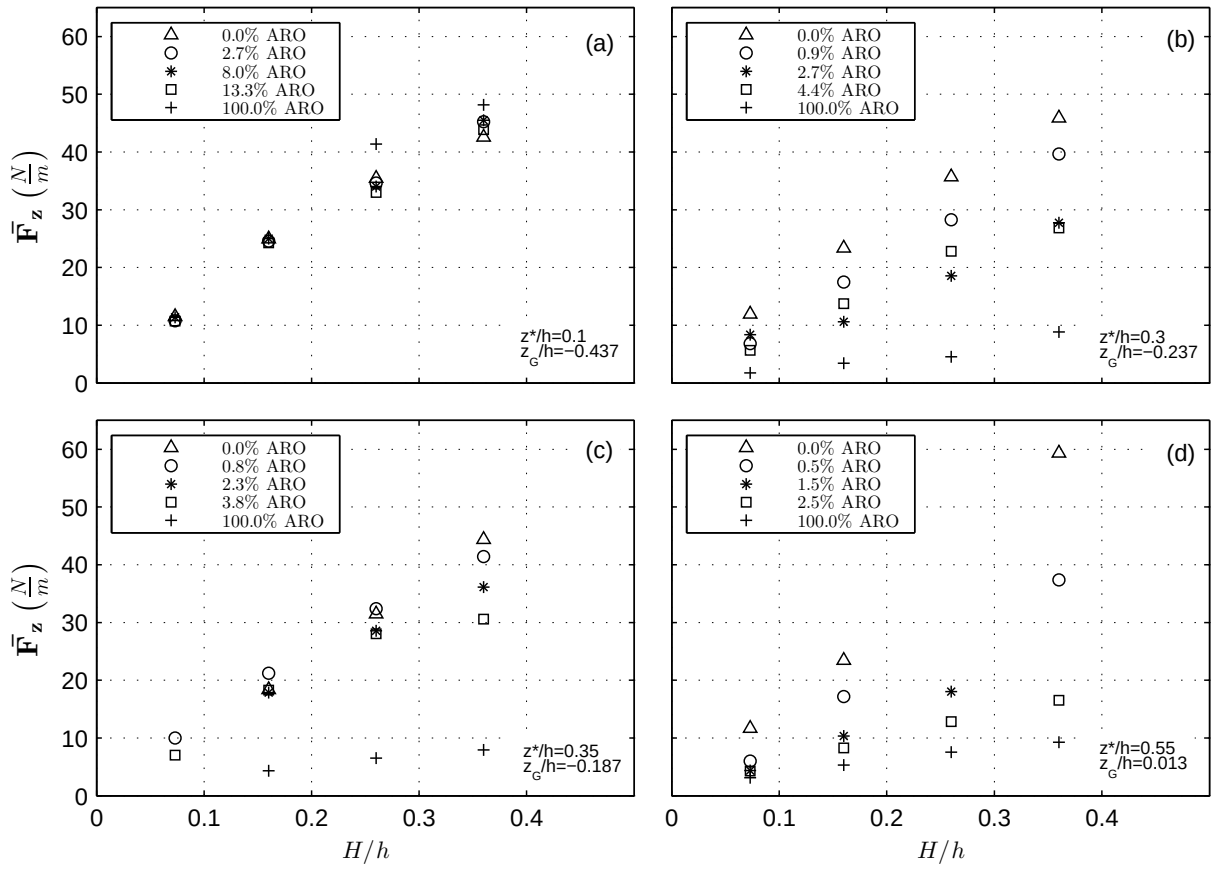

Figure 6.17: Vertical uplift forces are measured on the bridge model for percentages of air relief opening (ARO) from $0.0\% - 100.0\%$ and at wave heights approximately 0.1 - 0.4 times the water depth of $h = 0.071$ m with wavelength $\lambda = 1.9$ m for elevations (a) $z^*/h = 0.1$,$z_G/h = -0.437$ (b) $z^*/h = 0.3$, $z_G/h = -0.237$ (c) $z^*/h = 0.35$, $z_G/h = -0.187$ (d) $z^*/h = 0.55$, $z_G/h = 0.013$

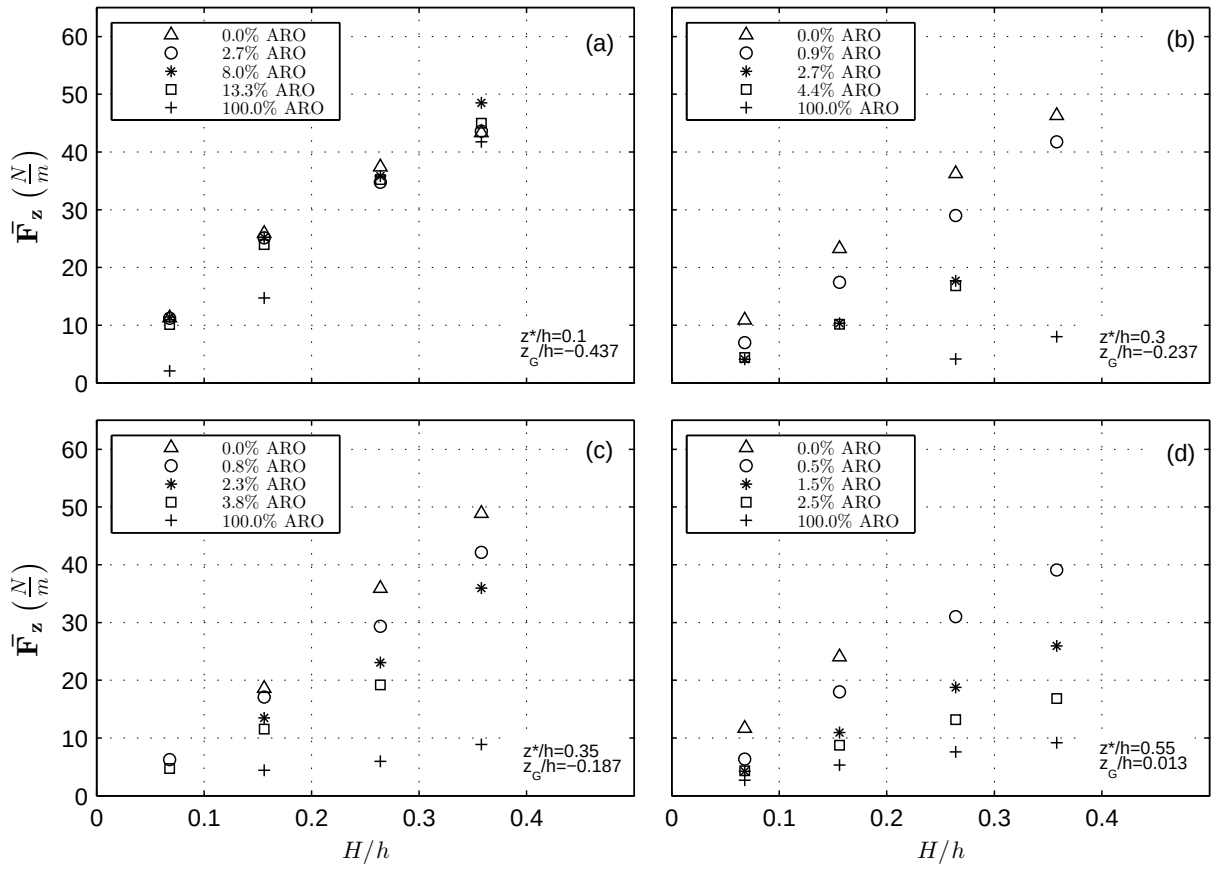

Figure 6.18: Vertical uplift forces are measured on the bridge model for percentages of air relief opening (ARO) from $0.0\% - 100.0\%$ and at wave heights approximately 0.1 - 0.4 times the water depth of $h = 0.071$ m with wavelength $\lambda = 2.1$ m for elevations (a) $z^*/h = 0.1$,$z_G/h = -0.437$ (b) $z^*/h = 0.3$, $z_G/h = -0.237$ (c) $z^*/h = 0.35$, $z_G/h = -0.187$ (d) $z^*/h = 0.55$, $z_G/h = 0.013$

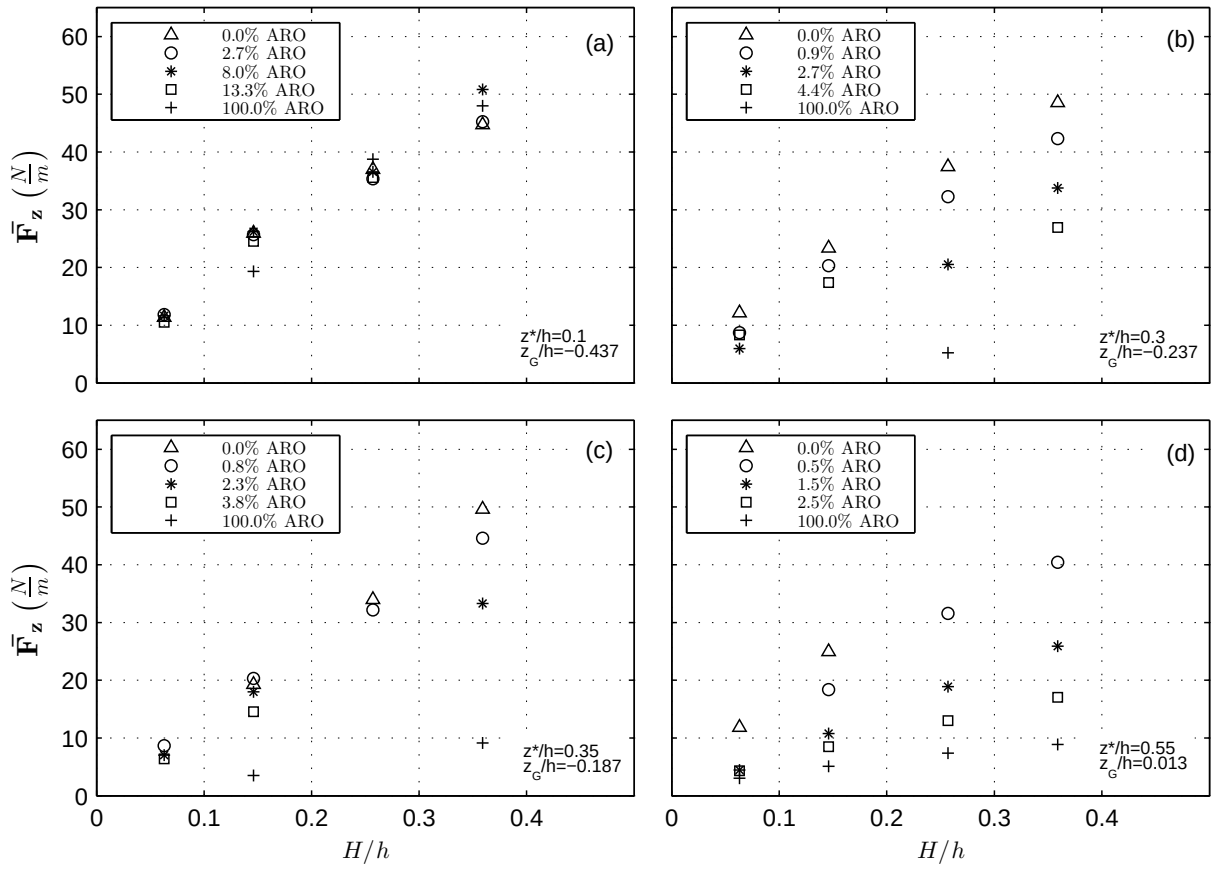

Figure 6.19: Vertical uplift forces are measured on the bridge model for percentages of air relief opening (ARO) from $0.0\% - 100.0\%$ and at wave heights approximately 0.1 - 0.4 times the water depth of $h = 0.071$ m with wavelength $\lambda = 2.3$ m for elevations (a) $z^*/h = 0.1$,$z_G/h = -0.437$ (b) $z^*/h = 0.3$, $z_G/h = -0.237$ (c) $z^*/h = 0.35$, $z_G/h = -0.187$ (d) $z^*/h = 0.55$, $z_G/h = 0.013$

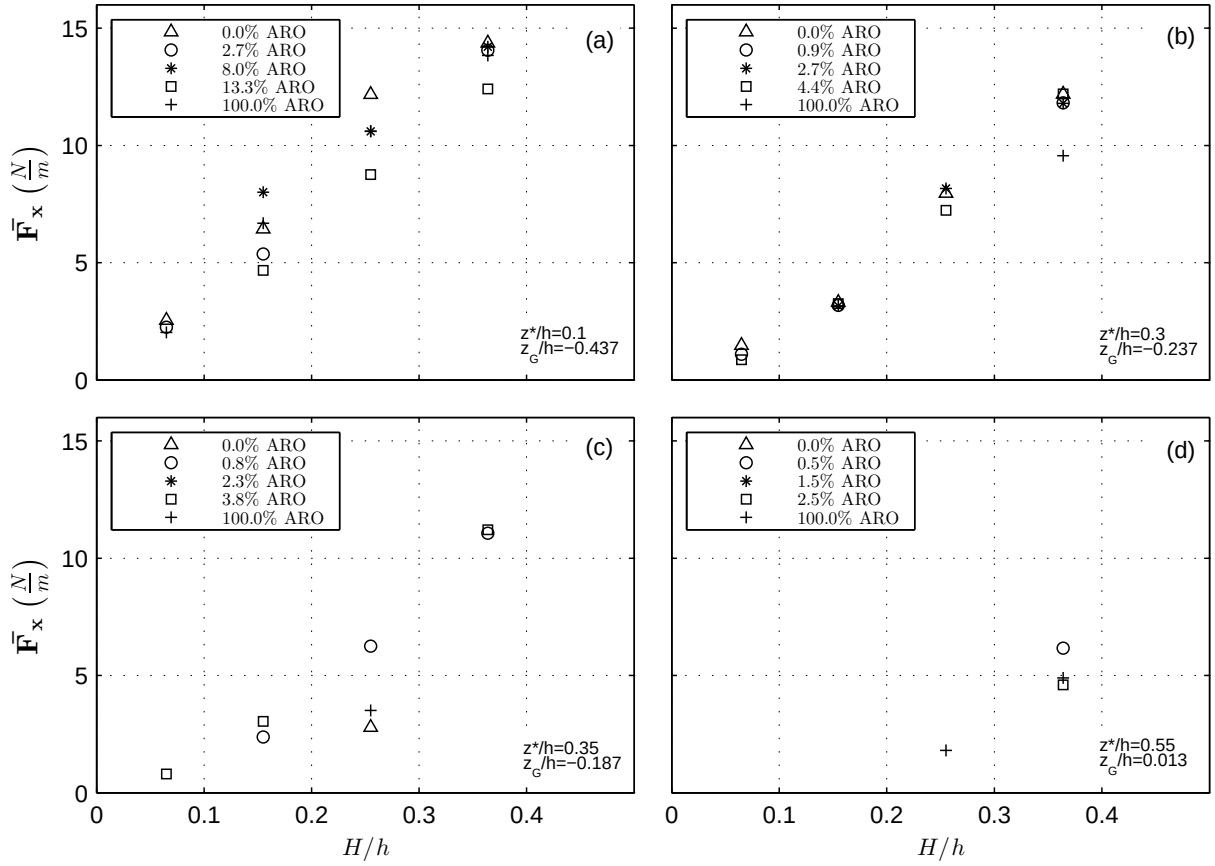

Figure 6.20: Positive horizontal forces are measured on the bridge model for percentages of air relief opening (ARO) from $0.0\% - 100.0\%$ and at wave heights approximately 0.1 - 0.4 times the water depth of $h = 0.071$ m with wavelength $\lambda = 1.4$ m for elevations (a) $z^*/h = 0.1$,$z_G/h = -0.437$ (b) $z^*/h = 0.3$, $z_G/h = -0.237$ (c) $z^*/h = 0.35$, $z_G/h = -0.187$ (d) $z^*/h = 0.55$, $z_G/h = 0.013$

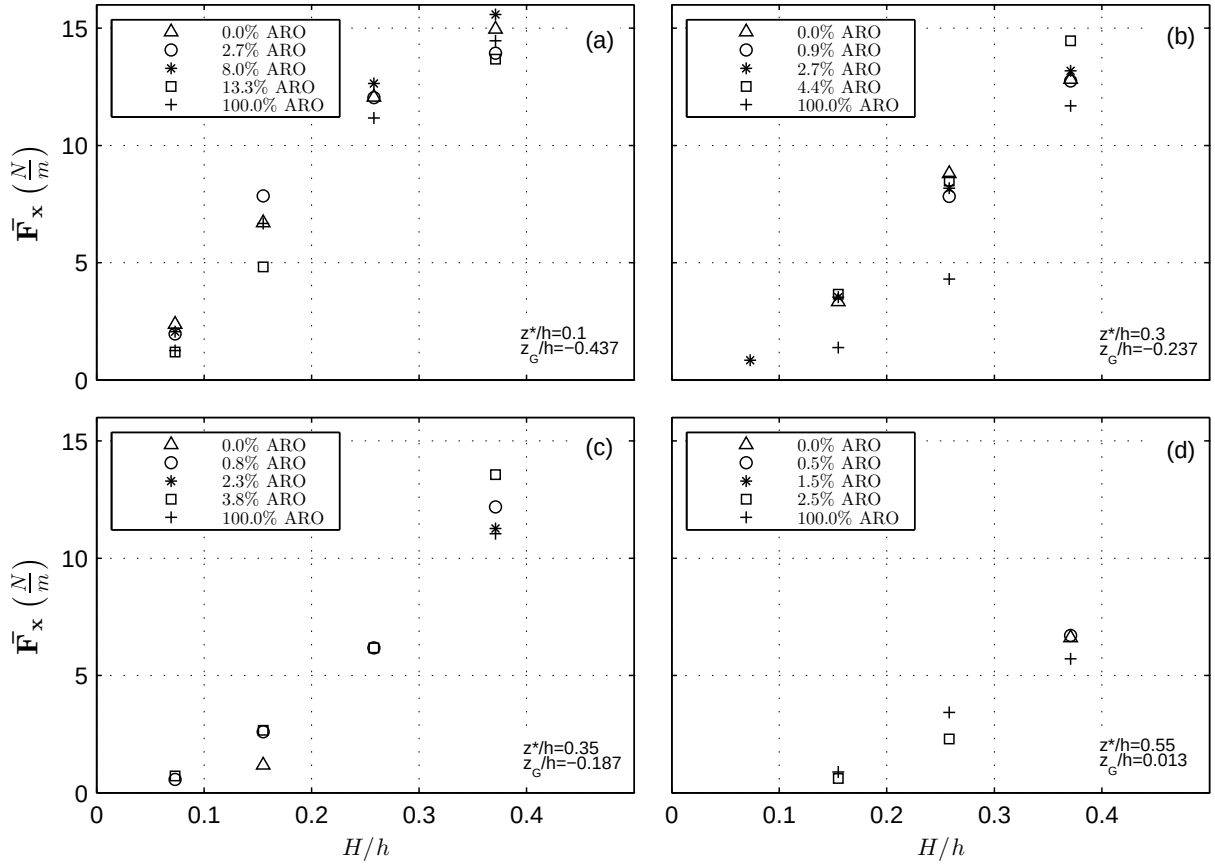

Figure 6.21: Positive horizontal forces are measured on the bridge model for percentages of air relief opening (ARO) from $0.0\% - 100.0\%$ and at wave heights approximately 0.1 - 0.4 times the water depth of $h = 0.071$ m with wavelength $\lambda = 1.7$ m for elevations (a) $z^*/h = 0.1$,$z_G/h = -0.437$ (b) $z^*/h = 0.3$, $z_G/h = -0.237$ (c) $z^*/h = 0.35$, $z_G/h = -0.187$ (d) $z^*/h = 0.55$, $z_G/h = 0.013$

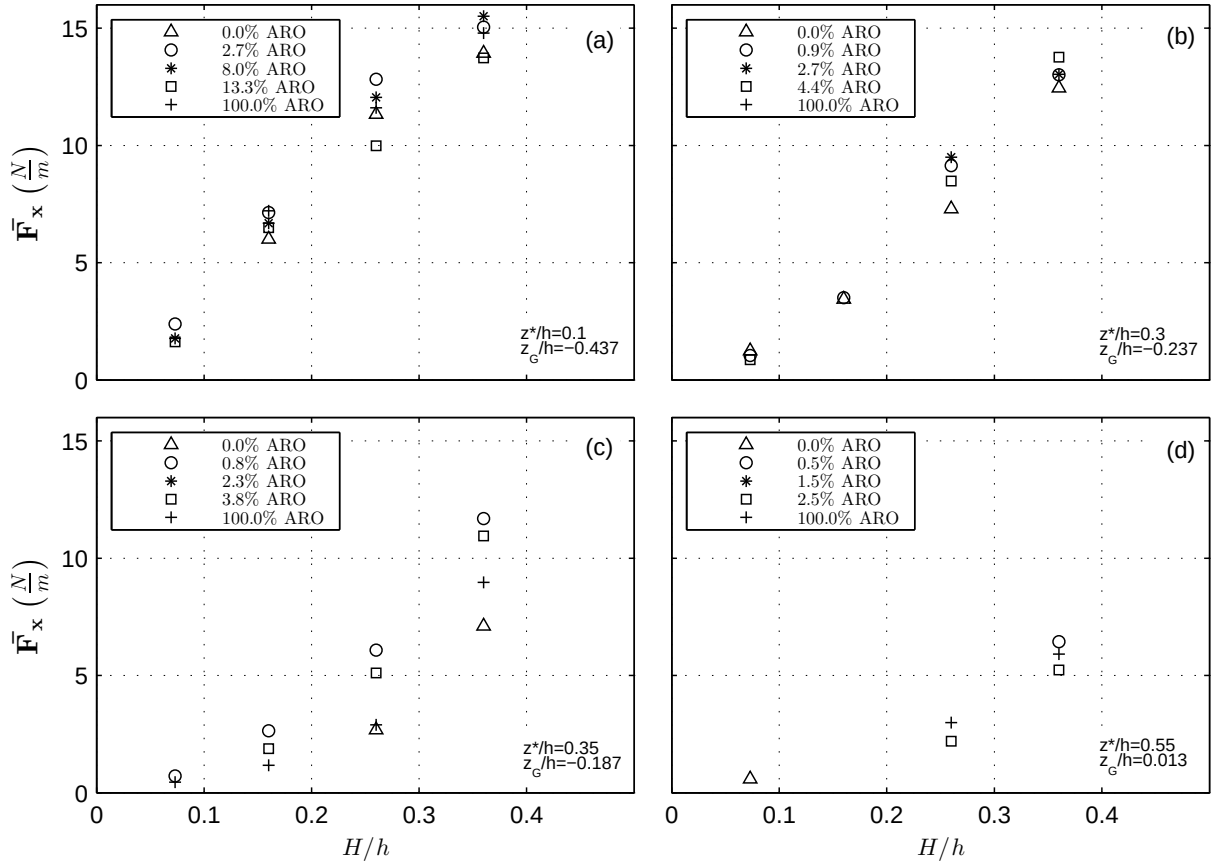

Figure 6.22: Positive horizontal forces are measured on the bridge model for percentages of air relief opening (ARO) from $0.0\% - 100.0\%$ and at wave heights approximately 0.1 - 0.4 times the water depth of $h = 0.071$ m with wavelength $\lambda = 1.9$ m for elevations (a) $z^*/h = 0.1$,$z_G/h = -0.437$ (b) $z^*/h = 0.3$, $z_G/h = -0.237$ (c) $z^*/h = 0.35$, $z_G/h = -0.187$ (d) $z^*/h = 0.55$, $z_G/h = 0.013$

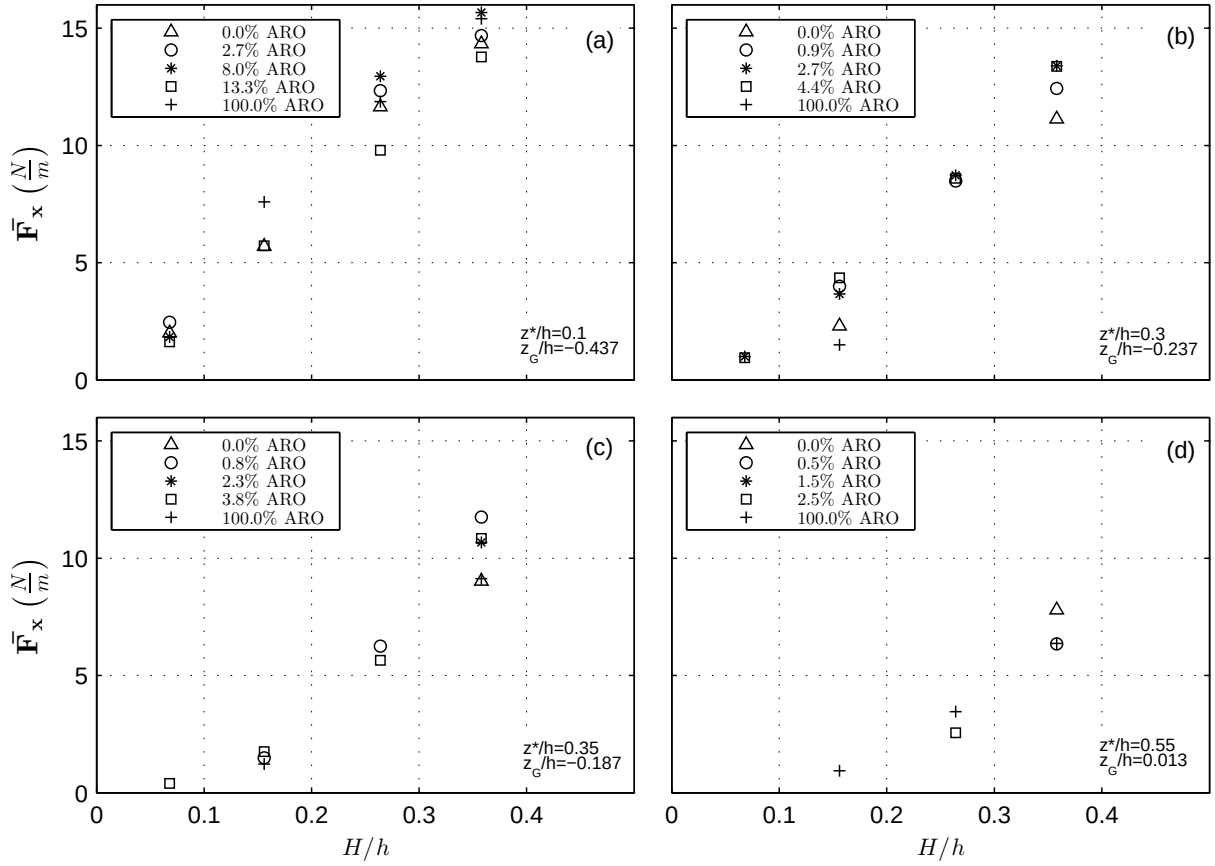

Figure 6.23: Positive horizontal forces are measured on the bridge model for percentages of air relief opening (ARO) from $0.0\% - 100.0\%$ and at wave heights approximately 0.1 - 0.4 times the water depth of $h = 0.071$ m with wavelength $\lambda = 2.1$ m for elevations (a) $z^*/h = 0.1$,$z_G/h = -0.437$ (b) $z^*/h = 0.3$, $z_G/h = -0.237$ (c) $z^*/h = 0.35$, $z_G/h = -0.187$ (d) $z^*/h = 0.55$, $z_G/h = 0.013$

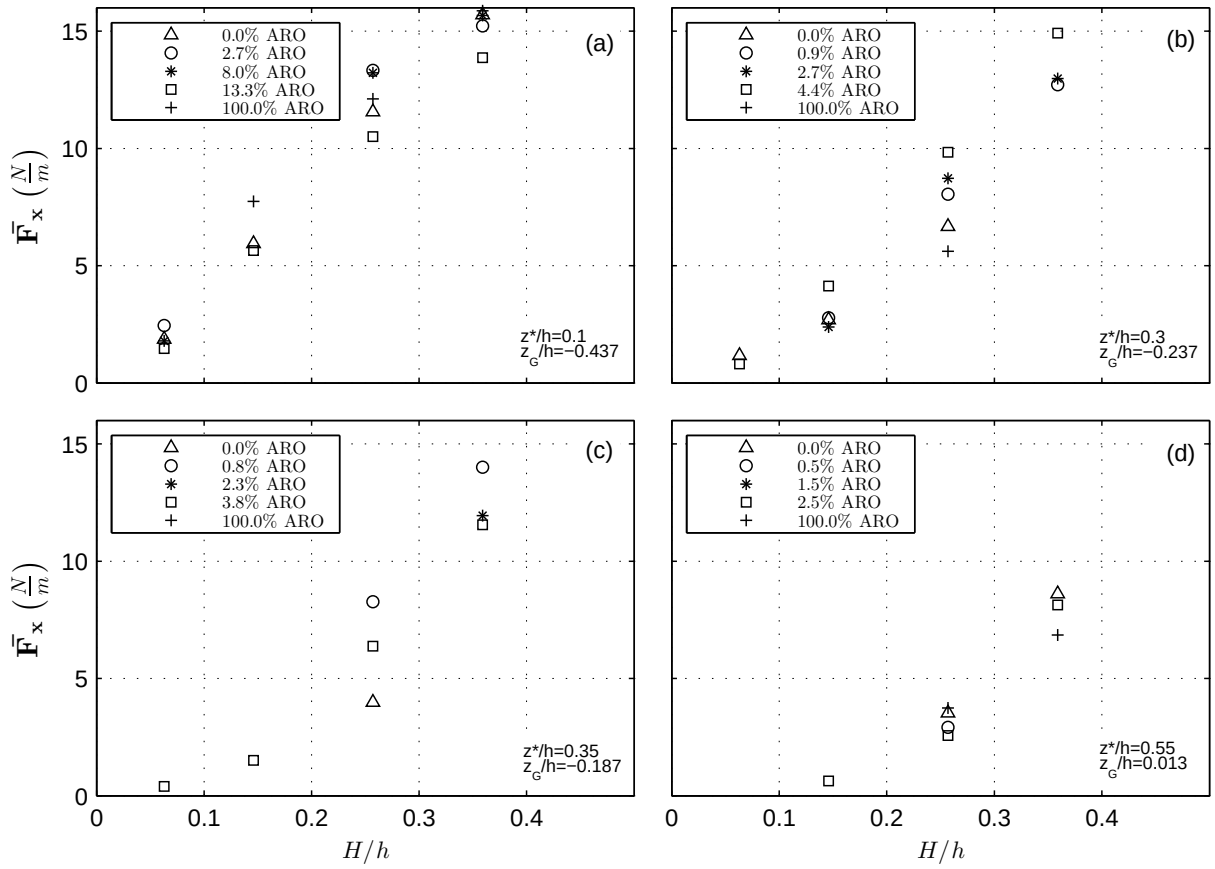

Figure 6.24: Positive horizontal forces are measured on the bridge model for percentages of air relief opening (ARO) from $0.0\% - 100.0\%$ and at wave heights approximately 0.1 - 0.4 times the water depth of $h = 0.071$ m with wavelength $\lambda = 2.3$ m for elevations (a) $z^*/h = 0.1$,$z_G/h = -0.437$ (b) $z^*/h = 0.3$, $z_G/h = -0.237$ (c) $z^*/h = 0.35$, $z_G/h = -0.187$ (d) $z^*/h = 0.55$, $z_G/h = 0.013$

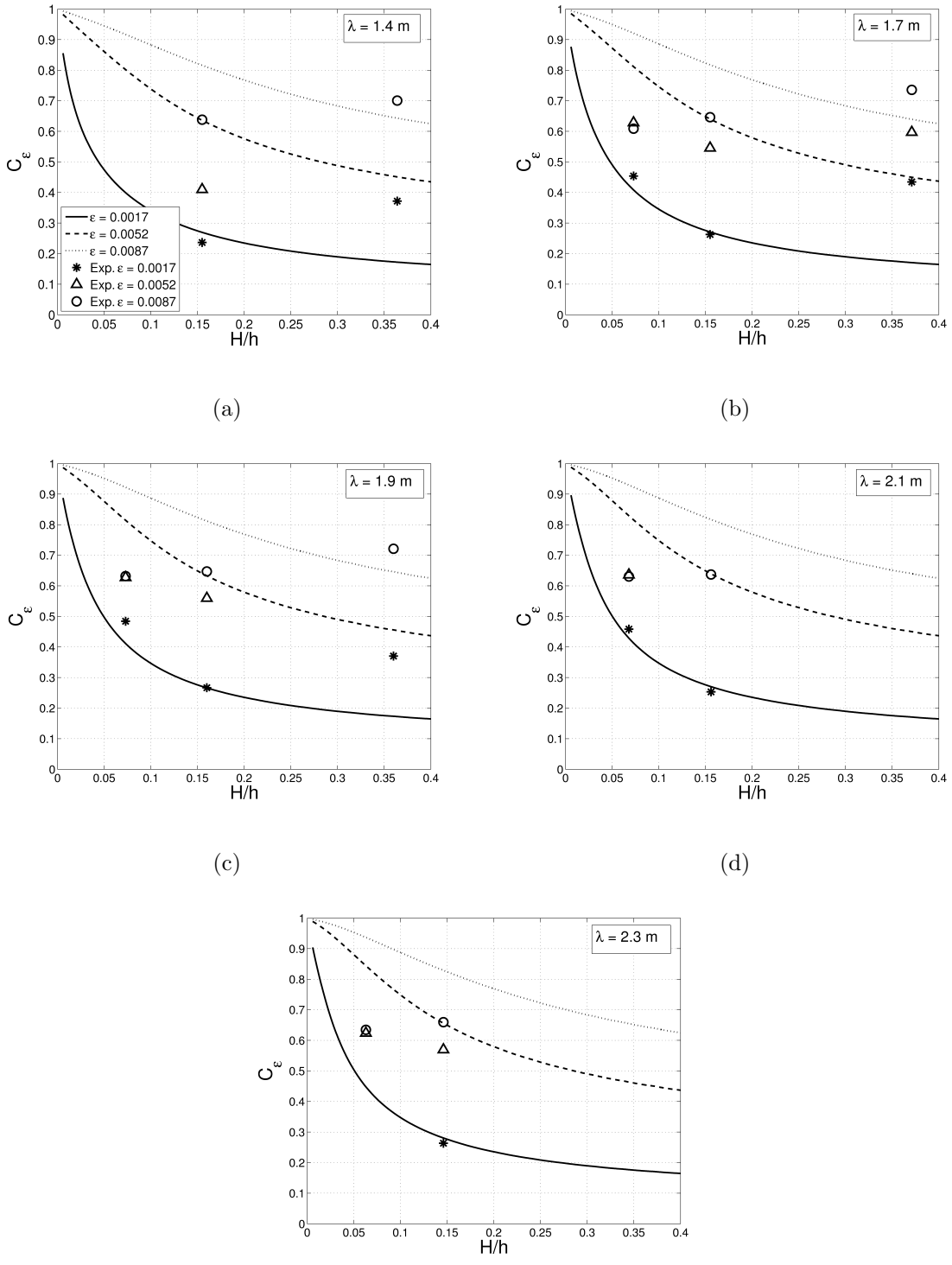

(a) (b)

(c) (d)

(e)

Figure 6.25: The reduction coefficient C_ϵ is calculated following the Bagnold-Mitsuyasu model, and is compared with the reduction measured during laboratory experiments for wave lengths $\lambda = 1.4 - 2.3$ m in (a) - (e).

6.3 Effects of Compressibility of Air

In this section, forces are calculated on the bridge model with girders using both incompressible and compressible Euler's equations. The incompressible calculations have been previously presented by Hayatdavoodi, Seiffert & Ertekin (2014*b*), and here the compressible calculations are presented. The case chosen for this comparison is the case most likely to experience effects of compressibility. This corresponds to the case $h = 0.143$ m and $z^*/h = 0.3$, where the bridge model is fully elevated above the SWL and air is trapped between the girders. Figure 6.26 shows the time series for surface elevation and vertical and horizontal forces calculated using incompressible and compressible Euler's equations as well as experimental measurements for comparison, for $h = 0.143$ m, $z^*/h = 0.3$, and $a/h = 0.2$. Figures 6.27, 6.28 and 6.29 show time series for vertical and horizontal force calculations and measurements for $a/h = 0.1, 0.3$ and 0.4, respectively. The incompressible calculations show slightly larger vertical impulse forces in Fig. 6.27 and 6.28 (a) but overall there is very little difference between the incompressible and compressible calculations for both vertical and horizontal forces. These small reductions in impulse force could be due to the cushioning effect as air compresses slightly, as suggested by Takahashi et al. (1985) in their work on effects of air compression on uplift forces.

6.4 Effects of Scale

In this section, effects of model scale on vertical and horizontal forces are considered. Vertical and horizontal force calculations are done by solving compressible Euler's equations at both the model and prototype scale. The calculated forces on the model as well as experimental measurements are scaled to the prototype scale using Froude scaling and are presented in Figs. 6.30 - 6.33 for the water depth of $h = 0.143$ m, $z^*/h = 0.3$ and $a/h =$

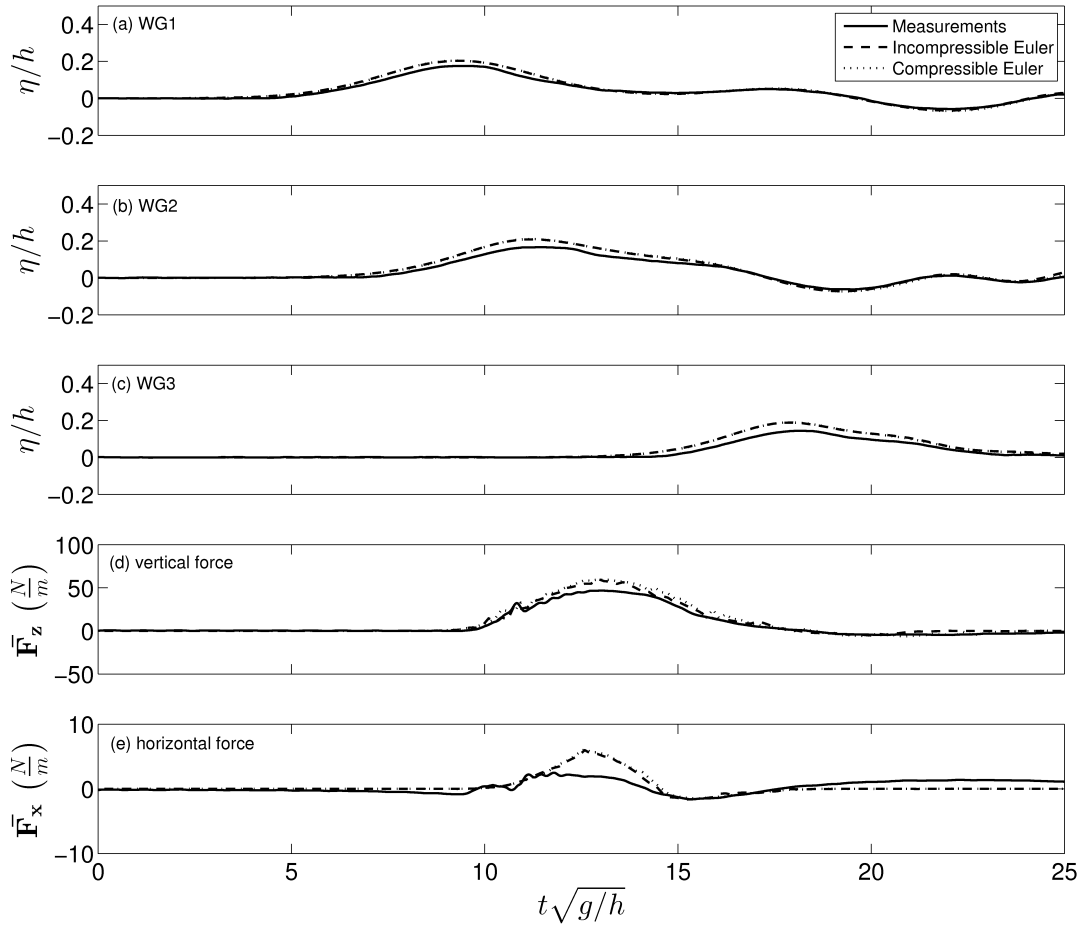

Figure 6.26: Time series for surface elevation and vertical and horizontal forces calculated using both incompressible and compressible Euler's equations are compared with laboratory measurements for a solitary wave propagating over an elevated bridge model with air trapped between girders at $h = 0.143$ m, $z^*/h = 0.3$, and $a/h = 0.2$.

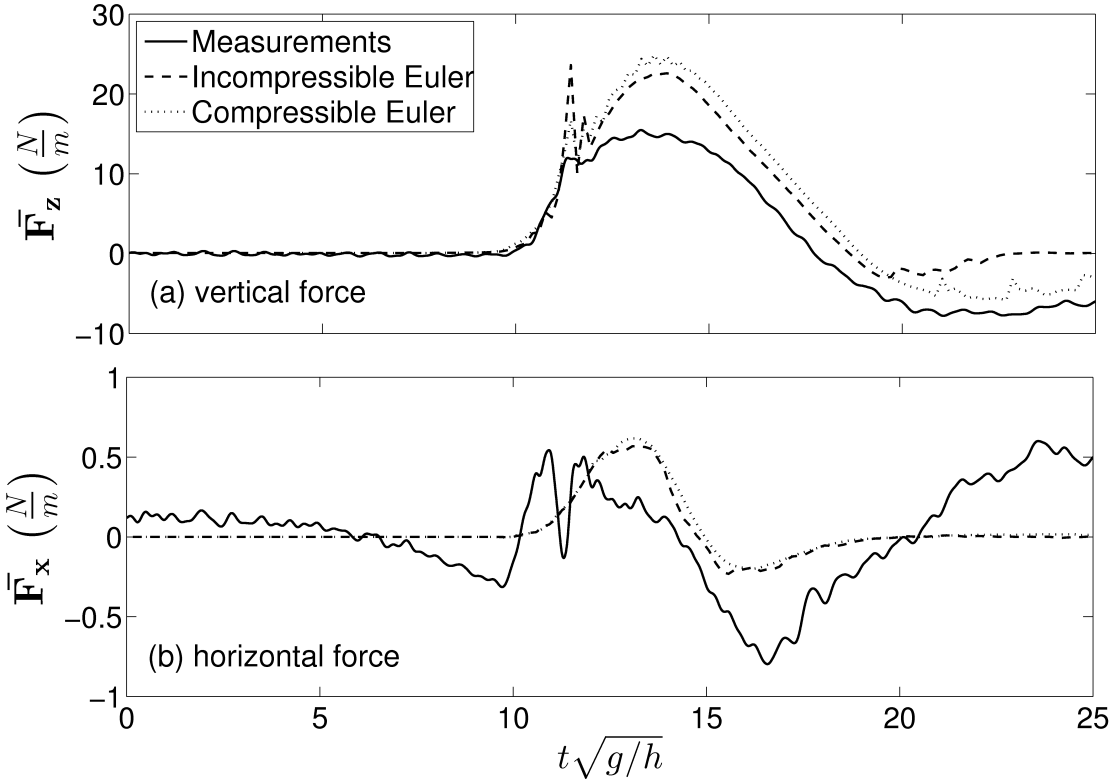

Figure 6.27: Time series for vertical and horizontal forces calculated using both incompressible and compressible Euler's equations are compared with laboratory measurements for a solitary wave propagating over an elevated bridge model with air trapped between girders at $h = 0.143$ m, $z^*/h = 0.3$, and $a/h = 0.1$.

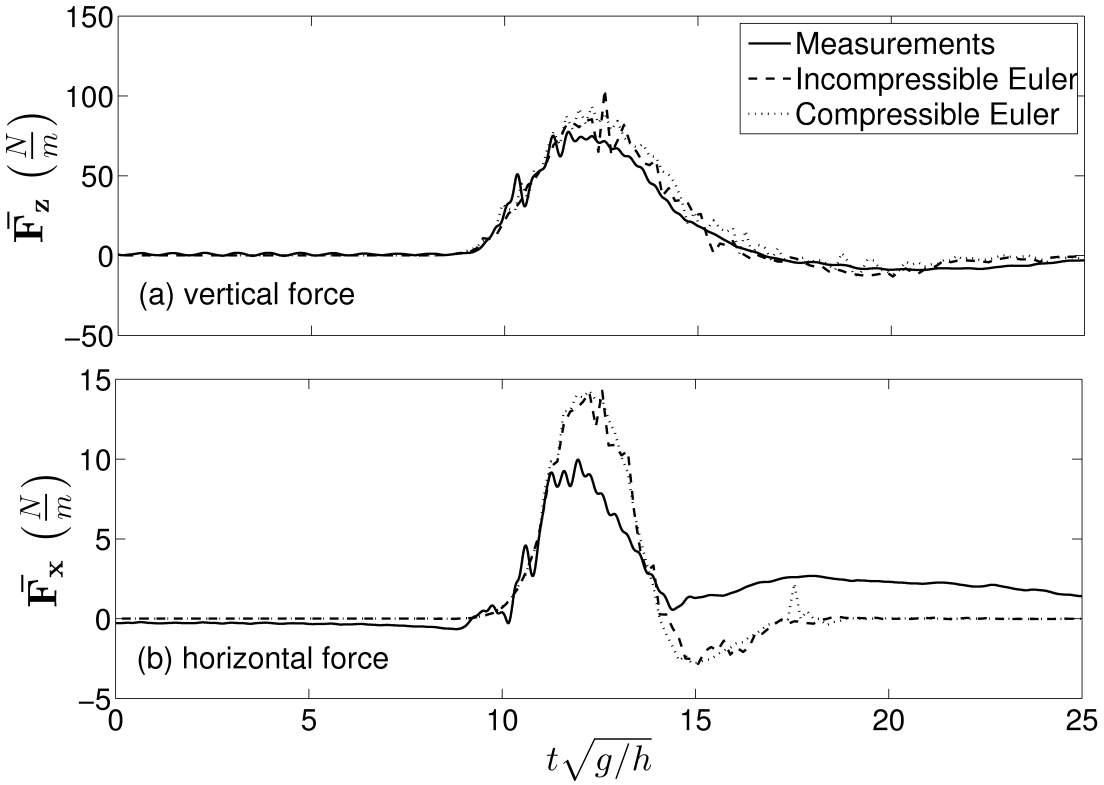

Figure 6.28: Time series for vertical and horizontal forces calculated using both incompressible and compressible Euler's equations are compared with laboratory measurements for a solitary wave propagating over an elevated bridge model with air trapped between girders at $h = 0.143$ m, $z^*/h = 0.3$, and $a/h = 0.3$.

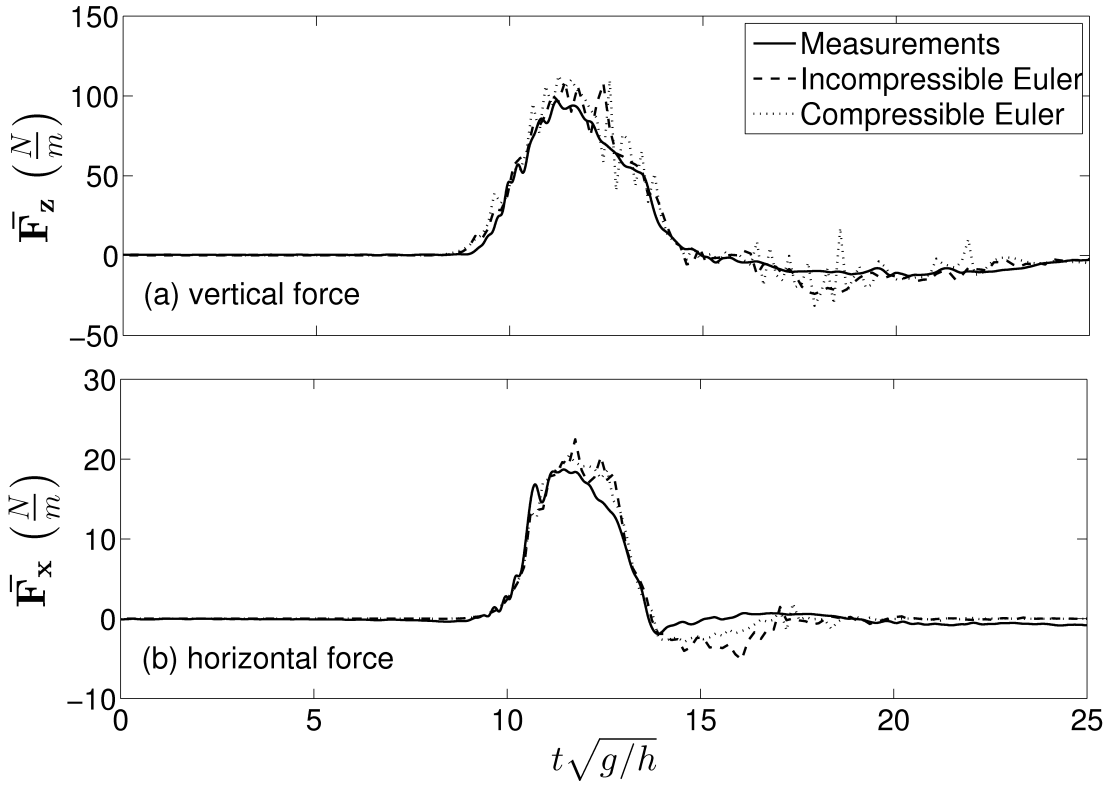

Figure 6.29: Time series for vertical and horizontal forces calculated using both incompressible and compressible Euler's equations are compared with laboratory measurements for a solitary wave propagating over an elevated bridge model with air trapped between girders at $h = 0.143$ m, $z^*/h = 0.3$, and $a/h = 0.4$.

$0.1 - 0.4$. Forces are slightly overpredicted by scaling the model to prototype scale at $a/h = 0.1$ but overall the scaled forces on the model predict the prototype forces well. There is a large uplift impact force seen at the prototype scale and not the model scale at $a/h = 0.4$ in Fig. 6.33. The experimental measurements however, do show an impact force. In fact, the magnitude of the impact force may be similar to the calculated force at the prototype scale but because of the data filtering explained in Section 2.5.2, it appears smaller.

There has been some discussion in literature as to whether forces at the model scale will overpredict forces at the prototype scale in cases where air becomes entrapped (see e.g., Takahashi et al. (1985), Cuomo et al. (2009), and Bullock et al. (2001)). Bagnold (1939) introduced the phenomena of entrapped air pockets leading to large impact pressures, and the smaller the air pocket, the larger the impact pressure. Takahashi et al. (1985) demonstrated that compression of an air pocket reduces impact pressure, but distorts the scale of the model. Air pockets can be caused by the crest of a breaking wave curling over and trapping air as it makes contact with the structure. According to Takahashi et al. (1985), for example, using Froude similitude law to scale this impact pressure from the model scale to prototype scale will overestimate the impact pressure at the prototype scale. However, for the cases presented in this study, waves remain unbroken as they interact with the structure and, therefore, in our case we do not have air pockets in the water, but rather completely separated bodies of air and water. In addition, the results here are presented as force, which is the integrated pressure over an area. Therefore, any impact pressure will be averaged out over the entire body.

Another way in which scaling from the model to prototype using Froude similitude can overestimate forces on the prototype is by underestimating the reduced buoyancy force due to air compression. As the water level rises due to the approaching wave, air is trapped between the girders and is compressed as the wave continues propagating towards the structure. This

compression of air reduces the volume of water displacement by the air, causing hydrostatic forces to be smaller. The equation for isothermal compressibility,

$$\beta \equiv -\frac{1}{V}\left(\frac{\partial V}{\partial p}\right), \tag{6.3}$$

where V is volume, indicates that air compressibility cannot be scaled (since atmospheric air pressure cannot be scaled) and therefore air will compress less at the model scale than at the prototype scale. Therefore, the water volume displacement due to air between the girders at the model scale will be less than at the prototype scale, which could cause hydrostatic forces to be overestimated. Figure 6.34 shows density calculations at the time of maximum uplift force for calculations at the model and prototype scale. At the model scale, shown in Fig. 6.34(a), air is being compressed in between the girders, which allows the water level to rise between the girders. At the prototype scale, shown in Fig. 6.34(b), air has been compressed slightly more than at the model scale, allowing more water to enter the chambers between the girders. However, as Figs. 6.34(a) and (b) show, this difference is small. These findings suggest that even though compression of air between the girders cannot be scaled when using Froude scaling, the effect this has on the overall force for the cases presented is negligible. Therefore, forces at the model scale for experiments where air is either fully trapped or fully released, can be approximated at the prototype scale using Froude scaling. This is in agreement with results of others, such as Bozorgnia et al. (2010) and Bullock et al. (2001). However, the situation may change for the case of air relief openings as difficulties scaling the release of trapped air through air relief openings mean only a qualitative comparison can be made for these cases, as suggested by Falcão & Henriques (2014) for oscillating water column (OWC) devices.

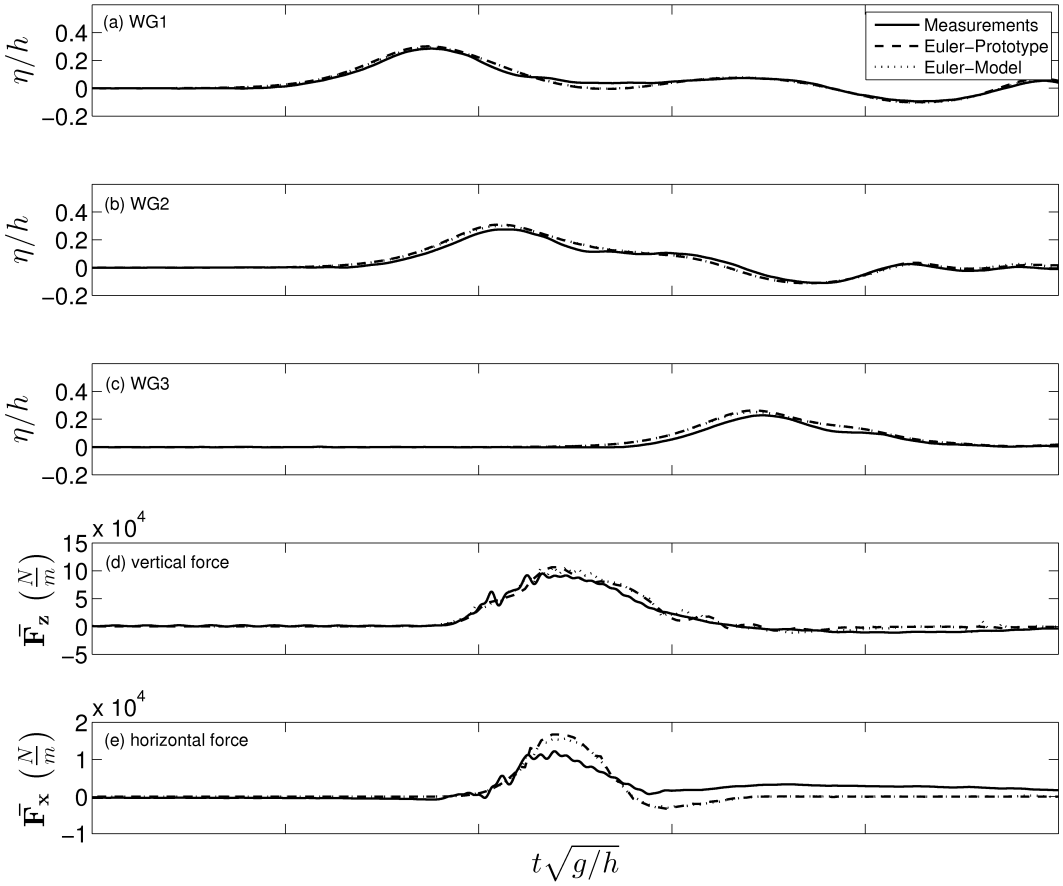

Figure 6.30: Time series for surface elevation and vertical and horizontal forces calculated at the model and prototype scale using Euler's equations are compared with laboratory measurements for a solitary wave propagating over an elevated bridge model with air trapped between girders at model water depth $h = 0.143$ m (prototype water depth $h = 5.005$ m), $z^*/h = 0.3$, and $a/h = 0.3$.

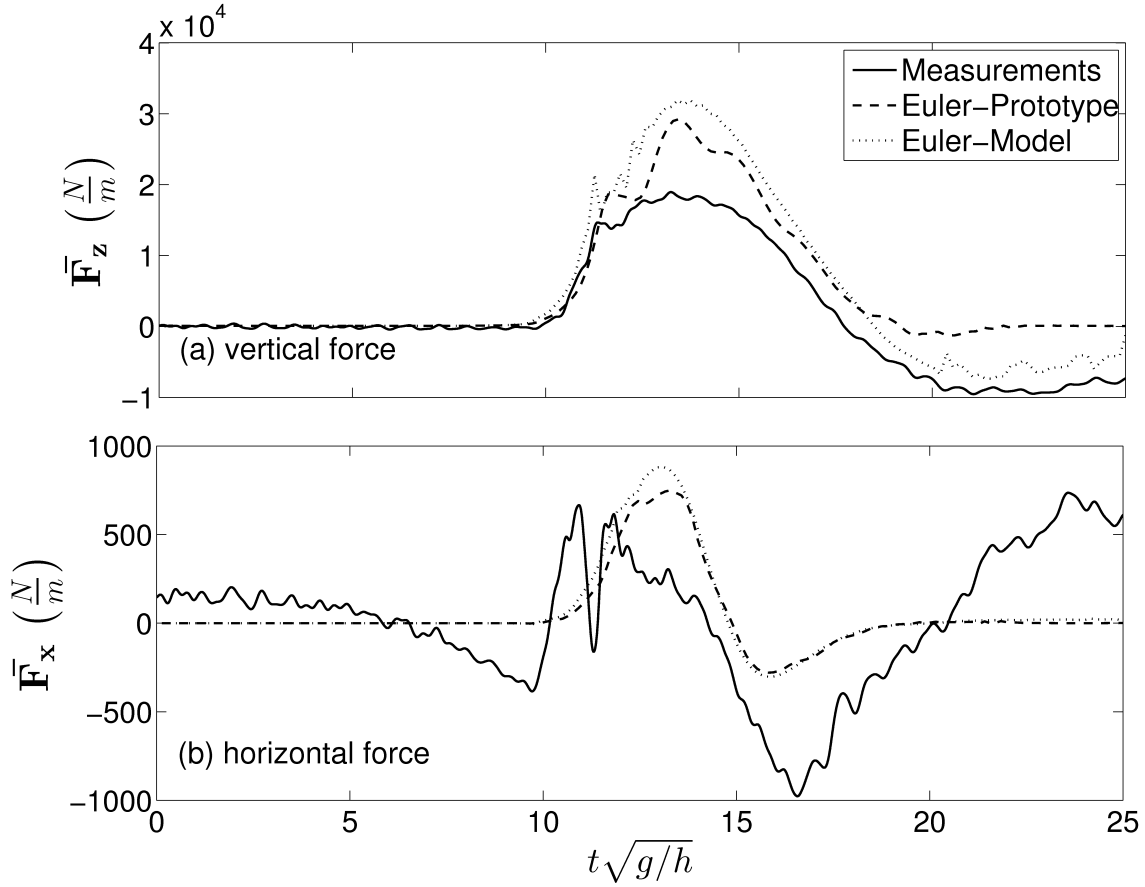

Figure 6.31: Time series for vertical and horizontal forces calculated at the model and prototype scale using Euler's equations are compared with laboratory measurements for a solitary wave propagating over an elevated bridge model with air trapped between girders at model water depth $h = 0.143$ m (prototype water depth $h = 5.005$ m), $z^*/h = 0.3$, and $a/h = 0.1$.

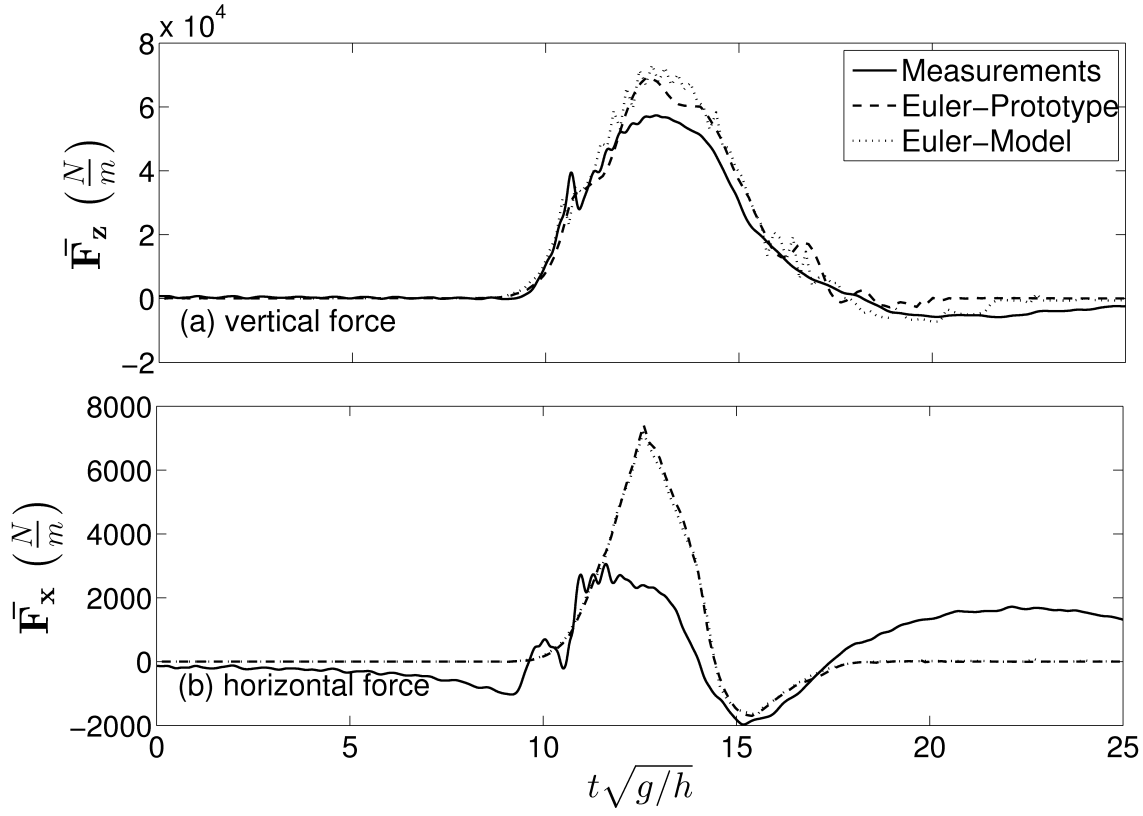

Figure 6.32: Time series for vertical and horizontal forces calculated at the model and prototype scale using Euler's equations are compared with laboratory measurements for a solitary wave propagating over an elevated bridge model with air trapped between girders at model water depth $h = 0.143$ m (prototype water depth $h = 5.005$ m), $z^*/h = 0.3$, and $a/h = 0.2$.

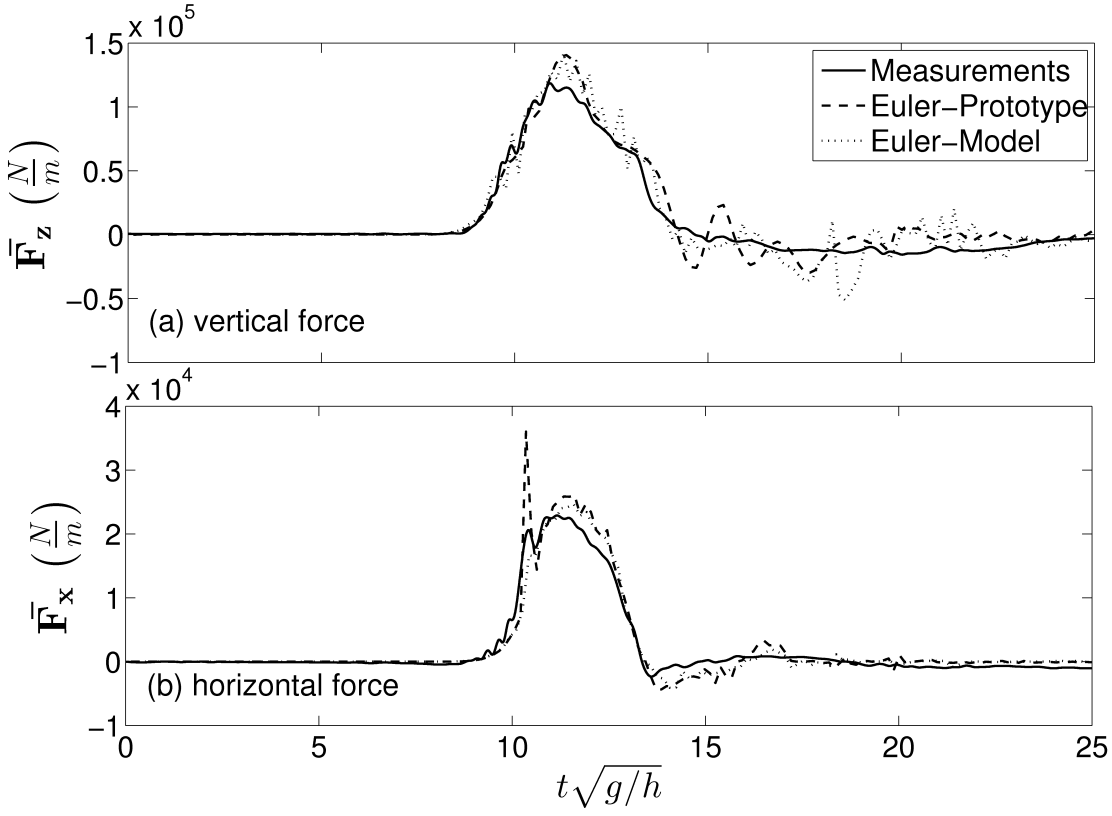

Figure 6.33: Time series for vertical and horizontal forces calculated at the model and prototype scale using Euler's equations are compared with laboratory measurements for a solitary wave propagating over an elevated bridge model with air trapped between girders at model water depth $h = 0.143$ m (prototype water depth $h = 5.005$ m), $z^*/h = 0.3$, and $a/h = 0.4$.

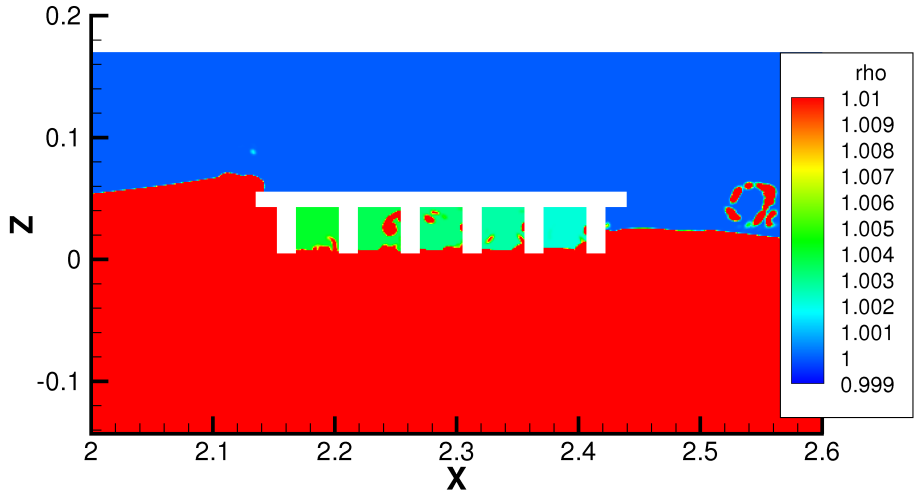

(a)

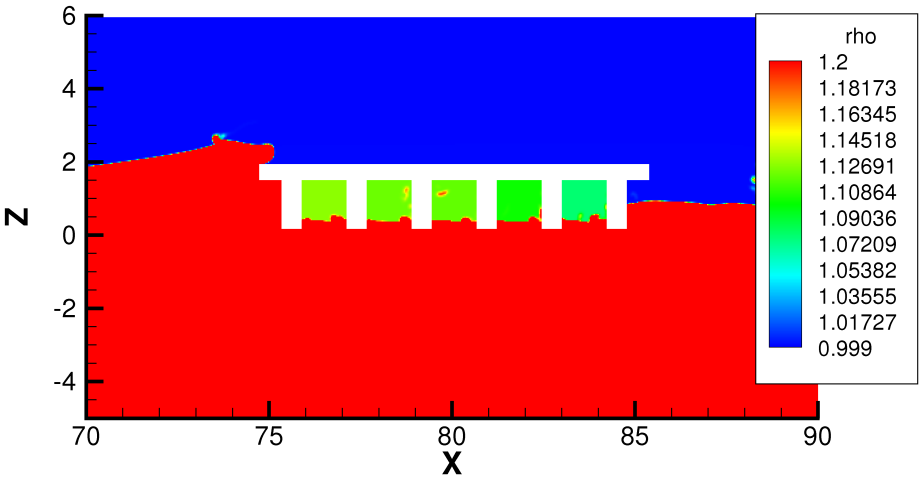

(b)

Figure 6.34: Density (rho) (kg/m^3) is calculated at the time of maximum uplift force for the (a) model and (b) prototype scale at the water depth $h = 0.143$ m, $a/h = 0.3$.

Chapter 7

Summary and Conclusions

Laboratory experiments are conducted to measure the vertical and horizontal forces due to solitary and cnoidal waves propagating over a horizontal flat plate, a bridge model with girders and a bridge model where different percentages of air is trapped between the girders. The models are at a 1:35 scale of a typical two-lane bridge common to a coastal community. A range of water depths, wave periods and wave amplitudes are tested for conditions where the model is fully or partially submerged, to fully elevated above the SWL.

Time-series data for solitary and cnoidal wave forces on a horizontal flat plate and bridge model are compared with calculations done using incompressible Euler's equations from Hayatdavoodi (2013), Seiffert, Hayatdavoodi & Ertekin (2014), and Hayatdavoodi, Seiffert & Ertekin (2014*b*) with excellent agreement for both surface elevation and vertical and horizontal forces. Differences in surface elevation are attributed to wave attenuation due to viscous effects and the small scale of the experiments. Differences between the calculated and measured forces can be partially attributed to viscous effects, the small scale of experiments, and wave breaking.

As the wave initially interacts with the model, there is an initial vertical uplift force followed by a positive horizontal force as the wave advances further toward the model. The

uplift force is explained by hydrostatic force of the incoming wave, as well as water particle accelerations causing a large difference in pressure between the bottom and top of the model. The horizontal force is due to water particle accelerations causing a difference in pressure at the leading and trailing edges of the model when the crest is at the leading edge of the model. As the wave travels over the model, a downward force is measured, mainly due to the weight of the water under the wave crest. As the wave leaves the model, a negative horizontal force is measured on the model due to the water particle accelerations causing a pressure differential between the trailing and leading edges of the model.

Vertical and horizontal forces have a weakly linear relationship with wave amplitude. Although there is some oscillation, there is little difference between the forces measured for the different wave lengths used in this study when wave height, water depth and submergence depth are constant. However, it is noted that the wave lengths were very long compared to the water depth and model length in this study. Overall, the largest forces on the model occur when the plate or deck is close to the SWL. This is where the water particle accelerations are the largest as the wave impacts the model. For cases where the bridge deck is elevated above the SWL, a large decrease in uplift forces occurs when the wave crest is such that it does not reach the underside of the deck, indicating wave interaction with the bridge deck has the greatest contribution to uplift force in these cases. Both calculations and measurements for solitary and cnoidal waves propagating over a submerged plate or bridge model show larger downward forces than upward forces provided the wave remains unbroken. Once the wave breaks, the downward forces are less than the uplift forces.

Cnoidal wave forces on a submerged horizontal flat plate are also compared with those estimated using the Long Wave Approximation given by Patarapanich (1984) and those calculated using the GN equation given in Hayatdavoodi (2013). The LWA does not accurately estimate forces on the bridge model except for the more linear cases, likely due to the LWA

being a linear theory. Agreement is much better between measurements and the nonlinear GN theory. Differences can be attributed partially to viscous effects or the assumption of the plate thickness being zero in the GN theory.

Cnoidal wave forces on an elevated flat plate and bridge model are compared with estimations made by using the empirical relations of Douglass et al. (2006). Cnoidal wave forces on an elevated flat plate are also compared with the empirical relations of McPherson (2008). There is some agreement between the laboratory measurements and empirical results, however, differences suggest that the force on a bridge due to waves cannot be estimated based on hydrostatic force alone, but hydrodynamic forces, as well as wave breaking, must also be taken into consideration. In addition, experimental data suggests the coefficient of $C_r = 0.4$, suggested by Douglass et al. (2006) in their relation for estimating horizontal force, may be too conservative, and a coefficient of $C_r = 0.2$ shows better agreement.

Entrapped air can significantly increase uplift forces on a coastal bridge model with girders, especially when the bridge is such that the girders are fully elevated above the SWL or partially submerged. Therefore, even if the bridge deck is at an elevation higher than the wave crest, the bridge will experience large uplift forces if there are no adequately-sized air relief openings. When the girders are fully elevated and the wave amplitude is less than the deck elevation, increased uplift forces due to entrapped air are primarily due to hydrostatic forces. When wave amplitude is larger than the deck elevation, or when girders are slightly submerged, effects of entrapped air pockets on overall uplift forces are reduced as there is a larger hydrodynamic component due to wave impact force. In addition, entrapped air and release of entrapped air through air relief openings slows and modifies the wave and therefore the wave-induced forces, introducing a hydrodynamic effect as well. Unlike the implicit assumptions made by existing empirical relations such as by Douglass et al. (2006) and McPherson (2008), both hydrostatic and hydrodynamic forces must be considered when

calculating wave loads on a bridge structure with or without entrapped air.

Entrapped air has a relatively smaller effect on horizontal forces in the direction of wave propagation. In fact, these forces tend to be smaller when air is trapped due to the wave only being free to interact with the first upwave girder, whereas the wave is free to interact with all the girders when air can escape.

Numerical calculations are done using the CFD software OpenFOAM to solve compressible Euler's equations at both the model and prototype scale. Comparisons between the vertical and horizontal forces calculated using compressible and incompressible Euler's equations suggest compressibility has very little effect on forces in these cases. There is evidence of a slight cushioning effect due to compressibility but the effect is small.

Forces measured during laboratory experiments and numerical calculations done at the model scale are scaled to the prototype scale using Froude similitude law and are compared with numerical calculations done at the prototype scale with excellent agreement. This suggests measurements taken during the laboratory experiments can be accurately scaled to a prototype scale using Froude scaling. It is noted however, that Froude scaling can be applied to the flat plate model or the bridge model with no trapped air, or air fully trapped between the girders. It is the author's conjecture, that the cases where air can escape through relief openings cannot be scaled using Froude scaling, based on the comparison with the Bagnold-Mitsuyasu model for reduction coefficient, as well as discussion from relevant literature, such as Falcão & Henriques (2014).

Bibliography

AASHTO (2008), *Guide Specifications for Bridges Vulnerable to Coastal Storms*, American Association of State Highway and Transportation Officials, viii+55 pp.

Andersson, J. (2011), Simulation of wave induced forces on semi submerged horizontal cylinders using openfoam, Master's thesis, Chalmers University of Technology, Göteborg, Sweden.

Bagnold, R. A. (1939), 'Interim report on wave pressure research', *Jour. of Inst. of Civil Engineers* **12**, 201–226.

Boussinesq, M. J. (1871), 'Théorie de l'intumescence liquide, appelée onde solitaire ou de translation se propageant dans un canal rectangulaire', *Acad. Sci. Paris, Comptes Rendus* **72**, 755–759.

Bozorgnia, M. (2012), Computational fluid dynamic analysis of highway bridge superstructures exposed to hurricane waves, PhD thesis, University of Southern California.

Bozorgnia, M., Lee, J.-J. & Raichlen, F. (2010), Wave structure interaction: role of entrapped air on wave impact and uplift forces, *in* 'Coastal Engineering Proceedings', Vol. 32, pp. 1–12.

Bradner, C. (2008), Large-scale laboratory observations of wave forces on a highway bridge superstructure, Master's thesis, Oregon State University, Corvallis, OR.

Brater, E. F., McNown, J. S. & Stair, L. D. (1958), 'Wave forces on submerged structures', *J. Hydraulics Division, ASCE* **84**, 1–26.

Bricker, J. D., Kawashima, K. & Nakayama, A. (2012), CFD analysis of bridge deck failure due to tsunami, *in* 'Proc. of the International Symposium on Engineering Lessons Learned from the 2011 Great East Japan Earthquake', Tokyo, Japan, pp. 1398–1409.

Brossard, J., Perret, G., Blonce, L. & Diedhiou, A. (2009), 'Higher harmonics induced by a submerged horizontal plate and a submerged rectangular step in a wave flume', *Coastal Engineering* **56**(1), 11–22.

Bullock, G. N., Crawford, A. R., Hewson, P. J., Walkden, M. J. A. & Bird, P. A. D. (2001), 'The influence of air and scale on wave impact pressures', *Coastal Engineering* **42**, 291–312.

Carter, R. W. (2005), Wave energy converters adn a submerged horizontal plate, Master's thesis, Univ. of Hawaii at Manoa, Honolulu, HI.

Carter, R. W., Ertekin, R. C. & Lin, P. (2006), On the reverse flow beneath a submerged plate due to wave action, *in* 'OMAE2006 25th International Conference on Offshore Mechanics and Arctic Engineering, Hamburg, Germany', ASME, pp. 595–602.

Chella, M. A., Tørum, A. & Myrhaug, D. (2012), 'An Overview of Wave Impact Forces on Offshore Wind Turbine Substructures', *Energy Procedia* **20**, 217–226.

Chen, Q., Wang, L. & Zhao, H. (2009), 'Hydrodynamic Investigation of Coastal Bridge Collapse during Hurricane Katrina', *Journal of Hydraulic Engineering* **135**(3), 175–186.

Chen, Y. (2013), Experimental Study of Counter-Propagating Solitary Wave Collisions, PhD thesis, Oregon State University, Corvallis, OR.

Cho, Y. S. (2003), 'A note on estimation of the jacobian elliptic parameter in cnoidal wave theory', *Ocean Engineering* **30**, 1915–1922.

Cuomo, G., Shimosako, K. & Takahashi, S. (2009), 'Wave-in-deck loads on coastal bridges and the role of air', *Coastal Engineering* **56**, 793–809.

Cuomo, G., Tirindelli, M. & Allsop, W. (2007), 'Wave-in-deck loads on exposed jetties', *Coastal Engineering* **54**(9), 657–679.

Denson, K. H. (1978), Wave forces on causeway-type coastal bridges, Technical Report MS 39762, Water Resources Research Institute, Mississippi State University.

Douglass, S. L., Chen, Q., Olsen, J. M., Edge, B. L. & Brown, D. (2006), Wave forces on bridge decks, Technical report, U.S. Department of Transportation, Office of Bridge Technology, Washington, DC, vi+74 pp.

El Ghamry, O. A. (1963), *Wave Forces on a Dock*, University of California, Berkeley, Hydraulic Engineering Laboratory, Institute of Engineering Research Technical Report.

Ertekin, R. C. (1984), Soliton Generation by Moving Disturbances in Shallow Water: Theory, Computation and Experiment, PhD thesis, University of California at Berkeley.

Ertekin, R. C. & Becker, J. M. (1998), 'Nonlinear diffraction of waves by a submerged shelf in shallow water', *J. Offshore Mech. Arct. Eng., ASME,* **120**, 212–220.

Ertekin, R. C. & Wehausen, J. V. (1986), Some soliton calculations, *in* W. Webster, ed., 'Proc. 16th Symp. on Naval Hydrodynamics', National Academy Press, Washington, D.C., 1987, Berkeley, pp. 167–184.

Falcão, A. F. O. & Henriques, J. C. C. (2014), 'Model-prototype similarity of oscillating-water-column energy converters.', *International Journal of Marine Energy* **6**, 18–34.

French, J. A. (1979), Wave uplift pressures on horizontal platforms, Technical report, W. M. Keck Laboratory of Hydraulics and Water Resources, Division of Engineering and Applied Science, California Institute of Technology, Report No. KH-R-19, Pasadena, California, xi+415 pp.

Goring, D. G. (1979), Tsunamis – the propagation of long waves onto a shelf, PhD thesis, California Institute of Technology, Pasadena, CA, xviii+337 pp.

Goring, D. G. & Raichlen, F. (1980), The generation of long waves in the laboratory, *in* 'Proceedings of the 17th Coastal Engineering Conference', American Society of Civil Engineers, pp. 763–783.

Graw, K.-U. (1993), Shore protection and electricity by submerged plate wave energy converter, *in* 'Proc. European Wave Energy Symp.', National Engineering Laboratory Executive Agency, East Kilbride, Scotland, pp. 379–384.

Green, A. E. & Naghdi, P. M. (1974), 'On the theory of water waves', *Proceedings of the Royal Society of London. Series A, Mathematical and Physical Sciences* **338**(1612), 43–55.

Guizien, K. & Barthelemy, E. (2002), 'Accuracy of solitary wave generation by a piston wave maker', *Journal of Hydraulic Research* **40**(3), 321–331.

Hayatdavoodi, M. (2013), Nonlinear Wave Loads On Decks Of Coastal Structures, PhD thesis, University of Hawaii at Manoa, December, xiv+186 pp.

Hayatdavoodi, M. (2014), personal communication.

Hayatdavoodi, M. & Ertekin, R. C. (2012), Nonlinear forces on a submerged, horizontal plate : The GN theory, *in* '27th International Workshop On Water Waves And Floating Bodies', Copenhagen, Denmark, pp. 69–72.

Hayatdavoodi, M., Seiffert, B. & Ertekin, R. C. (2014*a*), 'Experiments and calculations of cnoidal wave loads on a flat plate in shallow water', *J. Ocean Engineering and Marine Energy* (Submitted), Springer.

Hayatdavoodi, M., Seiffert, B. & Ertekin, R. C. (2014*b*), 'Experiments and computations of solitary-wave forces on a coastal-bridge deck. Part II: Deck with girders', *Coastal Engineering* **88**(June), 210–228.

Higuera, P., Lara, J. L. & Losada, I. J. (2013), 'Simulating coastal engineering processes with openfoam', *Coastal Engineering* **71**, 119–134.

Hoshikuma, J., Zhang, G., Nakao, H. & Sumimura, T. (2013), Tsunami-induced effects on girder bridges, *in* 'Proc. International Symposium for Bridge Earthquake Engineering in Honor of Retirement of Prof. Kazuhiko Kawashima', pp. 1–13.

Huang, W. & Xiao, H. (2009), 'Numerical Modeling of Dynamic Wave Force Acting on Escambia Bay Bridge Deck during Hurricane Ivan', *Journal of Waterway, Port, Coastal and Ocean Engineering* **135**(4), 163–174.

Hughes, S. A. (1993), *Physical Models and Laboratory Techniques in Coastal Engineering*, Vol. 7 of *Advanced series on ocean engineering*, World Scientific.

Isaacson, M. & Bhat, S. (1996), 'Wave Forces on a Horizontal Plate', *International Journal of Offshore and Polar Engineering* **6**(1), 19–26.

Jacobsen, N. G., Fuhrman, D. R. & Fredsoe, J. (2012), 'A wave generation toolbox for the open-source CFD library : OpenFoam', *Int. J. for Numerical Methods in Fluids* **70**(9), 1073–1088.

Jasak, H., Tukovic, Z. & Jemcov, A. (2007), Openfoam:a c ++ library for complex physics

simulations, *in* 'International Workshop on Coupled Methods in Numerical Dynamics', Dubrovnik, Croatia.

Jin, J. & Meng, B. (2011), 'Computation of wave loads on the superstructures of coastal highway bridges', *Ocean Engineering* pp. 1–16.

Kulin, G. (1958), Solitary wave forces on submerged cylinders and plates, Technical Report 5876, National Bureau of Standards.

Lau, T. L., Ohmachi, T., Inoue, S. & Lukkunaprasit, P. (2011), Experimental and Numerical Modeling of Tsunami Force on Bridge Decks, *in* M. Mokhtari, ed., 'Tsunami - A Growing Disaster', number 2005, InTech, chapter 6, pp. 105–130.

Le Mehaute, B. (1969), An introduction to hydrodynamics and water waves, vol. 2: Water wave theories, Technical report, U.S. Dept. of Commerce, Environmental Science Services Administration, Pacific Oceanographic Laboratories.

Liu, C., Huang, Z. & Tan, S. K. (2009), 'Nonlinear scattering of non-breaking waves by a submerged horizontal plate: Experiments and simulations', *Ocean Engineering* **36**(17-18), 1332–1345.

Lo, H.-y. & Liu, P. L. (2014), 'Solitary Waves Incident on a Submerged Horizontal Plate', *Journal of Waterway Port Coastal and Ocean Engineering* **140**(May/June), 04014009–1:17.

Lysenko, D. a., Ertesvåg, I. S. & Rian, K. E. (2013), 'Modeling of turbulent separated flows using openfoam', *Computers & Fluids* **80**, 408–422.

Madsen, O. S. (1971), 'On the generation of long waves', *Journal of Geophysical Research* **76**(36), 8672–8683.

Malek-Mohammadi, S. & Testik, F. Y. (2010), 'New methodology for laboratory generation of solitary waves', *Journal of Waterway, Port, Coastal, and Ocean Engineering* pp. 286–294.

Marin, J. M. (2009), Wave Loading on a Horizontal Plate, PhD thesis, University of Florida, Gainesville, FL.

McConnell, K., Allsop, W. & Cruickshank, I. (2004), *Piers, jetties, and related structures exposed to waves: Guidelines for hydraulic loadings*, first edn, Thomas Telford Press, London, xvi+148 pp.

McPherson, R. L. (2008), Hurricane induced wave and surge forces on bridge decks, Master's thesis, Texas A&M University, xii+90 pp.

Mitsuyasu, H. (1966), Shock pressure of breaking wave, *in* 'Proc. of 10th Conference on Coastal Engineering', pp. 268–283.

Newman, J. N. (1978), *Marine Hydrodynamics*, Cambridge: MIT Press.

OpenFOAM (2014), Openfoam, the open source cfd toolbox, user guide version 2.3.0, Technical report.

Overbeek, J. & Klabbers, I. M. (2001), Design of jetty decks for extreme vertical wave loads, *in* 'A.S. of Civil Engineers, ed., 'Ports 2001", ASCE, pp. 1–10.

Patarapanich, M. (1984), 'Forces and moment on a horizontal plate due to wave scattering', *Coastal Engineering* **8**(3), 279–301.

Rayleigh, L. (1876), 'On waves', *Philos. Mag.* **1**, 257–279.

Rey, V. & Touboul, J. (2011), 'Forces and moment on a horizontal plate due to regular and irregular waves in the presence of current', *Applied Ocean Research* **33**(2), 88–99.

Robertson, I. N., Yim, S., Riggs, H. R. & Young, Y. L. (2007), Coastal bridge performance during Hurricane Katrina, *in* 'Proceedings of the International Conference on Structural Engineering, Mechanics and Computation 2April 2001, Cape Town, South Africa', Millpress, The Netherlands, pp. 1864–1870.

Russell, S. (1844), Report on waves, *in* J. Murray, ed., 'Brit. Assoc. Adv. Sci. Rep., 14th Mtg. York, 1844', London, pp. 311–390.

Sarpkaya, T. & Isaacson, M. (1981), *Mechanics of wave forces on offshore structures*, Litton Educational Publishing, Inc., xiv+651 pp.

Seiffert, B., Ertekin, R. C. & Robertson, I. N. (2014*a*), 'Effect of entrapped air on solitary wave forces on a coastal bridge deck with girders', *J. Bridge Engineering* (Submitted), ASCE.

Seiffert, B., Ertekin, R. C. & Robertson, I. N. (2014*b*), Experimetnal investigation on the role of entrapped air on solitary wave forces on a coastal bridge deck, *in* 'Proc. 33rd Int. Conf. on Ocean, Offshore and Arctic Engineering, OMAE '14, ASME,', San Francisco, California, USA, p. 8.

Seiffert, B., Hayatdavoodi, M. & Ertekin, R. C. (2014), 'Experiments and computations of solitary-wave forces on a coastal-bridge deck. Part I: Flat plate', *Coastal Engineering* **88**(June), 194–209.

Sheppard, D. M. & Marin, J. (2009), Wave loading on bridge decks, Technical report, Florida Department of Transportation, Gainsville, Florida.

Shih, R. W. K. & Anastasiou, K. (1992), A laboratory study of the wave-induced vertical loading on platform decks, *in* 'Proceedings of the ICE - Water Maritime and Energy', Vol. 96, pp. 19–33.

Siew, P. F. & Hurley, D. G. (1977), 'Long surface waves incident on a submerged horizontal plate', *J. Fluid Mechanics* **83**, 141–151.

Sun, X. (1991), Some theoretical and numerical studies on cnoidal-wave-diffraction problems, Master's thesis, University of Hawaii at Manoa, Honolulu, HI, xii+149 pp.

Suponitsky, V., Barsky, S. & Froese, A. (2014), 'Richtmyer-meshkov instability of a liquid-gas interface driven by a cylindrical imploding pressure wave', *Computers & Fluids* **89**, 1–19.

Synolakis, C. E. (1990), 'Generation of long waves in laboratory', *Journal of Waterway, Port, Coastal and Ocean Engineering* **116**(2), 252–266.

Takahashi, S., Tanimoto, K. & Miyanaga, S. (1985), 'Uplift wave forces due to compression of enclosed air layer and their similitude law', *Coastal Engineering in Japan* **28**, 191–206.

Takaki, M. (2001), Hydrodynamic Forces on a Submerged Plate, *in* 'Proc. 11th International Offshore and Polar Engineering Conference', Vol. III, pp. 518–524.

Tirindelli, M., Cuomo, G., Allsop, W. & McConnell, K. (2002), Exposed jetties: Inconsistencies and gaps in design methods for wave-induced forces, *in* 'Proceedings of the International Conference on Coastal Engineering, Wales, United Kingdom, ASCE', pp. 1684–1696.

Trask, N. A. (2010), Implementation of an eulerian atomization model to characterize primary spray formation, Master's thesis, University of Massachusetts, Amherst, Massachusetts.

Wang, H. (1970), 'Water wave pressure on horizontal plate', *J. Hydraulics Division, ASCE* **96**(10), 1997–2016.

Weller, H. G., Tabor, G., Jasak, H. & Fureby, C. (1998), 'A tensorial approach to com-

putational continuum mechanics using object-oriented techniques', *Computers in Physics* **12**(6), 620–631.

Yeh, H. (2013), personal communication.